Measurement of the Diffractive Structure Function of the Antiproton in 1.8-TeV Proton-Antiproton Collisions

Hosai NAKADA

A dissertation submitted to the Doctoral Program
in Physics, the University of Tsukuba
in partial fulfillment of the requirements
for the degree of Doctor of Philosophy (Science)

January 2001

Abstract

We present the measurement of the diffractive structure function of the antiproton in proton-antiproton collisions at the center-of-mass energy of 1.8 TeV. The data were collected during the 1995-1996 Tevatron collider run using the Collider Detector at Fermilab (CDF). Diffractive events are characterized by the recoil $\bar{p}$ and the forward rapidity gap in the fnal state. In order to tag the recoil $\bar{p}$, we installed a Roman-pot type antiproton spectrometer (RPS), and using the forward calorimeter and the beam-beam counter, we identify the rapidity gap. In order to identify a hard collision, we require the presence of two or more jets. In this analysis, we calculate the hard scale in the interaction (Q^2), the momentum fraction of antiproton carried by struck parton ($x_{\overline{p}}$), and the fractional momentum of the struck parton in the exchanged object (β).

We obtained the diffractive structure function as a function of β and Q^2 in the kinematic region of $0.035 \leq \xi \leq 0.095$ and $|t| \leq 1$ GeV^2. We observe no Q^2 dependence in the diffractive structure function of the antiproton in the Q^2 region measured in this study. This is consistent with the H1 result at HERA *ep* collider experiment. The absolute value of the diffractive structure function measured at CDF is smaller than that of the H1 result by, approximately, a factor of 1/7. The discrepancy is also observed in other results at CDF such as the diffractive W and b-quark production where the cross section is about 20% of the prediction using the Donnachie-Landshoff pomeron flux. These results suggest that the diffractive cross section is not described by using the universal diffractive structure function of the antiproton.

Acknowledgments

I would like to thank my advisor, Professor Shinhong Kim, for his guidance and encouragement throughout my graduate years. He has provided me with advice in many phases of my study. I would like to thank Professor Kunitaka Kondo and Professor Koji Takikawa, who gave me not only the opportunity to join the CDF experiment and the support in working on CDF but also advice physics on.

My deep appreciation is due to Professor Konstantin Goulianos, Drs. Michael Albrow, Kiyoshi Yasuoka, Philip Mélèse , Junsuke Iwai, Kerstin Borras, Hirofumi Ikeda, Koji Terashi and Mr. Ken-ichi Hatakeyama, who not only led our experiment using the Roman-pot spectrometer to success but also gave me many valuable advice, help and discussion. And I would like to thank Professor Anwar Bhatti and Doctor Robert Blair for their help and discussion.

I would like to thank people from the Accelerator Division, especially Dr. Craig Moore for not only giving us their valuable informations about Tevatron accelerator elements but also advising us how to handle the Roman-pot data. I also would like to thank Dr. Dave Carey for his detailed explanation of the TRANSPORT program.

I would like to thank Professor Fumihiko Ukegawa, Professor Kazuhiko Hara, Professor Yoshihiro Seiya, Drs. Ryutaro Oishi, Takashi Asakawa, Jun-ichi Suzuki, Takeshi Takano, Mr. Toshiharu Uchida, Mr. Masahiko Yokoyama, and Mr. Tomohiro Kaneko for the encouragement throughout my graduate years as well as for their valuable suggestions, and I had a very good time with them. Many thanks go to Dr. and Mrs. Syu-ichi Kunori, Dr. and Mrs. Nobuaki Oshima, and Dr. Luc Demortier for their help in my private life in the USA. I would like to thank the members of the Tsukuba high energy physics group, for their help and discussion.

I thank the Fermilab staffs and the technical staffs of the participating institutions for their vital contributions. I thank many CDF collaborators who have developed the detector and other analysis environment.

I want to express my great appreciation to Mrs. Kyoko Kunori, Mrs. Kazuko Kumashiro, Mrs. Mutsumi Uenishi, Mrs. Deedee Hahn and Mrs. Carol Picciolo for their help through their secretary works.

Many thanks go to Mr. Daijirou Takano and the all members of my volleyball club team for their encouragement.

Finally and most importantly I thank my parents, sister and brother for their constant support and encouragement.

This work was supported by the U. S. Department of Energy and National Science Foundation; the Italian Istituto Nazionale di Fisica Nucleare; the Ministry of Education, Science and Culture of Japan; the Natural Sciences and Engineering Research Council of Canada; the National Science Council of the Republic of China; and the A. P. Sloan Foundation.

Contents

List of Figures

List of Tables

The CDF Collaboration

F. Abe,[17] H. Akimoto,[39] A. Akopian,[31] M. G. Albrow,[7] A. Amadon,[5] S. R. Amendolia,[27] D. Amidei,[20] J. Antos,[33] S. Aota,[37] G. Apollinari,[31] T. Arisawa,[39] T. Asakawa,[37] W. Ashmanskas,[5] M. Atac,[7] P. Azzi-Bacchetta,[25] N. Bacchetta,[25] S. Bagdasarov,[31] M. W. Bailey,[22] P. de Barbaro,[30] A. Barbaro-Galtieri,[18] V. E. Barnes,[29] B. A. Barnett,[15] M. Barone,[9] G. Bauer,[19] T. Baumann,[11] F. Bedeschi,[27] S. Behrends,[3] S. Belforte,[7] G. Bellettini,[27] J. Bellinger,[40] D. Benjamin,[35] J. Bensinger,[3] A. Beretvas,[7] J. P. Berge,[7] J. Berryhill,[5] S. Bertolucci,[9] S. Bettelli,[27] B. Bevensee,[26] A. Bhatti,[31] K. Biery,[7] C. Bigongiari,[27] M. Binkley,[7] D. Bisello,[25] R. E. Blair,[1] C. Blocker,[3] K. Bloom,[20] S. Blusk,[30] A. Bodek,[30] W. Bokhari,[26] G. Bolla,[29] Y. Bonushkin,[4] K. Borras,[31] D. Bortoletto,[29] J. Boudreau,[28] L. Breccia,[2] C. Bromberg,[21] N. Bruner,[22] R. Brunetti,[2] E. Buckley-Geer,[7] H. S. Budd,[30] K. Burkett,[11] G. Busetto,[25] A. Byon-Wagner,[7] K. L. Byrum,[1] M. Campbell,[20] A. Caner,[27] W. Carithers,[18] D. Carlsmith,[40] J. Cassada,[30] A. Castro,[25] D. Cauz,[36] A. Cerri,[27] P. S. Chang,[33] P. T. Chang,[33] H. Y. Chao,[33] J. Chapman,[20] M. -T. Cheng,[33] M. Chertok,[34] G. Chiarelli,[27] C. N. Chiou,[33] F. Chlebana,[7] L. Christofek,[13] R. Cropp,[14] M. L. Chu,[33] S. Cihangir,[7] A. G. Clark,[10] M. Cobal,[27] E. Cocca,[27] M. Contreras,[5] J. Conway,[32] J. Cooper,[7] M. Cordelli,[9] D. Costanzo,[27] C. Couyoumtzelis,[10] D. Cronin-Hennessy,[6] R. Culbertson,[5] D. Dagenhart,[38] T. Daniels,[19] F. DeJongh,[7] S. Dell'Agnello,[9] M. Dell'Orso,[27] R. Demina,[7] L. Demortier,[31] M. Deninno,[2] P. F. Derwent,[7] T. Devlin,[32] J. R. Dittmann,[6] S. Donati,[27] J. Done,[34] T. Dorigo,[25] N. Eddy,[13] K. Einsweiler,[18] J. E. Elias,[7] R. Ely,[18] E. Engels, Jr.,[28] W. Erdmann,[7] D. Errede,[13] S. Errede,[13] Q. Fan,[30] R. G. Feild,[41] Z. Feng,[15] C. Ferretti,[27] I. Fiori,[2] B. Flaugher,[7] G. W. Foster,[7] M. Franklin,[11] J. Freeman,[7] J. Friedman,[19] H. Frisch,[5] Y. Fukui,[17] S. Gadomski,[14] S. Galeotti,[27] M. Gallinaro,[26] O. Ganel,[35] M. Garcia-Sciveres,[18] A. F. Garfinkel,[29] C. Gay,[41] S. Geer,[7] D. W. Gardes,[20] P. Giannetti,[27] N. Giokaris,[31] P. Giromini,[9] G. Giusti,[27] M. Gold,[22] A. Gordon,[11] A. T. Goshaw,[6] Y. Gotra,[28] K. Goulianos,[31] H. Grassmann,[36] C. Green,[29] L. Groer,[32] C. Grosso-Pilcher,[5] G. Guillian,[20] J. Guimaraes da Costa,[15] R. S. Guo,[33] C. Haber,[18] E. Hafen,[19] S. R. Hahn,[7] R. Hamilton,[11] T. Handa,[12] R. Handler,[40] W. Hao,[35] F. Happacher,[9] K. Hara,[37] A. D. Hardman,[29] R. M. Harris,[7] F. Hartmann,[16] J. Hauser,[4] E. Hayashi,[37] J. Heinrich,[26] A. Heiss,[16] B. Hinrichsen,[14] K. D. Hoffman,[29] C. Holck,[26] R. Hollebeek,[26] L. Holloway,[13] Z. Huang,[20] B. T. Huffman,[28] R. Hughes,[23] J. Huston,[21] J. Huth,[11] H. Ikeda,[37] M. Incagli,[27] J. Incandela,[7] G. Introzzi,[27] J. Iwai,[39] Y. Iwata,[12]

E. James,[20] H. Jensen,[7] U. Joshi,[7] E. Kajfasz,[25] H. Kambara,[10] T. Kamon,[34] T. Kaneko,[37] K. Karr,[38] H. Kasha,[41] Y. Kato,[24] T. A. Keaffaber,[29] K. Kelley,[19] R. D. Kennedy,[7] R. Kephart,[7] D. Kestenbaum,[11] D. Khazins,[6] T. Kikuchi,[37] M. Kirk,[3] B. J. Kim,[27] H. S. Kim,[14] S. H. Kim,[37] Y. K. Kim,[18] L. Kirsch,[3] S. Klimenko,[8] D. Knoblauch,[16] P. Koehn,[23] A. Köngeter,[16] H. Kondo,[37] J. Konigsberg,[8] K. Kordas,[14] A. Korytov,[8] E. Kovacs,[1] W. Kowald,[6] J. Kroll,[26] M. Kruse,[30] S. E. Kuhlmann,[1] E. Kuns,[32] K. Kurino,[12] T. Kuwabara,[37] A. T. Laasanen,[29] S. Lami,[27] S. Lammel,[7] J. I. Lamoureux,[3] M. Lancaster,[18] M. Lanzoni,[27] G. Latino,[27] T. LeCompte,[1] S. Leone,[27] J. D. Lewis,[7] M. Lindgren,[4] T. M. Liss,[13] J. B. Liu,[30] Y. C. Liu,[33] N. Lockyer,[26] O. Long,[26] M. Loreti,[25] D. Lucchesi,[27] P. Lukens,[7] S. Lusin,[40] J. Lys,[18] K. Maeshima,[7] P. Maksimovic,[11] N. Mangano,[27] M. Mariotti,[25] J. P. Marriner,[7] G. Martignon,[25] A. Martin,[41] J. A. J. Matthews,[22] P. Mazzanti,[2] K. McFarland,[30] P. McIntyre,[34] P. Melese,[31] M. Menguzzato,[25] A. Menzione,[27] E. Meschi,[27] S. Metzler,[26] C. Miao,[20] T. Miao,[7] G. Michail,[11] R. Miller,[21] H. Minato,[37] S. Miscetti,[9] M. Mishina,[17] S. Miyashita,[37] N. Moggi,[27] E. Moore,[22] Y. Morita,[17] A. Mukherjee,[7] T. Muller,[16] A. Munar,[27] P. Murat,[27] S. Murgia,[21] M. Musy,[36] H. Nakada,[37] T. Nakaya,[5] I. Nakano,[12] C. Nelson,[7] D. Neuberger,[16] C. Newman-Holmes,[7] C.- Y. P. Ngan,[19] H. Niu,[3] L. Nodulman,[1] A. Nomerotski,[8] S. H. Oh,[6] T. Ohmoto,[12] T. Ohsugi,[12] R. Oishi,[37] M. Okabe,[37] T. Okusawa,[24] J. Olsen,[40] C. Pagliarone,[27] R. Paoletti,[27] V. Papadimitriou,[35] S. P. Pappas,[41] N. Parashar,[27] A. Parri,[9] D. Partos,[3] J. Patrick,[7] G. Pauletta,[36] M. Paulini,[18] A. Perazzo,[27] L. Pescara,[25] M. D. Peters,[18] T. J. Phillips,[6] G. Piacentino,[27] M. Pillai,[30] K. T. Pitts,[7] R. Plunkett,[7] A. Pompos,[29] L. Pondrom,[40] J. Proudfoot,[1] F. Ptohos,[11] G. Punzi,[27] K. Ragan,[14] D. Reher,[18] M. Reischl,[16] A. Ribon,[25] F. Rimondi,[2] L. Ristori,[27] W. J. Robertson,[6] A. Robinson,[14] T. Rodrigo,[27] S. Rolli,[38] L. Rosenson,[19] R. Roser,[13] T. Saab,[14] W. H. Sakumoto,[30] D. Saltzberg,[4] A. Sansoni,[9] L. Santi,[36] H. Sato,[37] P. Schlabach,[7] E. E. Schmidt,[7] M. P. Schmidt,[41] A. Scott,[4] A. Scribano,[27] S. Segler,[7] S. Seidel,[22] Y. Seiya,[37] F. Semeria,[2] T. Shah,[19] M. D. Shapiro,[18] N. M. Shaw,[29] P. F. Shepard,[28] T. Shibayama,[37] M. Shimojima,[37] M. Shochet,[5] J. Siegrist,[18] A. Sill,[35] P. Sinervo,[14] P. Singh,[13] K. Sliwa,[38] C. Smith,[15] F. D. Snider,[15] J. Spalding,[7] T. Speer,[10] P. Sphicas,[19] F. Spinella,[27] M. Spiropulu,[11] L. Spiegel,[7] L. Stanco,[25] J. Steele,[40] A. Stefanini,[27] R. Ströhmer,[7*] J. Strologas,[13] F. Strumia,[10] D. Stuart,[7] K. Sumorok,[19] J. Suzuki,[37] T. Suzuki,[37] T. Takahashi,[24] T. Takano,[24] R. Takashima,[12] K. Takikawa,[37] M. Tanaka,[37] B. Tannenbaum,[4] F. Tartarelli,[27] W. Taylor,[14] M. Tecchio,[20] P. K. Teng,[33] Y. Teramoto,[24] K. Terashi,[37] S. Tether,[19] D. Theriot,[7] T. L. Thomas,[22] R. Thurman-Keup,[1] M. Timko,[38] P. Tipton,[30] A, Titov,[31] S. Tkaczyk,[7] D. Toback,[5] K. Tollefson,[30] A. Tollestrup,[7] H. Toyoda,[24] W. Trischuk,[14] J. F. de Troconiz,[11] S. Truitt,[20] J. Tseng,[19] N. Turini,[27] T. Uchida,[37] F. Ukagawa,[26] J. Valls,[32] S. C. van den Brink,[15] S. Vejcik, III,[20] G. Velev,[27]

I. Volobouev,[18] R. Vidal,[7] R. Vilar,[7*] D. Vucinic,[19] R. G. Wagner,[1] R. L. Wagner,[7] J. Wahl,[5] N. B. Wallace,[27] A. M. Walsh,[32] C. Wang,[6] C. H. Wang,[33] M. J. Wang,[33] A. Warburton,[14] T. Watanabe,[37] T. Watts,[32] R. Webb,[34] C. Wei,[6] H. Wenzel,[16] W. C. Wester, III,[7] A. B. Wicklund,[1] E. Wicklund,[7] R. Wilkinson,[26] H. H. Williams,[26] P. Wilson,[7] B. L. Winer,[23] D. Winn,[20] D. Wolinski,[20] J. Wolinski,[21] S. Worm,[22] X. Wu,[10] J. Wyss,[27] A. Yagil,[7] W. Yao,[18] K. Yasuoka,[37] G. P. Yeh,[7] P. Yeh,[33] J. Yeh,[7] C. Yosef,[21] T. Yoshida,[24] I. Yu,[7] A. Zanetti,[36] F. Zetti,[27] and S. Zucchelli [2]

[1] *Argonne National Labaratory, Argonne, Illinois, 60439*

[2] *Istituto Nazionale di Fisica Nucleare, University of Bologna, I-40127, Bologna, Italy*

[3] *Brandeis University, Waltham, Massachusetts 02254*

[4] *University of California at Los Angels, Los Angels, California 90024*

[5] *University of Chicago, Chicago, Illinois 60637*

[6] *Duke University, Durham, North Caroline 27708*

[7] *Fermi National Accelerator Laboratory, Batavia, Illinois 60510*

[8] *University of Florida, Gainesville, Florida 32611*

[9] *Laboratori Nazionali di Frascati, Istituto Nazionale di Fisica Nucleare, I-00044 Frascati, Italy*

[10] *University of Geneva, CH-1211 Geneva 4, Switzerland*

[11] *Harvard University, Cambridge, Massachusetts 02138*

[12] *Hiroshima University, Higashi-Hiroshima 724, Japan*

[13] *University of Illinois, Urbana, Illinois 61801*

[14] *Institute of Particle Physics, McGill University, Montreal H3A 2T8, and University of Toronto, Toronto M5S 1A7, Canada*

[15] *The Johns Hopkins University, Baltimore, Maryland 21218*

[16] *Institut für Experimentelle Kernphysik, Universität Karlsruhe, 76128 Karlsruhe, Germany*

[17] *National Laboratory for High Energy Physics (KEK), Tsukuba, Ibaraki 305, Japan*

[18] *Ernest Orlando Lawrence Berkeley National Laboratory, Berkeley, California 94720*

[19] *Massachusetts Institute of Technology, Cambridge, Massachusetts 02139*

[20] *University of Michigan, Ann Arbor, Michigan 48109*

[21] *Michigan State University, East Lansing, Michigan 48824*

[22] *University of New Mexico, Albuquerque, New Mexico 87131*

[23] *The Ohio State University, Columbus, Ohio 43210*

[24] *Osaka City University, Osaka 588, Japan*

[25] *Universita di Padova, Istituto Nazionale di Fisica Nucleare, Sezione di Padova, I-35131 Padova, Italy*

[26] *University of Pennsylvania, Philadelphia, Pennsylvania 19104*

[27] *Istituto Nazionale di Fisica Nucleare, University and Scuola Normale Superiore of Pisa, I-56100 Pisa, Italy*

[28] *University of Pittsburgh, Pittsburgh, Pennsylvania 15260*

[29] *Purdue University, West Lafayette, Indiana 47907*

[30] *University of Rochester, Rochester, New York 14627*

[31] *Rockefeller University, New York, New York 10021*

[32] *Rutgers University, Piscataway, New Jersey 08855*

[33] *Academia Sinica, Taipei, Taiwan 11530, Republic of China*

[34] *Texas A&M University, College Station, Texas 77843*

[35] *Texas Yech University, Lubbock, Texas 79409*

[36] *Istituto Nazionale di Fisica Nucleare, University of Trieste/ Udine, Italy*
[37] *University of Tsukuba, Tsukuba, Ibaraki 305, Japan*
[38] *Tufts University, Medford, Massachusetts 02155*
[39] *Waseda University, Tokyo 169, Japan*
[40] *University of Wisconsin, Madison, Wisconsin 53706*
[41] *Yale University, New Haven, Connecticut 06520*

Chapter 1

Introduction

Quantum Chromodynamics (QCD) has succeeded in the high precision tests of the hard process for high energy experiments [1]–[5]. Although we believe QCD is the theory for strong interaction, it is difficult to describe a scattering process with a small momentum transfer ("soft") since the renormalization coupling constant is not small enough in such a low energy scale to use a perturbative technique.

On the other hand, inclusive hadron-hadron interactions in soft processes are well described by Regge theory [6] where the interactions are considered as due to exchanges of Regge poles [7, 8]. One of possible Regge poles has the quantum numbers of the vacuum, which is generally called *pomeron* [9]. The Regge pole phenomenology is based on the observed hadron spectroscopy and some general postulates such as the unitarity and the analyticity of the S-matrix. The validity of the Regge pole phenomenology is restricted in the soft processes. The single diffractive dissociation is one of such soft processes. The first interpretation of diffraction, due to M. L. Good and W. D. Walker [10], was that different components of the projectile were differently absorbed by the target, leading to the creation of new physical states. This was the first indication for the composite nature of hadrons. The diffractive dissociation can be viewed as involving two processes with different time scales; a slow process of emitting a pomeron from a hadron, and an interaction of the pomeron with another incoming particle. A. Donnachie and P. V. Landshoff derived the pomeron flux factor (DL pomeron flux factor) and the structure of the pomeron [11].

The total single diffractive cross section was measured in several experiments [12]–[16]. The most important consequence of the pomeron being a pole is the factorization property. Due to the pomeron intercept being larger than one, it has been observed that the extrapolated $p\overline{p}$ single diffractive cross section based on a triple-Regge formula is much larger than the measured one at Tevatron energies by a factor of $5 \sim 10$ and it could become larger than the total cross section. Some phenomenologists claim that this discrepancy comes from a wrong pomeron flux factor, and the others suggest that it is due to a wrong proton-pomeron cross section [17]–[19].

Instead of directly considering the soft processes using non-perturbative QCD, one can study the pomeron, the object emerging from the soft process, in its hard collisions where one might be able to apply perturbative QCD. This approach was first discussed by G. Ingelman and P. Schlein (IS model) [20], and experimentally pioneered by UA8 [21] observing dijet production in the single diffractive events using CERN $Sp\overline{p}S$ collider operated at $\sqrt{s} = 630\,\mathrm{GeV}$. Although one of the hadrons escapes essentially unscathed, a high-p_T jet pair, which is necessarily associated with a high virtuality in the intermediate state, is produced in the central rapidity range.

Recently, the structure of the pomeron have been studied by many experiments. The UA8 collaboration reported that the pomeron exhibits a "hard structure" like, $zf(z) \sim z(1-z)$, where z is a momentum fraction of the struck parton in the pomeron. The ZEUS collaboration reported the first experimental evidence for the gluon content of the pomeron in diffractive hard scattering processes using the HERA ep collider. Their data indicated that the momentum fraction between 30% and 80% of the pomeron carried by partons is due to hard gluons [22]. The CDF collaboration reported not only the gluon fraction in the pomeron but also the event rate against the triple-Regge prediction by combining the results of the diffractive dijet, W, and b-quark production cross sections [23, 24]. They conclude that the gluon fraction is consistent with the result of the ZEUS collaboration, but the measured event rate is smaller than that of the triple-Regge prediction by a factor of 0.2. The H1 and ZEUS collaborations measured the structure of the pomeron using 1994 data by performing the QCD fit [25, 26]. The CDF collaboration installed a Roman-pot type antiproton spectrometer [27] in order to tag a recoil $\overline{p}$ in diffractive scattering processes in 1995, and measured the diffractive structure function of the antiproton. In 2000, by comparing it with the H1 result [28, 29], the CDF pointed out that there is a large discrepancy in the absolute value of the diffractive structure function (about factor of 10) between these two experiments, and concluded that the hard diffractive processes cannot be de-

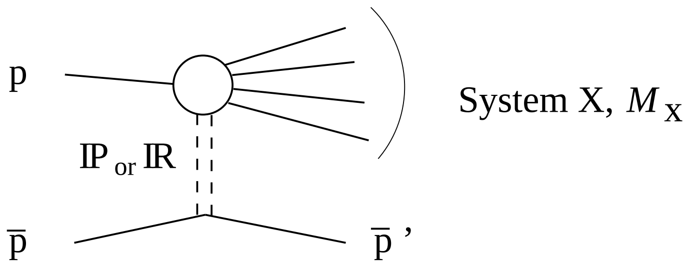

Figure 1.1: Single diffraction.

scribed in terms of parton level cross section convoluted with the universal diffractive structure function.

1.1 Kinematics of the single diffraction

The single diffraction process, $p + \bar{p} \to \bar{p} + X$, is schematically shown in Figure 1.1. We assign four-momenta of the initial and final states as follows;

$$
\begin{aligned}
p_p &= (E_p, \vec{p}_p) = (E_{\text{beam}}, 0, 0, p_{\text{beam}}), \\
p_{\overline{p}} &= (E_{\overline{p}}, \vec{p}_{\overline{p}}) = (E_{\text{beam}}, 0, 0, -p_{\text{beam}}), \\
p_{\text{X}} &= (E_{\text{X}}, \vec{p}_{\text{X}}) = (E_{\text{X}}, p_{\text{X}x}, p_{\text{X}y}, p_{\text{X}z}), \\
p_{\overline{p}'} &= (E_{\overline{p}'}, \vec{p}_{\overline{p}'}) = (E_{\overline{p}'}, p_{\overline{p}'x}, p_{\overline{p}'y}, p_{\overline{p}'z}).
\end{aligned}
$$

Some kinematical variables are frequently used to describe the single diffraction process. Using the four-momenta of the initial beam particles $(p_p, p_{\overline{p}})$ and the final systems $(p_{\overline{p}'}, p_{\text{X}})$, the following three independent variables are defined;

$$
s \equiv (p_p + p_{\overline{p}})^2 = (p_{\overline{p}'} + p_{\text{X}})^2, \tag{1.1}
$$

$$
t \equiv (p_{\overline{p}} - p_{\overline{p}'})^2 = (p_{\text{X}} - p_p)^2, \tag{1.2}
$$

$$
M_{\text{X}}^2 \equiv p_{\text{X}}^2 = (p_p + p_{\overline{p}} - p_{\overline{p}'})^2, \tag{1.3}
$$

where s is a center-of-mass energy squared, t is a momentum transfer squared, and M_{X} is an invariant mass of the diffractive system X. Equation 1.1 can be modified as follows by using the energy E_{X} and the mass M_{X} of the system X;

$$
\begin{aligned}
s &= (p_{\overline{p}'} + p_{\text{X}})^2 = (2p_{\text{X}} + p_{\overline{p}'} - p_{\text{X}})(p_{\overline{p}'} + p_{\text{X}}) \\
&= 2p_{\text{X}} \cdot (p_{\overline{p}'} + p_{\text{X}}) + (p_{\overline{p}'} - p_{\text{X}})(p_{\overline{p}'} + p_{\text{X}}) \\
&= 2E_{\text{X}}\sqrt{s} + m_p^2 - M_{\text{X}}^2,
\end{aligned}
$$

where m_p is the proton mass. This formula leads to the following expression of the energy of the system X,

$$E_{\mathrm{X}} = \frac{s + M_{\mathrm{X}}^2 - m_p^2}{2\sqrt{s}}. \tag{1.4}$$

An absolute value of the 3-momentum of the leading antiproton $\vec{p}_{\overline{p}'}$ can be expressed with s and M_{X} using Equation 1.4,

$$\begin{aligned}
\left|\vec{p}_{\overline{p}'}\right|^2 &= \left|\vec{p}_{\mathrm{X}}\right|^2 \\
&= E_{\mathrm{X}}^2 - M_{\mathrm{X}}^2 \\
&= \frac{(s + M_{\mathrm{X}}^2 - m_p^2)^2}{4s} - M_{\mathrm{X}}^2 \\
&\xrightarrow{s, M_{\mathrm{X}}^2 \gg m_p^2} \frac{(s - M_{\mathrm{X}}^2)^2}{4s} \\
\left|\vec{p}_{\overline{p}'}\right| &= \left|\vec{p}_{\mathrm{X}}\right| = \frac{s - M_{\mathrm{X}}^2}{2\sqrt{s}}.
\end{aligned} \tag{1.5}$$

Now we introduce another frequently used variable, the Feynman variable x_F,

$$x_F = \frac{p_{\overline{p}'z}}{p_{\overline{p}z}}. \tag{1.6}$$

Since $p_{\overline{p}'z} \approx \left|\vec{p}_{\overline{p}'}\right|$, $p_{\overline{p}z} \approx E_{\overline{p}} = E_{\mathrm{beam}} = \frac{1}{2}\sqrt{s}$, and Equation 1.5, we arrive at,

$$x_F \approx \frac{\left|\vec{p}_{\overline{p}'}\right|}{\sqrt{s}/2} = \frac{2\left|\vec{p}_{\overline{p}'}\right|}{\sqrt{s}} \approx 1 - \frac{M_{\mathrm{X}}^2}{s}. \tag{1.7}$$

Instead of x_F, ξ variable is also used frequently,

$$\xi \equiv \frac{M_{\mathrm{X}}^2}{s} = 1 - x_F. \tag{1.8}$$

The rapidity distribution of the final states is schematically shown in Figure 1.2. In general $p\overline{p}$ collisions, the maximum and minimum rapidities of the generated particles are calculated as,

$$\begin{aligned}
y^{\max} &= \frac{1}{2}\ln\left.\frac{E + p_z}{E - p_z}\right|_{\max} = \frac{1}{2}\ln\left.\frac{(E + p_z)^2}{E^2 - p_z^2}\right|_{\max} \\
&\approx \frac{1}{2}\ln\frac{(2E_{\mathrm{beam}})^2}{m_p^2} = \ln\frac{\sqrt{s}}{m_p},
\end{aligned} \tag{1.9}$$

and

$$y^{\min} = -\ln\frac{\sqrt{s}}{m_p}, \tag{1.10}$$

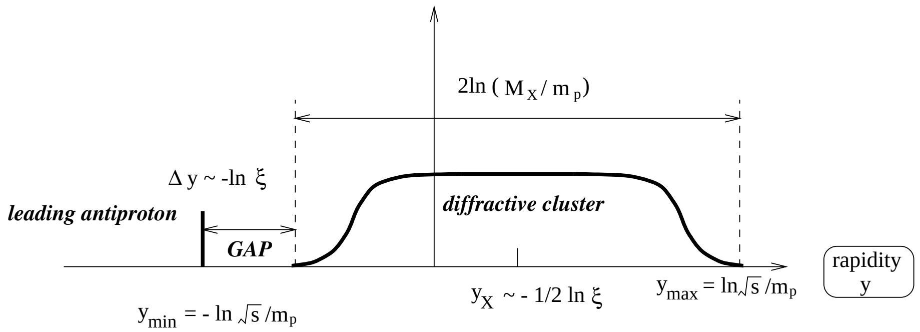

Figure 1.2: The kinematics of the single diffraction.

respectively. The rapidity of the recoil $\overline{p}$ can be calculated in the same way as above by using $E_{\overline{p}'} = (1-\xi)E_{\rm beam}$, and $\vec{p}_{\overline{p}'} \approx (1-\xi)\vec{p}_{\overline{p}}$;

$$\begin{aligned} y_{\overline{p}'} &= \frac{1}{2}\ln\frac{E_{\overline{p}'}+p_{\overline{p}'z}}{E_{\overline{p}'}-p_{\overline{p}'z}} = \frac{1}{2}\ln\frac{E_{\overline{p}'}-|p_{\overline{p}'z}|}{E_{\overline{p}'}+|p_{\overline{p}'z}|} \approx \frac{1}{2}\ln\frac{E_{\overline{p}}-|\vec{p}_{\overline{p}}|}{E_{\overline{p}}+|\vec{p}_{\overline{p}}|} \\ &= y^{\rm min} = -\ln\frac{\sqrt{s}}{m_p}. \end{aligned} \tag{1.11}$$

The center of the rapidity for the diffractive system X is similarly obtained using Equations 1.4 and 1.5,

$$\begin{aligned} y_{\rm X} &= \frac{1}{2}\ln\frac{E_{\rm X}+p_{{\rm X}z}}{E_{\rm X}-p_{{\rm X}z}} \approx \frac{1}{2}\ln\frac{E_{\rm X}+|\vec{p}_{\rm X}|}{E_{\rm X}-|\vec{p}_{\rm X}|} \\ &= \frac{1}{2}\ln\frac{(E_{\rm X}+|\vec{p}_{\rm X}|)^2}{M_{\rm X}^2} = \frac{1}{2}\ln\left(\frac{1}{M_{\rm X}^2}\cdot\frac{4s^2-4sm_p^2+m_p^4}{4s}\right) \\ &\approx \frac{1}{2}\ln\frac{s}{M_{\rm X}^2} = \frac{1}{2}\ln\frac{1}{\xi}. \end{aligned} \tag{1.12}$$

The width of the system X can be calculated using Equations 1.8, 1.9 and 1.12,

$$\begin{aligned} y_{\rm X}^{\rm width} &= 2(y^{\rm max}-y_{\rm X}) = 2\left(\ln\frac{\sqrt{s}}{m_p}-\frac{1}{2}\ln\frac{1}{\xi}\right) \\ &= \ln\left(\frac{s}{m_p^2}\cdot\xi\right) = 2\ln\left(\frac{M_{\rm X}}{m_p}\right). \end{aligned} \tag{1.13}$$

Thus, the size of the rapidity gap between the cluster and the recoil $\overline{p}$ is obtained,

$$\begin{aligned} \Delta y &= y_{\rm X} - \frac{1}{2}y_{\rm X}^{\rm width} - y_{\overline{p}'} \\ &= \frac{1}{2}\ln\frac{1}{\xi} - \ln\frac{M_{\rm X}}{m_p} + \ln\frac{\sqrt{s}}{m_p} = \ln\left(\frac{1}{\sqrt{\xi}}\cdot\frac{m_p}{M_{\rm X}}\cdot\frac{\sqrt{s}}{m_p}\right) \\ &= \ln\left(\frac{1}{\sqrt{\xi}}\cdot\frac{\sqrt{s}}{\sqrt{\xi s}}\right) = -\ln\xi. \end{aligned} \tag{1.14}$$

The signature of the single diffraction is characterized with this forward rapidity gap and the existence of the recoil $\overline{p}$.

In the CDF experiment, the rapidity of the recoil $\overline{p}$ and the rapidity gap width are calculated as follows;

$$\begin{aligned} y_{\overline{p}'} &= -\ln(\frac{\sqrt{s}}{m_p}) \approx -7.6, \\ \Delta y &= -\ln \xi \approx 1.0 \sim 1.5, \ (0.035 \leq \xi \leq 0.095). \end{aligned}$$

We identify the single diffractive events by tagging the recoil $\overline{p}$ and the rapidity gap. In order to tag the recoil $\overline{p}$, we installed a Roman-pot type antiproton spectrometer (RPS) [27], and using the forward calorimeter and the beam-beam counter, we identify the rapidity gap.

In the parton level twobody-to-twobody process, $1+2 \rightarrow 3+4$, we assign four-momenta of the initial and final partons as follows;

$$p_1 = (E_1, \vec{p}_1) = E_{\text{beam}}(x_p, 0, 0, x_p), \tag{1.15}$$

$$p_2 = (E_2, \vec{p}_2) = E_{\text{beam}}(x_{\overline{p}}, 0, 0, -x_{\overline{p}}), \tag{1.16}$$

$$p_3 = (E_3, \vec{p}_3) = (E_3, p_{3x}, p_{3y}, p_{3z}), \tag{1.17}$$

$$p_4 = (E_4, \vec{p}_4) = (E_4, p_{4x}, p_{4y}, p_{4z}), \tag{1.18}$$

where x_p ($x_{\overline{p}}$) is the momentum fraction of the struck parton in the (anti)proton. Assuming the mass of each final parton is massless, Equations of (1.17) and (1.18) can be modified as

$$p_3 = (E_{3T} \cosh \eta_3, p_{3x}, p_{3y}, E_{3T} \sinh \eta_3), \tag{1.19}$$

$$p_4 = (E_{4T} \cosh \eta_4, p_{4x}, p_{4y}, E_{4T} \sinh \eta_4), \tag{1.20}$$

where E_{3T} (E_{4T}) and η_3 (η_4) mean a transverse energy and a pseudorapidity of the parton 3 (4). Because $p_1 + p_2 = p_3 + p_4$, the following equations are obtained;

$$p_{3x} + p_{4x} = p_{3y} + p_{4y} = 0,$$

$$(x_p + x_{\overline{p}})E_{\text{beam}} = \sum_j E_{jT} \cosh \eta_j, \tag{1.21}$$

$$(x_p - x_{\overline{p}})E_{\text{beam}} = \sum_j E_{jT} \sinh \eta_j. \tag{1.22}$$

Therefore using (1.21) and (1.22), x_p can be expressed as;

$$\begin{aligned} x_p\sqrt{s} &= \sum_j E_{jT}(\cosh\eta_j + \sinh\eta_j) = \sum_j E_{jT}\exp(\eta_j), \\ x_p &= \frac{1}{\sqrt{s}}\sum_j E_{jT}\exp(\eta_j). \end{aligned} \quad (1.23)$$

In the same way, $x_{\overline{p}}$ can be expressed as;

$$x_{\overline{p}} = \frac{1}{\sqrt{s}}\sum_j E_{jT}\exp(-\eta_j). \quad (1.24)$$

The fractional momentum of the struck parton in the pomeron (β) can be calculated as;

$$x_{\overline{p}} = \beta \times \xi \quad (1.25)$$

$$\longrightarrow \beta = \frac{1}{\xi\sqrt{s}}\sum_j E_{jT}\exp(-\eta_j). \quad (1.26)$$

The squared invariant mass of the two initial partons is defined as;

$$\hat{s} = (p_1 + p_2)^2 = (p_3 + p_4)^2 = x_p x_{\overline{p}} s = m_{\text{final}}^2,$$

where m_{final} represents the invariant mass of the final state. The quantity of the hard scale q^2 is written as

$$\begin{aligned} q^2 &= (p_1 - p_3)^2 = (p_2 - p_4)^2 = -\frac{\hat{s}}{2}(1 - \cos\theta^*), \\ \longrightarrow Q^2 &= -q^2 = \frac{m_{\text{final}}^2}{2}(1 - \cos\theta^*), \end{aligned} \quad (1.27)$$

where θ^* is the polar angle of the leading parton 3 in the center-of-mass frame of the hard scattering [2] ($0 < \theta^* < \pi/2$). In this analysis, basically we use two jets. If the event has the third jet with E_T larger than 5 GeV, we take into account of the third jet. Therefore the summation in Equations of (1.23), (1.24) and (1.26) is performed over the two or three jets in the final state. And the mass m_{final} is also calculated by using four-momenta of the two or three jets.

1.2 Outline of analysis procedure

Scaling the non-diffractive structure function (proton parton density function, PDF) according to the measured cross section ratio of the diffractive to the non-diffractive dijet production, we measure the diffractive (anti)proton structure function.

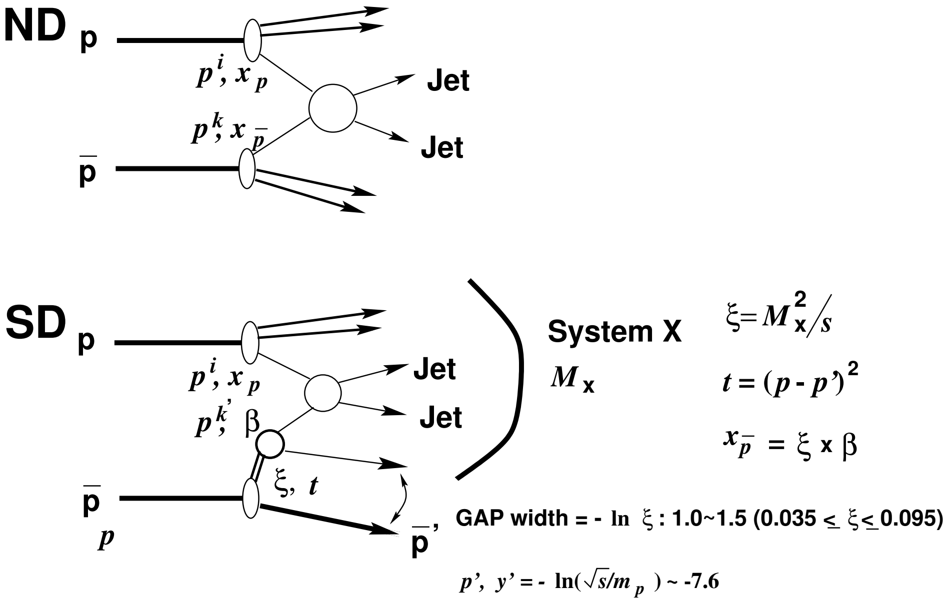

Figure 1.3: Diagrams of single diffractive and non-diffractive dijets.

Figure 1.3 shows schematically the diffractive and non-diffractive dijet productions. The cross sections of the non-diffractive and diffractive dijet productions are given by

$$\frac{d^3\sigma_{\rm ND}(p\bar{p} \to JJ + X)}{dx_p\, dx_{\bar{p}}\, d\hat{t}} = \sum_{i,k} f_{p^i/p}(x_p, Q^2) f_{p^k/\bar{p}}(x_{\bar{p}}, Q^2) \frac{d\hat{\sigma}(p^i p^k \to JJ)}{d\hat{t}}, \quad (1.28)$$

and

$$\frac{d^5\sigma_{\rm SD}(p\bar{p} \to p\mathcal{P} + \bar{p'} \to JJ + \bar{p'} + X)}{dx_p\, d\xi\, dt\, d\beta\, d\hat{t}}$$
$$= \sum_{i,k'} f_{p^i/p}(x_p, Q^2) f^{\rm SD}_{p^{k'}/\mathcal{P}/\bar{p}}(\xi, t, \beta^{k'}, Q^2) \frac{d\hat{\sigma}(p^i p^{k'} \to JJ)}{d\hat{t}}, \quad (1.29)$$

where $\mathcal{P}$ represents the exchanged colorless object, the pomeron, $f_{p^i/p}(x_p, Q^2)$ $(f_{p^k/\bar{p}}(x_{\bar{p}}, Q^2))$ means the parton density function, PDF, of the (anti)proton, and $f^{\rm SD}_{p^{k'}/\mathcal{P}/\bar{p}}(\xi, t, \beta^{k'}, Q^2)$ represents the diffractive structure function of the (anti)proton. The summations, $\sum_{i,k}$, $\sum_{i,k'}$, are performed over all flavors. In order to obtain a ratio of the diffractive structure function to the antiproton PDF, we need to cancel the contributions from

- proton PDF $(f_{p^i/p}(x_p, Q^2))$, and
- cross section for the parton subprocesses $(d\hat{\sigma}/d\hat{t})$,

in Equations (1.28) and (1.29). Since the proton PDF is a function of (x_p, Q^2), we measure the cross section ratio in the same (x_p, Q^2) region. The cross section for the parton subprocesses is not only a function of $(x_p, x_{\overline{p}}, Q^2)$ but also a combination of struck parton types. Therefore, taking account of color factor, * we define the following non-diffractive and diffractive structure functions:

$$\begin{aligned} F^{\rm ND}(x,Q^2) &\equiv x\left[f_{g/p}(x,Q^2)+\frac{4}{9}\sum\{f_{q/p}(x,Q^2)+f_{\bar{q}/p}(x,Q^2)\}\right], \quad (1.30)\\ F^{\rm SD}(x,Q^2) &\equiv x\left[f_{g/p}(x,Q^2)+\frac{4}{9}\sum\{f_{q/p}(x,Q^2)+f_{\bar{q}/p}(x,Q^2)\}\right]\\ &\times\ A(x,Q^2), \quad (1.31)\end{aligned}$$

where $f_{g/p}(x,Q^2)$, $f_{q/p}(x,Q^2)$, and $f_{\bar{q}/p}(x,Q^2)$ denote gluon, quark, and anti-quark densities in the proton PDF, $A(x,Q^2)$ represents the ratio of the diffractive structure function of the antiproton to the proton PDF integrated over ξ and $|t|$, and the summation is performed over all quarks. Using Equations (1.30) and(1.31), Equations (1.28) and (1.29) can be modified,

$$\frac{d^3\sigma_{\rm SD}}{dx_p dx_{\overline{p}} d\hat{t}} = A(x_{\overline{p}},Q^2)\frac{d^3\sigma_{\rm ND}}{dx_p dx_{\overline{p}} d\hat{t}}. \quad (1.32)$$

Thus, the cross section ratio of the diffractive to the non-diffractive dijet production is equal to the ratio of the corresponding structure functions;

$$\begin{aligned} R_{\rm JJ}^{\rm SD/ND}(x_{\overline{p}},Q^2) &\equiv \frac{d^2\sigma_{\rm SD}}{dx_{\overline{p}}dQ^2}\Bigg/\frac{d^2\sigma_{\rm ND}}{dx_{\overline{p}}dQ^2} = A(x_{\overline{p}},Q^2) \quad (1.33)\\ &= \frac{F^{\rm SD}(x_{\overline{p}},Q^2)}{F^{\rm ND}(x_{\overline{p}},Q^2)}. \quad (1.34)\end{aligned}$$

For the non-diffractive (proton) PDF, we used GRV98LO PDF [30]. Therefore, the diffractive structure function can be extracted by integrating a product of the cross section ratio and the proton PDF ($F^{\rm ND}(x,Q^2)$) over ξ, t, and x_p. The integration can be modified into the summation as follows:

$$F^{\rm SD}(\beta,Q^2) = \sum_{\text{jet events}} \frac{1}{N^{\rm SD}(x_{\overline{p}},Q^2)} R_{\rm JJ}^{\rm SD/ND}(x_{\overline{p}},Q^2)\cdot F^{\rm ND}(x_{\overline{p}},Q^2), \quad (1.35)$$

where $N^{\rm SD}(x_{\overline{p}},Q^2)$ is the number of diffractive dijet events in a bin of $(x_{\overline{p}},Q^2)$ corrected with efficiencies, and its normalization satisfies

$$\sum_{\text{jet events}} \frac{1}{N^{\rm SD}(x_{\overline{p}},Q^2)} = 1.$$

This weight factor was introduced for avoiding the non-uniform contribution over $x_{\overline{p}}$.

*Because the ratio of the following amplitudes is approximately, $gg \to gg : qg \to qg : \bar{q}g \to \bar{q}g : q\bar{q} \to q\bar{q} \simeq 1 : (4/9) : (4/9) : (4/9)^2$.

Chapter 2

Experimental setup

The diffractive data at the center-of-mass energy of 1.8 TeV were collected with the Collider Detector at Fermilab (CDF) including the Roman-pot type antiproton spectrometer (RPS). The collider run was carried out from late November 1995 to February 1996. The collider run in this period is called "Run-1C". In this chapter, we describe the Fermilab accelerator complex briefly and the CDF detector with emphasis on the detector components which are relevant to this analysis.

2.1 Accelerator complex

The accelerator complex at Fermilab is made up of five accelerators, as shown in Figure 2.1. In the Cockcroft-Walton accelerator, negative hydrogen ions (H^-) are accelerated to an energy of 750 keV by a DC electric field. The second stage of the acceleration process utilizes a 500-foot-long linear accelerator (LINAC). The H^- ions are accelerated to 400 MeV in the LINAC and injected into the Booster. The Booster is a synchrotron with a diameter of approximately 500 feet, located in a tunnel 20 feet below the ground. At the injection into the Booster, the ions pass through a carbon foil, which strips off the electrons thereby leaving only the protons circulating around the Booster ring. The protons are accelerated by the Booster to 8 GeV and injected into the Main Ring, a synchrotron with a diameter of 2 km. The Main Ring is operated at room temperature in an underground tunnel and is used for two purposes, accelerating protons (antiprotons) to 150 GeV for injection into the Tevatron and generating

120 GeV protons for antiproton production.

During antiproton stacking the 120 GeV protons are extracted from the Main Ring onto a tungsten target. Every two seconds, approximately 10^7 antiprotons are produced for 2×10^{15} protons striking the target and are collected in the Debuncher, which is roughly triangular with three straight sections of low dispersion. The Debuncher reduces the momentum spread of the antiprotons and reduces transverse profile with the stochastic cooling. The antiprotons are then transferred into the Accumulator. The accumulator ring is located in the same tunnel as Debuncher. The antiprotons are merged into a single beam, cooled further and stored in the Accumulator. The antiprotons are rebunched and injected into the Main Ring. The Main Ring is used to accelerate the antiprotons to 150 GeV, and injects them into the Tevatron.

The 150 GeV proton and antiproton bunches are accelerated to 900 GeV by the Tevatron. The Tevatron consists of superconducting magnets and is located below the Main Ring. The Tevatron operates with six proton and six antiproton bunches colliding in two luminous regions, B0 and D0. The CDF detector is located at B0. The Tevatron provided two typical average instantaneous luminosities of about $10^{31}\,\mathrm{cm}^{-2}\mathrm{s}^{-1}$ (high luminosity run) and $10^{29}\,\mathrm{cm}^{-2}\mathrm{s}^{-1}$ (low luminosity run) during Run-1C.

2.2 The CDF detector

A schematic drawing of the major detector components is shown in Figure 2.2. As shown in the figure, the CDF detector is a forward-backward and azimuthally symmetrical detector surrounding the interaction point in $p\overline{p}$ collisions [31].

2.2.1 The CDF coordinate system

Before describing the overview of the CDF detector, it is worth showing the coordinate system used in CDF. CDF uses basically the right-handed Cartesian coordinate system given by (x, y, z). The origin is at the center of the detector and it is also nominally an interaction point in $p\overline{p}$ collisions. The beam axis is taken as the z axis, and the proton beam direction is regarded as positive z direction. The x (y) axis is defined as the direction pointing horizontally outwards (vertically upwards) of the Tevatron ring. Also, note that a positive z direction is called "East" which is frequently used in

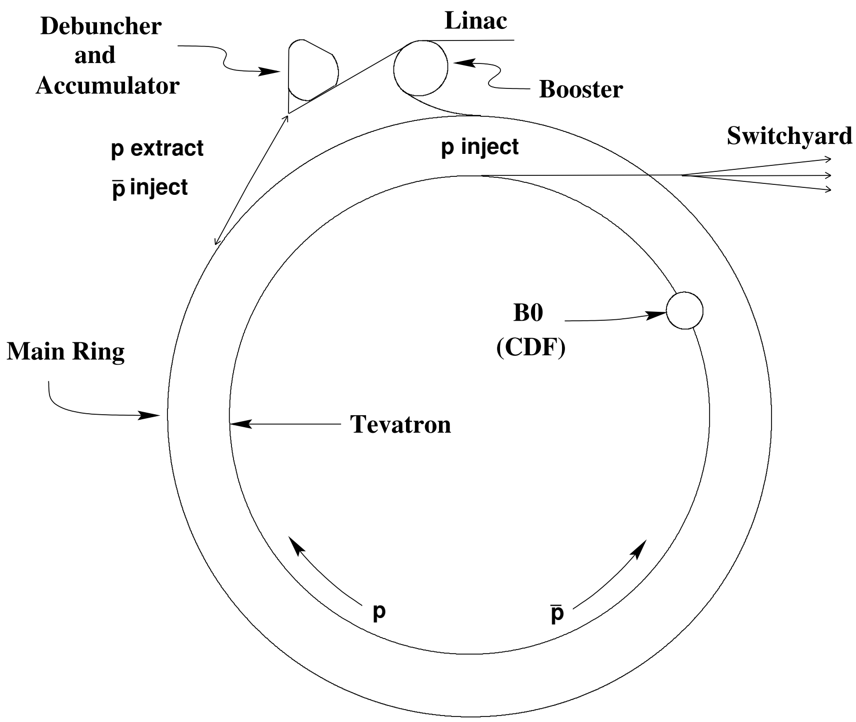

Figure 2.1: The accelerator complex at Fermilab.

the thesis. Accordingly the negative z direction is called "West". In addition to this coordinate system, the cylindrical coordinate system (r, θ, ϕ) is often used to describe the detectors and the characteristics of the particles nominally produced from the origin. The radius, r, is measured from the z axis. The polar angle, θ, is defined as the angle measured from the positive z axis, and the azimuthal angle measured from the positive x axis. The coordinate system used in CDF is shown in the inset of Figure 2.3.

2.2.2 Physical quantities in collider physics

Rapidity (y) and pseudorapidity (η)

In a collider physics, the quantity called *rapidity*, y, is frequently used instead of the polar angle. The rapidity of a particle is defined as

$$y \equiv \frac{1}{2} \ln \left(\frac{E + p_z}{E - p_z} \right). \tag{2.1}$$

The particle density in rapidity space, dN/dy, is in variant under the Lorentz boost along with the z axis because the rapidity transforms as $y \to y + \tanh^{-1} \beta$, where the

$\beta = p/E$, and the p and E are the momentum and energy of the particle. For relativistic particles (i.e., $p \gg mc$), the rapidity is well approximated by the *pseudorapidity*, η, given by;

$$\eta = -\ln\left(\tan\frac{\theta}{2}\right). \tag{2.2}$$

The pseudorapidity is also approximately invariant under the Lorentz boost in the case of $p \gg mc$. An obvious advantage of using a pseudorapidity rather than a rapidity is that it can be defined to the particle whose mass is unknown, and it allows us to measure the direction of the particle using the detector.

In the analysis of experimental data, we often use the two forms of pseudorapidity: 1) the detector η and 2) the event η. The former is measured from the center of the detector (nominal $p\overline{p}$ interaction point), and the latter is measured from the actual $p\overline{p}$ interaction point along with the z axis for each event. Each z position of $p\overline{p}$ collision (called Z_{VTX}) does not exactly matched with $z = 0$, but it is well approximated by the Gaussian distribution with $\sigma_z \approx 30\,\mathrm{cm}$ because the beam bunches have a similar Gaussian longitudinal profile with sigma of $35\,\mathrm{cm}$ (nominal value).

Transverse energy (E_T) and transverse momentum (p_T)

The *transverse energy*, E_T, with respect to the incident beam direction is important because it is not only a Lorentz invariant quantity but also a measure for hardness of the interaction. It is defined as;

$$E_T \equiv E\sin\theta, \tag{2.3}$$

where E is the energy of a cluster or a particle, and θ is the polar angle of the energy center of the cluster (particle). The *transverse momentum*, p_T, is also defined as the similar form: $p_T \equiv p\sin\theta$. Both the quantities can be defined for the tracks or the jets (energy clusters), but the E_T for the clusters is usually measured with the calorimeter while the p_T for the charged tracks is measured with the tracking detector surrounding by the calorimeter in CDF.

Missing transverse energy ($\not\!\!E_T$) and missing transverse energy significance (S)

In $p\overline{p}$ collisions we expect that a large fraction of the longitudinal momentum escapes outside the detector coverage towards the forward regions. This would lead to an imbalance of the longitudinal momentum when summing up all momenta of the particles observed in the detector. However, the transverse momentum and energy should balance, because transverse momenta of two incident struck partons are negligible small. An imbalance of the transverse energy indicates that a portion of the particle escapes out of the detector through the uninstrumental area ("cracks"). Several particles such as neutrinos or muons, hardly leave the trace in the calorimeter, therefore, they could also become the source of the imbalance. We defined the missing transverse energy significance [32]

$$S \equiv \not{E}_T \Big/ \left[\sum_i e_{Ti}\right]^{1/2}, \tag{2.4}$$

where the missing transverse energy is

$$\not{E}_T \equiv \left|\sum_i \vec{e}_{Ti}\right|, \tag{2.5}$$

and the $\vec{e}_{Ti}$ represents a vector which points from the interaction point to the calorimeter cell and has a magnitude equal to the cell e_{Ti}. In the analysis, we require that the $\not{E}_T$ is not significantly large for every event in order to ensure that the imbalance coming from the detector crack or the noises is small.

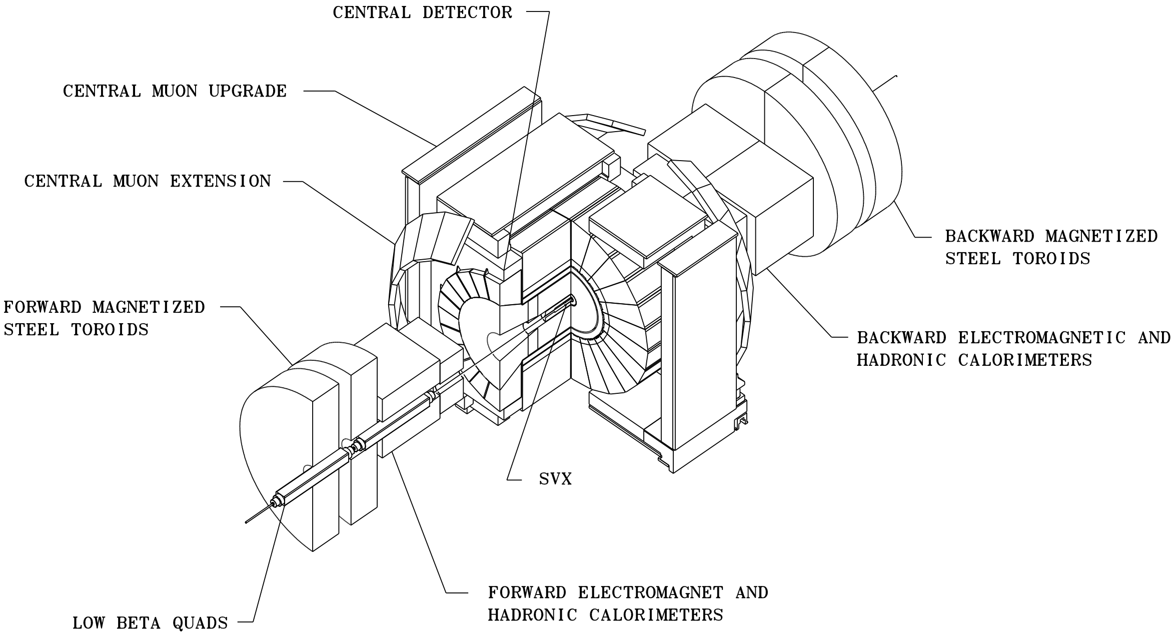

Figure 2.2: An isometric view of the main CDF detector components.

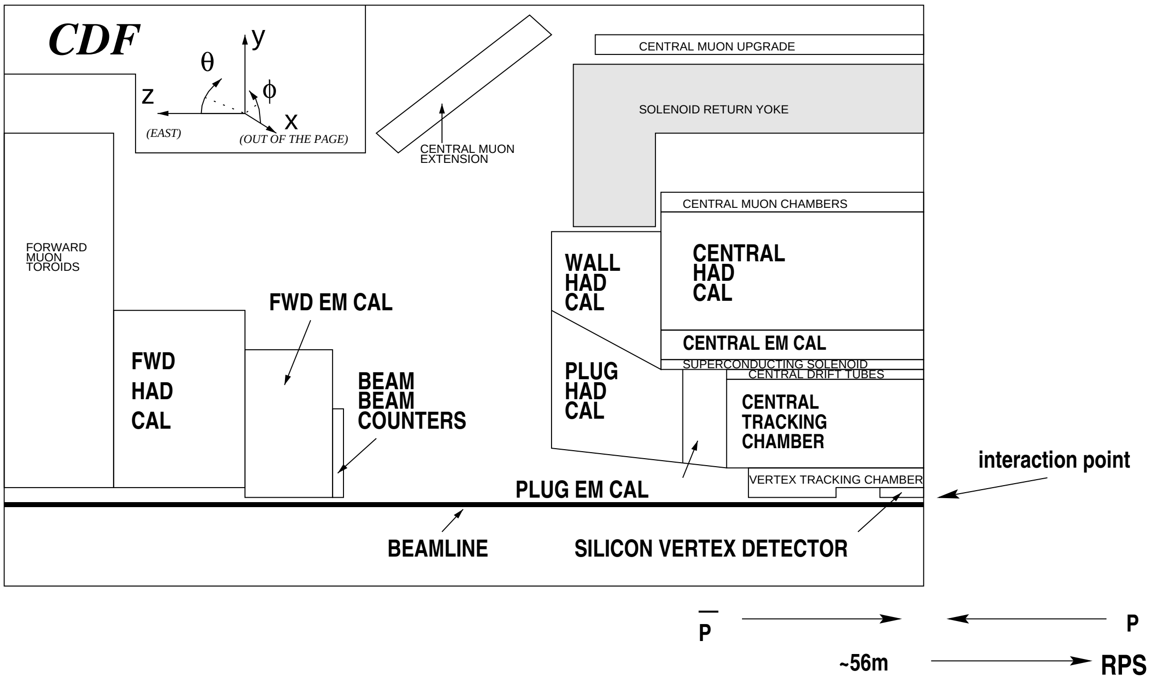

Figure 2.3: A quarter view of the cross section of the CDF detector.

2.2.3 The CDF detector overview

The CDF detector is shown in Figure 2.2 for three dimensional view, and in Figure 2.3 for the cross-sectional view of a quarter section. The basic design goal for the CDF detector is to measure the energy and momentum of the particles, and identify (where possible) them produced in $p\overline{p}$ collisions at the Tevatron, for as a wide solid angle as possible around the interaction region. For this purpose, the detector was designed to surround the interaction region by the detector layers and the subsystems each of which has a particular task (A detector with 4π coverage, called Full Acceptance Detector, is an ideal detector).

From the most inner region, close to the $p\overline{p}$ collisions, a beam pipe made of Be, tracking detectors, a superconducting solenoid magnet, calorimeters, muon detectors are equipped. The tracking detectors consist of three systems; a silicon vertex detector (SVX), vertex time projection chambers (VTX), and a central tracking chamber (CTC), which are used to detect charged particles and measure their momenta. The superconducting solenoid magnet surrounding the tracking detectors gives a 1.4 T magnetic field, which enables us to measure the charge and momentum of the particles. Surrounding the solenoid magnet are calorimeter systems used to measure the electromagnetic energy of electrons and photons and the hadronic energy of jets. The calorimeter system consists of the three regions, the central, end plug and forward. Each region has an electromagnetic calorimeter in front of a corresponding hadron calorimeter. The central electromagnetic calorimeter (CEM) is covered with two hadron calorimeter systems, the central hadron (CHA) and the wall hadron calorimeter (WHA), while a single system of the plug hadron (PHA) and the forward hadron (FHA) calorimeters overlaps the plug electromagnetic (PEM) and the forward electromagnetic (FEM) calorimeters, respectively. The muon chambers outside the calorimeters detect the muons which can easily pass the calorimeters without leaving any trace. In front of the each forward calorimeter, there is a beam-beam counter (BBC) in order to provide a "minimum-bias" trigger for the detector, and also to be used as the luminosity monitor.

In the analysis, the calorimeter plays an important role. It is essential not only to reconstruct jet cluster and to measure its energy but also to search for the rapidity gap signal in events. The BBC is also used to detect the rapidity gap signal.

Descriptions of these detectors which are relevant in the analysis are given below.

2.2.4 Tracking detector

Silicon vertex detector: SVX

The silicon vertex detector (SVX) [33] is a new device installed in 1992 and provides the high precision tracking information in the $r-\phi$ plane. The SVX is located between the beam pipe and the VTX along with the beam direction. The SVX is made up of two cylindrical modules with a total active length of 51 cm and a gap of 2.15 cm between the modules. This module is referred to as "barrel" and is shown in Figure 2.4. The $p\overline{p}$ interaction points at CDF distribute roughly according to Gaussian with a standard deviation of $\sigma \approx 30$ cm in the z direction. The geometrical acceptance of the SVX is about 60% of the interaction region at CDF.

The SVX barrel consists of four radial layers of single-sided silicon strip detectors segmented into twelve 30 degree wedges. The layers of the SVX are labelled $0-3$ in increasing radius from the beam line. The basic characteristics of the SVX are listed in Table 2.1. The pitch of the strips is 60 μm for layers $0-2$ and 55 μm for layer 3. The silicon detectors are 8.5 cm long and 300 μm thick with different widths for each as listed in Table 2.1. Three detectors are bonded to each other along the beam direction composing a "ladder", as shown in Figure 2.5.

Because of the degradation due to the radiation damage, the SVX was replaced for Run-1B by the SVX$'$ with the radiation-hard electronics. The geometries of these two detectors are nearly identical. The major difference is a radius of the innermost layer. For the SVX$'$, the radius of layer 0 is 2.8612 cm, while it is 3.0049 cm for the SVX.

The spatial resolution of the SVX and SVX$'$ are approximately 13 μm.

Vertex time projection chamber: VTX

The vertex time projection chamber (VTX) is a set of drift chamber surrounding the SVX along the beam axis. The VTX has an outer radius of 22 cm and the pseudorapidity coverage of the VTX is $|\eta| < 3.5$. A longitudinal view of the VTX is shown in an event display of Figure 2.6. As shown in the figure, the VTX consists of 28 modules attached end-to-end along the z axis. Each module is divided into two drift regions by a central high voltage grid. In azimuth, a module is segmented into 8 wedges, each of which has the coverage of 45°. For each wedge, 24 pairs of sense wires are arranged az-

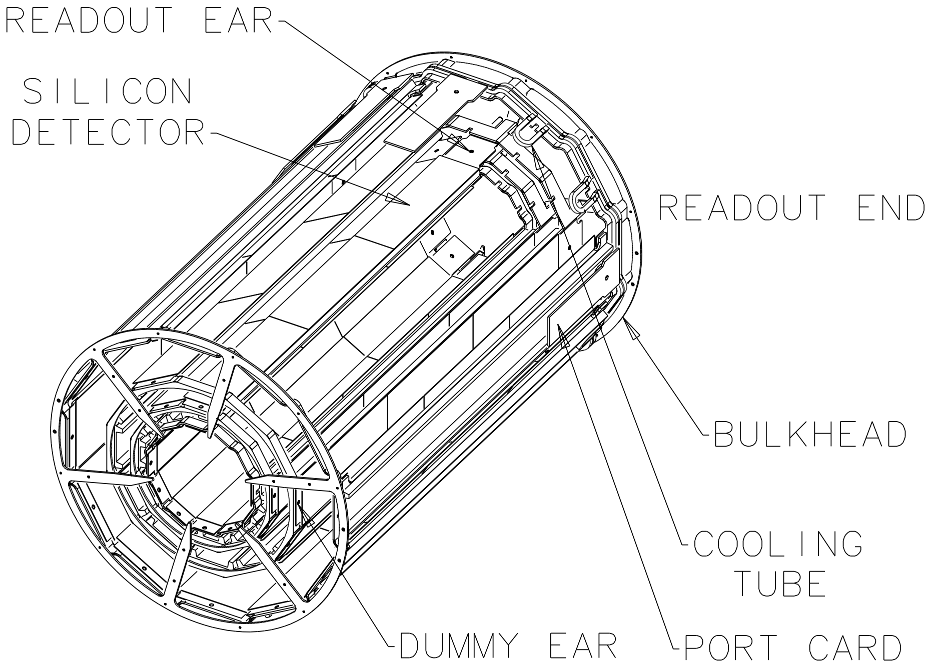

Figure 2.4: A sketch of one of the SVX barrels.

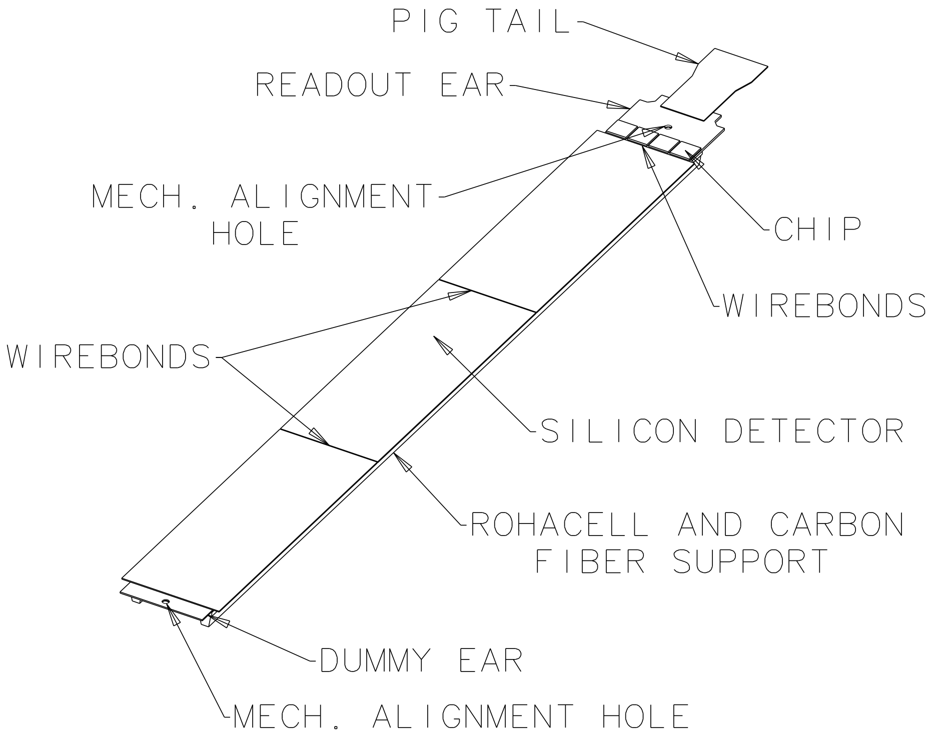

Figure 2.5: A sketch of the SVX ladder.

	SVX	SVX′
Channels	46,080	
Readout Strip L0	256	
L1	384	
L2	512	
L3	768	
Radius L0	3.0049 cm	2.8612 cm
L1	4.2560 cm	
L2	5.6872 cm	
L3	7.8658 cm	
Length	8.5 cm	
Thickness	300 μm	
Active Area Width L0	15,360 μm	
L1	23,040 μm	
L2	30,720 μm	
L3	42,240 μm	
Gain	15 mV/fC	21 mV/fC
Typical Occupancy	7 – 10%	5%
Maximum Occupancy	12 – 20%	25%

Table 2.1: The basic characteristics of the SVX and SVX′.

imuthally for the 10 end modules (bigger ones), and 16 pairs are arranged azimuthally for the 18 inner modules (smaller ones). Main functions of the VTX are to provide precise tracking information for charged particles in the r-z plane, and to measure the vertex position along the z axis. As shown in Figure 2.6, the largest cross with the bars at the ends shows a primary vertex with the highest multiplicity of the track (class 12), and the smaller ones are the vertices with less classes. It is also used to find the seed for the three dimensional reconstruction of the track in the CTC. The VTX was designed for the amount of material to be minimized to reduce the secondary interactions causing the background, such as the photon conversion electrons ($\gamma \rightarrow e^+e^-$).

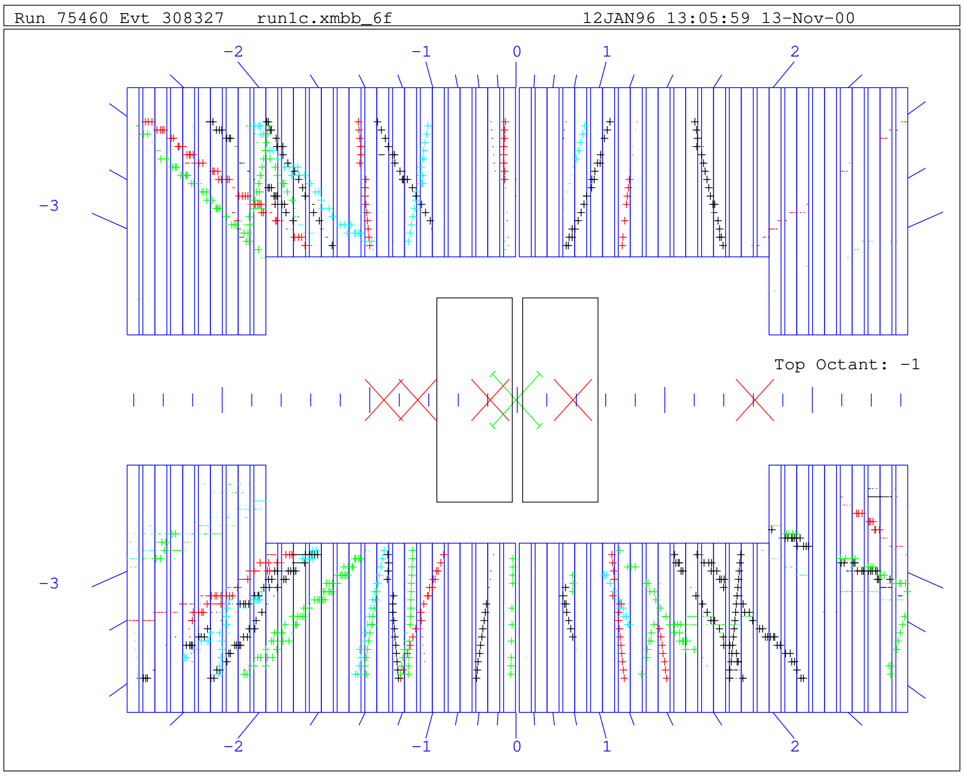

Figure 2.6: A longitudinal view of the VTX on an event display. The beam line passes horizontally through the center of the picture. The two boxes in center of the VTX represent the SVX detector. The crosses along the center line represent the vertices found by the VTX. The largest cross with the bars at the ends shows a primary vertex with the highest multiplicity of the track (class 12), and the smaller ones are the vertices with less classes. The several crosses and dots on the VTX represent the reconstructed VTX hits. Numbers on top and bottom of the VTX (-3:3) are the event pseudorapidities measured to the position of a primary vertex.

Central tracking chamber: CTC

The central tracking chamber (CTC) [34] is a 1.3 m radius and 3.2 m long cylidrical drift chamber with excellent spacial and momentum resolution used to measure charged tracks in the central region, $40° < \theta < 140°$ ($-1 < \eta < 1$).

The CTC has 84 layers of sense wires arranged into 9 *superlayers*. Five of the superlayers contain 12 sense wires parallel to the beam line. These five axial layers are interleaved with four superlayers of stereo wires tilted at $+3°$ or $-3°$ with respect to the beam direction as shown in Figure 2.7. Each stereo superlayer contains 6 sense wires. Both axial and stereo superlayers are divided into cells so that the maximum drift distance is less than 40 mm, corresponding to a drift time of about 800 ns.

Axial and stereo data are combined to form a three-dimentional track. When the track is constrained to come from the beam, the z resolution is approximately 4 mm, and the momentum resolution is

$$\frac{\delta p_T}{p_T} = 0.002 p_T,$$

where p_T has unit of GeV/c.

2.2.5 Calorimeter

The CDF calorimeter is split into electromagnetic (EM) and hadronic (HAD) components, and furthermore partitioned into four detector regions defined by the pseudorapidity coverage: the central EM and HAD ($|\eta| <\sim 1.0$), the WHA ($0.7 < |\eta| < 1.3$), the plug EM and HAD ($\sim 1.2 < |\eta| < 2.4$), and the forward EM and HAD ($\sim 2.2 < |\eta| < 4.2$) calorimeters [31]. The CEM contains a central strip chamber (CES) which measures the transverse shower profile at the depth where the longitudinal shower development becomes maximum on average. The pseudorapidity coverage, the energy and position resolutions, and the thickness are listed in Table 2.2 for the calorimeter components except for the CES. In the Table 2.2, the symbol "$\oplus$" denotes a quadrature sum, $a \oplus b \equiv \sqrt{a^2 + b^2}$.

All the CDF calorimeters are sampling calorimeters with the absorber (lead or steel) interleaved with the layers of active media. The central and plug/forward calorimeters use the different active media (described later). All calorimeters use a "tower" geometry with the approximately constant segmentation for the pseudorapidity and

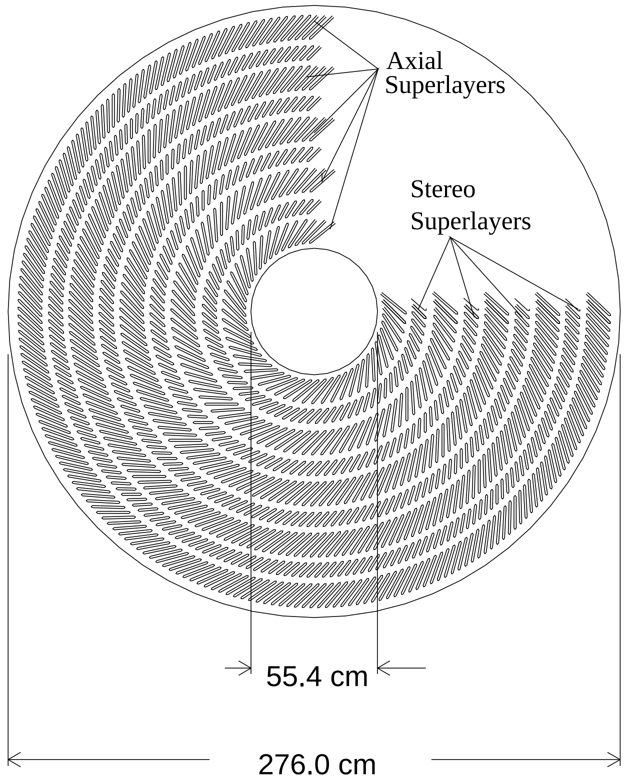

Figure 2.7: The CTC end-plate showing the wire slots.

azimuthal angle. The tower structure is projective, i.e., each tower points back to the center of the detector. Each tower has an electromagnetic shower counter in front of a corresponding hadronic calorimeter, so that a comparison between EM and hadronic energy depositions on a tower-by-tower basis enables us to identify the electrons, photons and hadrons. In addition, the electromagnetic shower counters have a precise spatial resolution of about 2 mm over the entire solid angle coverage.

The tower segmentation and the coverage of the calorimeters in one of eight identical $\eta - \phi$ quadrants ($\eta > 0$, $0^\circ < \phi < 90^\circ$) is shown in Figure 2.8. The size ($\eta \times \phi$) of each tower is $0.1(\eta) \times 15^\circ(\phi)$ in the central/wall calorimeters, and $0.1(\eta) \times 5^\circ(\phi)$ in the plug/forward calorimeters. Therefore the physical size of a tower ranges from about $24\,\mathrm{cm}\,(\eta)\times\ 46\,\mathrm{cm}\,(\phi)$ in the central region to $1.8\,\mathrm{cm}\ (\eta)\times\ 1.8\,\mathrm{cm}\,(\phi)$ in the forward region.

	$\lvert\eta\rvert$ coverage	Energy Resol. σ/E	Position Resol. [cm^2]	Thickness
Central				
EM	0 – 1.1	$13.5\%/\sqrt{E_T} \oplus 1.7\%$	0.2×0.2	$18\,X_0$
HAD	0 – 0.9	$75\%/\sqrt{E_T} \oplus 3\%$	10×5	$4.5\,\lambda_0$
End-Wall				
HAD	0.7 – 1.3	$75\%/\sqrt{E_T} \oplus 3\%$	10×5	$4.5\,\lambda_0$
Plug				
EM	1.1 – 2.4	$28\%/\sqrt{E_T} \oplus 2\%$	0.2×0.2	$18 - 23\,X_0$
HAD	1.3 – 2.4	$130\%/\sqrt{E_T} \oplus 4\%$	2×2	$5.7\,\lambda_0$
Forward				
EM	2.2 – 4.2	$25\%/\sqrt{E_T} \oplus 2\%$	0.2×0.2	$25\,X_0$
HAD	2.3 – 4.2	$130\%/\sqrt{E_T} \oplus 4\%$	3×3	$7.7\,\lambda_0$

Table 2.2: A summary of the CDF calorimeter information. The symbol "$\oplus$" denotes a quadrature sum, $a \oplus b \equiv \sqrt{a^2 + b^2}$. The E_T is the transverse energy in units of GeV. Thickness of each calorimeter component is given in units of X_0 (*radiation length*) for the EM calorimeters, and λ_0 (*interaction length*) for the Hadron calorimeters.

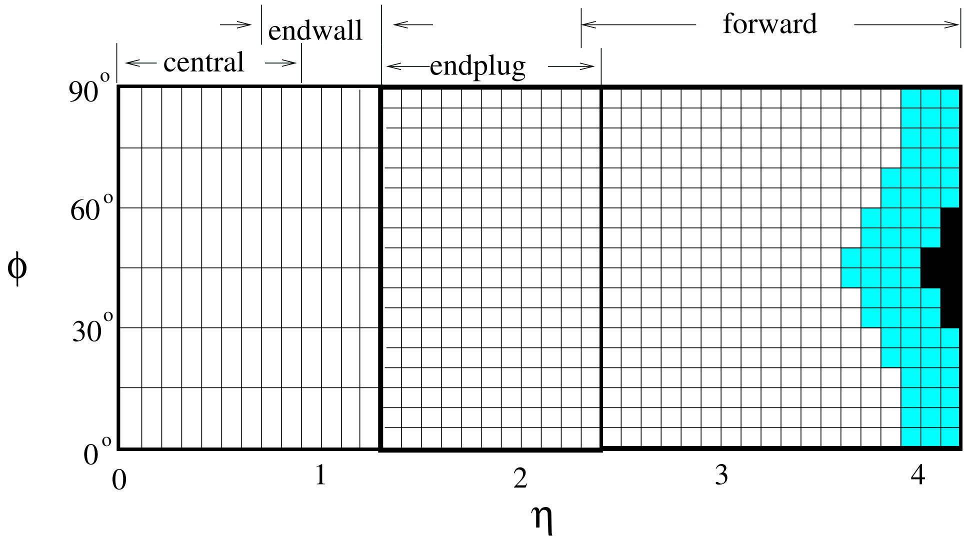

Figure 2.8: Projective tower structure of the calorimeter. Gray towers have only partial depth coverage due to overlapped low beta quadrapoles. Black towers around $\phi = 45°$ have no coverage.

Central electromagnetic calorimeter: CEM

The electromagnetic part of the central calorimeter, central electromagnetic calorimeter (CEM) [35], has the coverage of $|\eta| < 1.1$ in pseudorapidity and full 2π coverage in azimuth (all calorimeters basically have full coverage in ϕ, so only η coverage is shown for the other calorimeters). The size of a tower is $0.1(\eta) \times 15°(\phi)$. The inner (outer) radius of the CEM is 173 cm (208 cm), and the thickness is 18 radiation lengths. The CEM consists of 31 layers each of which has 3.2 mm thick lead absorber interleaved with 5 mm thick polystyrene scintillator plate. Through the two wavelength shifters per tower, the scintillation light is directed to the photomultiplier tubes.

The energy resolution of the CEM was obtained using the test beam of electrons. By changing the electron energy from 10 to 100 GeV, it was measured to be;

$$\frac{\sigma(E)}{E} = \frac{13.5\%}{\sqrt{E_T}} \oplus 2\%,$$

where the E_T is in units of GeV. Initially the towers of the CEM were calibrated with 50 GeV electrons.

Central and end-wall hadron calorimeter: CHA

The central hadron calorimeter (CHA) and end-wall hadron calorimeter (WHA) [36] are the calorimeters for hadronic particles such as charged pions, kaons. The pseudorapidity coverage is $|\eta| < 0.9$ for the CHA and $0.7 < |\eta| < 1.3$ for the WHA. The size of a CHA or WHA tower is the same as the CEM tower, $0.1(\eta) \times 15°(\phi)$, so that the first 9 towers are in the CHA, the intermediate 3 towers are shared between the CHA and WHA, and the last 3 towers are completely in the WHA. The CHA has 32 layers of 2.5 cm think steel absorber interleaved with 1.0 cm thick plastic scintillator. The WHA also has the similar structure: 15 layers of 5.0 cm thick steel absorber alternating with 1.0 cm thick plastic scintillator. The depth is 4.5 interaction lengths for both calorimeters.

Energy responses of the CHA and WHA were investigated with the beam of charged pions. For the energy range 10 – 150 GeV of the pion beams, the energy resolution of the CHA was obtained to be;

$$\frac{\sigma(E)}{E} = \frac{75\%}{\sqrt{E_T}} \oplus 3\%.$$

It was found that the WHA also has the similar energy resolutions to the CHA.

Plug electromagnetic calorimeter: PEM

The calorimeters which fit into the 30° holes like end caps, are called the plug calorimeters. As well as the central calorimeter, the plug calorimeter consists of the plug electromagnetic calorimeter (PEM) [37] and the plug hadron calorimeter (PHA) [38]. The coverage of the PEM is $1.1 < |\eta| < 2.4$ in pseudorapidity. The PEM has the gas proportional tube array (50%-50% mixture of argon-ethane with a small addition of the alcohol) as the active medium, interleaved with lead absorber. A quadrant with an azimuthal angle of 90° contains 34 layers of proportional tube arrays alternating with 2.7 mm think lead absorber layers. The PEM is segmented into 16 projective towers in η and the η size is approximately 0.1 (although a few towers have small segmentation of 0.05). The full azimuth is segmented into 72 towers each of which has the ϕ coverage of 5°. Each tower has 3 segmentations in depth: the first 5 layers for the first, the intermediate 24 layers for the second, and the last 5 layers for the third segments. The geometrical size of the PEM is 2.5 m in diameter and 50 cm in longitudinal depth. The path length from the center of the detector is about 18 – 23 radiation lengths depending on the polar angle.

The energy resolution was measured with 20 – 200 GeV electron beams to be;

$$\frac{\sigma(E)}{E} = \frac{28\%}{\sqrt{E_T}} \oplus 2\%.$$

All the towers of the PEM were calibrated with 100 GeV electrons.

Plug hadron calorimeter: PHA

The PHA [38] has the pseudorapidity coverage of $1.3 < |\eta| < 2.4$. The PHA is also a gas calorimeter that consists of a sandwich of the gas tubes (active media) and the steel (absorber). Since the PHA is not continuously connected with the WHA, there is a "crack" at the interface of the PHA and WHA. The PHA consists of 20 layers of proportional gas tube arrays interleaved with 5.0 cm thick steel absorber. Each tower has the same segmentation, $0.1(\eta) \times 5°(\phi)$, as the PEM.

Charged pion beam was used in the calibration of the PHA. By changing the beam energy from 20 to 230 GeV, the energy resolution was measured to be;

$$\frac{\sigma(E)}{E} = \frac{130\%}{\sqrt{E_T}} \oplus 4\%.$$

The energy response was found to be linear within the above range.

Forward electromagnetic calorimeter: FEM

The forward and backward regions ($2.2 < |\eta| < 4.2$) are covered by the forward electromagnetic calorimeter (FEM) [39] followed by the forward hadron calorimeter (FHA) [40]. Note that there is a crack between the plug and forward calorimeters in pseudorapidity, but the azimuthal direction is basically fully covered. The FEM is a sampling calorimeter with 30 layers of gas proportional tubes interleaved with 4.8 mm thick absorber made up of 94% lead and 6% antimony (Sb). The projective tower has two segmentations in depth, each of which has the thickness of 15 layers. The η segmentation of the FEM is 20 and each tower has the size of 0.1 in η except for the first tower with 0.03. The azimuthal segmentation is the same as the plug calorimeters, 5° in ϕ. The FEM is located about 6.5 m away from the nominal interaction point along the z axis and has the longitudinal depth of 1 m which approximately corresponds to 25 radiation lengths.

Calibrating the individual towers in the FEM with 20 – 200 GeV electron beams, the energy resolution was measured to be;

$$\frac{\sigma(E)}{E} = \frac{25\%}{\sqrt{E_T}} \oplus 2\%.$$

The energy response was found to be linear within the above range.

Forward hadron calorimeter: FHA

The FHA [40] is a calorimeter which measures the hadronic energy, placed behind the FEM in the small angle region. The coverage is $2.3 < |\eta| < 4.2$ in pseudorapidity, which corresponds to $11^\circ > \theta > 2^\circ$ in polar angle. The FHA on one side is segmented into four 90° sections around the beam pipe as the FEM. A quarter section consists of 27 steel absorber and alternating 27 gas proportional chambers with cathode pad readout. The projective tower structure is the same as the FEM, $0.1(\eta) \times 5^\circ(\phi)$, so a quadrant is segmented into 19 towers in η, and 18 towers in ϕ.

The FHA was also calibrated with charged pion beam. By varying the energy from 20 to 200 GeV, the energy resolution was measured to be;

$$\frac{\sigma(E)}{E} = \frac{130\%}{\sqrt{E_T}} \oplus 4\%.$$

Good linearity was also observed up to 200 GeV.

layer #	counter #	η_{min}	η_{max}	$\Delta\eta$
0	0, 4, 8, 12	-5.89	-5.228	0.662
1	1, 5, 9, 13	-5.228	-4.565	0.663
2	2, 6, 10, 14	-4.565	-3.903	0.662
3	3, 7, 11, 15	-3.903	-3.24	0.663

Table 2.3: The pseudorapidity coverage of the west BBC (at $z \approx -6\,\mathrm{m}$).

2.2.6 Beam-Beam counter: BBC

The beam-beam counter (BBC) consists of 4 layers $\times$ 4 scintillation counters in both east and west sides, in total 32 scintillators. The layers are labelled $0-3$ in increasing radius from the beam line, and their positions are listed in Table 2.3. They provide the "minimum-bias" trigger and are also used as a primary luminosity monitor [31]. These scintillators are arranged in a rectangle around the beam pipe as shown in Figure 2.9. They cover a region $3.24 < |\eta| < 5.90$ in pseudorapidity. Excellent time resolution ($\sigma < 200\,\mathrm{ps}$) of these counters provides the best measurement of the interaction time. As shown in Figure 2.9, two photomultiplier tubes (PMTs) are used as read out of each scintillation counter. As the counters overlap with each other, a single particle can give one or two hits and these counters are not ideal multiplicity counters.

As the luminosity monitor, the BBC can provide the instantaneous (integrated) luminosity by measuring the rate (number) of the coincidences in the counters, divided by the effective BBC cross section. From the CDF measurement of the total, elastic and single diffractive cross sections at $\sqrt{s} = 1.8\,\mathrm{TeV}$ [41, 42, 16], and CDF Run-1A data analysis, we obtain the following effective BBC cross section [43];

$$\sigma_{BBC} \;=\; 51.15 \,\pm\, 1.60\,\mathrm{mb}. \tag{2.6}$$

In the study of hard diffraction, the BBC is an important tool as well as the forward calorimeters which cover the forward regions. We use the BBC and the forward calorimeters as "gap detectors" in a search for diffractive event signal.

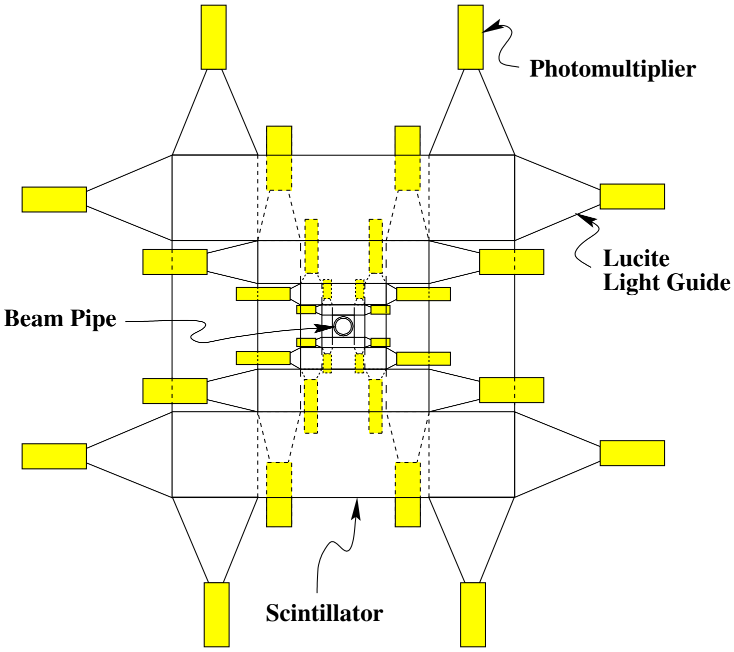

Figure 2.9: A beam-eye view of a beam-beam counter (BBC) plane. The beam pipe passes the center of the BBC. The shaded parts show the photomultiplier tubes for read out.

2.2.7 Roman pot antiproton spectrometer: RPS

To investigate the hard diffraction dissociation, a set of Roman pot proton spectrometer (RPS) [27] was installed in the beam pipe about 56 meter downstream of the CDF detector in the $\overline{p}$ direction (A48 station) after the Run-1B collider operation. Diffractive scattering in proton-antiproton collisions is characterized by a recoil antiproton (or proton) with momentum larger than 90% of the incident antiproton (proton) beam. The recoil antiproton with slightly lower momentum is bent into inner side with respect to the antiproton beam orbit when it passes through a magnetic field of the Tevatron dipole magnets, but it stays inside of the beam pipe. (Here the case that the antiproton remains intact and the proton dissociates is discussed because this is the case for our study.) Therefore, by inserting a tracking detector inside the beam pipe at a suitable position, we can detect a recoil antiproton track and measure its position and angle, to give the four-momentum of recoil antiproton together with vertex information. Using this information we obtain the following kinematic variables for each diffraction event; the Feynman variable x_F, ξ, and the momentum transfer squared t at the antiproton vertex. The measurement with the RPS is clearly better than that with only the rapidity gap technique where t is unknown and only ξ can be measured with some ambiguity.

Using the RPS detector, we can also trigger the events where the recoil $\overline{p}$ momentum is larger than 90.5% of beam momentum (i.e. $x_F > 0.905$). The RPS was used to detect the recoil $\overline{p}$ system giving the fractional momentum loss (ξ) of the initial $\overline{p}$ momentum and the four-momentum transfer squared (t). The RPS covers a kinematical region of $0.035 < \xi < 0.095$ and $|t| < 1.0$ GeV^2 with high efficiency. We will apply a cut to select events in this region.

The structure of the RPS is shown in Figure 2.10. Three Roman pot type vacuum chambers [27] are separated from each other by 98.5 cm (a total length including beam pipe is 266.54 cm). A schematic view of a Roman pot vacuum chamber with tracking detector is shown in Figure 2.11. The tracking detector consists of two dimensional scintillating fiber (SCSF81) hodoscope and the trigger counter (Bicron BC404). The detector is placed inside the vessel (14.8 cm diameter, 0.4 mm thick steel) filled with air which is attached to the vacuum chamber with 19.7 cm diameter through the bellows as shown in Figure 2.11. A recoil antiproton hits the tracking detector positioned at the top of the vessel. Scintillation light from the hit fibers is directed to the MCPMT, 80-channel HAMAMATSU H5828, placed at the bottom. The trigger scintillator behind the tracking detector is 2.1 cm square and 8 mm thick and provides the timing information used in the diffractive trigger.

Scintillating fiber hodoscope

The detecting part of the spectrometer is a fiber hodoscope which consists of 80 scintillating fiber ribbons. As shown in Figure 2.10, the two fiber arrays give X and Y hit positions, respectively. Each fiber array consists of two sub-layers with 20 fiber ribbons.

The structure of the fiber ribbon is shown in Figure 2.12. The fiber material is KURARAY SCSF81 with single cladding, and one fiber is 20 cm long and 0.833 mm$\times$0.833 mm square in cross section. A scintillating core is 0.800 mm$\times$0.800 mm square. One fiber ribbon is made of four such fibers. On the detecting side, the fibers are arranged in line along the beam direction to increase the path length of the particle, while on the MCPMT side the fibers are rearranged into a square to fit with the shape of the

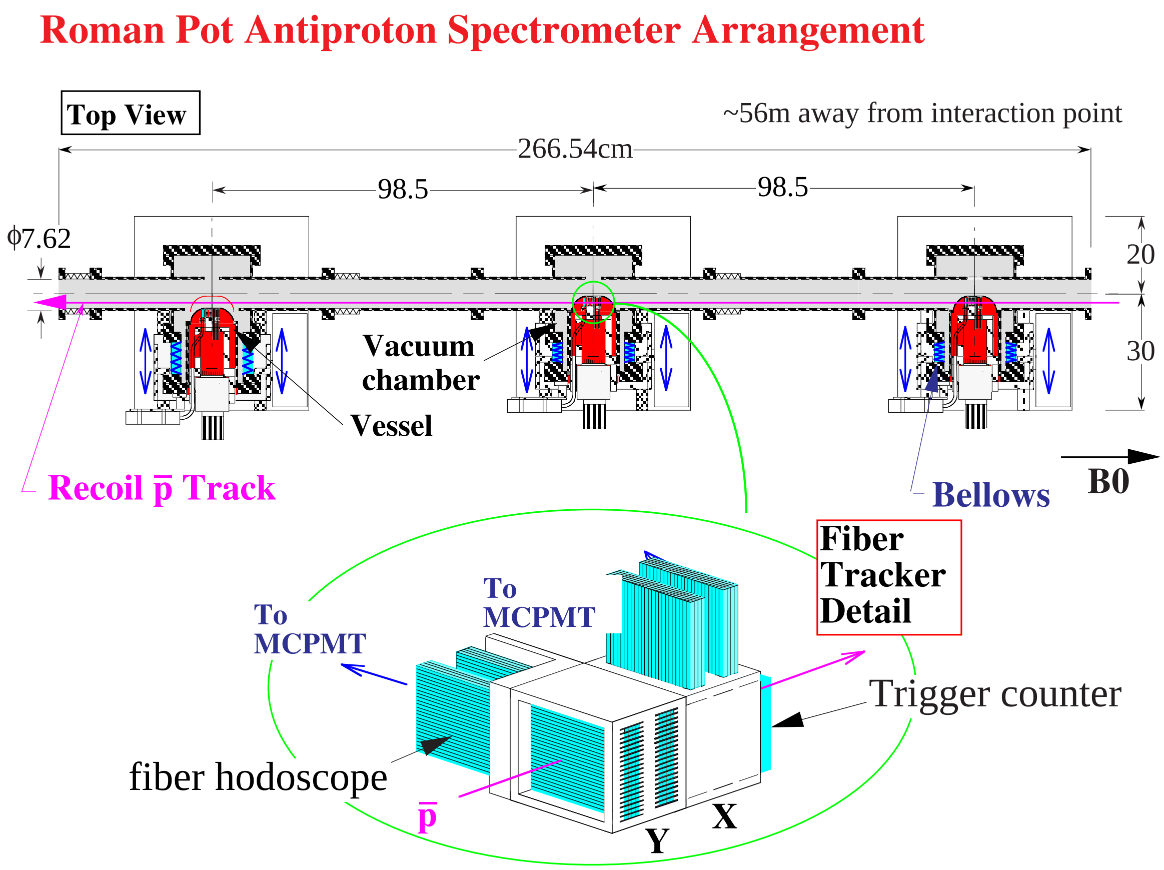

Figure 2.10: A top view of the RPS. The B0 interaction point is 56 m away from the RPS in the right direction so that recoil $\overline{p}$ in the diffractive scattering travels from right to left. In this arrangement the right pot is called Pot1, the middle one is Pot2 and the left is Pot3. The fiber tracker structure of the hodoscope is also shown.

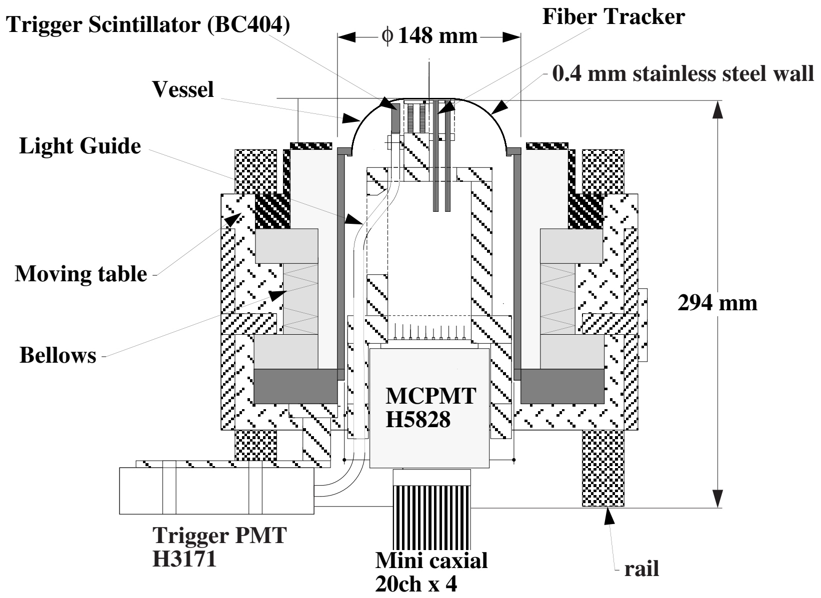

Figure 2.11: A schematic view of a Roman pot vacuum chamber.

MCPMT photo-cathode.

The arrangement of the fiber ribbons is shown in Figure 2.13. This figure shows the array of the X (or Y) detection layers (the size and distance are not scaled). Two sub-layers in a fiber array are placed parallel to each other. The fiber ribbon spacing in a sub-layer is 0.267 mm corresponding to one third of the scintillating fiber core width (equivarent to a bin width). The spaces between the ribbons are filled up with the aluminized mylar. The distance between of the two sub-layer centers is 8.5 mm. The fiber hit information of the three fiber arrays enables us to reconstruct a charged

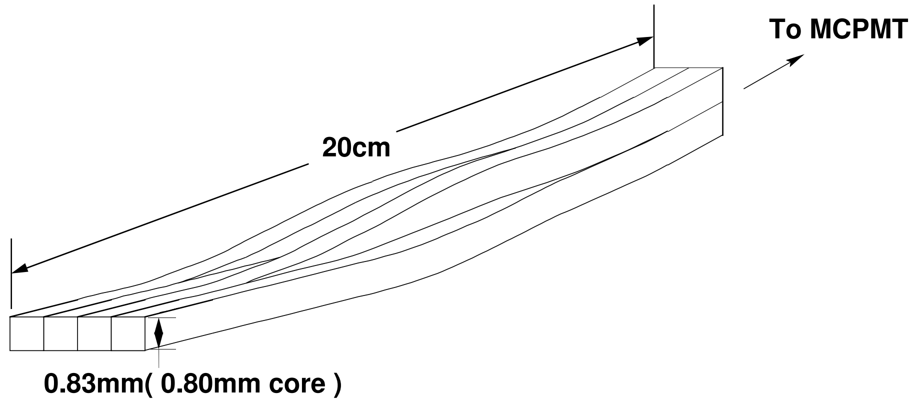

Figure 2.12: A sketch of a fiber ribbon.

particle track as shown in Figure 2.13.

The geometry of the fiber hodoscope at the operation mode is shown in Figure 2.14. The p beam is closer to the spectrometer than the $\overline{p}$ beam by 4.4 mm (=2.2 mm×2). The typical distance between the $\overline{p}$ beam orbit and the RPS detector (aluminum fiber array holder) edge was set to 1.261 cm (=1.44+0.075-0.254)*.

Between the RPS detector edge to the fiber, the following materials exist: the detector wall (fiber holder, 0.7 mm thick aluminum), the aluminized mylar (0.067 mm) and the acrylic clad (0.0167 mm). Therefore, the distance between the $\overline{p}$ beam orbit and the edge of the first fiber is 1.339 cm (after RPS position calibration). As shown in Figure 2.14, the fiber ribbons were numbered as 1 to 40 in the X or Y directions (i.e., the fiber #40 of Y detector is at $y = 0$). As we have 40 fiber ribbons and the above one-third spacing in a fiber array, we have 79 bins in the X or Y detector. Consequently the total number of effective bins for the track reconstruction is 77 excluding the two edge bins, #1 and #79. This means that the detection area of the fiber hodoscope is 2.05 cm×2.05 cm in the $X-Y$ plane. The RPS detector covers the area of $-3.25\,\mathrm{cm} \leq x \leq -1.17\,\mathrm{cm}$ $(-1.17 = -1.339 + 0.22 - 0.0266 \times 2)$ and $-1.01\,\mathrm{cm} \leq y \leq 1.01\,\mathrm{cm}$, effectively.

RPS position calibration

Diffractive variables, ξ and t, are sensitive to the reconstructed track in RPS. Therefore, it is important to calibrate the position of each fiber hodoscope. We perforemed the calibration by comparing the real diffractive data to the pseudoexperiment data of diffractive event. The precise discussion is given in Appendix A. We found the extra-displacements of fiber hodoscopes typically 0.75 mm, and 800 μm at maximum as described in Appendix A. After the calibration, we estimate the RPS acceptance, the position and angle resolutions of RPS, and the resolutions of ξ and t. We found the RPS position resolution of X (Y) to be 103 (99) μm, and the angle resolution to be 0.074 (0.071) milli-radians, ξ resolution to be 1.0×10^{-3}, and t resolution to be $0.08\,\mathrm{GeV}^2$ at $t = -0.1\,\mathrm{GeV}^2$, $0.25\,\mathrm{GeV}^2$ at $t = -1\,\mathrm{GeV}^2$.

*From the RPS position calibration (described in Appendix A), we found extra-displacements of fiber hodoscopes typically 0.75 mm, and 800 μm at maximum. It corresponds to a wall of the Roman pot vessel (0.4 mm thick steel) and air gap (0.35 mm).

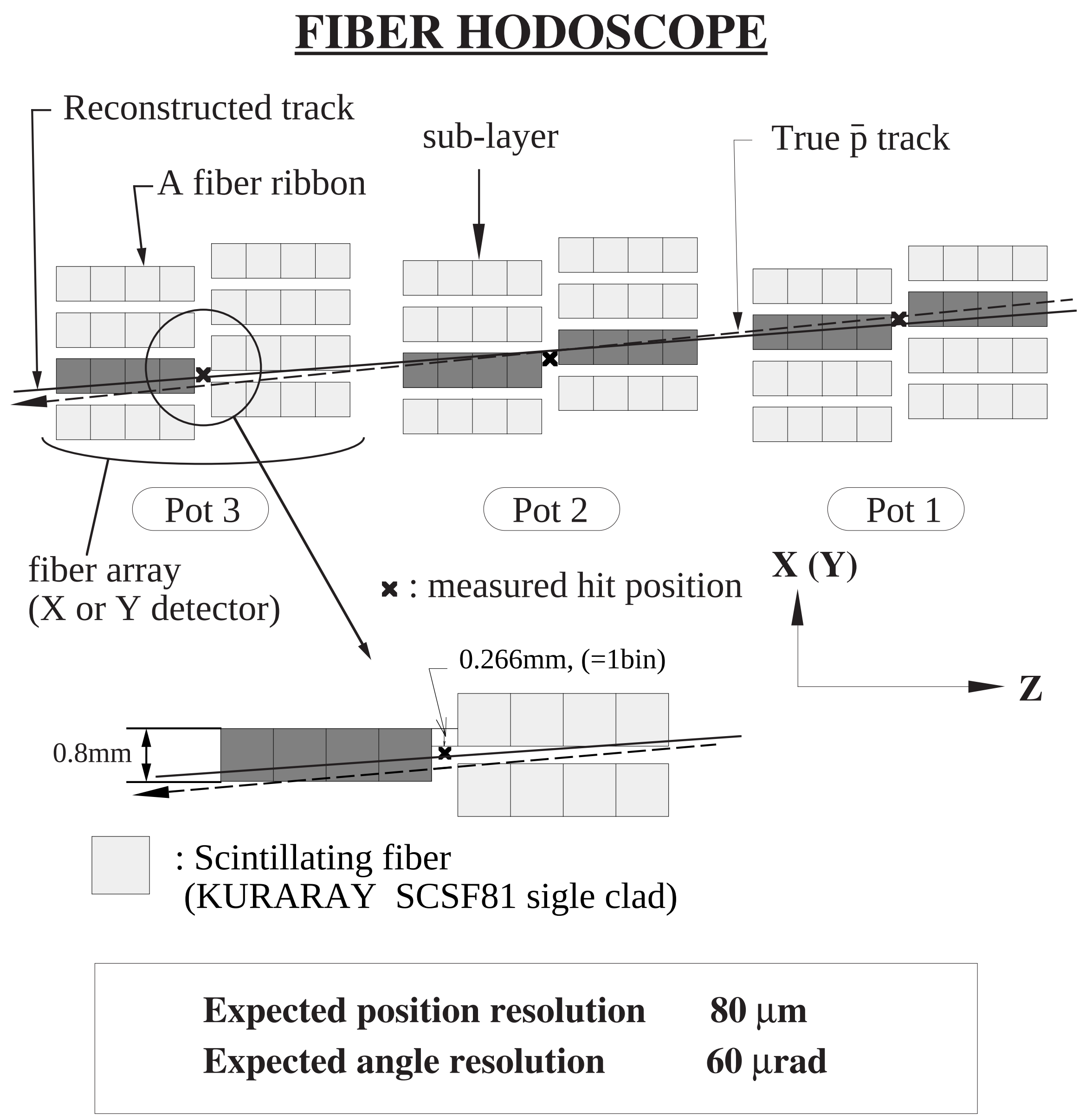

Figure 2.13: The RPS track reconstruction from the hits of the fibers. Only the X (or Y) detection layers are shown.

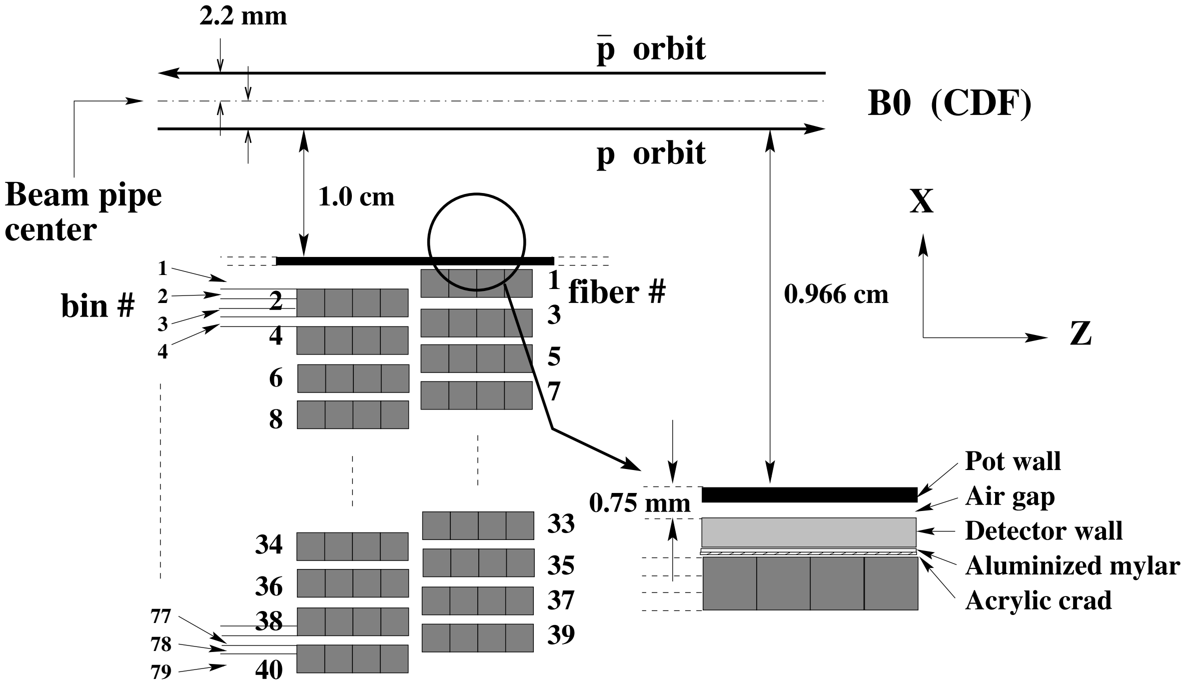

Figure 2.14: Arrangement of the fiber hodoscope in the RPS. The B0 interaction point is on the right side. The numbering scheme for the fibers (1–40) and the bins (1–79) shown in the figure is adopted only to the X detector. The two edge bins (1 and 79) are not used in the track reconstruction.

2.3 Trigger system

The beam crossing rate at the Tevatron is about 300 kHz (= 1 crossing/3.5 μs). At higher luminosities the average number of $p\overline{p}$ interactions per crossing exceeds one. CDF writes out events at the rate of a few Hz ($5-7$ Hz), thus keeping the amount of data for offline processing to a manageable level. This requires the use of a trigger system that has a rejection factor of about 5,000 to 1.

CDF utilizes the three-level trigger system in order to achieve the above rejection factor. The lowest level trigger (level-1) makes a decision in hardware during the time between beam crossings. The events that pass the level-1 trigger are considered by the level-2 trigger system. The level-2 trigger is also implemented in hardware, but uses microprocessors for some of its work. The level-2 trigger decision requires $25-35\,\mu$s and $7-10$ beam crossings are lost during this time since the data has not been buffered at this stage. Those events that pass the level-2 requirements are digitized and then read out by scanners into a buffer (taking about 3 ms). Once the event scan is complete, the level-1 and level-2 trigger systems are reenabled and begin to look at a new data from beam crossings again. The buffered events are passed to the level-3 trigger system. The level-3 trigger is entirely based on software. The events that pass the level-3 requirements are written out to 8mm magnetic tape. About 35 million events were recorded onto tape during Run-1.

Chapter 3

Event selection

In this chapter, we describe the diffractive trigger in the data acquisition and the selection of diffractive event in the offline analysis. In addition to the diffractive events, we use the non-diffractive events in inelastic $p\bar{p}$ collisions to study the background against the diffractive events.

In this analysis, we use the data taken during Run-1C low luminosity run from January 18 to January 23 in 1996.

3.1 Jet definition

The CDF jet clustering algorithm uses a cone of a fixed radius to define a jet [44]. For this analysis, the cone radius (R) is chosen to be 0.7. The transverse energies and momenta in the jet definition depend only on the energy deposition observed in the calorimeter. The observed quantities differ from the true partonic values for a variety of reasons. Some of these are the result of limitations in the detector performance.

- The calorimeter response to low-energy charged pions exhibits a non-linearity for momenta below 10 GeV.

- Charged particles with transverse momenta below $\approx 400\,\mathrm{MeV}$ bend sufficiently in the magnetic field that they do not reach the calorimeter. At slightly higher transverse momenta, the magnetic field can bend particles outside the clustering cone.

- Particles that shower in boundary regions of the calorimeter will, on average, have a smaller energy reported than for regions of uniform response.

Others result from fundamental elements of the physics process.

- Energy not associated with the hard-scattering process ("underlying event") will be collected within the clustering cone*.
- Transverse spreading of the jet due to fragmentation effects to be lost outside the clustering cone.
- Energy in neutrinos and muons, which deposit either zero or some small fraction of their energy in the calorimeter.

A correction function which takes into account these effects is generated and applied to jets in the data sample. This function is a map of detector response for different energies and values of detector-η. The procedure for generating the response map has three parts. The first is the determination of the response of the central calorimeter to jets. This is facilitated by the use of CTC to measure jet-fragmentation properties, and to provide an in situ measurement of response to low momentum charged particles. Second, the response in the central calorimeter is then extended into other regions of the detector, where charged-particle momentum determination is not available, using a technique where the E_T of jets in the central calorimeter is required to balance the E_T of jets in the plug and forward calorimeters. Finally, corrections are determined for energy escaping the jet cone, and being added by the underlying event.

we defined a jet by the following criteria;

- E_T of a jet cluster ($R = 0.7$) with the jet energy correction to be larger than 5 GeV,
- absolute value of pseudorapidity of the jet to be less than 4.2.

*The underlying energy depends on not only the physics process but also the instantaneous luminosity. According that we use low luminosity data, we measured the underlying energy for the diffractive dijets (described in Appendix B and [45]).

trigger level	trigger condition and trigger rate	
Level-1	4-fold coincidence of the RPS trigger signals and $\overline{p}$ timing Prescaled to 50-200 Hz	
Level-2	Split into 2 paths	
	"Diffractive Inclusive"	**"Diffractive Dijet"**
		≥ 2 clusters with $E_T \geq 3\,\mathrm{GeV}$
	Dynamic prescale only	No prescaling
	Prescale factor $= \begin{cases} 100 \sim 1000 & \text{(high luminosity run)} \\ 1 \sim 10 & \text{(low luminosity run)} \end{cases}$	
	Total trigger rate : $\sim 1\,\mathrm{Hz}$	
Level-3	• Requiring the primary vertex; Primary vertex : ≥ 1 vertices at class ≥ 5 ≤ 1 vertex at class 12 • No too many hits in the RPS sub-layers; The numbers of sub-layers with more than 6 hits should be less than 4. • $\geq$2 jet clusters with $E_T \geq 5\,\mathrm{GeV}$ (only for the diffractive dijet trigger)	

Table 3.1: The diffractive trigger summary.

3.2 Diffractive trigger

The diffractive event is characterized by the existence of a recoil $\overline{p}$ with a momentum larger than 90% of the incident $\overline{p}$ beam. The recoil $\overline{p}$ is bent into inside of the Tevatron ring by the magnetic field of Tevatron dipole magnets. Therefore, we trigger the diffractive events by tagging the recoil $\overline{p}$ signal with trigger counters in the RPS. The diffractive trigger is summarized in Table 3.1.

3.2.1 Level-1 trigger

The level-1 trigger is a 4-fold coincidence of the following signals;

- three signals from trigger counters in the RPS, and

- a gate signal of $\overline{p}$ which is provided from accelerator clock at the A48 station (the location of the RPS).

The trigger rate is set to 50-200 Hz by prescaling the number of event triggers.

3.2.2 Level-2 trigger

The level-2 trigger is split into two paths: one is the "diffractive inclusive" trigger where we only require the event passes the level-1 diffractive trigger, and reduce the trigger rate to about 1 Hz by taking one event per the prescale number of events. The prescale factor is varied dynamically, on event-by-event basis, depending on instantaneous luminosity; the other is the "diffractive dijet" trigger where two or more level-2 clusters[†] with $E_T > 3\,\mathrm{GeV}$ are required in addition to the level-1 trigger signal without prescaling.

A level-2 dynamic prescaling information is archived in LUMMON (luminosity monitor) database. Looking at the database, we estimate the averaged dynamic prescaling factor (DPS) for each run. The table 3.2 shows the summary of the prescaling factor.

3.2.3 Level-3 trigger

In the level-3 trigger, there are two common requirements on the primary vertex and the RPS hits for both the diffractive inclusive and the diffractive dijet triggers. Furthermore there is the dijet requirement for the diffractive dijet trigger. In order to reject empty events, where no particles are detected in the CDF detector, we require at least one vertex in any class. Then we require the event has one or less vertex at class 12 to reject the multiple interaction background. For the RPS hits, if the number of sub-layers (X or Y) with 6 or more hits is larger than 4 (out of 12 sub-layers), the event is rejected as the RPS multi-hit background. The main background source is the hadron shower produced by a recoil $\overline{p}$ or a beam halo interacting at the beam pipe or the RPS detector wall. In addition, the second "level-3 jet[‡]" E_T is required to be larger than 5 GeV for the diffractive dijet trigger.

[†]The level-2 cluster is reconstructed by hardware. The cluster size is $\Delta\eta \times \Delta\phi = 0.2 \times 15°$.

[‡]The level-3 jet cluster is reconstructed by software with cone algorithm.

run number	number of triggers		averaged DPS
	before prescaling	after prescaling	
75647	2779561	712413	3.902
75648	1341300	450406	2.978
75650	204193	39076	5.226
75674	4964469	750063	6.619
75675	366543	84212	4.353
75676	216598	52416	4.132
75677	696494	653859	1.065
75678	790921	381012	2.076
75713	1341870	539472	2.487
75715	692039	461256	1.500
75733	394707	40408	9.768
75734	950339	139931	6.791
75737	2456967	323883	7.586
75738	2698415	390284	6.914
overall	19894416	5018691	3.964

Table 3.2: The number of triggers before and after level-2 dynamic prescaling, and averaged prescale factor.

Selection Cuts	Number of events	
	SD inclusive trigger data	SD JJ trigger data
All events	2,705,609	
• RPS position 1.6 cm away from the $\overline{p}$ beam orbit		
• CDF good runs		
Preselection	2,656,169	
LUMMON and SVXBPO database		
missing E_T cut		
loose RPS track cut		
L3 vertex cut	2,344,237	
Vertex cut	2,160,677	
RPS cut		
one-MIP cut	1,389,519	
RPS acceptance cut	1,265,717	
West multiplicity cut		
Inner BBC multiplicity cut	1,200,295	
Tower multiplicity cut	1,195,558	
	1,194,509	1,420
Jet multiplicity cut	10,766	
	9,834	1,260

Table 3.3: Event selection cuts, and the number of events after the cuts for diffractive data. Finally, we have approximately 1,195,000 of diffractive inclusive events and 11,000 diffractive dijet events.

3.3 Diffractive dijet event selection

We took about 2.7 million events at $\sqrt{s} = 1800\,\text{GeV}$ with the above diffractive triggers during Run-1C low luminosity run ($\approx 1.9 \times 10^{29}\,\text{s}^{-1}\text{cm}^{-2}$). These data were taken with the RPS operating position 1.6 cm away from the $\overline{p}$ beam orbit. We applied the selection cuts as listed in Table 3.3.

3.3.1 Preselection

As a preselection, we require: 1) existence of LUMMON and SVXBPO (SVX beam position) databases; 2) no large missing E_T given by $\not{E}_T$ significance ≤ 3, and $\not{E}_T$

$\leq 20\,\mathrm{GeV}$; and 3) the number of RPS tracks ($N_{\mathrm{TRK}}^{\mathrm{RPS}}$) less than 20. The missing E_T distributions are shown in Figure 3.1 together with these thresholds. The number of RPS tracks distribution is shown in Figure 3.2 together with the threshold.

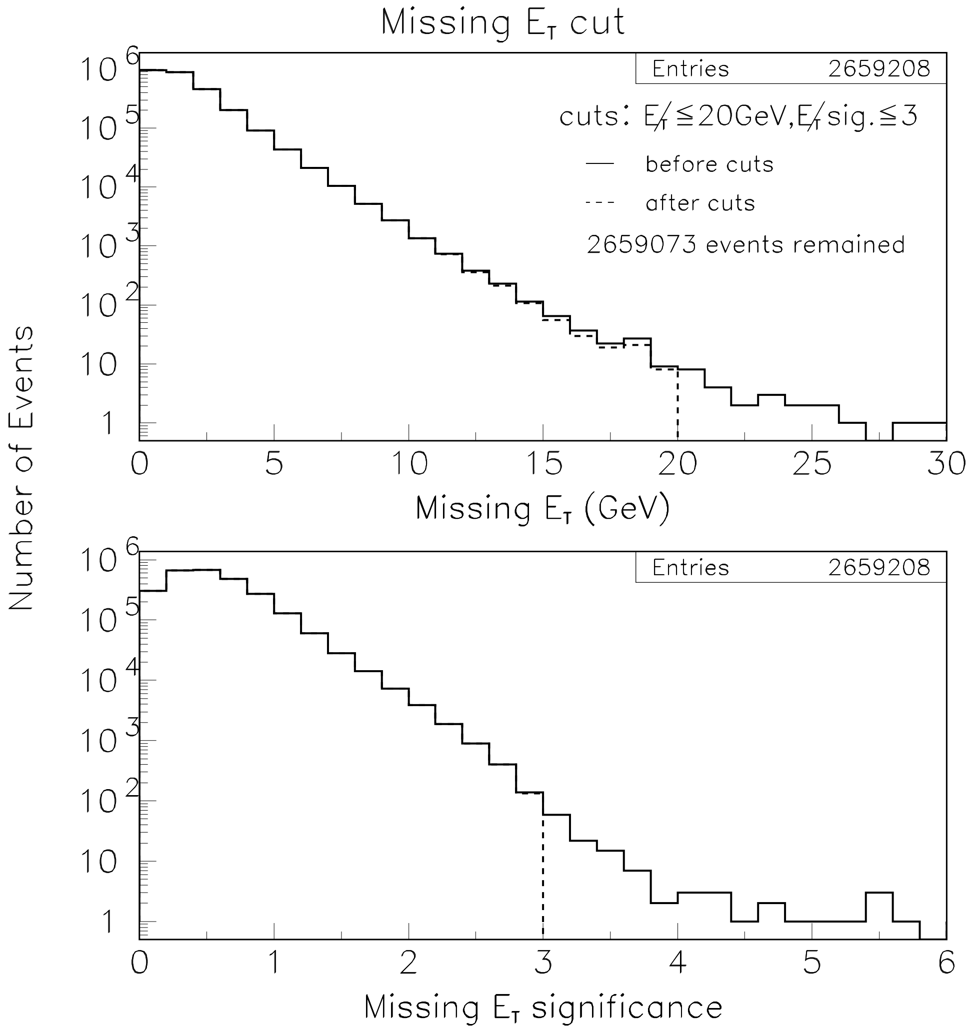

Figure 3.1: Missing E_T (top) and missing E_T significance (bottom) distributions for diffractive trigger data. We require $\not{E}_T$ to be less than 20 GeV and $\not{E}_T$ significance to be less than 3. The solid line shows before the cut, and the dashed line shows after the cut. After this cut, 2659073 events remained.

3.3.2 Vertex cut

Since we did not have the level-3 trigger of the number of vertices in a few runs, we apply the same criteria as the level-3 trigger of $N_{\mathrm{VTX}}^{12} \leq 1$ and $N_{\mathrm{VTX}}^{\mathrm{ANY}} \geq 1$, where N_{VTX}^{12} is the number of vertices with class 12 (highest quality), and $N_{\mathrm{VTX}}^{\mathrm{ANY}}$ is the number

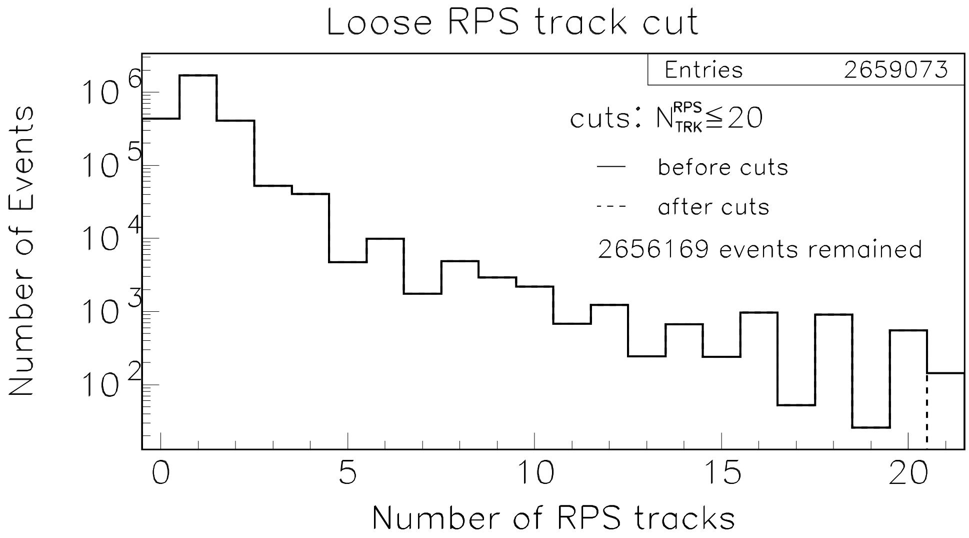

Figure 3.2: Number of RPS tracks distribution. We require the number of tracks to be less than 20. The solid line shows before the cut, and the dashed line shows after the cut. After this cut, 2656169 events remained.

of any class vertices. The number of vertices distributions are shown in Figure 3.3 together with the thresholds.

Then, we require the event Z-vertex to be within a window of 60 cm around the center of the CDF detector; $|Z_{\mathrm{VTX}}| \leq 60$ cm. The Z-vertex distribution is shown in Figure 3.4 together with the threshold.

3.3.3 Diffractive event selection

We apply several *diffraction selection* cuts. In order to reduce the RPS multiple-hit and noise, we require one-MIP signal in the RPS. The "one-MIP signal" means a signal caused by a minimum ionizing particle consistent with $\overline{p}$. We require that the pulse-height of each trigger scintillator ($R_i^{\mathrm{TRG}}, i = 1, 2$ and 3) should be above 250 ADC counts, the sum of the pulse-heights should be less than 1800 ADC counts, and one track should be reconstructed with 3 X hits and 3 Y hits in the RPS consistent with the one-MIP signal;

- $R_1^{\mathrm{TRG}}, R_2^{\mathrm{TRG}}$, and $R_3^{\mathrm{TRG}} \geq 250$ ADC counts,
- $\sum_{i=1}^{3} R_i^{\mathrm{TRG}} \leq 1800$ ADC counts, and
- The number of tracks in the RPS ($N_{\mathrm{TRK}}^{\mathrm{RPS}}$) should be equal to one.

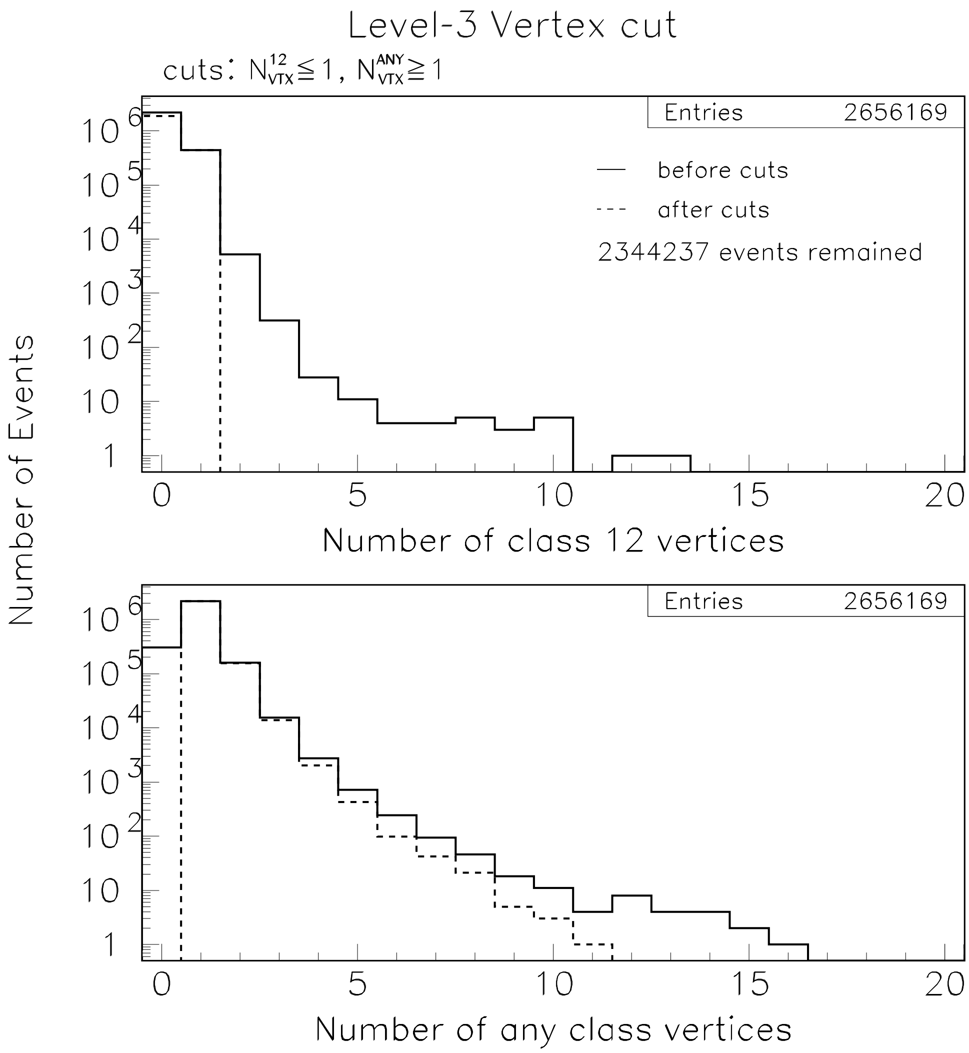

Figure 3.3: Number of class 12 vertices (top) and any class (bottom) vertices distributions for diffractive data. We require the same criteria as level-3 VTX trigger, the number of class 12 vertices to be less than 2 and the number of any class vertices to be larger than 0, The solid line shows before the cut, and the dashed line shows after the cut. After this cut, 2344237 events remained.

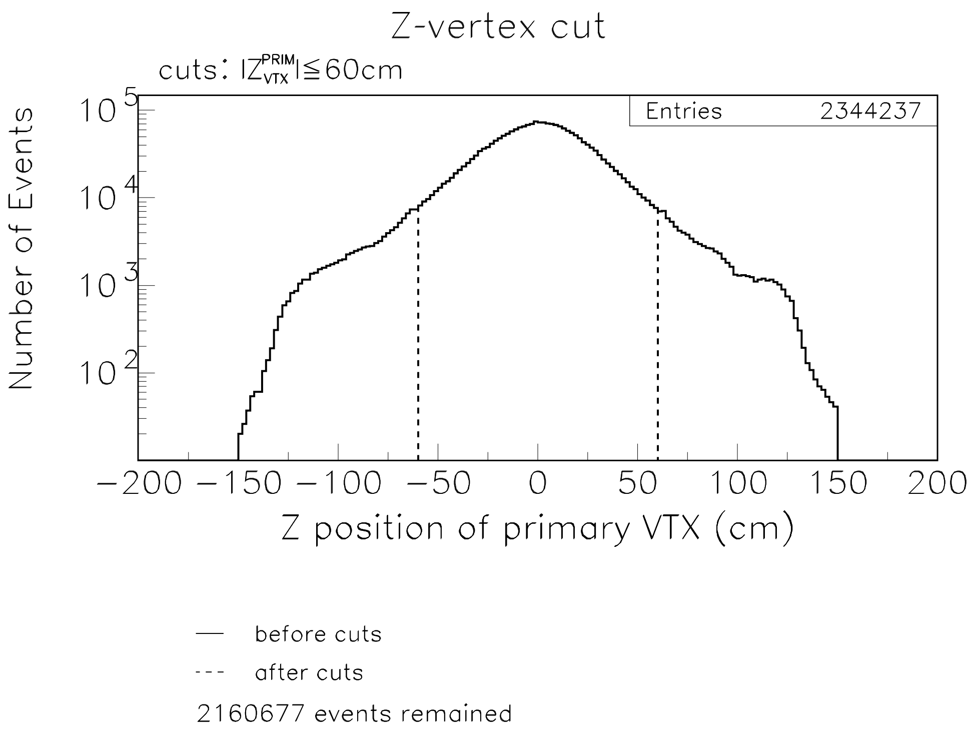

Figure 3.4: The primary Z-vertex distribution for diffractive trigger events. We require an absolute value of Z-vertex to be less than 60 cm. The solid line shows before the cut, and the dashed line shows after the cut. After this cut, 2160677 events remained.

The distributions of trigger pulse-heights and the number of tracks in the RPS are shown in Figure 3.5 together with the thresholds.

The RPS acceptance cut is introduced in order to remove events with a fake track due to the beam halo. We select the events in the following kinematic region with high effeciency: $0.035 \leq \xi \leq 0.095$ and $|t| \leq 1\,\mathrm{GeV}^2$. The ξ and the t distributions are shown in Figure 3.6 together with the thresholds.

An "inner BBC multiplicity cut" and a "tower multiplicity cut" are applied to reduce the overlap background, due to two $p\overline{p}$ collisions in a bunch which cause a non-diffractive dijet event and a diffractive inclusive event. The non-diffractive dijet event has more particles in the forward region than the diffractive dijet event. Therefore we introduce the inner BBC multiplicity cut where at least one of the inner-most BBC counters should have no hit. The BBC is a hodoscope which consists of 4 sets of 4 scintillation counters labelled as $0-15$ as shown in Figure 3.7. The channel 0 and 14 in the west BBC were dead during Run-1C where still 14 beam-beam counters were alive. We named these runs "BBC14" runs. All of the inner-most counters were dead

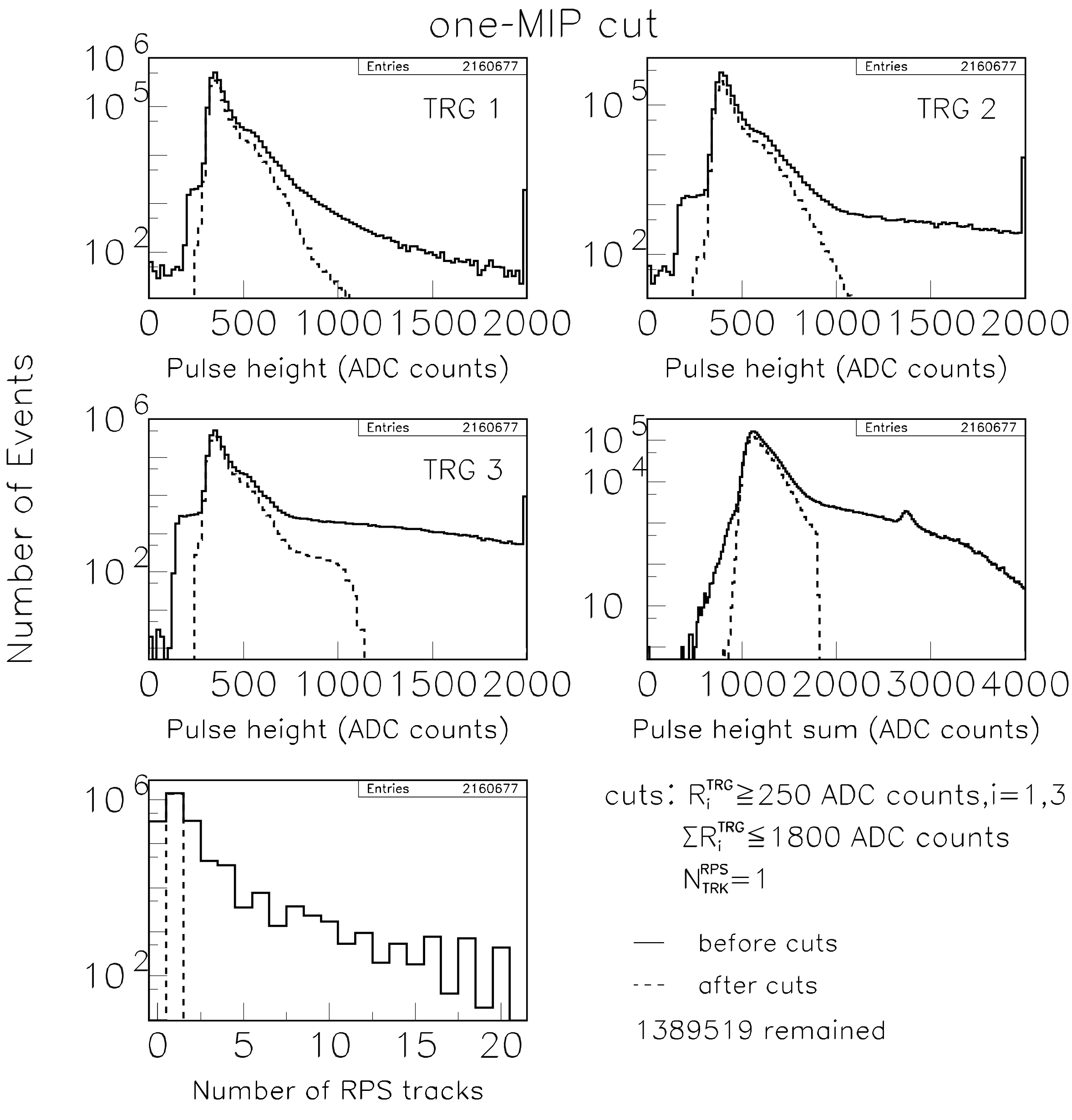

Figure 3.5: Pulse height of 3 RPS trigger counters (2 top and middle-left plots), sum of the pulse heights (middle-right), and the number of RPS tracks (bottom) distributions. We require each pulse height of RPS trigger counter to be larger than 250 ADC counts, sum of the pulse heights to be less than 1800 ADC counts, and number of RPS tracks to be equal to 1. The solid line shows before the cut, and the dashed line shows after the cut. After this cut, 1389519 events remained.

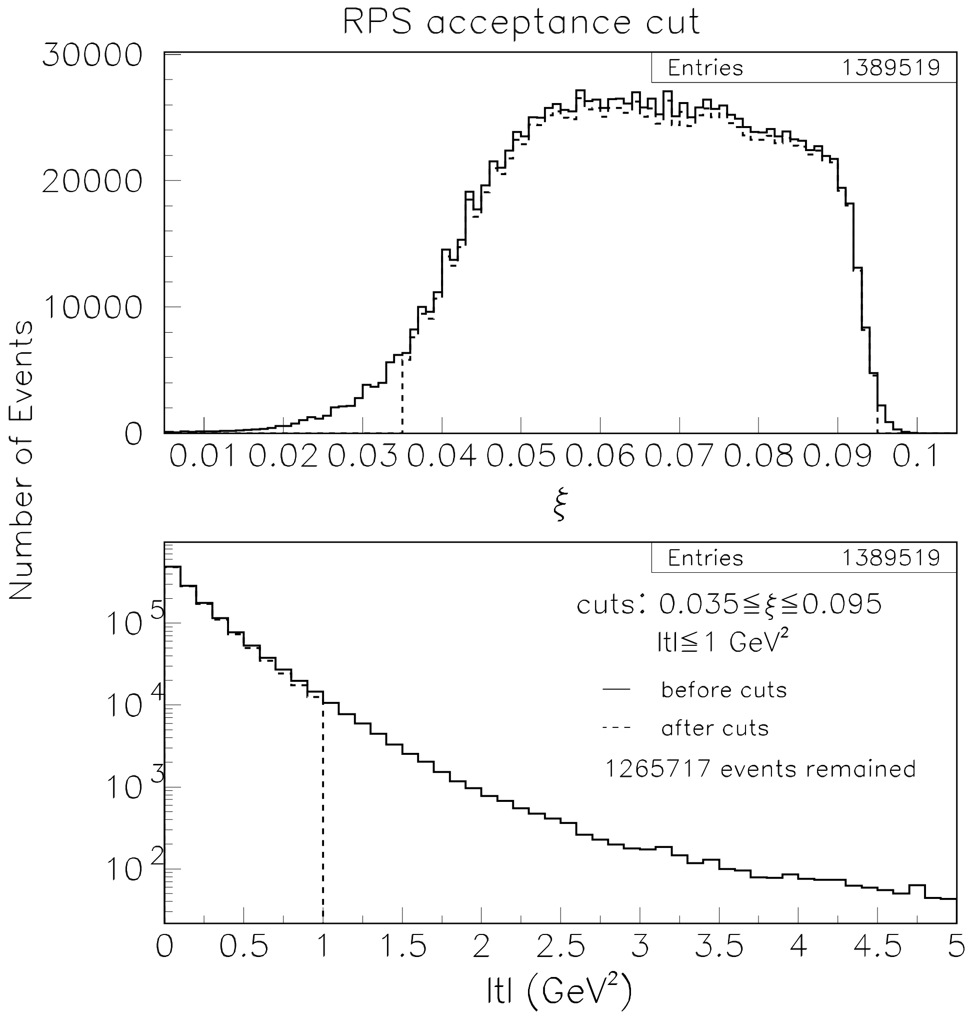

Figure 3.6: ξ (top) and $|t|$ (bottom) distributions. we require $0.035 \leq \xi \leq 0.095$ and $|t| \leq 1\,\mathrm{GeV}^2$. The solid line shows before the cut, and the dashed line shows after the cut. After this cut, 1265717 events remained.

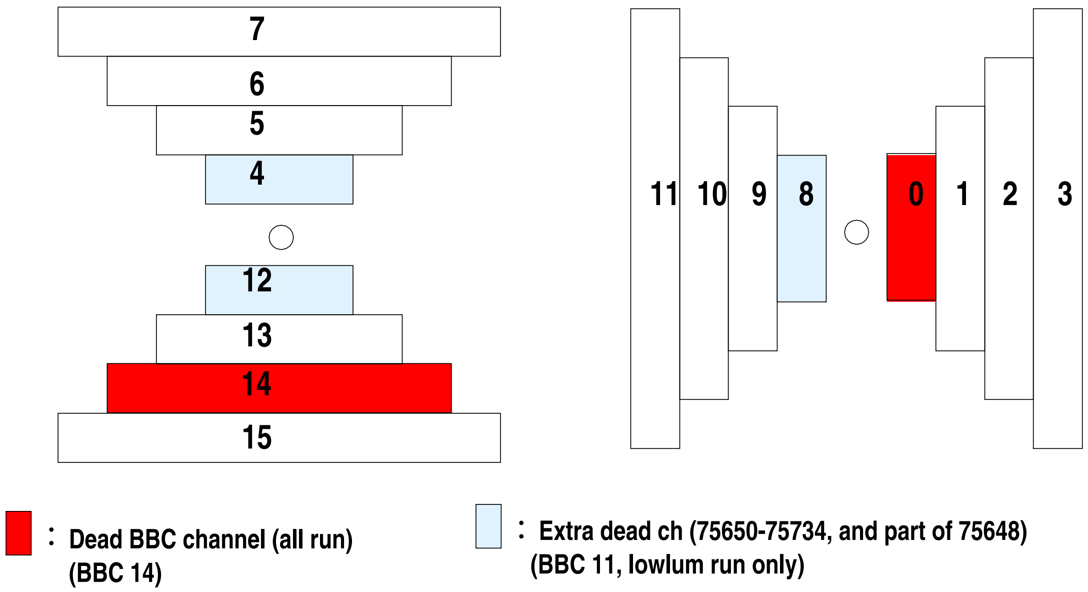

Figure 3.7: West BBC condition in Run-1C, lowluminosity run.

in some runs where still 11 counters were alive. We named these runs "BBC11" runs. We define the inner BBC multiplicity cut as the follows;

- The number of BBC hits in the inner-most counters (layer 0) should be less than 3 ($N_{\rm BBC}^{\rm Ly0} \leq 2$) for BBC14 runs, or
- The number of BBC hits in the next-to inner-most counters (layer 1) should be less than 4 ($N_{\rm BBC}^{\rm Ly1} \leq 3$) for BBC11 runs.

We define the tower multiplicity cut as follows;

- The number of hit towers in the forward calorimeter ($N_{\rm TWR}$) in the region of $-4.2 \leq \eta \leq -2.4$ should be less than 16 ($N_{\rm TWR} \leq 15$),

where a hit tower means a tower with E_T above the following threshold:

$$\text{Threshold } E_T \text{ (GeV)} = \begin{cases} 0.2 & (|\eta| < 1.1) \\ 0.450 \times \sin[2\arctan\{\exp(-\eta)\}] & (1.1 \leq |\eta| \leq 1.5) \\ 0.2 & (1.5 < |\eta| \leq 2.3) \\ -0.143 \times |\eta| + 0.579 & (2.3 < |\eta| \leq 3.0) \\ -0.0625 \times |\eta| + 0.3375 & (3.0 < |\eta| \leq 4.2) \end{cases} .$$

We call the combination of the inner BBC multiplicity cut and the tower multiplicity cut as "west multiplicity cut". The west multiplicity cut removes a small (ξ-dependent) fraction of the diffractive dijet events and its effect is discussed in Section 4.4. Figures 3.8–3.9 show the difference of forward activities between diffractive and non-diffractive events. The top-left plots in these figures show the correlation between the hit multiplicity of the west layer 0/1 BBC and the tower multiplicity in the region of $-4.2 \leq \eta \leq -2.4$ for the diffractive events, the top-right plots show those for the non-diffractive events, and the bottom-left plots show those for the diffractive events superimposed with the normalized non-diffractive events. After the west multiplicity cut, 1.2 million events remained as the diffractive inclusive events. The inner BBC multiplicity and the tower multiplicity distributions are shown in Figure 3.10 together with the thresholds.

3.3.4 Dijet event selection

We further require that at least 2 jets with $E_T \geq 5\,\mathrm{GeV}$ should exist, the average E_T of leading two jets (E_T^*) be larger than $10\,\mathrm{GeV}$ and the two jets should not be associated with calorimeter noise spots ("Hot tower spots"). Before detailed document of the calorimeter noise filter is given in Appendix C. After these cuts, about 11,000 events remained as diffractive dijet events. The distribution of jet multiplicity is shown in Figure 3.11.

For these events, we binned these data into six E_T^* ranges as listed in Table 3.4. We show a typical diffractive dijet event in Figure 3.12.

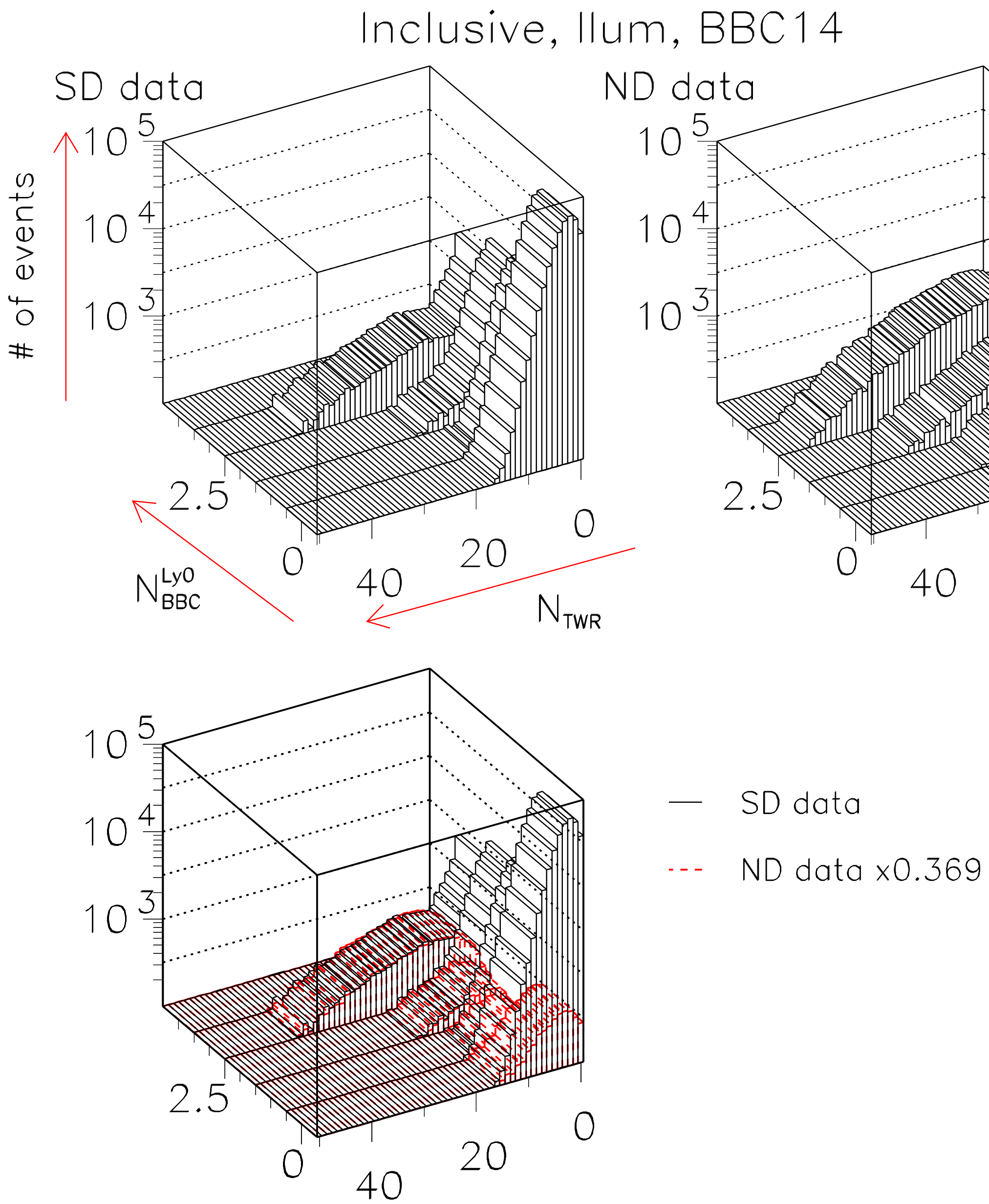

Figure 3.8: Correlation plots between BBC layer 0 hit multiplicity and tower multiplicity in the forward calorimeter during BBC14 runs. These plots show the different characteristics in forward activities between diffractive and non-diffractive event. And non-diffractive background in diffractive events is well reproduced by minimum-bias trigger data.

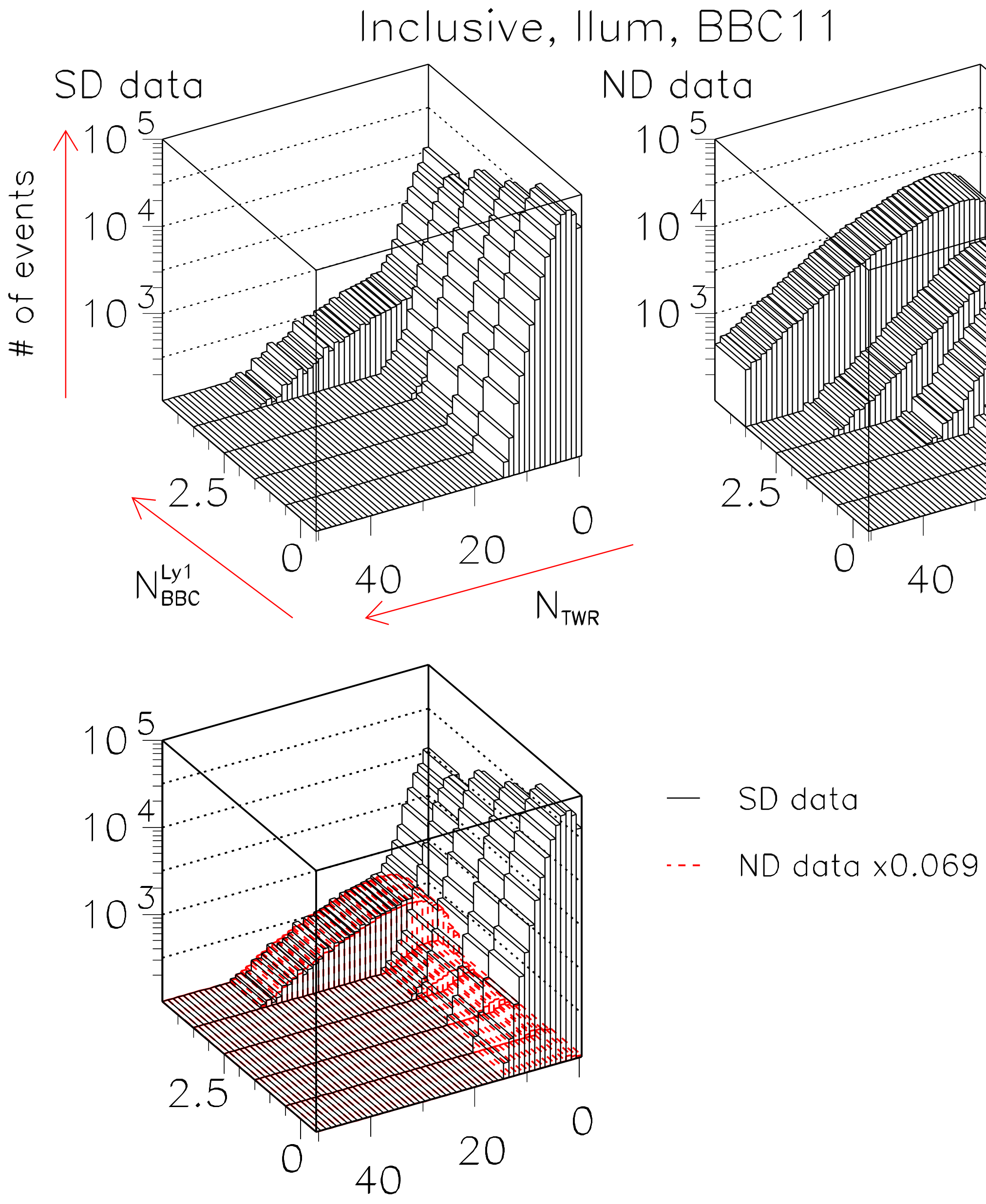

Figure 3.9: Correlation plots between BBC layer 1 hit multiplicity and tower multiplicity in the forward calorimeter during BBC11 runs.

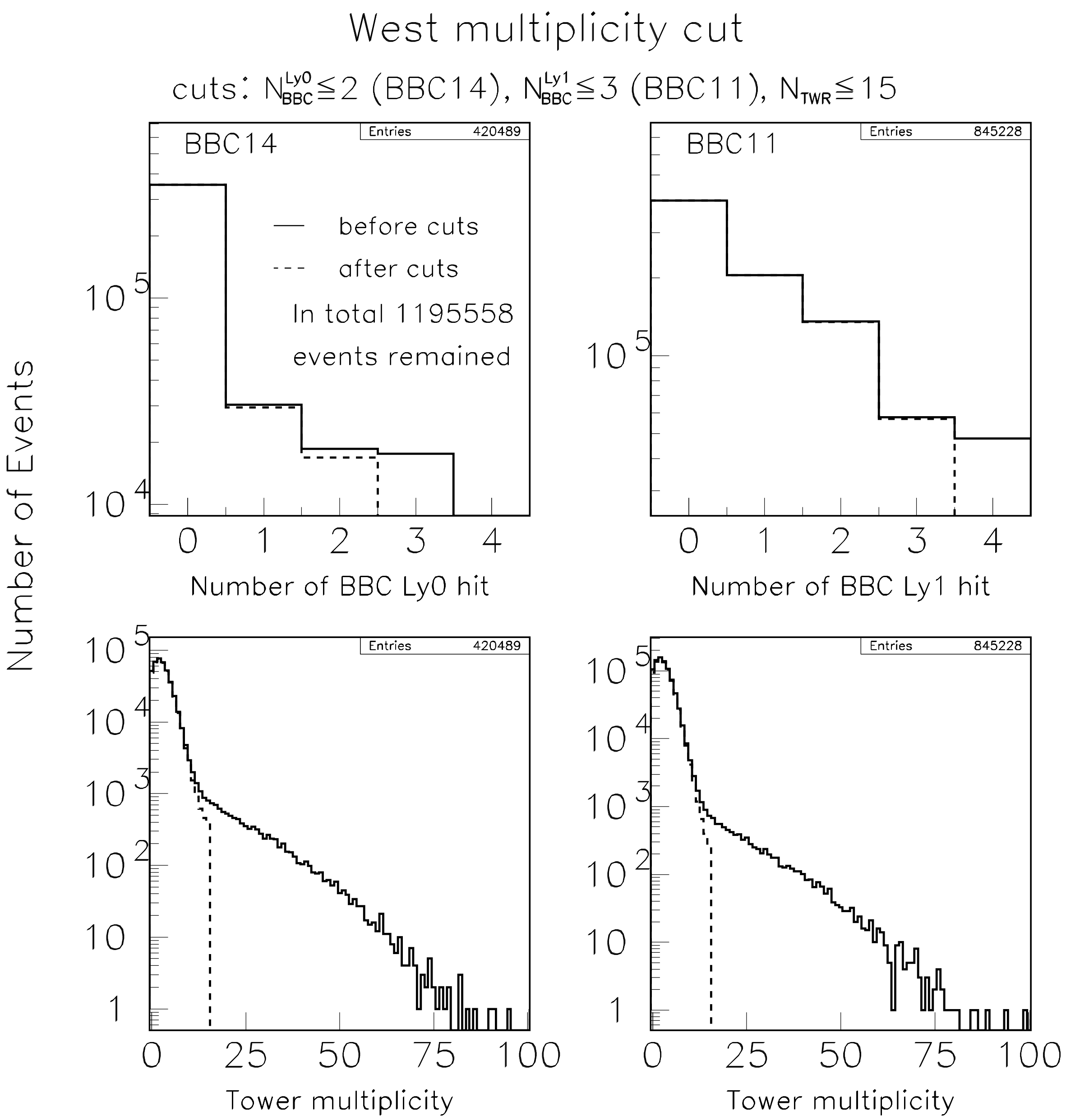

Figure 3.10: Hit multiplicity of BBC layer 0 (top-left), that of BBC layer 1 (top-right), Tower multiplicity (2 bottom plots) distributions. We required the number of layer 0 BBC hit to be less than 2 (runs those 3 layer 0 counters are alive), the number of layer 1 BBC hit to be less than 3 (runs those all layer 0 counters are dead), and tower multiplicity to be less than 15. The solid line shows before the cut, and the dashed line shows after the cut. After this cut, 1194509 events from diffractive inclusive trigger, 1420 events from diffractive dijet trigger, in total 1195558 events remained.

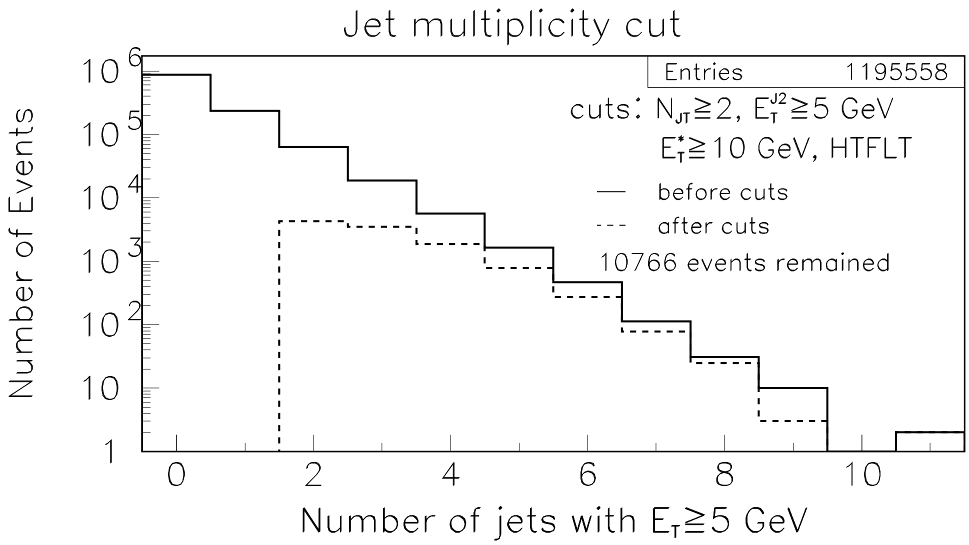

Figure 3.11: Jet multiplicity distribution for diffractive dijet events. We require the second jet E_T to be larger than 5 GeV and the average E_T of leading two jets to be larger than 10 GeV. The solid line shows in case before applying the "jet multiplicity cut" (in Table 3.3), and the dashed line shows in case after applying the cut. After this cut, 9,834 events from diffractive inclusive trigger, 1,260 events from diffractive dijet trigger, in total 10,766 events remained.

E_T^* range	# of events			
	INCL TRIG		JJ TRIG	
	BBC14	BBC11	BBC14	BBC11
Inclusive	399,034	795,475		
$10 \leq E_T^* \leq 11$ GeV	1,293	2,454	26	22
$11 \leq E_T^* \leq 12$ GeV	776	1,483	41	47
$12 \leq E_T^* \leq 15$ GeV	951	1,755	140	164
$15 \leq E_T^* \leq 20$ GeV	297	587	183	212
$20 \leq E_T^* \leq 25$ GeV	56	114	102	135
$E_T^* \geq 25$ GeV	28	40	87	101

Table 3.4: The number of diffractive dijet events for each average E_T range.

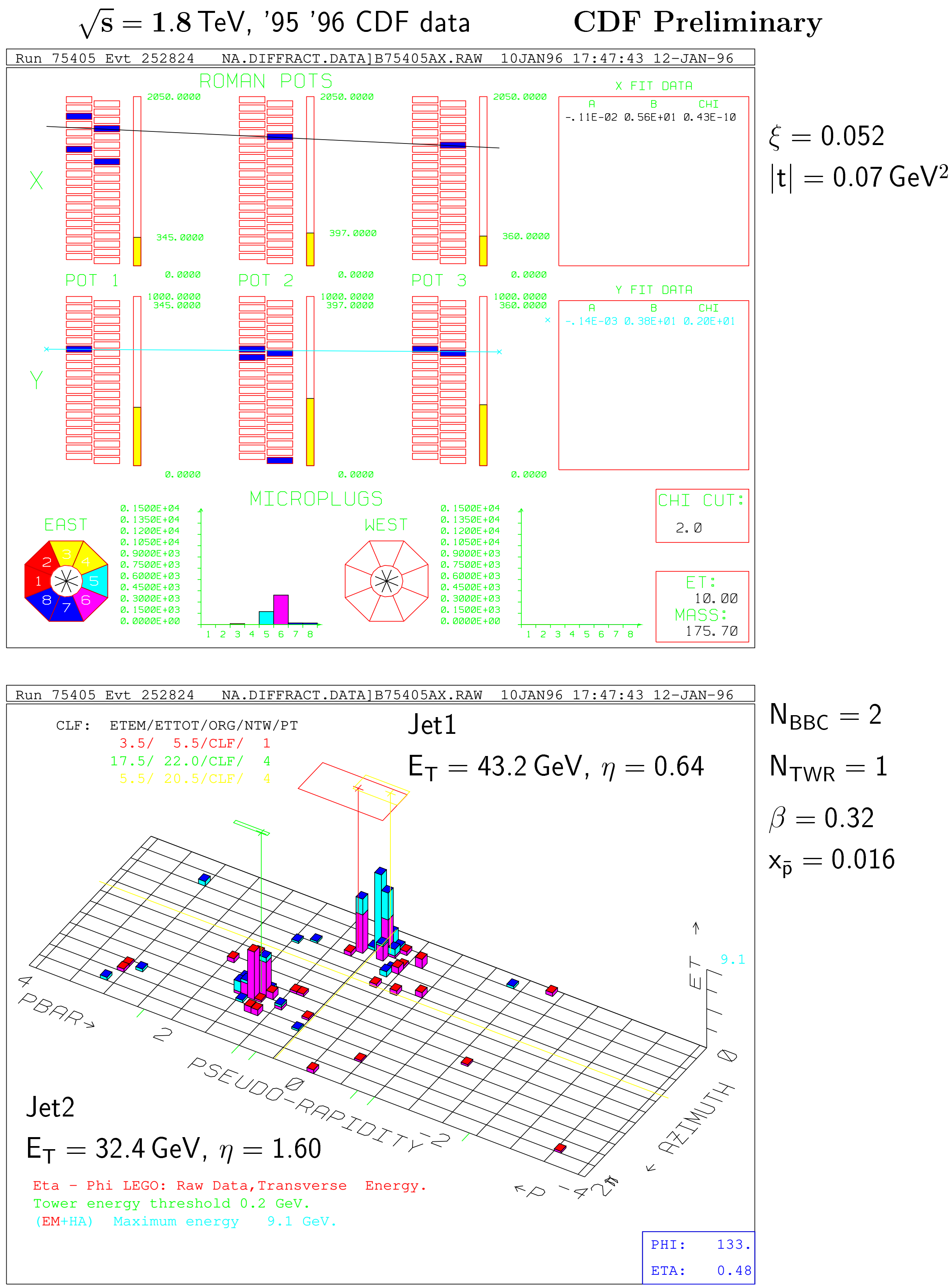

Figure 3.12: A typical diffractive dijet event. RPS track and μPlug response views (top) and calorimeter response in the η-ϕ view (bottom).

3.4 Minimum-bias trigger

The minimum-bias trigger is provided by BBC, and a "BBC hit" corresponds to responses from both phototubes to be larger than threshold within a ± 15 nsec timing window of the beam crossing. A coincidence of both the east and west counters with at least one BBC hit defines a minimum-bias event, and it is required at level-1 trigger. At level-2 and level-3, there is no special requirement, the triggers select events just keeping the trigger rate. Note that diffractive events will not be efficiently accepted by the minimum-bias trigger. During Run-1C, low luminosity runs, we prepared *special* minimum-bias trigger, that requires only level-1 criteria. Once the event passing the level-1 trigger, it is automatically accepted level-2 and level-3 triggers without prescaling. And the non-diffractive data is selected from the special minimum-bias trigger data set.

3.5 Non-diffractive dijet event selection

There are about 460,000 events collected by the special minimum-bias trigger during Run-1C low luminosity run ($\mathcal{L}_{\rm INST} \approx 5.3 \times 10^{29} {\rm s}^{-1}{\rm cm}^{-2}$).

We apply the vertex cut and the jet multiplicity cut to these events as listed in Table 3.5, which are the same crirteria as the diffractive dijet events. We obtained 355,347 non-diffractive inclusive events, and 21,347 non-diffractive dijet events. We show the distributions of these selection cut parameters in Figures 3.13–3.15.

For these events, we binned the data into six E_T^* ranges as listed in Table 3.6.

Selection Cuts	Number of events
All events	401,717
Preselection	
• CDF good runs	401,703
missing E_T cut	401,702
• $\not{E}_T$ significance ≤ 3	
• $\not{E}_T \leq 20\,\text{GeV}$	
Vertex cut	355,347
•$\|Z_{VTX}\| \leq 60\,\text{cm}$	
Jet multiplicity cut	21,347
• Exist at least 2 jets	
• $E_T^{\text{Jet2}} \geq 5\,\text{GeV}$	
• $E_T^* \geq 10\,\text{GeV}$	
• The 2 jets are not associated with calorimeter noise spots	

Table 3.5: Event selection cuts, the number of events after the cuts for non-diffractive events.

E_T^* range	# of events		
	BBC14	BBC11	Total
Inclusive	66,003	289,344	355,347
$10 \leq E_T^* \leq 11$ GeV	1,227	5,199	6,426
$11 \leq E_T^* \leq 12$ GeV	863	3,469	4,332
$12 \leq E_T^* \leq 15$ GeV	1,289	5,607	6,896
$15 \leq E_T^* \leq 20$ GeV	603	2,355	2,958
$20 \leq E_T^* \leq 25$ GeV	87	448	535
$E_T^* \geq 25$ GeV	39	161	200

Table 3.6: The number of non-diffractve dijet events for each E_T^* range.

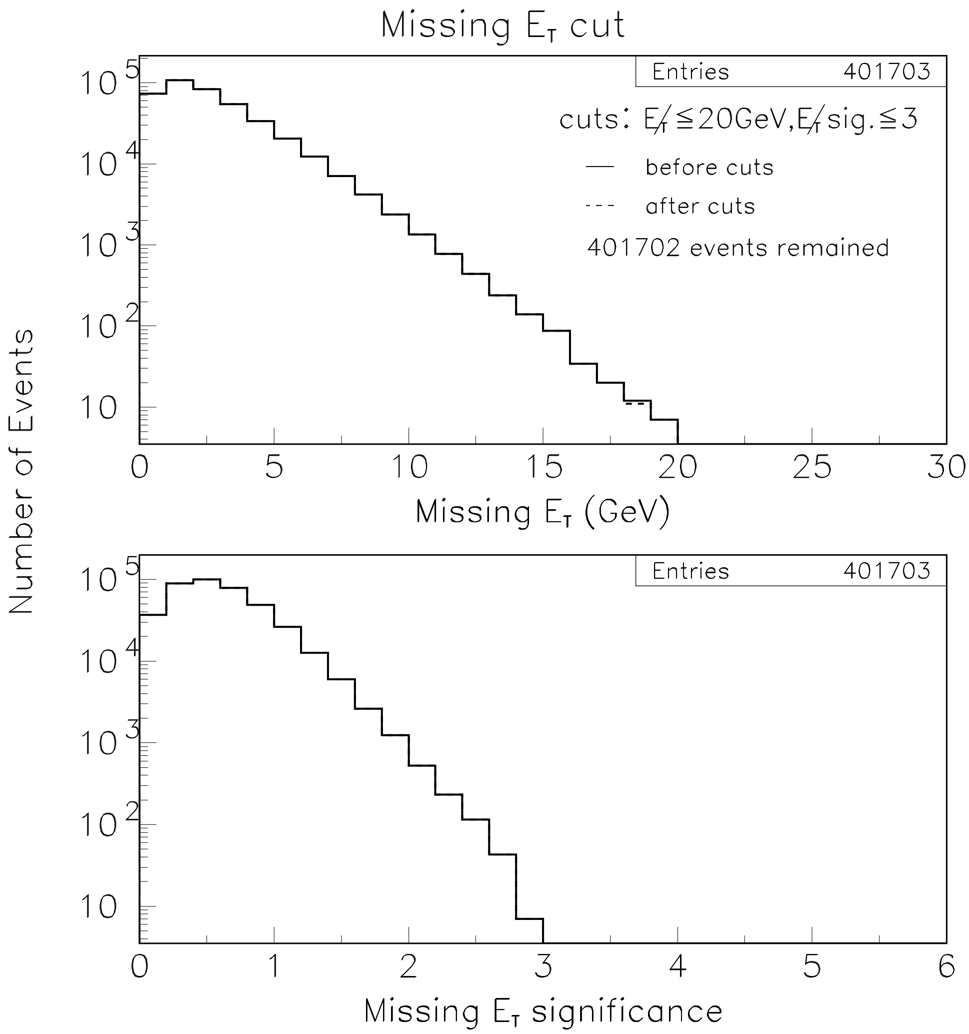

Figure 3.13: Missing E_T (top) and missing E_T significance (bottom) distributions for minimum-bias trigger data. We require $\not\!\!E_T$ to be less than 20 GeV and $\not\!\!E_T$ significance to be less than 3. The solid line shows before the cut, and the dashed line shows after the cut. One event was rejected by the cut.

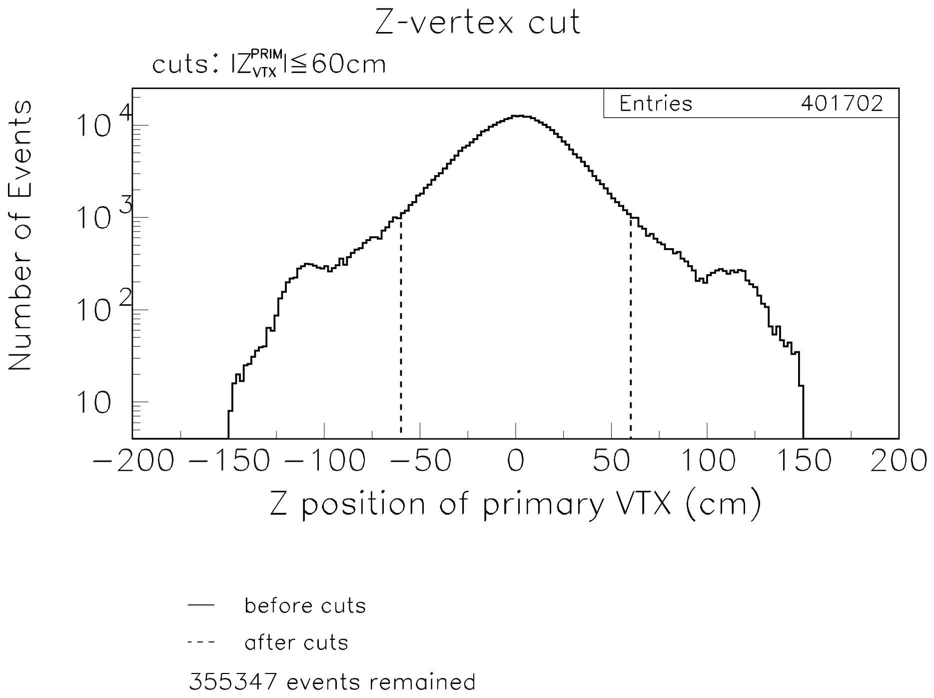

Figure 3.14: The primary Z-vertex distribution for minimum-bias trigger events. We require an absolute value of Z-vertex to be less than 60 cm. The solid line shows before the cut, and the dashed line shows after the cut. After this cut, 355,347 events remained.

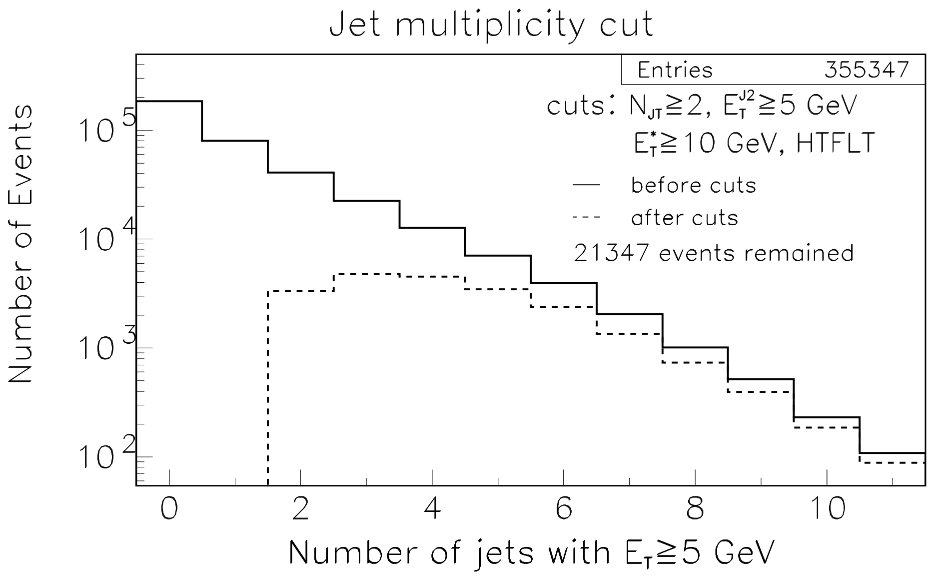

Figure 3.15: Jet multiplicity distribution for non-diffractive dijet events. We require the second jet E_T to be larger than 5 GeV and the average E_T of leading two jets to be larger than 10 GeV. The solid line shows in case before applying the "Jet Multiplicity cut" in Table 3.5), and the dashed line shows in case after applying the cut. After this cut, 21,347 events remained.

Chapter 4

Diffractive dijet cross section

In order to obtain diffractive dijet cross section, we need to estimate the following numbers;

- Total diffractive cross section for normalization,
- Dynamic prescaling factor of diffractive inclusive trigger at level-2 (only for diffractive dijet sample),
- RPS acceptance (described in Appendix A),
- Background fraction,
- West multiplicity cut efficiency,
- Diffractive dijet trigger efficiency (only for diffractive dijet sample),
- Calorimeter noise filter efficiency (HTFLT, described in Appendix C), and
- $E_T^{\rm Jet2} \geq 5\,{\rm GeV}$ cut efficiency.

4.1 Total diffractive cross section

We measured the diffractive cross section as a function of (ξ, t) by using the 1988 – 1989 (Run-0) CDF data [16]. We integrate this cross section over the region of $0.035 \leq \xi \leq 0.095$ and $|t| \leq 1$ GeV^2 to obtain the integrated diffractive cross section of

$$\sigma_{\rm SD}^{\rm INCL} = 0.78 \pm 0.16 \ \ {\rm (syst.)\ mb}\ (0.035 \leq \xi \leq 0.095 \text{ and } |{\rm t}| \leq 1\ {\rm GeV}^2). \qquad (4.1)$$

4.2 RPS acceptance

The RPS acceptance is obtained by making a pseudoexperiment, which is performed in the following procedure;

1. Generate a recoil $\overline{p}$ with ξ, t and ϕ at the interaction point according to the measured ξ and t distributions,
2. Transport the recoil $\overline{p}$ to the RPS (at the A48 position),
   Reject events if the recoil $\bar{p}$ goes out of beampipe and/or accelerator elements,
3. Perform the RPS detector simulation,
4. Reconstruct ξ, t and ϕ and calculate the acceptance in each (ξ, t) bin.

The precise description is written in Appendix A. The result acceptance distribution is shown in Figure 4.1.

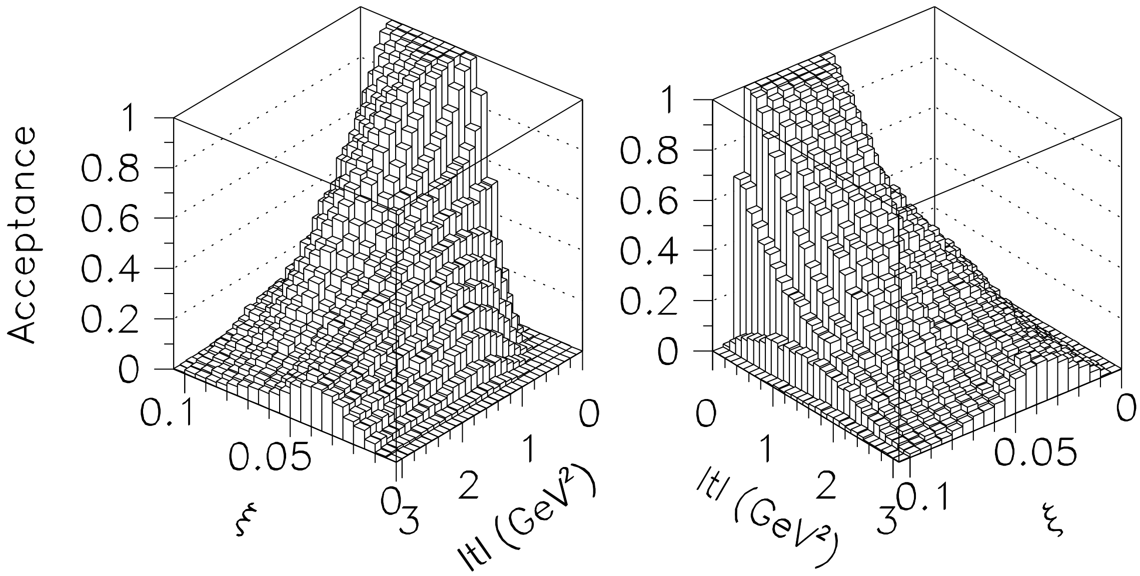

Figure 4.1: The RPS acceptance distribution as a function of (ξ, t).

4.3 Non-diffractive background

There is significant difference between the diffractive and the non-diffractive events, in the correlation between the inner BBC hit multiplicity and the forward tower hit multiplicity as described in section 3.3.3. We estimate the non-diffractive background contamination utilizing this difference as follows;

1. make two-dimensional distribution of the inner BBC hit multiplicity and the forward tower hit multiplicity for the diffractive and non-diffractive events,

2. normalize the distribution for the non-diffractive events to that for the diffractive events by fitting in the background rich region ($N_{\mathrm{TWR}} > 15$),

3. background fraction is given by;

$$\begin{aligned} fr_{\mathrm{BG}} &= \frac{f_{\mathrm{NORM}} N_{\mathrm{ND}}}{N_{\mathrm{SD}}} \\ fr_{\mathrm{BG}}^{\mathrm{TOTAL}} &= \frac{fr_{\mathrm{BG}}^{\mathrm{BBC14}} N_{\mathrm{SD}}^{\mathrm{BBC14}} + fr_{\mathrm{BG}}^{\mathrm{BBC11}} N_{\mathrm{SD}}^{\mathrm{BBC11}}}{N_{\mathrm{SD}}^{\mathrm{BBC14}} + N_{\mathrm{SD}}^{\mathrm{BBC11}}}, \end{aligned}$$

   where f_{NORM} is the normalization factor, and $N_{\mathrm{SD}}(N_{\mathrm{ND}})$ is the number of (non-)diffractive events in the following region;

   - BBC14 run : $N_{\mathrm{TWR}} \leq 15$, $N_{\mathrm{BBC}}^{\mathrm{Ly0}} \leq 2$
   - BBC11 run : $N_{\mathrm{TWR}} \leq 15$, $N_{\mathrm{BBC}}^{\mathrm{Ly1}} \leq 3$.

Typical fit results are shown in Figure 4.2, and the background fraction is summarized in Table 4.1.

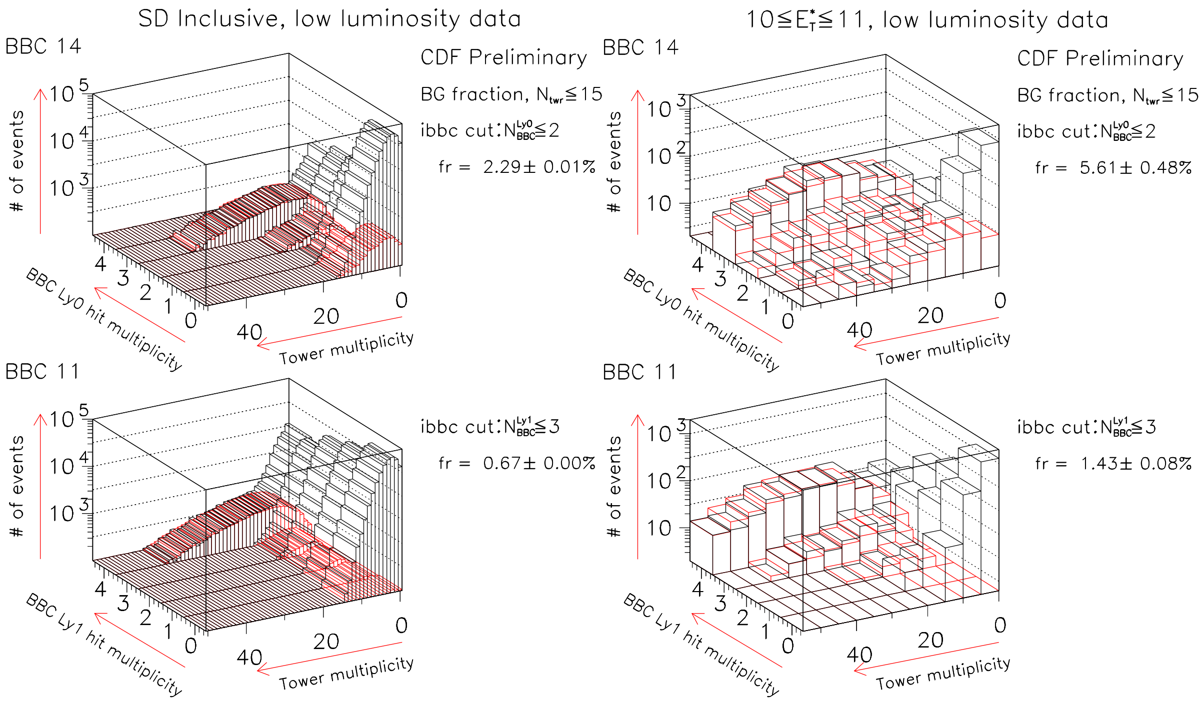

Figure 4.2: Background fit results. The left two plots show those for the diffractive inclusive events, and the right two plots show those for the diffractive dijet events. The black line shows the diffractive events, and the red line shows the normalized non-diffractive events representing the background. In these plots, there are significant diffractive signals in the $N_{\mathrm{TWR}} \leq 15$ region. On the other hand, there are a background tail in the $N_{\mathrm{TWR}} > 15$ region, and the normalized non-diffractive events reproduce the background well.

E_T^* range	background fraction (%)		
	BBC14	BBC11	Overall
$\boxed{\text{SD INCL TRIG.}}$			
Inclusive	2.29 ± 0.01	$0.67 \pm 0.00_2$	1.21 ± 0.01
$10 \leq E_T^* \leq 11\,\text{GeV}$	5.61 ± 0.48	1.43 ± 0.08	2.87 ± 0.17
$11 \leq E_T^* \leq 12\,\text{GeV}$	5.47 ± 0.57	1.55 ± 0.11	2.90 ± 0.21
$12 \leq E_T^* \leq 15\,\text{GeV}$	5.52 ± 0.52	1.53 ± 0.09	2.94 ± 0.19
$15 \leq E_T^* \leq 20\,\text{GeV}$	6.43 ± 0.90	1.56 ± 0.15	3.19 ± 0.31
$20 \leq E_T^* \leq 25\,\text{GeV}$	3.70 ± 1.48	1.86 ± 0.36	2.47 ± 0.54
$E_T^* \geq 25\,\text{GeV}$	7.46 ± 3.99	4.00 ± 1.48	5.43 ± 1.86
$10 \leq E_T^* \leq 12\,\text{GeV}$			2.88 ± 0.27
$12 \leq E_T^* \leq 15\,\text{GeV}$			2.94 ± 0.19
$15 \leq E_T^* \leq 25\,\text{GeV}$			3.08 ± 0.63
$\boxed{\text{SD JJ TRIG.}}$			
$12 \leq E_T^* \leq 15\,\text{GeV}$	12.6 ± 1.55	3.86 ± 0.36	7.91 ± 0.70
$15 \leq E_T^* \leq 20\,\text{GeV}$	7.54 ± 1.11	2.38 ± 0.27	4.77 ± 0.52
$20 \leq E_T^* \leq 25\,\text{GeV}$	3.62 ± 1.41	2.29 ± 0.43	2.86 ± 0.66
$E_T^* \geq 25\,\text{GeV}$	3.52 ± 1.80	1.72 ± 0.60	2.55 ± 0.89

Table 4.1: Summary table of the estimated remaining background fraction.

4.4 West multiplicity cut efficiency

The west multiplicity cut is a combination of the inner BBC multiplicity cut and the tower multiplicity cut. The rapidity gap width in the diffractive events does not depend on the jet activity, but only on ξ. To estimate the efficiencies for both cuts, we use the diffractive inclusive events because of large statistics.

The rapidity gap in the diffractive events is killed when the diffractive event is overlapped with a non-diffractive event. It is called the overlapped background. The amount of the overlap background is a function of instantaneous luminosity. According to the following procedure, we estimate the inner BBC multiplicity cut efficiency;

1. Divide the diffractive data into six ξ bins,
2. Calculate the cut efficiency as a function of instantaneous luminosity in each bin,
3. Extrapolate the efficiency to the "0" instantaneous luminosity by an exponential fit;

$$\begin{aligned} \epsilon &= \lim_{\mathcal{L}_{\mathrm{INST}} \to 0} \epsilon_{\mathrm{evt\ passing}} \\ &= \lim \left\{ \frac{N^{\mathrm{SD}}_{\mathrm{BBC}}(\mathrm{pass}) + N^{\mathrm{BG}}_{\mathrm{BBC}}(\mathrm{pass})}{N^{\mathrm{SD}}_{\mathrm{BBC}}(\mathrm{all}) + N^{\mathrm{BG}}_{\mathrm{BBC}}(\mathrm{all})} \right\} \Rightarrow \frac{N^{\mathrm{SD}}_{\mathrm{BBC}}(\mathrm{pass})}{N^{\mathrm{SD}}_{\mathrm{BBC}}(\mathrm{all})}, \end{aligned}$$

where $N^{\mathrm{SD}}_{\mathrm{BBC}}(\mathrm{all})$ ($N^{\mathrm{SD}}_{\mathrm{BBC}}(\mathrm{pass})$) means the number of diffractive events before (after) the inner BBC multiplicity cut, and $N^{\mathrm{BG}}_{\mathrm{BBC}}(\mathrm{all})$($N^{\mathrm{BG}}_{\mathrm{BBC}}(\mathrm{pass})$) means the number of non-diffractive background events before (after) the inner BBC multiplicity cut. Shown in Figure 4.3 is the plots of the inner BBC multiplicity cut efficiency as a function of instantaneous luminosity. This plot was fitted to $\epsilon \exp(-b\mathcal{L}_{\mathrm{INST}})$, where ϵ is the cut efficiency and b is the slope.

The inner BBC multiplicity cut efficiencies before and after the tower multiplicity cut are shown in Table 4.2 and Table 4.3, respectively. As shown in the two bottom plots in Figure 3.10, the tower multiplicity cut efficiency is larger than 99%, so does not affect the west multiplicity cut efficiency.

4.5 Diffractive dijet trigger efficiency

The diffractive dijet trigger required the following criteria;

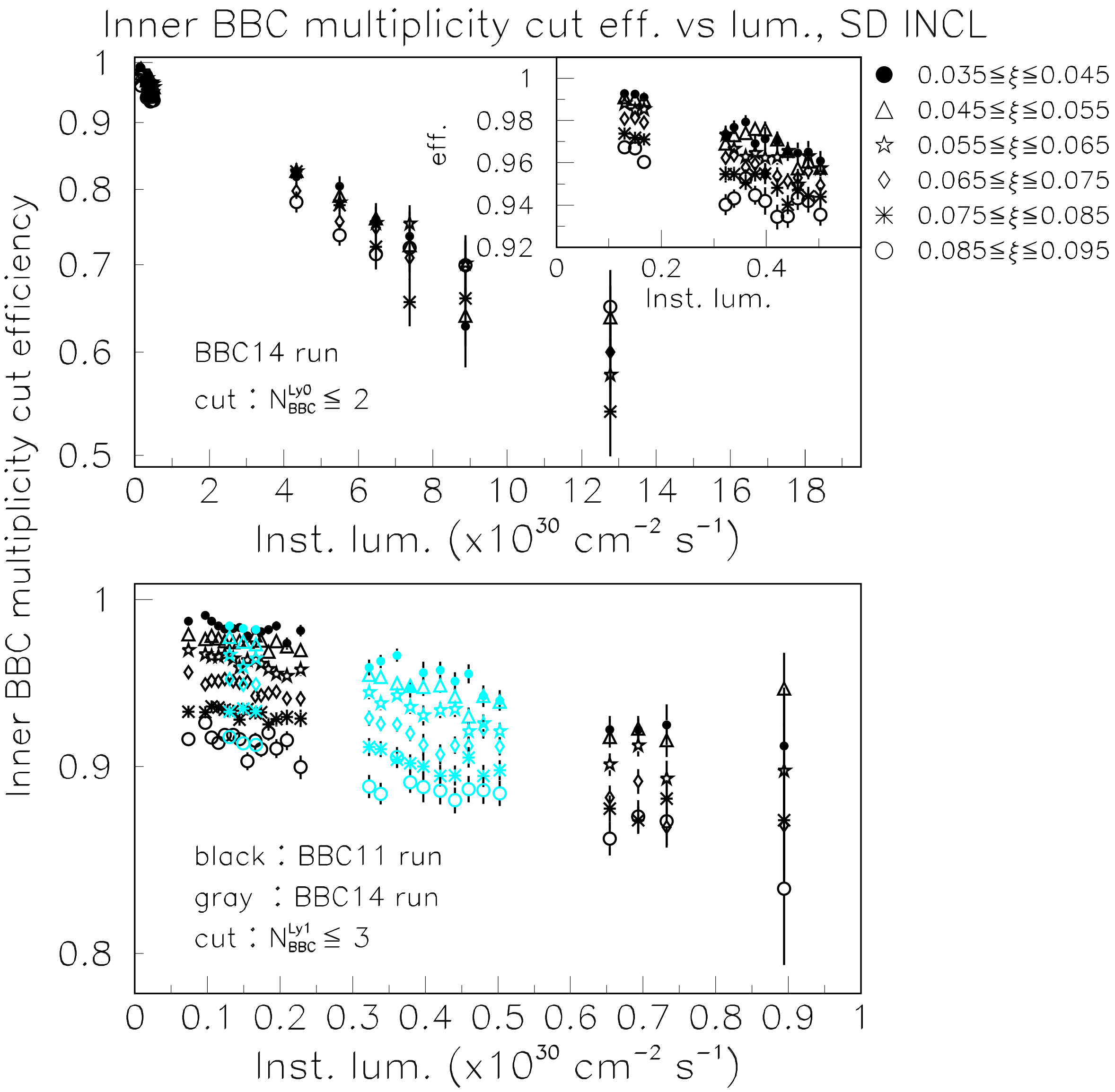

Figure 4.3: Inner BBC multiplicity cut efficiency as a function of instantaneous luminosity. The top plot shows the efficiency in the BBC14 run where the innermost BBC layer is good. The bottom plot shows that in the BBC11 run using the next-to-innermost layer, because the innermost layer is dead. Since the overlap background increases with the instantaneous luminosity, the efficiency decreases with the instantaneous luminosity. We fit the plots in all ξ bins with an exponential curve, and extrapolate the curve to the "0" luminosity in order to obtain the inner BBC multiplicity cut efficiencies.

ξ bins	Fit results			
	BBC14		BBC11	
	Efficiency	Slope	Efficiency	Slope
$0.035 \leq \xi \leq 0.045$	0.998 ± 0.001	-0.048 ± 0.002	0.997 ± 0.001	-0.104 ± 0.008
$0.045 \leq \xi \leq 0.055$	0.996 ± 0.001	-0.047 ± 0.002	0.986 ± 0.001	-0.092 ± 0.006
$0.055 \leq \xi \leq 0.065$	0.991 ± 0.001	-0.047 ± 0.001	0.977 ± 0.001	-0.114 ± 0.007
$0.065 \leq \xi \leq 0.075$	0.985 ± 0.001	-0.050 ± 0.002	0.963 ± 0.001	-0.125 ± 0.008
$0.075 \leq \xi \leq 0.085$	0.976 ± 0.001	-0.047 ± 0.002	0.944 ± 0.001	-0.103 ± 0.009
$0.085 \leq \xi \leq 0.095$	0.970 ± 0.001	-0.049 ± 0.002	0.926 ± 0.002	-0.095 ± 0.011

Table 4.2: Exponential fit results of the west multiplicity cut (both the inner BBC multiplicity cut and the tower multiplicity cut) efficiency as a function of instantaneous luminosity in each ξ bin.

ξ bins	Fit results			
	BBC14		BBC11	
	Efficiency	Slope	Efficiency	Slope
$0.035 \leq \xi \leq 0.045$	0.998 ± 0.001	-0.093 ± 0.003	1.002 ± 0.001	-0.192 ± 0.010
$0.045 \leq \xi \leq 0.055$	0.996 ± 0.001	-0.092 ± 0.002	0.993 ± 0.001	-0.196 ± 0.008
$0.055 \leq \xi \leq 0.065$	0.991 ± 0.001	-0.093 ± 0.002	0.985 ± 0.001	-0.223 ± 0.008
$0.065 \leq \xi \leq 0.075$	0.985 ± 0.001	-0.096 ± 0.002	0.971 ± 0.001	-0.239 ± 0.009
$0.075 \leq \xi \leq 0.085$	0.976 ± 0.001	-0.095 ± 0.002	0.951 ± 0.001	-0.212 ± 0.010
$0.085 \leq \xi \leq 0.095$	0.968 ± 0.001	-0.094 ± 0.002	0.935 ± 0.002	-0.226 ± 0.013

Table 4.3: Exponential fit results of the inner BBC multiplicity cut (west tower multiplicity cut off) efficiency in each ξ bin.

- two clusters with $E_T \geq 3\,\mathrm{GeV}$ in the level-2 trigger, and
- the second leading jet E_T should be larger than $5\,\mathrm{GeV}$ in the level-3 trigger.

We estimate the level-2 and the level-3 diffractive dijet trigger efficiencies separately.

Level-2 trigger cluster map

At first, we study whether the trigger had the detector-η, ϕ dependence or not. The hit map of the level-2 trigger cluster position is shown in Figure 4.4. We found the level-2 trigger rate was significantly different between the central detector ($|\eta| \leq 1.3$) and the forward detector ($|\eta| \geq 1.3$). Therefore, we estimate the level-2 trigger efficiency in the two regions.

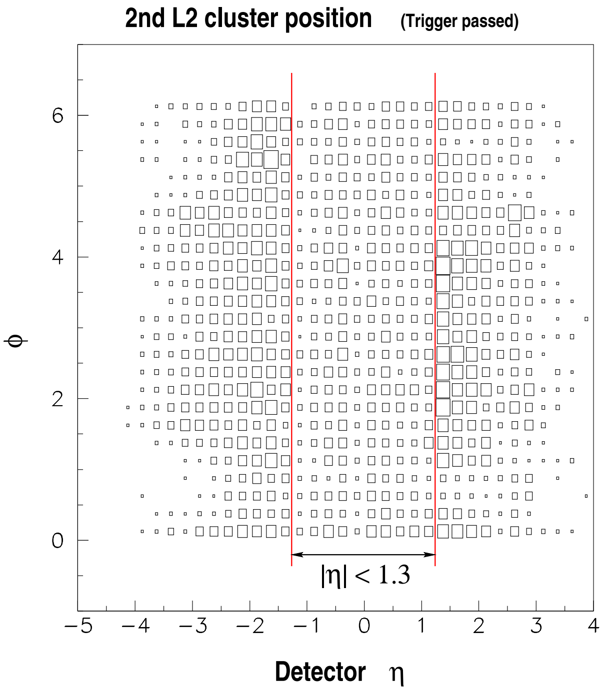

Figure 4.4: Hit position of the level-2 trigger cluster in the detector-η, ϕ space. The trigger frequency is significantly different between the central detector and the forward detector.

Level-2 dijet trigger efficiency

We apply the following selection criteria to the diffractive inclusive trigger data to obtain the diffractive inclusive event sample:

- $|Z_{\rm VTX}| \leq 60$ cm,
- RPS acceptance cut,
- one-MIP cut,
- west multiplicity cut,
- hot tower filter,
- $E_T^{\rm Jet2} \geq 5\,{\rm GeV}$.

For this event sample, we obtain the fraction of the events with a level-2 dijet trigger bit against the average E_T as shown in Figure 4.5. We fit this to the following two-Fermi function;

$$F(x) = \begin{cases} \frac{N_1}{1+\exp\{-A_1(x-B)\}}, & x < B \\ \frac{N_2}{1+\exp\{-A_2(x-B)\}} - N_2 + 1, & x \geq B \\ N_1 + N_2 = 2,\ A_1N_1 = A_2N_2,\ 1 \leq N_2 \leq 2 \end{cases} . \tag{4.2}$$

The fit result is shown in Figure 4.5 and Table 4.4.

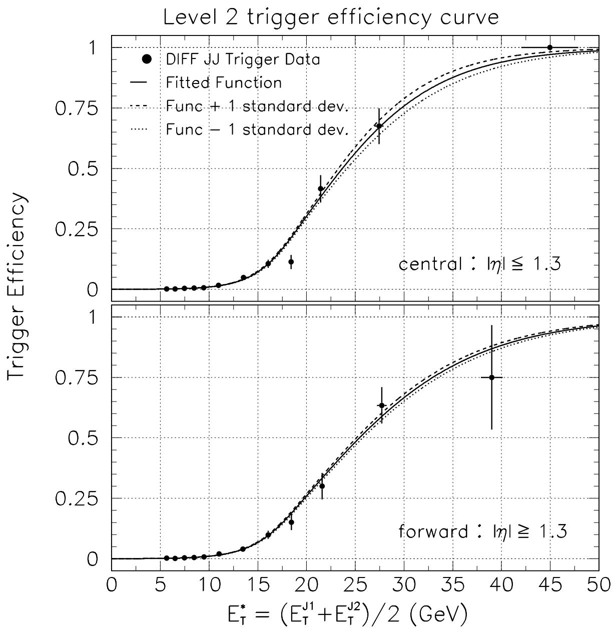

Figure 4.5: Level-2 diffractive dijet trigger efficiency curve for the central detector (top plot) and the forward detector (bottom plot). The solid point shows that for the diffractive data. The solid line shows the fitted function curve. The dashed (dotted) curve shows the fitted function +(−) 1 standard deviation.

	central ($|\eta| \leq 1.3$)	forward ($|\eta| \geq 1.3$)
A_2	0.152 ± 0.016	0.121 ± 0.005
B	19.3 ± 0.4	19.4 ± 0.2
N_2	1.48 ± 0.05	1.54 ± 0.02

Table 4.4: Fit result of the level-2 diffractive dijet trigger efficiency.

Level-3 dijet trigger efficiency

At first, the detector dependence of the level-3 trigger is investigated. Since we found there was no significant detector dependence in the level-3 trigger, we estimate the efficiency with combined data of the central and the forward regions. We fit this plot with the following Fermi function;

$$F(x) = \frac{1}{1 + \exp\{-A(x - B)\}},$$

and obtain the result as shown in Figure 4.6 and Table 4.5. We found no significant detector dependence in this level-3 trigger efficiency.

	central ($|\eta| \leq 1.3$)	forward ($|\eta| \geq 1.3$)	overall
A	0.88 ± 0.10	0.86 ± 0.11	0.87 ± 0.07
B	12.1 ± 0.2	12.0 ± 0.2	12.0 ± 0.2

Table 4.5: Fit result of the level-3 diffractive dijet trigger efficiency.

4.6 $E_T^{\mathrm{Jet2}} \geq 5\,\mathrm{GeV}$ cut efficiency

We measure the diffractive structure function by scaling the non-diffractive structure function (GRV98LO) according to the measured cross section ratio of the diffractive to the non-diffractive dijet production. Though we need to measure the cross section ratio of two jets in the final state, we have significant difference of the three-jet event fraction between diffractive dijets and the non-diffractive ones as shown in Figure 4.7.

We need not only the cross section ratio but also the real $x_{\bar{p}}$ distribution of diffractive events to calculate the structure function. Most of the systematic uncertainty on

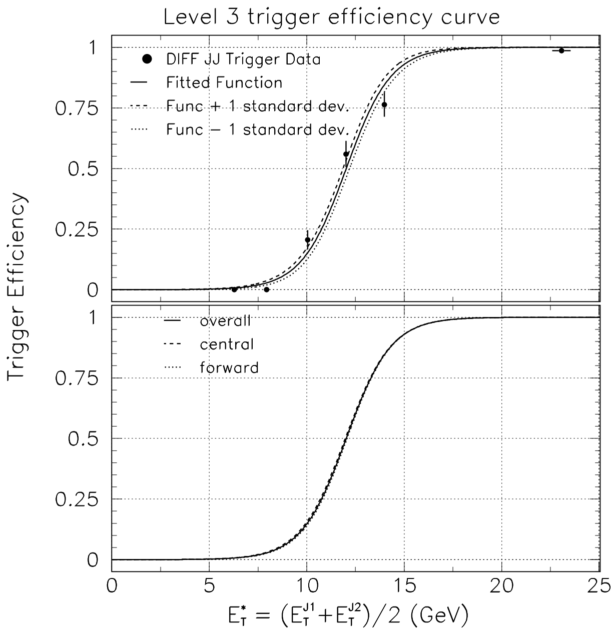

Figure 4.6: Level-3 diffractive dijet trigger efficiency curve. In the top plot, the solid point shows that for the diffractive data, the solid curve shows the fitted function, and the dashed (dotted) curve shows the fitted function +(−) 1 standard deviation. The bottom plot shows the detector dependence of the trigger efficiency.

the cut efficiency are canceled out in the cross section ratio, but completely remains in the $x_{\overline{p}}$ distribution for the diffractive events. Therefore, we study the $E_T^{\text{Jet2}} \geq 5\,\text{GeV}$ cut efficiency in the low average E_T (E_T^*) region for both diffractive and non-diffractive dijet events. The systematics is mainly caused by the third jet radiation. We find the unbiased average E_T range from the average E_T distributions for three second jet E_T thresholds of 5, 7 and 10 GeV. Then we also look at the average E_T distribution for various $x_{\overline{p}}$ regions. There is significant $x_{\overline{p}}$ dependence of the average E_T distributions as shown in Figures 4.8 and 4.9 for the diffractive and the non-diffractive events, respectively. Therefore, we estimate the $E_T^{\text{Jet2}} \geq 5\,\text{GeV}$ cut efficiency in each $x_{\overline{p}}$ bin in the following procedure;

1. perform an unbinned likelihood fit of the average E_T distributions to the the following probability function, $Prob(E_T^*)$; †

$$Prob(E_T^*) \equiv (1-x_T)^{P_2} \cdot 10^{P_1 \ln(E_T^*)} \Big/ \int_{\text{threshold}}^{150\ \text{GeV}} (1-x_T)^{P_2} \cdot 10^{P_1 \ln(E_T^*)} dE_T^*,$$

†This function is reduced parameter function which was used in inclusive jet cross section PRL [1]

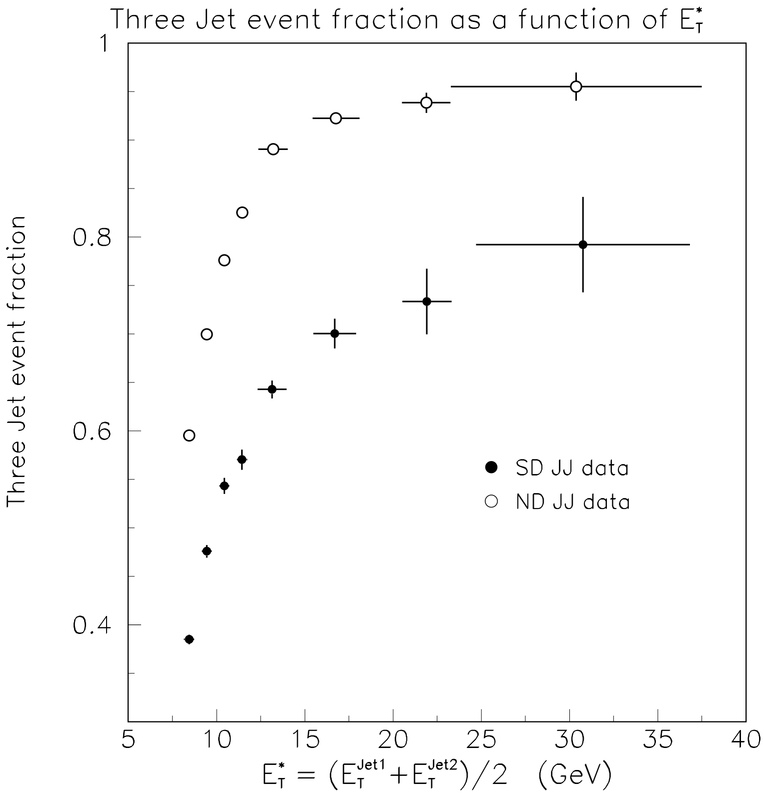

Figure 4.7: Three-jet event fraction. A jet is defined as a cluster with 0.7 cone size, $E_T \geq 5\,\text{GeV}$, and $|\eta| \leq 4.2$. Solid points show the diffractive dijet data, and open circles show the non-diffractive dijet one. The horizontal error bar shows the root-mean-square of the average E_T distribution, and the vertical error bar shows the error of the fraction.

where $x_T = \frac{2E_T^*}{\sqrt{s}}$. The fit result for the diffractive dijet events with $x_{\overline{p}} \leq 2.0 \times 10^{-3}$ is shown in Figure 4.10. Solid points show the diffractive dijet events, and the several curves ($f(E_T^*) = N \cdot Prob(E_T^*)$) show the fit results with different fit regions, where N is the normalization factor fixed to

$$N = \int_{\text{threshold}}^{150\ \text{GeV}} N_{\text{Jets}} dE_T^* \bigg/ \int_{\text{threshold}}^{150\ \text{GeV}} Prob(E_T^*) dE_T^*.$$

The dotted curve is the standard fit result, and other curves are those for systematic uncertainty study. Shown in Figure 4.11 is the fit results for the diffractive dijet events with the other $x_{\overline{p}}$ regions, and the fit results for the non-diffractive dijet events are shown in Figures 4.13–4.14.

2. calculate a ratio of the average E_T distribution to the fitted function; The ratio is the $E_T^{\text{Jet2}} \geq 5\,\text{GeV}$ cut efficiency. Solid points in Figure 4.12 shows the efficiency

for the diffractive dijet events, and those in Figure 4.15 shows that for the non-diffractive dijet events.

3. fit the $E_T^{\mathrm{Jet2}} \geq 5\,\mathrm{GeV}$ cut efficiency to the following function; <u>for ND data with $3.2 \times 10^{-2} \leq x_{\overline{p}} \leq 6.3 \times 10^{-2}$</u>;

$$F(x) = \begin{cases} \frac{N_1}{1+\exp\{-A_1(x-B)\}}, & x < B \\ \frac{N_2}{1+\exp\{-A_2(x-B)\}} - N_2 + 1, & x \geq B \quad (\mathrm{two-Fermi\ function}), \\ N_1 + N_2 = 2, A_1 N_1 = A_2 N_2 & \end{cases}$$

and <u>for the others</u>;

$$F(x) = \begin{cases} \frac{1}{4} N \cdot A \cdot (x - B) - N + 1, & x < B \\ \frac{N}{1+\exp\{-A(x-B)\}} - N + 1, & x \geq B \end{cases} \quad (\mathrm{linear-Fermi\ function}).$$

The fitted curves are also shown in Figure 4.12 for the diffractive events and in Figure 4.15 for the non-diffractive events.

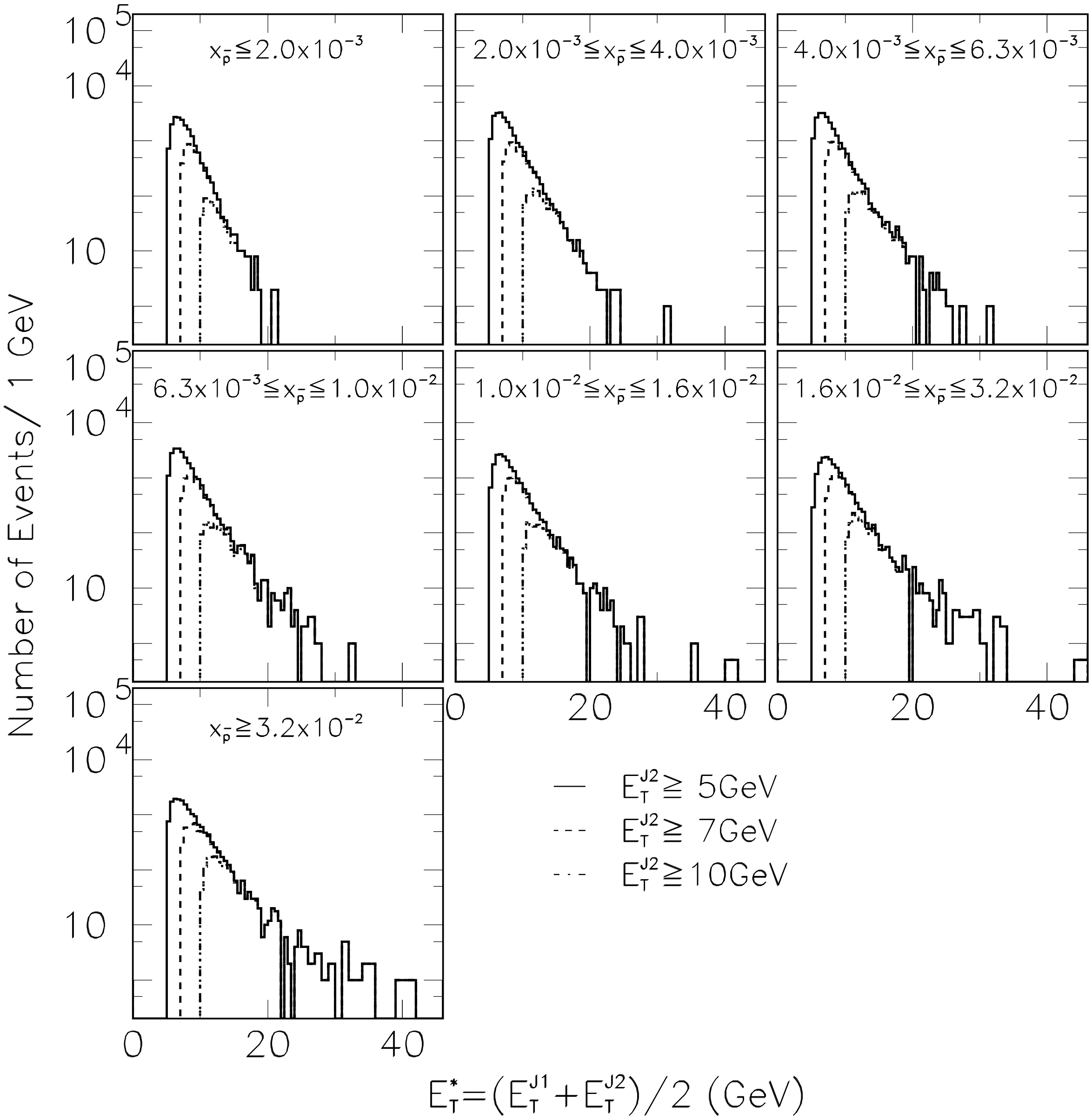

Figure 4.8: Average E_T (E_T^*) distributions for the diffractive dijet events in seven $x_{\overline{p}}$ regions and with three E_T^{Jet2} thresholds of 5, 7, and 10 GeV. The solid histogram shows the distribution with an E_T^{Jet2} threshold of 5 GeV, the dashed one shows that with 7 GeV threshold, and the dot-dashed one shows that with 10 GeV threshold.

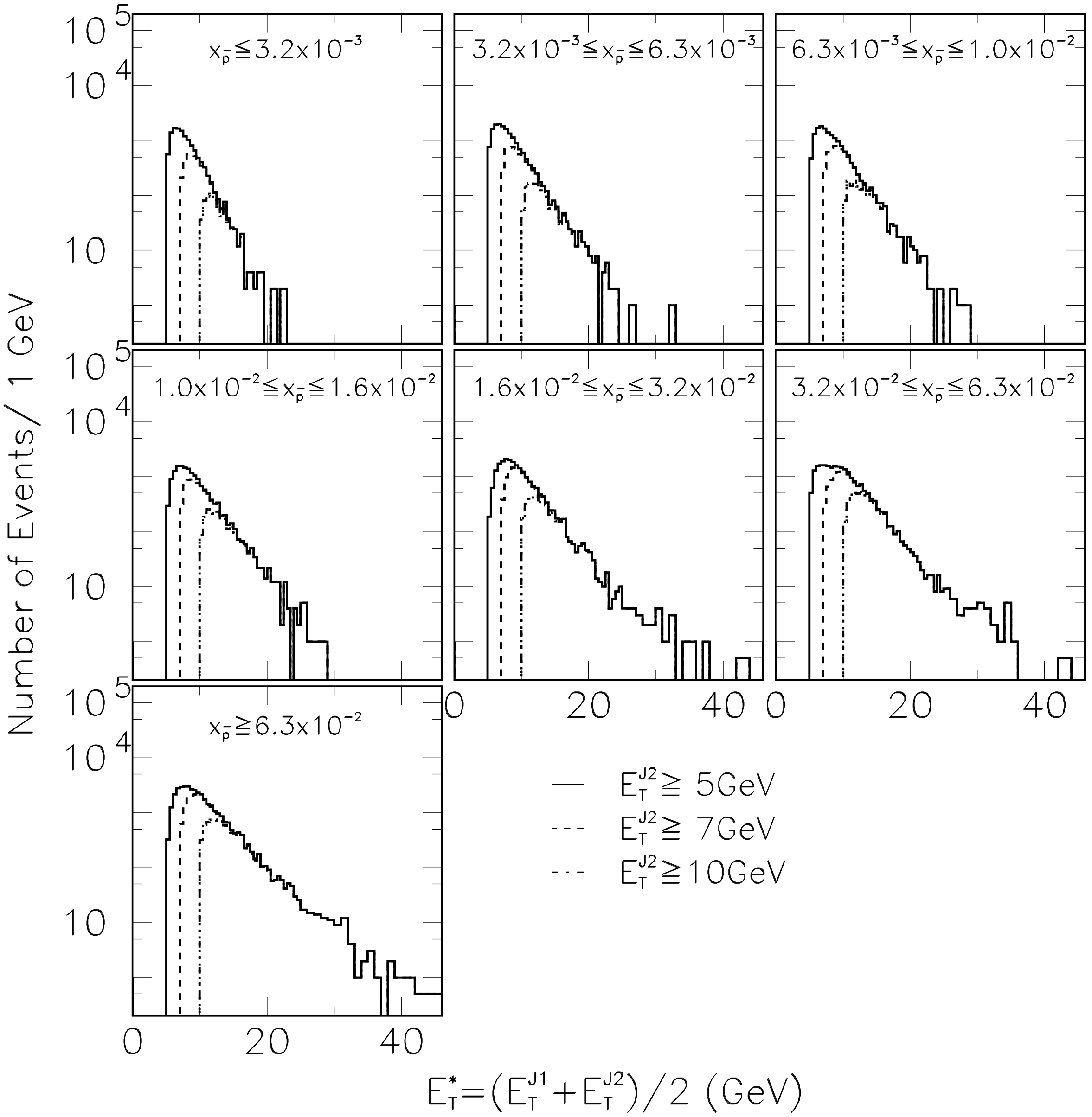

Figure 4.9: Average E_T (E_T^*) distributions for the non-diffractive dijet events in seven $x_{\overline{p}}$ regions and with three $E_T^{\rm Jet2}$ thresholds of 5, 7, and 10 GeV. The solid histogram shows the distribution with $E_T^{\rm Jet2}$ threshold of 5 GeV, the dashed one shows that with 7 GeV threshold, and the dot-dashed one shows that with 10 GeV threshold.

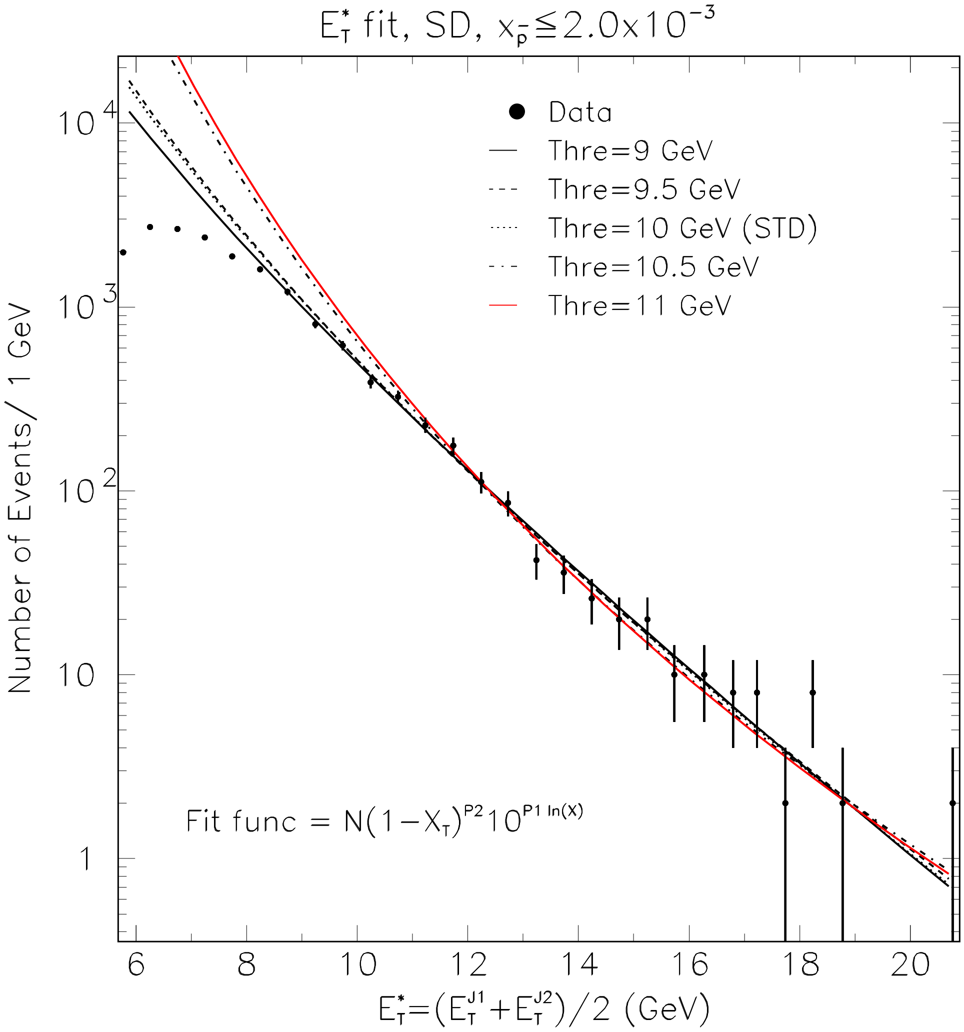

Figure 4.10: Fit result of average E_T distribution for the diffractive dijet events with the region of $x_{\overline{p}} \leq 2.0 \times 10^{-3}$. The solid point shows the diffractive dijet events, and the several curves are the fit results with different fit regions. The dotted curve shows the standard fit result, and the other curves are those for systematic uncertainty study.

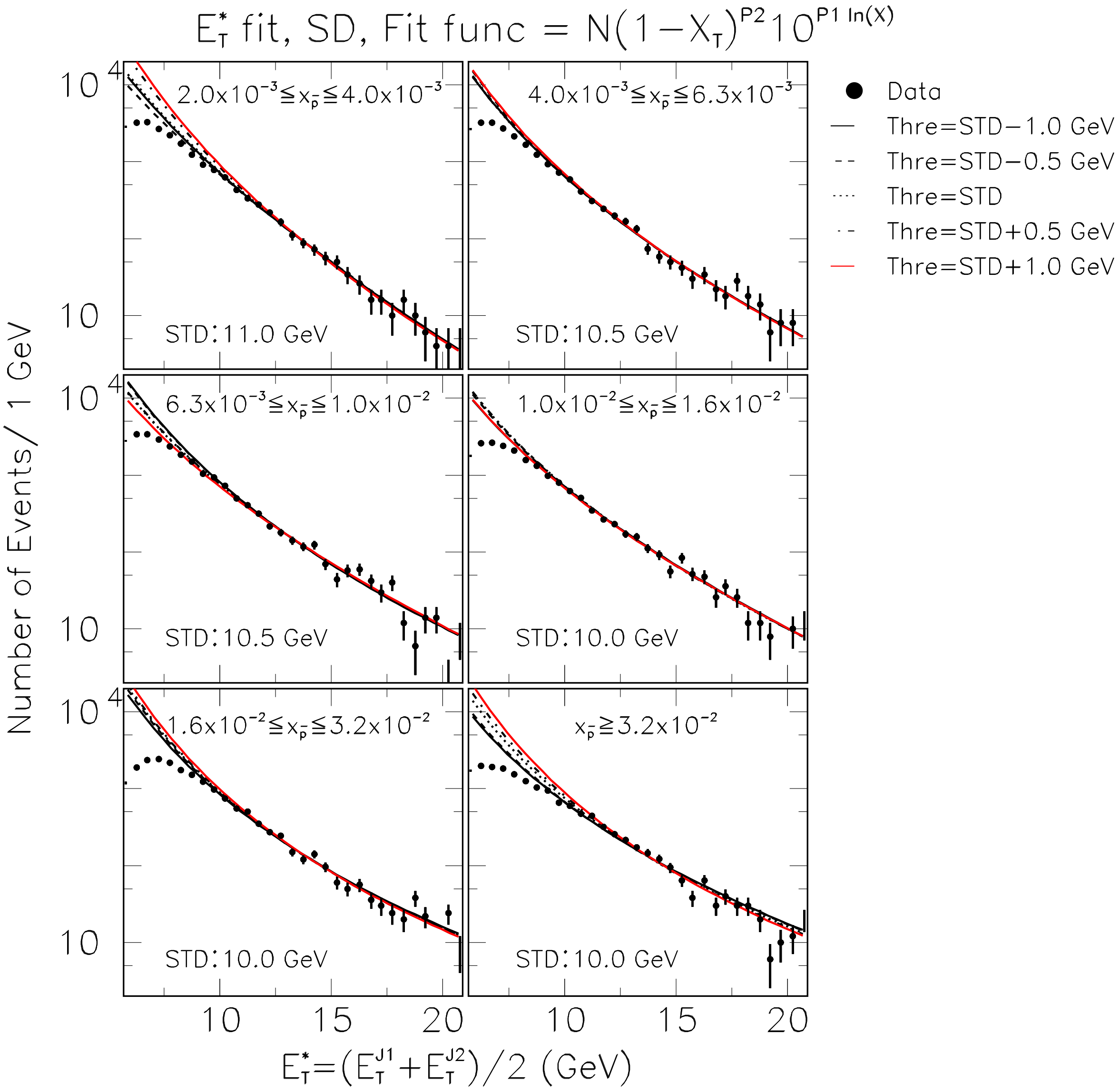

Figure 4.11: Fit results of average E_T distributions for the other $x_{\overline{p}}$ regions of the diffractive dijet events. The solid point shows the diffractive dijet events, and the several curves are the fit results with different fit regions. The dotted curve shows the standard fit result, and the other curves are those for systematic uncertainty study.

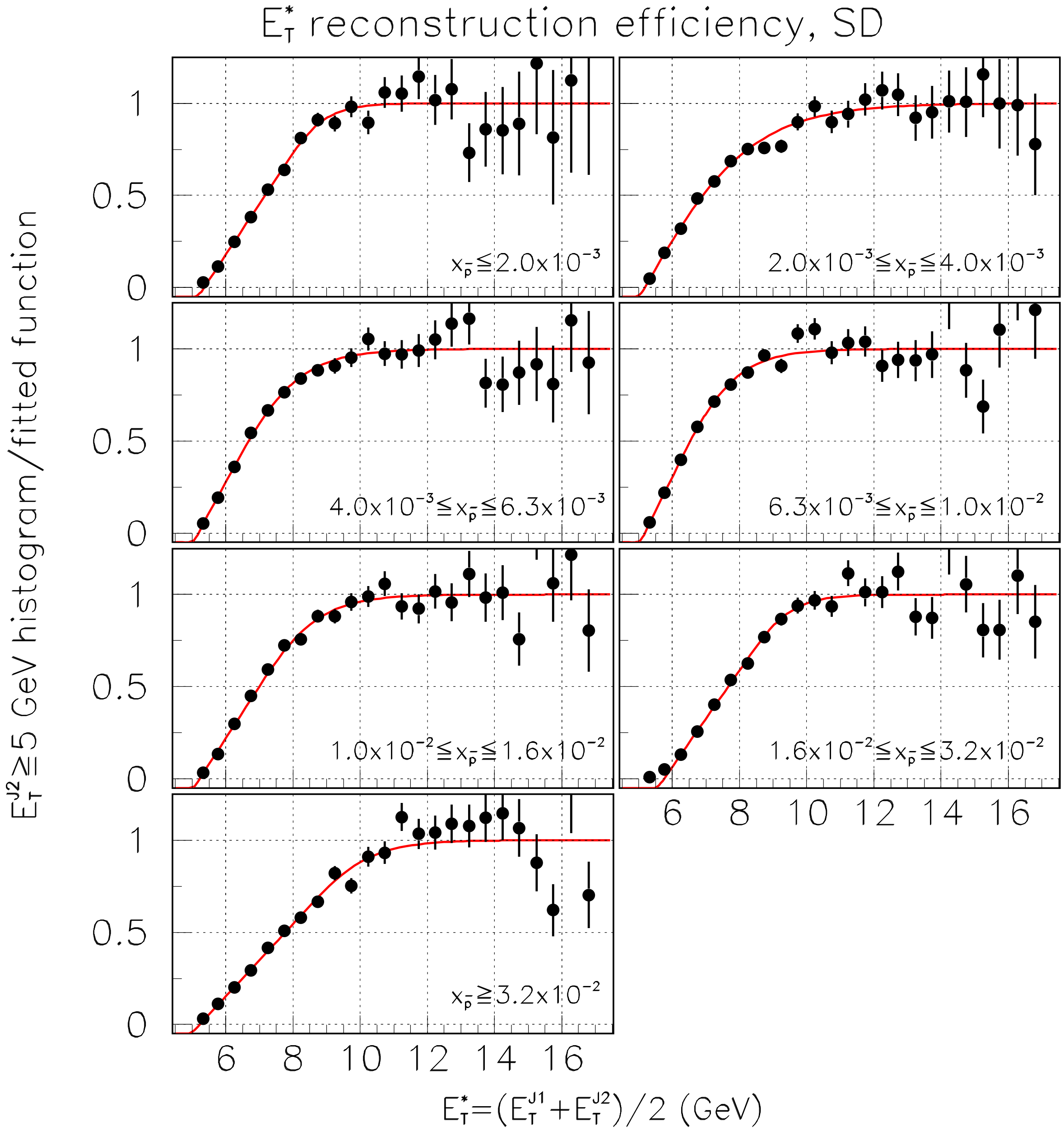

Figure 4.12: Ratio of the E_T^* distribution with $E_T^{\mathrm{Jet2}} \geq 5\,\mathrm{GeV}$ cut to the fitted function for seven $x_{\overline{p}}$ ranges as the $E_T^{\mathrm{Jet2}} \geq 5\,\mathrm{GeV}$ cut efficiency. Solid points show the diffractive dijet data. Solid curves show the fitted function. The fitted function is a combination of linear and Fermi functions.

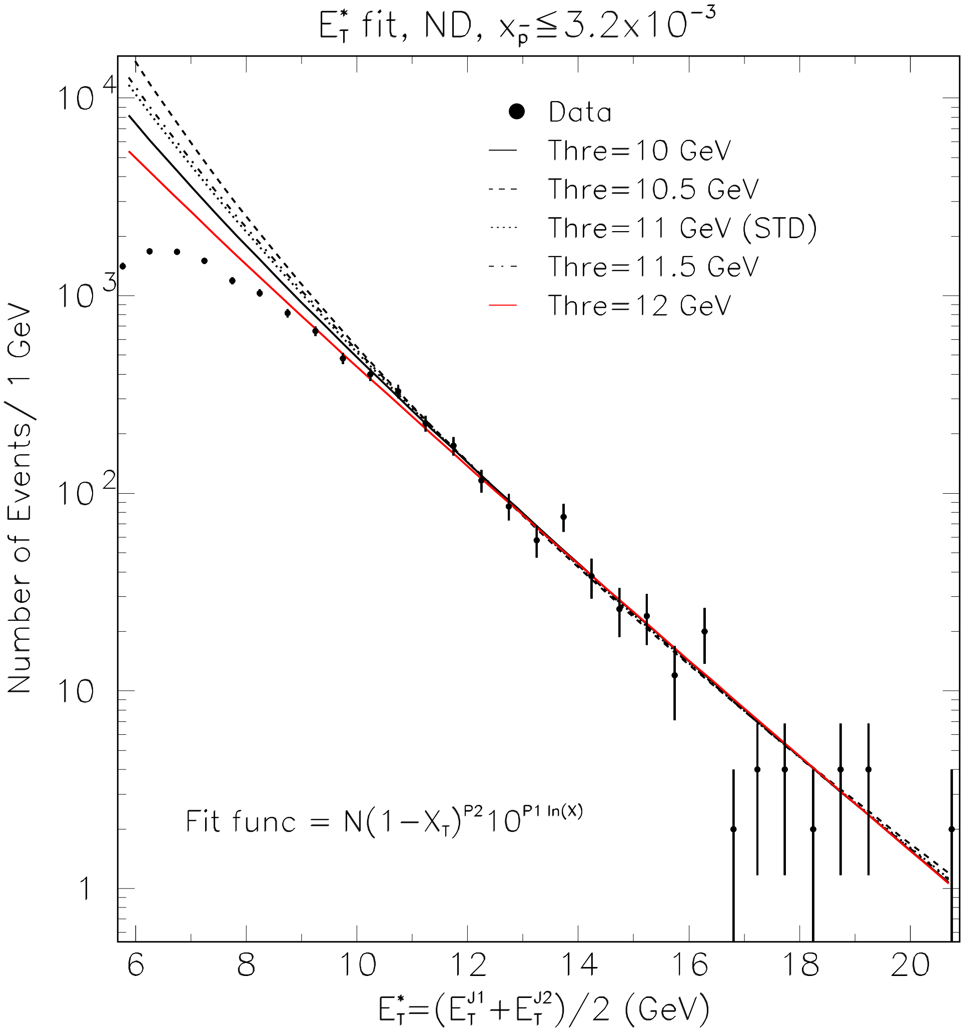

Figure 4.13: Fit result of average E_T distribution for the non-diffractive dijet events with the region of $x_{\overline{p}} \leq 3.2 \times 10^{-3}$. The solid point shows the non-diffractive dijet events, and the several curves are the fit results with different fit regions. The dotted curve shows the standard fit result, and the other curves are those for systematic uncertainty study.

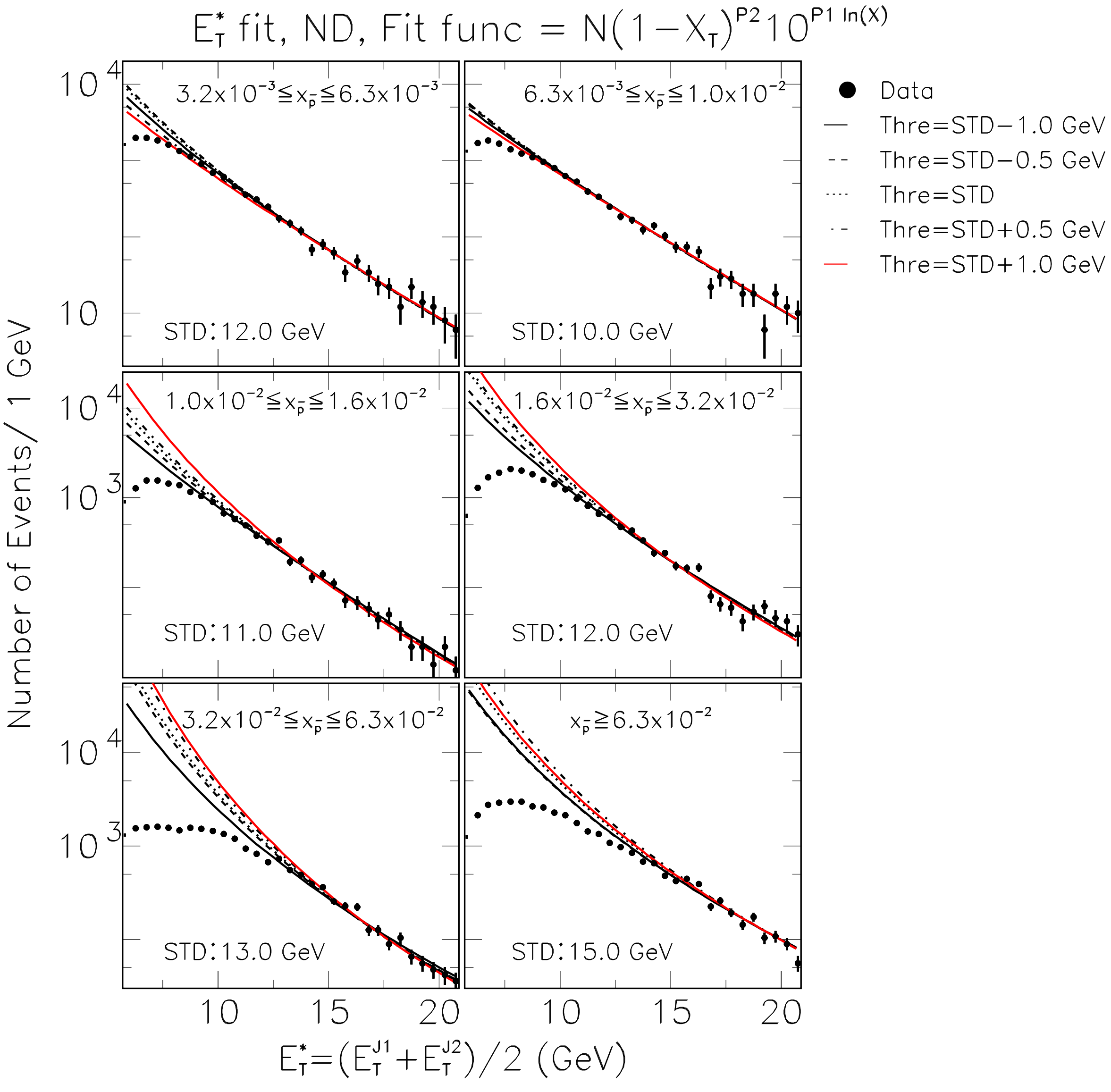

Figure 4.14: Fit results of average E_T distributions for the other $x_{\overline{p}}$ regions of the non-diffractive dijet data. The solid point shows non-diffractive dijet events, and the several curves are the fit results with different fit regions. The dotted curve shows the standard fit result, and the other curves are those for systematic uncertainty study.

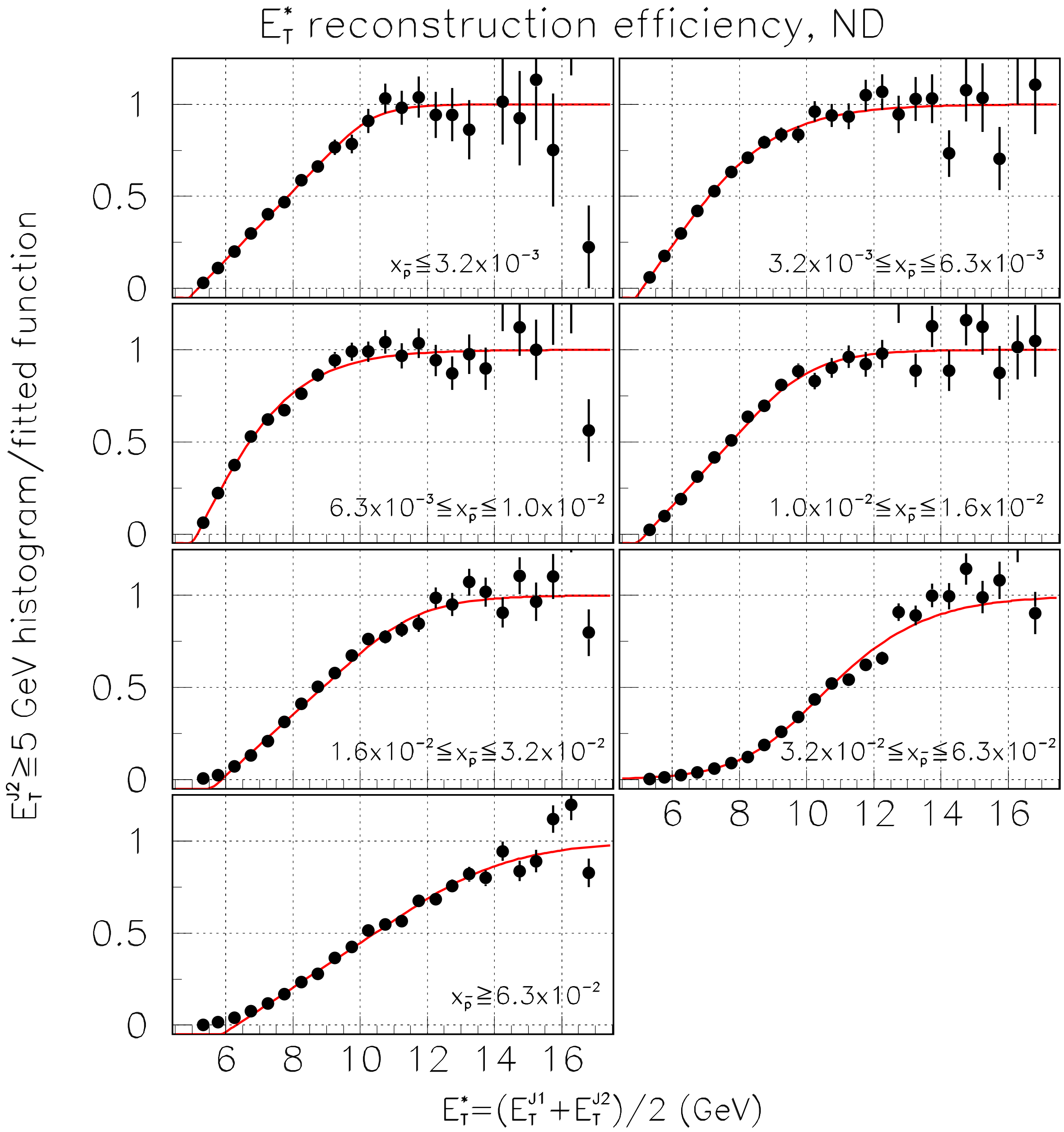

Figure 4.15: Ratio of the E_T^* distribution with $E_T^{\mathrm{Jet2}} \geq 5\,\mathrm{GeV}$ cut to the fitted function for seven $x_{\overline{p}}$ ranges as the $E_T^{\mathrm{Jet2}} \geq 5\,\mathrm{GeV}$ cut efficiency. Solid points show the non-diffractive dijet data. Solid curves show the fitted function. The fitted function is a combination of linear and Fermi functions. In the range of $3.2\times10^{-2} \leq x_{\overline{p}} \leq 6.3\times10^{-2}$, we fit the efficiency to the two-Fermi function in equation (4.2).

4.7 Diffractive dijet cross section

We obtain the diffractive dijet cross section without unfolding detector smearing as follows:

1. Using the diffractive inclusive trigger data, we obtain the following corrected number of diffractive inclusive events $N^{\rm corr}_{\rm INCL}$,

$$N^{\rm corr}_{\rm INCL} = \sum_{\rm all\ SD\ inclsive} \frac{1 - fr^{\rm BG}_{\rm INCL}}{\epsilon_{\rm RPS}(\xi, t) \cdot \epsilon_{\rm BBC}(\xi)},$$

   where $fr^{\rm BG}_{\rm INCL}$, $\epsilon_{\rm RPS}$ and $\epsilon_{\rm BBC}$ are the background fraction in the diffractive inclusive events, the RPS acceptance, and the inner BBC multiplicity cut efficiency, respectively.

2. The diffractive dijet cross section $\sigma^{\rm JJ}_{\rm SD}$ is given by

$$\sigma^{\rm JJ}_{\rm SD} = \sigma^{\rm INCL}_{\rm SD} \sum_{\rm jet\ events} \left[\frac{1 - fr^{\rm BG}_{\rm Jets}(E^*_T)}{\epsilon_{\rm RPS}(\xi, t) \cdot \epsilon_{\rm HTFLT} \cdot \epsilon_{E^*_T}(E^*_T) \cdot \epsilon_{\rm BBC}(\xi)} \right] \Big/ N^{\rm corr}_{\rm INCL}, \qquad (4.3)$$

   where $fr^{\rm BG}_{\rm Jets}$, $\epsilon_{\rm HTFLT}$, and $\epsilon_{E^*_T}$ are the background fraction in the diffractive dijet events, the hot tower filter efficiency, and the $E^{\rm Jet2}_T \geq 5\,{\rm GeV}$ cut efficiency, respectively.

3. Using the diffractive dijet trigger data, the diffractive dijet cross section $\sigma^{\rm JJ}_{\rm SDJJ}$ is given by

$$\begin{aligned} \sigma^{\rm JJ}_{\rm SDJJ} &= \sigma^{\rm INCL}_{\rm SD} \sum_{\rm jet\ events} \left[\frac{1 - fr^{\rm BG}_{\rm Jets}(E^*_T)}{\epsilon_{\rm RPS}(\xi, t) \cdot \epsilon_{\rm HTFLT} \cdot \epsilon_{E^*_T}(E^*_T) \cdot \epsilon_{\rm BBC}(\xi) \cdot \epsilon_{\rm L2}(E^*_T) \cdot \epsilon_{\rm L3}(E^*_T)} \right] \\ &\quad /(N^{\rm corr}_{\rm INCL} \cdot f_{\rm DPS}), \qquad (4.4) \end{aligned}$$

   where $\epsilon_{\rm L2}$ ($\epsilon_{\rm L3}$) and $f_{\rm DPS}$ are the level-2 (level-3) trigger efficiency and the averaged dynamic prescaling factor in the level-2 trigger.

The diffractive dijet cross section was obtained as a function of E^*_T as listed in Table 4.6.

4.8 Non-diffractive dijet cross section

In order to obtain the non-diffractive dijet cross section, we use the following quantities additionally;

E_T^* range	cross section (μb)	
	INCL TRIG sample	JJ TRIG sample
$10\leq E_T^* \leq 11\,\mathrm{GeV}$	2.55 ± 0.04	
$11\leq E_T^* \leq 12\,\mathrm{GeV}$	1.50 ± 0.03	
$12\leq E_T^* \leq 15\,\mathrm{GeV}$	1.76 ± 0.04	1.72 ± 0.12
$15\leq E_T^* \leq 20\,\mathrm{GeV}$	0.582 ± 0.021	0.507 ± 0.030
$20\leq E_T^* \leq 25\,\mathrm{GeV}$	0.112 ± 0.009	0.098 ± 0.007
$E_T^* \geq 25\,\mathrm{GeV}$	0.043 ± 0.005	0.043 ± 0.003
$10\leq E_T^* \leq 12\,\mathrm{GeV}$	4.06 ± 0.06	
$12\leq E_T^* \leq 15\,\mathrm{GeV}$	1.76 ± 0.04	1.72 ± 0.12
$15\leq E_T^* \leq 25\,\mathrm{GeV}$	0.695 ± 0.023	0.605 ± 0.031

Table 4.6: Diffractive dijet cross section in several average E_T bins. The errors are statistical uncertainties only.

- BBC cross section (σ_{BBC}) given by Equation 2.6 as described in section 2.2.6 for normalization [43],
- Z-vertex cut efficiency (ϵ_{ZVTX}).

The Z-vertex cut efficiency is evaluated as follows;

1. The primary Z-vertex distribution in minimum bias events can be fitted to the form,
$$\frac{d\mathcal{L}}{dZ} \propto \exp\left(\frac{-Z^2}{2\sigma_Z^2}\right) \Big/ \left(1 + \frac{(Z-\bar{Z})^2}{\beta^{*2}}\right),$$
where $\bar{Z}$ is the mean value of the Z-vertex distribution, β^* is the Tevatron low beta quadrupole magnet parameter (nominally, it is 35cm), and σ_Z is the longitudinal bunch length [47, 48, 49]. The fit result is shown in Figure 4.16.

2. The efficiency is obtained by calculating,
$$\epsilon_{\mathrm{ZVTX}} = \frac{\int_{-60\mathrm{cm}}^{+60\mathrm{cm}} \frac{d\mathcal{L}}{dZ} dZ}{\int_{-\infty}^{+\infty} \frac{d\mathcal{L}}{dZ} dZ}.$$
The integration in the denominator is performed within the region $|Z_{\mathrm{VTX}}| \leq 150\,\mathrm{cm}$. The Z-vertex cut efficiency is obtained to be
$$\epsilon_{\mathrm{ZVTX}} = 95.7 \pm 2.0\% \text{ (syst.)}. \tag{4.5}$$

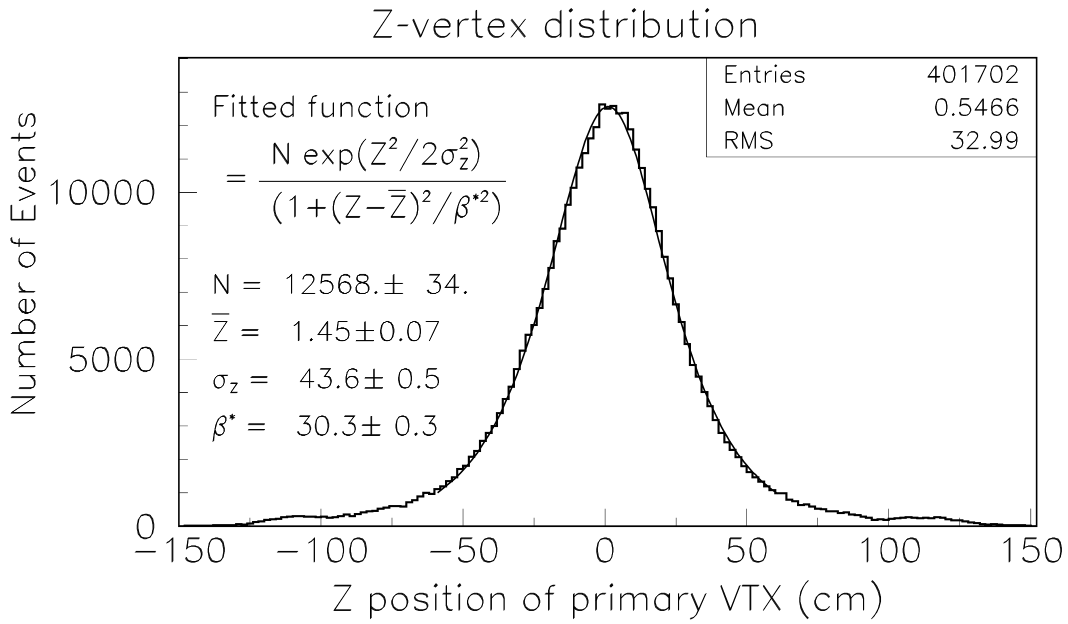

Figure 4.16: The Z-vertex distribution and Z-vertex fit result. The solid curve shows the Z-vertex position fit result.

And we assign 2.0% uncertainty as systematic uncertainty on the Z-vertex cut efficiency.

The non-diffractive dijet cross section $\sigma_{\mathrm{ND}}^{\mathrm{JJ}}$ is given by

$$\sigma_{\mathrm{ND}}^{\mathrm{JJ}} = \sigma_{\mathrm{BBC}} \sum_{\mathrm{jet\ events}} \frac{1}{\epsilon_{\mathrm{HTFLT}} \cdot \epsilon_{E_T^*}(E_T^*) \cdot \epsilon_{\mathrm{ZVTX}}} \Bigg/ \left(N_{\mathrm{ND}}^{\mathrm{INCL}}(\mathrm{obs}) \cdot \frac{<n>}{1-\exp(-<n>)}\right), \quad (4.6)$$

where $\mathcal{L}_{\mathrm{INST}}$ is the instantaneous luminosity, and the term $<n>/\{1-\exp(-<n>)\}$ means the average number of interactions per one bunch crossing. $<n>$ is the average number of interacted events per one bunch crossing and is calculated as $<n> = \mathcal{L}_{\mathrm{INST}} \cdot \sigma_{\mathrm{BBC}}(1 - 0.002704 \cdot \mathcal{L}_{\mathrm{INST}})/f_{\mathrm{TeV}}$, where f_{TeV} is the Tevatron bunch crossing frequency (= 286.28 kHz), and the term $(1 - 0.002704 \cdot \mathcal{L}_{\mathrm{INST}})$ is the correction factor for accidental coincidence in $\mathcal{L}_{\mathrm{INST}}$ [50]. We assign the 1.0% systematic uncertainty on the calculation of the average number of interactions per one bunch crossing. The non-diffractive dijet cross section was obtained as listed in Table 4.7.

E_T^* range	cross section (mb)
$10 \leq E_T^* \leq 11\,\mathrm{GeV}$	1.37 ± 0.018
$11 \leq E_T^* \leq 12\,\mathrm{GeV}$	0.773 ± 0.012
$12 \leq E_T^* \leq 15\,\mathrm{GeV}$	1.05 ± 0.013
$15 \leq E_T^* \leq 20\,\mathrm{GeV}$	0.406 ± 0.007
$20 \leq E_T^* \leq 25\,\mathrm{GeV}$	0.075 ± 0.003
$E_T^* \geq 25\,\mathrm{GeV}$	0.028 ± 0.002
$10 \leq E_T^* \leq 12\,\mathrm{GeV}$	2.14 ± 0.02
$12 \leq E_T^* \leq 15\,\mathrm{GeV}$	1.03 ± 0.01
$15 \leq E_T^* \leq 25\,\mathrm{GeV}$	0.476 ± 0.008

Table 4.7: Non-diffractive dijet cross section in several average E_T bins. The errors are statistical uncertainties only.

4.9 Corrected kinematic variables distribution

Regarding Equations (4.3), (4.4) and (4.6) as event weight, we obtain the corrected distributions of the several kinematical variables as shown in Figures 4.17–4.21.

Figure 4.17 shows the average E_T spectra (top) and the cross section ratio of the diffractive to the non-diffractive dijet production as a function of average E_T (bottom). The solid point in top plot shows the diffractive dijet events with $E_T^* \geq 10\,\mathrm{GeV}$ that is selected from the diffractive inclusive trigger data, the open circle in top plot shows the diffractive dijet events with $E_T^* \geq 15\,\mathrm{GeV}$ that is selected from the diffractive dijet trigger data (scaled by the factor of 1.025), and the open square in top plot shows the non-diffractive dijet events scaled by a factor of 1.862×10^{-3}. The solid point in the bottom plot shows the cross section ratio of the diffractive dijet selected from the diffractive inclusive trigger data to the non-diffractive dijet, and the open circle in the bottom plot shows the cross section ratio of the diffractive dijet selected from the diffractive dijet trigger data to the non-diffractive dijet. Using the diffractive dijet trigger data, we extend the observed average E_T range above 25 GeV. The cross section ratio of the diffractive to the non-diffractive dijet production is almost constant in the whole average E_T region.

Figure 4.18 shows the Q^2 spectra. The solid point shows the diffractive dijet events with $E_T^* \geq 10\,\mathrm{GeV}$ and $Q^2 \geq 50\,\mathrm{GeV}^2$ (selected from the diffractive inclusive trigger data), and the open circle shows the non-diffractive dijet events with the same criteria. The non-diffractive dijet events are scaled by a factor of 1.45×10^{-3}, and the factor is obtained by integrating the area over the region of $Q^2 \geq 600\,\mathrm{GeV}^2$.

Figure 4.19 shows the ξ (top) and $|t|$ (bottom) distributions for diffractive events. The solid point shows the diffractive inclusive events, the open circle shows the diffractive dijet events with $E_T^* \geq 10\,\mathrm{GeV}$ that is selected from the diffractive inclusive trigger data, and the star shows the diffractive dijet events with $E_T^* \geq 15\,\mathrm{GeV}$ that is selected from the diffractive dijet trigger data.

Figure 4.20 shows the average pseudorapidity distributions. The solid point in the top plot shows the diffractive dijet events with $E_T^* \geq 10\,\mathrm{GeV}$ that is selected from the diffractive inclusive trigger data, and the open circle in the top plot shows the non-diffractive dijet events with $E_T^* \geq 10\,\mathrm{GeV}$. The solid point in the bottom plot shows the diffractive dijet events with $E_T^* \geq 15\,\mathrm{GeV}$ that is selected from the diffractive dijet trigger data, and the open circle in the bottom plot shows the non-diffractive dijet events with $E_T^* \geq 15\,\mathrm{GeV}$. The diffractive dijet system in both plots is boosted against the recoil $\overline{p}$ direction though the non-diffractive dijet system is not.

Figure 4.21 shows the azimuthal angle difference between the leading two jets distributions. The solid point in the top plot shows the diffractive dijet events with $E_T^* \geq 10\,\mathrm{GeV}$ that is selected from the diffractive inclusive trigger data, and the open circle in the top plot shows the non-diffractive dijet events with $E_T^* \geq 10\,\mathrm{GeV}$. The solid point in the bottom plot shows the diffractive dijet events with $E_T^* \geq 15\,\mathrm{GeV}$ that is selected from the diffractive dijet trigger data, and the open circle in the bottom plot shows the non-diffractive dijet events with $E_T^* \geq 15\,\mathrm{GeV}$. The dijets in the diffractive events are more back-to-back than those in the non-diffractive ones.

4.10 Cross section ratio of the diffractive to the non-diffractive dijet production

Using the diffractive dijet and non-diffractive dijet cross sections in several average E_T bins as described in the previous section, we obtain the cross section ratio of the diffractive to the non-diffractive dijet production as shown in Table 4.8 and Figure 4.17.

As we mentioned in section 1.2, in order to cancel out the contributions from the

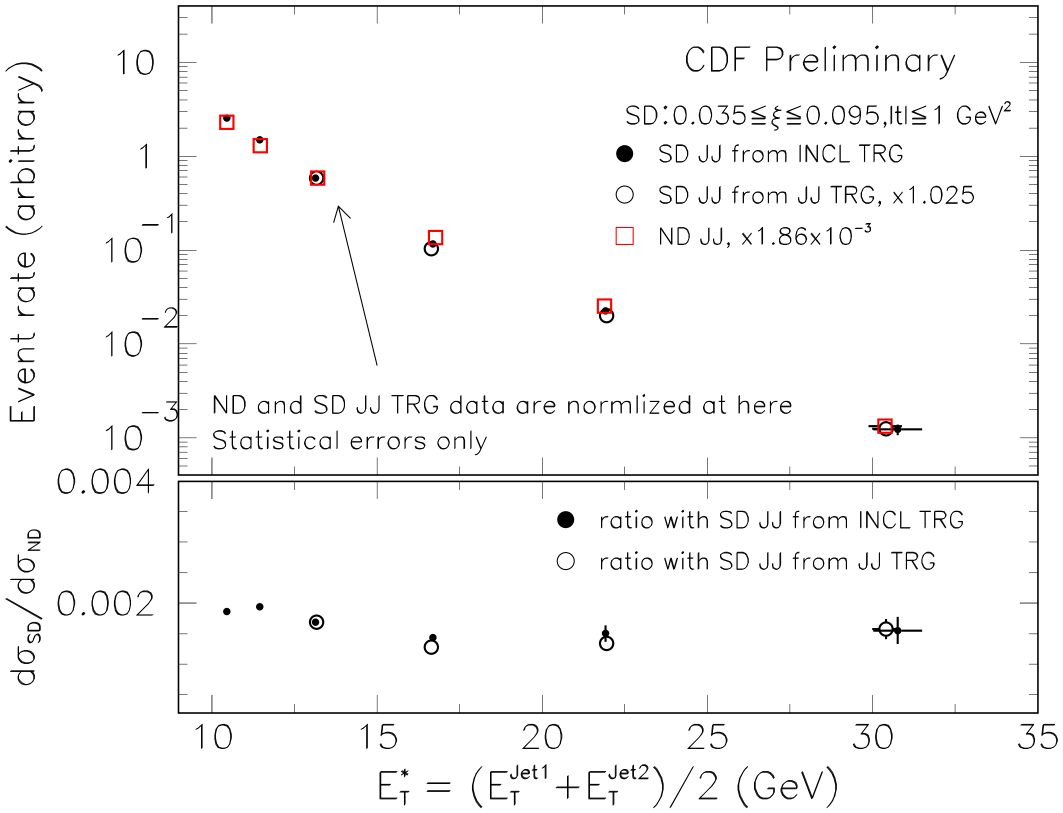

Figure 4.17: Diffractive dijet event rate (top) and cross section ratio (bottom) as a function of average E_T. In the top plot, the non-diffractive dijets are scaled by a factor of 1.862×10^{-3}. The cross section ratio is almost constant for average E_T above 10 GeV. By using diffractive dijet trigger data, we successfully extend this spectra above 25 GeV region.

proton PDF and the matrix element, we use the cross section ratio of the diffractive to the non-diffractive dijet production as a function of $x_{\overline{p}}$. Subtracting the non-diffractive background as described in the previous section, we obtain the $x_{\overline{p}}$ distribution of the diffractive and the non-diffractive dijet production, and then the cross section ratio in each $x_{\overline{p}}$ bin as shown in Figures 4.22–4.25. The dashed lines in the figures show the kinematical and detector acceptances. The right-side dashed line which is corresponds to $\log_{10}(\xi_{\rm MIN})$ shows the RPS detector acceptance. In the region above the line, β can be larger than 1 beyond the allowed range according to $x_{\overline{p}} = \xi \cdot \beta$. We can also remove the effect from the detector crack by this cut. The left-side dashed line shows the kinematical acceptance. This minimum $x_{\overline{p}}$ increases with increasing average E_T ($x_{\overline{p}}(\min) = (E_T^*(\min)/7) \times 10^{-3}$).

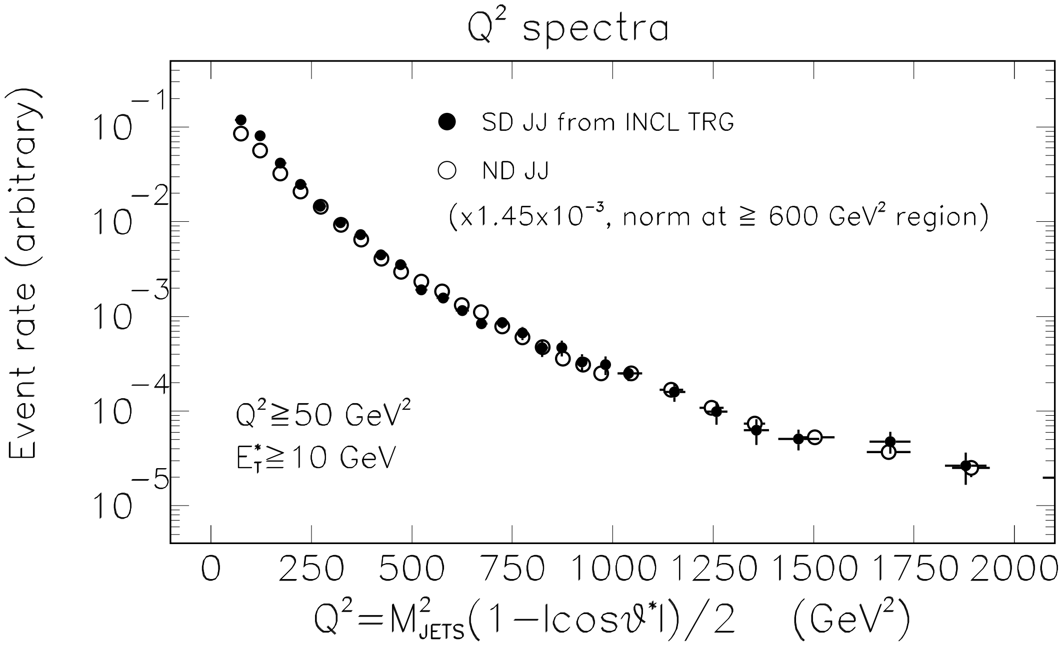

Figure 4.18: Q^2 spectra with $E_T^* \geq 10\,\mathrm{GeV}$ and $Q^2 \geq 50\,\mathrm{GeV}^2$ for the diffractive dijet events (solid circle), and the non-diffractive dijet events (open circle). Q^2 spectrum for the non-diffractive dijet events is scaled by a factor of 1.45×10^{-3}. The scale factor is obtained by integrating the area over the $Q^2 \geq 600\,\mathrm{GeV}^2$ region. The error bars show statistical uncertainties only.

CDF Preliminary

E_T^* range	cross section ratio (%)	
	INCL TRIG sample	JJ TRIG sample
$10 \leq E_T^* \leq 11\,\mathrm{GeV}$	0.186 ± 0.004	
$11 \leq E_T^* \leq 12\,\mathrm{GeV}$	0.194 ± 0.005	
$12 \leq E_T^* \leq 15\,\mathrm{GeV}$	0.168 ± 0.004	0.164 ± 0.011
$15 \leq E_T^* \leq 20\,\mathrm{GeV}$	0.143 ± 0.006	0.125 ± 0.008
$20 \leq E_T^* \leq 25\,\mathrm{GeV}$	0.150 ± 0.014	0.131 ± 0.011
$E_T^* \geq 25\,\mathrm{GeV}$	0.155 ± 0.023	0.153 ± 0.016
$10 \leq E_T^* \leq 12\,\mathrm{GeV}$	0.189 ± 0.003	
$12 \leq E_T^* \leq 15\,\mathrm{GeV}$	0.171 ± 0.004	0.167 ± 0.012
$15 \leq E_T^* \leq 25\,\mathrm{GeV}$	0.146 ± 0.005	0.127 ± 0.007

Table 4.8: Diffractive to non-diffractive dijet cross section ratio for several average E_T bins. The errors are statistical uncertainties only.

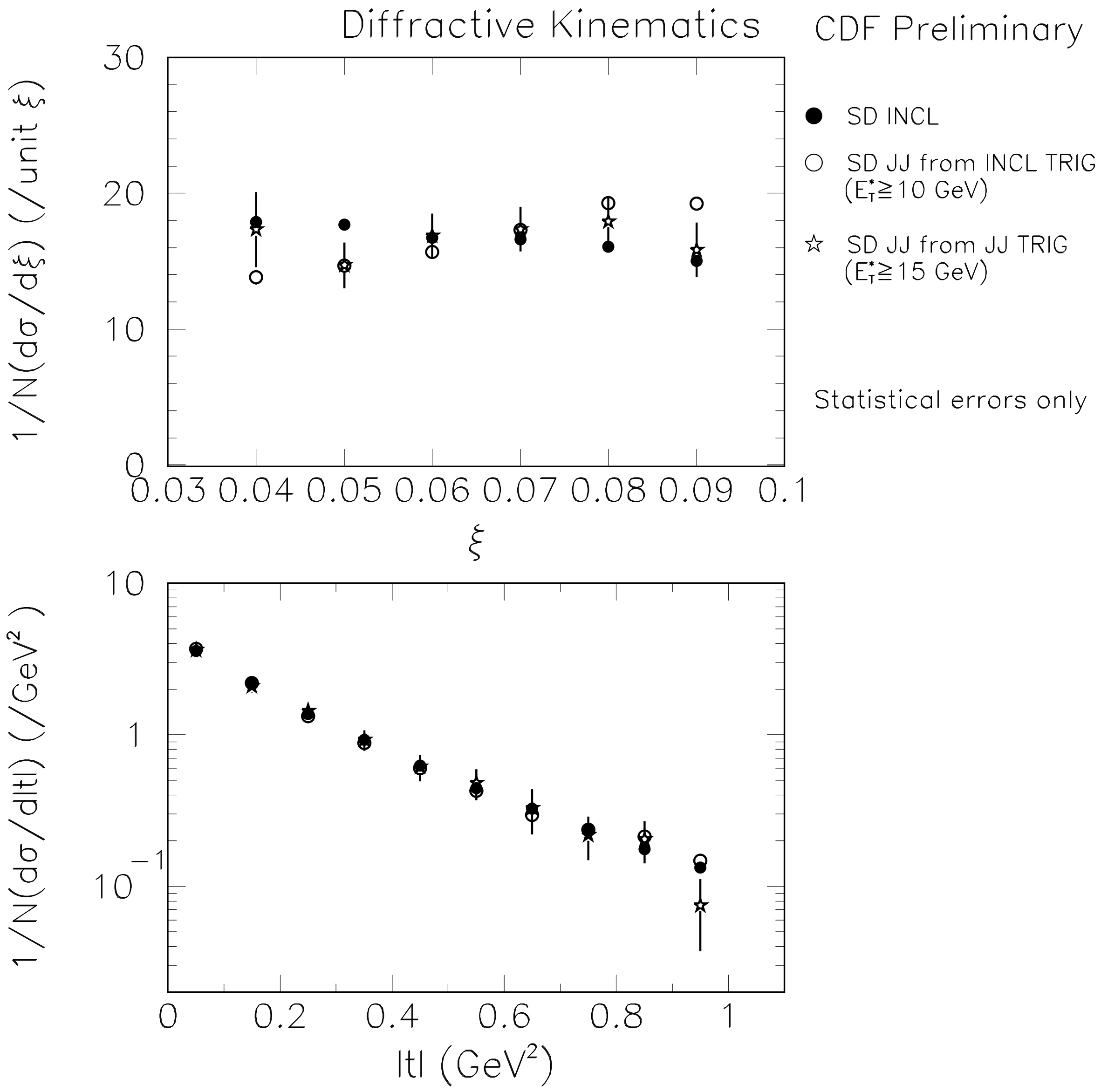

Figure 4.19: Distributions of ξ (top) and $|t|$ (bottom) for diffractive inclusive (solid), diffractive dijets with $E_T^* \geq 10$ GeV (open circle), and those with $E_T^* \geq 15$ GeV (star).

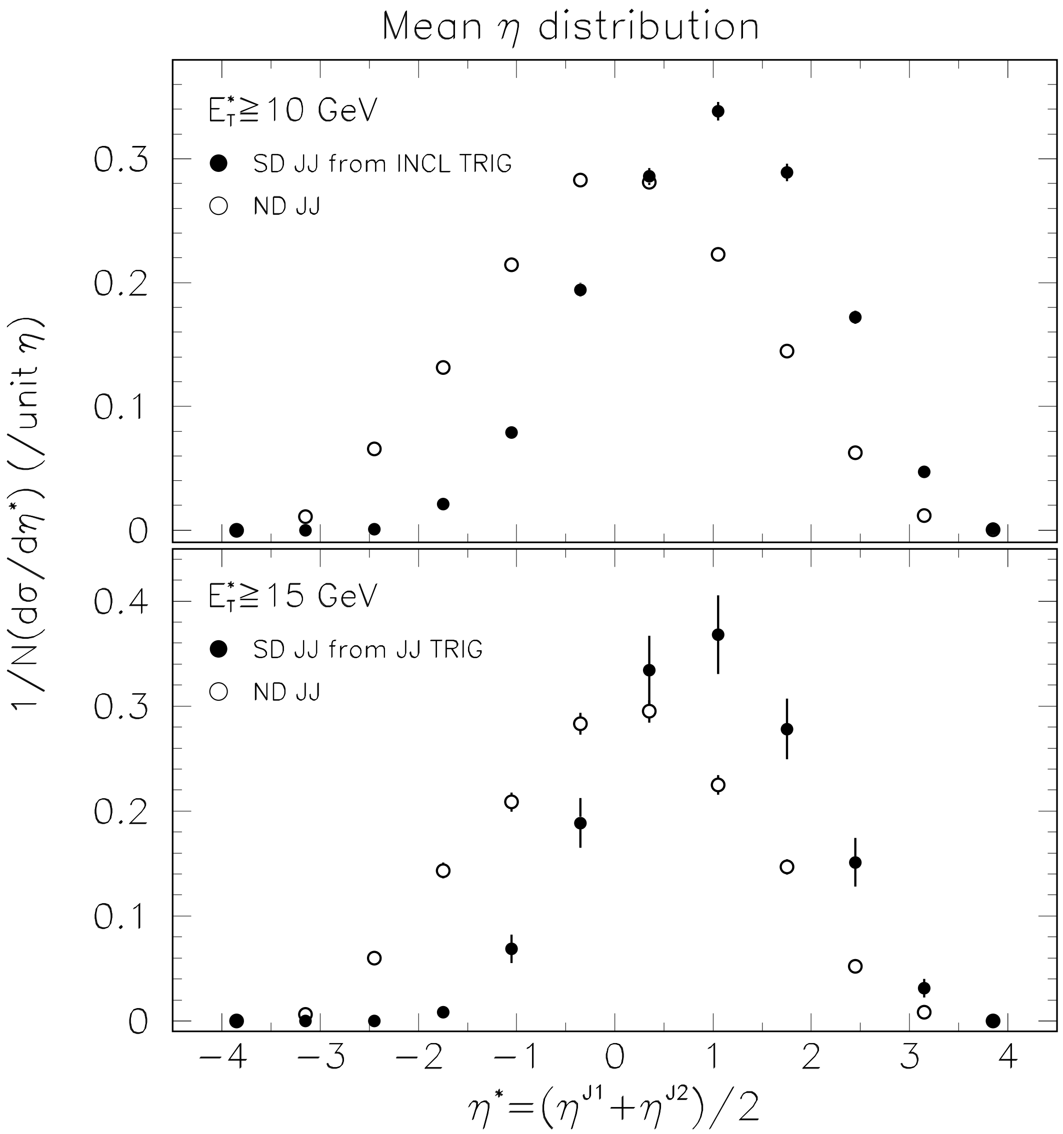

Figure 4.20: The top plot shows average η distribution with $E_T^* \geq 10\,\text{GeV}$, and the bottom plot shows that with $E_T^* \geq 15\,\text{GeV}$. The solid point shows diffractive dijets, the open circle shows non-diffractive dijets. Diffractive dijet system is boosted against the $\bar{p}$ direction. The error bars show statistical uncertainties only.

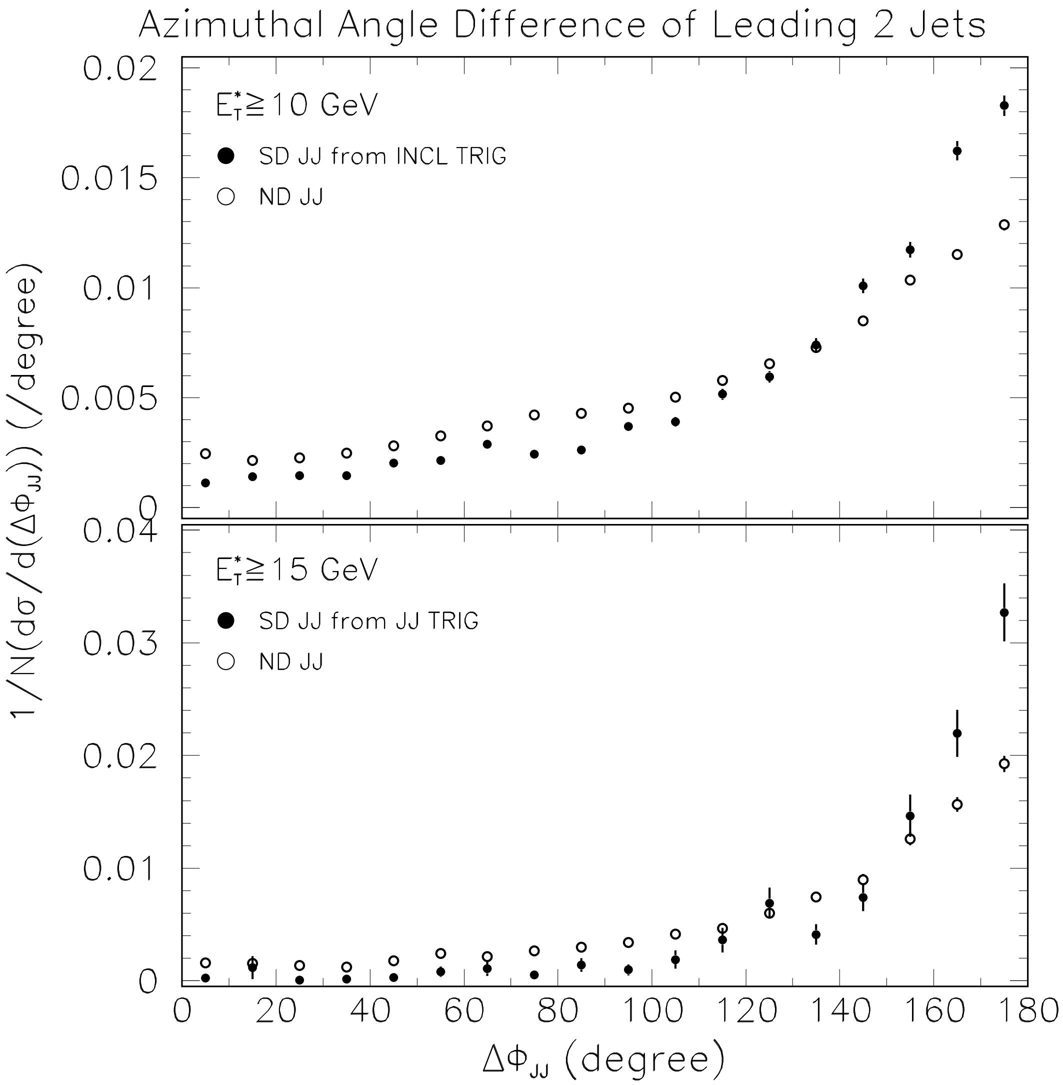

Figure 4.21: The top plot shows azimuthal angle difference of leading two jets with $E_T^* \geq 10\,\mathrm{GeV}$, and the bottom plot shows that with $E_T^* \geq 15\,\mathrm{GeV}$. The solid point shows diffractive dijets, the open circle shows non-diffractive dijets. Diffractive dijets are more back-to-back than non-diffractive ones. The error bars show statistical uncertainties only.

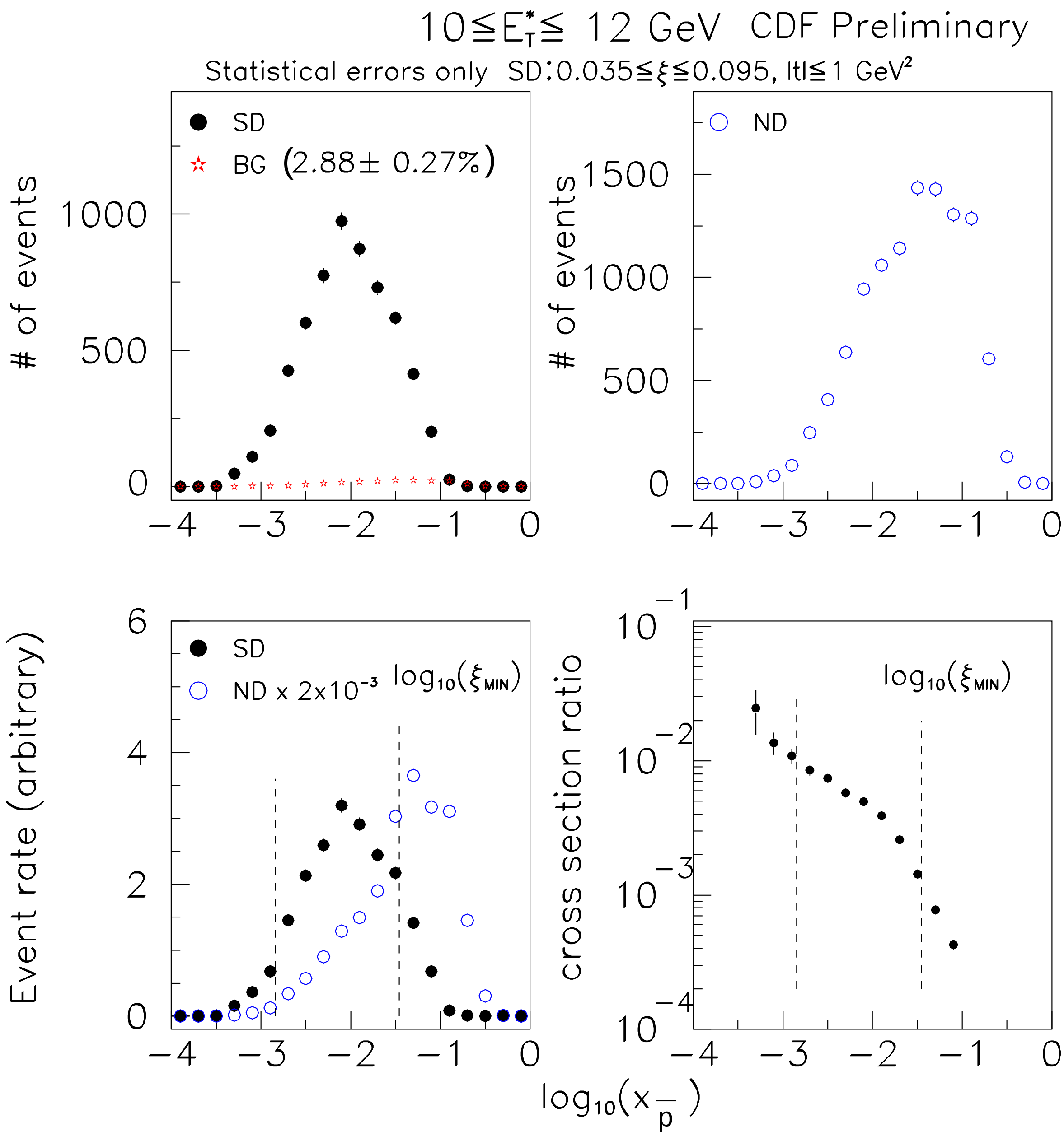

Figure 4.22: $x_{\overline{p}}$ distributions with $10 \leq E_T^* \leq 12\,\mathrm{GeV}$. The top-left plot shows the $x_{\overline{p}}$ distribution for the diffractive dijet events together with the non-diffractive background (2.9%, star). The top-right plot shows that for the non-diffractive dijet events. The bottom-left plot shows the dijet event rate as a function of $\log_{10}(x_{\overline{p}})$ for the diffractive and the non-diffractive dijet production (scaled by 2.0×10^{-3}). The dashed line shows the detector acceptance and the kinematical cut. The bottom-right plot shows the cross section ratio as a function of $\log_{10}(x_{\overline{p}})$.

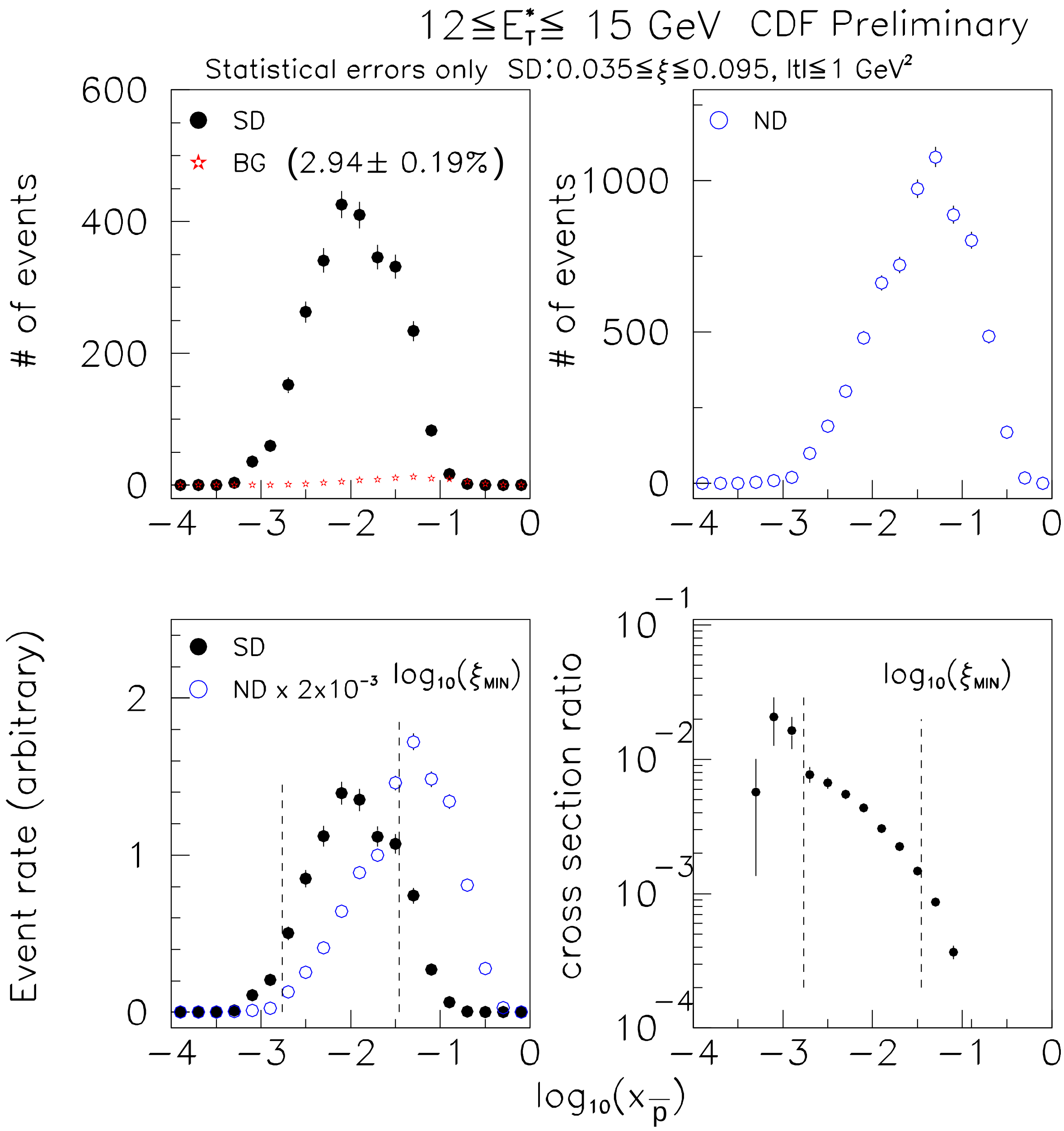

Figure 4.23: $x_{\overline{p}}$ distributions with $12 \leq E_T^* \leq 15\,\mathrm{GeV}$. The top-left plot shows the $x_{\overline{p}}$ distribution for the diffractive dijet events together with the non-diffractive background (2.9%, star). The top-right plot shows that for the non-diffractive dijet events. The bottom-left plot shows the dijet event rate as a function of $\log_{10}(x_{\overline{p}})$ for the diffractive and non-diffractive dijet production (scaled by 2.0×10^{-3}). The dashed line shows the detector acceptance and the kinematical cut. The bottom-right plot shows the cross section ratio as a function of $\log_{10}(x_{\overline{p}})$.

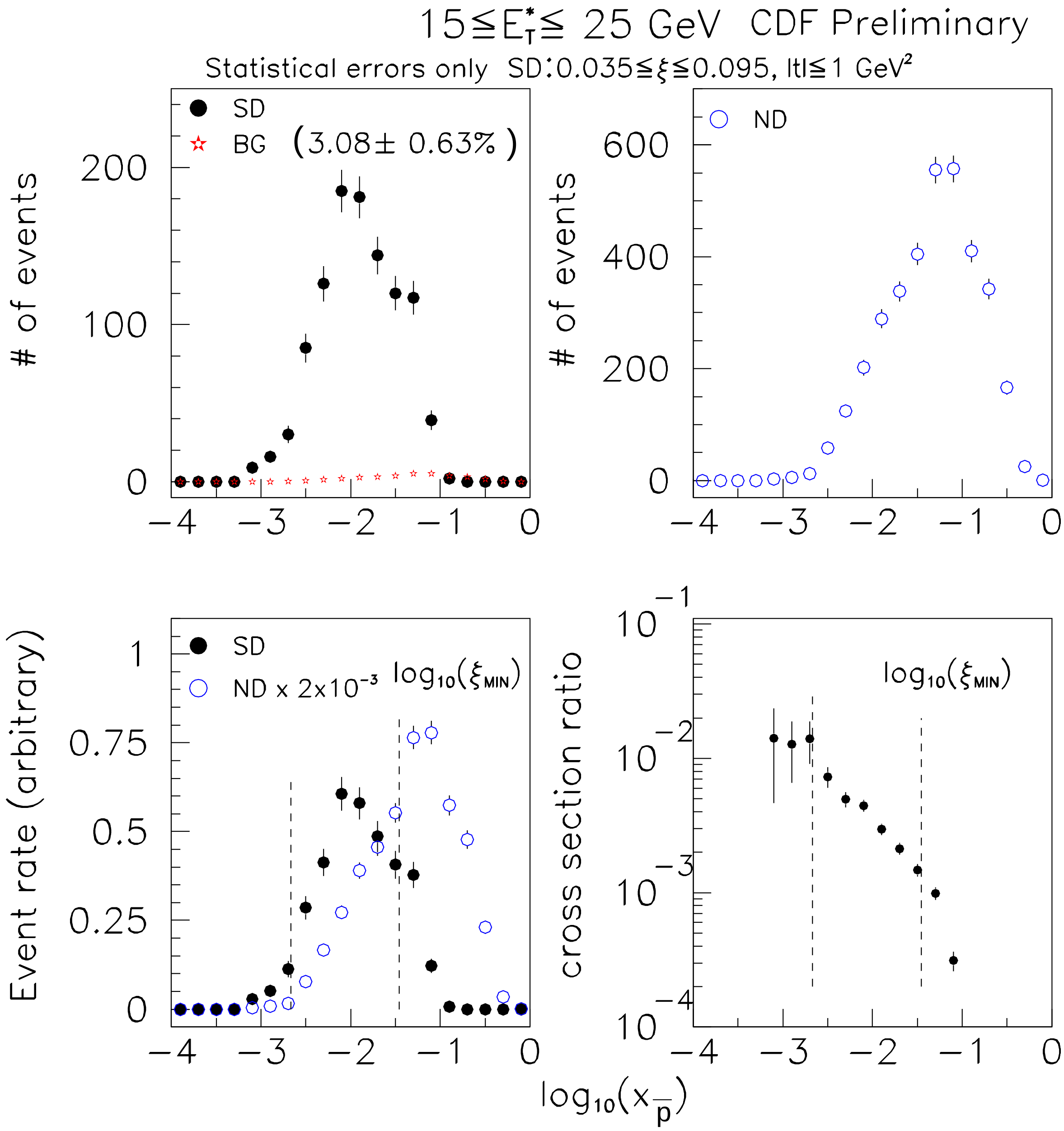

Figure 4.24: $x_{\overline{p}}$ distributions with $15 \leq E_T^* \leq 25\,\mathrm{GeV}$. The top-left plot shows the $x_{\overline{p}}$ distribution for the diffractive dijet events together with the non-diffractive background (3.1%, star). The top-right plot shows that for the non-diffractive dijet events. The bottom-left plot shows the dijet event rate as a function of $\log_{10}(x_{\overline{p}})$ for the diffractive and non-diffractive dijet production (scaled by 2.0×10^{-3}). The dashed line shows the detector acceptance and the kinematical cut. The bottom-right plot shows the cross section ratio as a function of $\log_{10}(x_{\overline{p}})$.

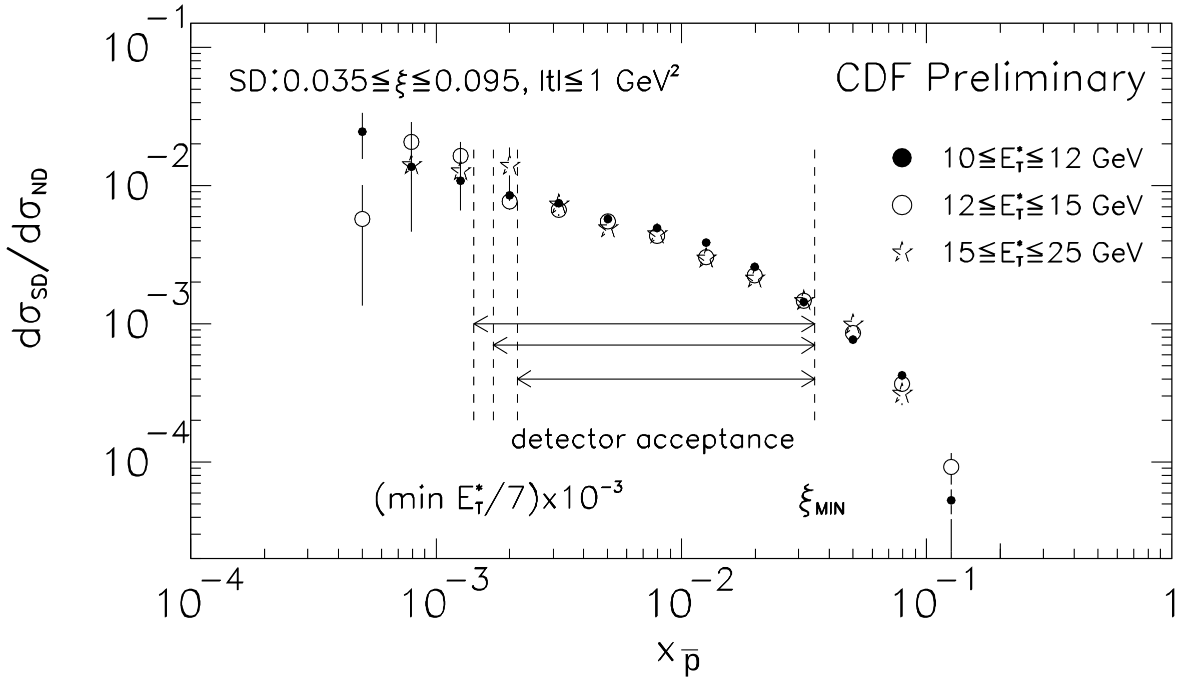

<Q²> (Unit: GeV²)

	$10 \leq E_T^* \leq 12$ GeV	$12 \leq E_T^* \leq 15$ GeV	$15 \leq E_T^* \leq 25$ GeV
SD :	162.7 ± 1.4	261.1 ± 3.2	522.7 ± 10.2
ND :	170.1 ± 1.1	268.7 ± 2.2	496.3 ± 6.1

Statistical errors only

Figure 4.25: Cross section ratio as a function of $x_{\overline{p}}$. The solid point shows data with the range of $10 \leq E_T^* \leq 12\,\mathrm{GeV}$, the open circle shows data with the range of $12 \leq E_T^* \leq 15\,\mathrm{GeV}$, and the star shows data with the range of $15 \leq E_T^* \leq 25\,\mathrm{GeV}$. The dashed line shows a detector acceptance. Below the plot, we show average Q^2 values for each region, each data.

Chapter 5

Diffractive structure function of the antiproton

5.1 Diffractive structure function

As described in section 1.2, the cross section ratio of the diffractive to the non-diffractive dijet production is equivalent to the ratio of the diffractive structure function of the antiproton to the non-diffractive structure function (proton PDF) as written in Equation 1.34. Therefore, the diffractive structure function, $F^{\mathrm{SD}}(\beta, Q^2)$, is extracted by integrating a product of the cross section ratio, $R_{\mathrm{JJ}}^{\mathrm{SD/ND}}(x_{\overline{p}}, E_T^*)$, and the proton PDF, $F^{\mathrm{ND}}(x, Q^2)$, over $x_{\overline{p}}$ according to the true $x_{\overline{p}}$ distribution as written in Equation 1.35.

We obtain the diffractive structure function in the three average E_T regions of $10 \leq E_T^* \leq 12\,\mathrm{GeV}$, $12 \leq E_T^* \leq 15\,\mathrm{GeV}$, and $15 \leq E_T^* \leq 25\,\mathrm{GeV}$, and calculate the average Q^2 in these three average E_T bins in order to investigate the Q^2 dependence of the diffractive structure function.

We extract the diffractive structure function in the following procedure;

1. divide the data into three E_T^* regions,
2. obtain the cross section ratio as a function of $x_{\overline{p}}$ in each E_T^* bin,
3. obtain the the number of diffractive dijet events in a bin of $(x_{\overline{p}}, Q^2(E_T^*))$ corrected

with efficiencies, and its normalization satisfies

$$\sum_{\text{jet events}} \frac{1}{N^{\rm SD}(x_{\overline{p}}, Q^2(E_T^*))} = 1.$$

This weight factor was introduced for avoiding the non-uniform contribution over $x_{\overline{p}}$.

4. take account of color factor to have a proton PDF, $F^{\rm ND}(x, Q^2)$;
$F^{\rm ND}(x, Q^2) = x \left[f_{g/p}(x, Q^2) + 4/9 \sum \{ f_{q/p}(x, Q^2) + f_{\bar{q}/p}(x, Q^2) \} \right]$,

5. integrate over the diffractive dijet events and calculate the diffractive structure function as a function of β;

$$F^{\rm SD}(\beta, Q^2(E_T^*)) = \sum_{\text{jet events}} \frac{1}{N^{\rm SD}(x_{\overline{p}}, Q^2(E_T^*))} R_{\rm JJ}^{\rm SD/ND}(x_{\overline{p}}, Q^2(E_T^*)) \cdot F^{\rm ND}(x_{\overline{p}}, Q^2(E_T^*)),$$

6. and calculate the average Q^2 in each (E_T^*,β) bin.

We obtain the diffractive structure function as shown in Figure 5.1, where the dashed line indicates the lower limit of kinematical acceptance. Rejecting the events outside of the kinematical acceptance, we obtain the results shown in Figure 5.2. We calculate the average Q^2 in the three E_T^* regions and six β bins as listed in Table 5.1.

Finally we obtain the diffractive structure function as a function of average Q^2 as shown in Figure 5.3 (standard result).

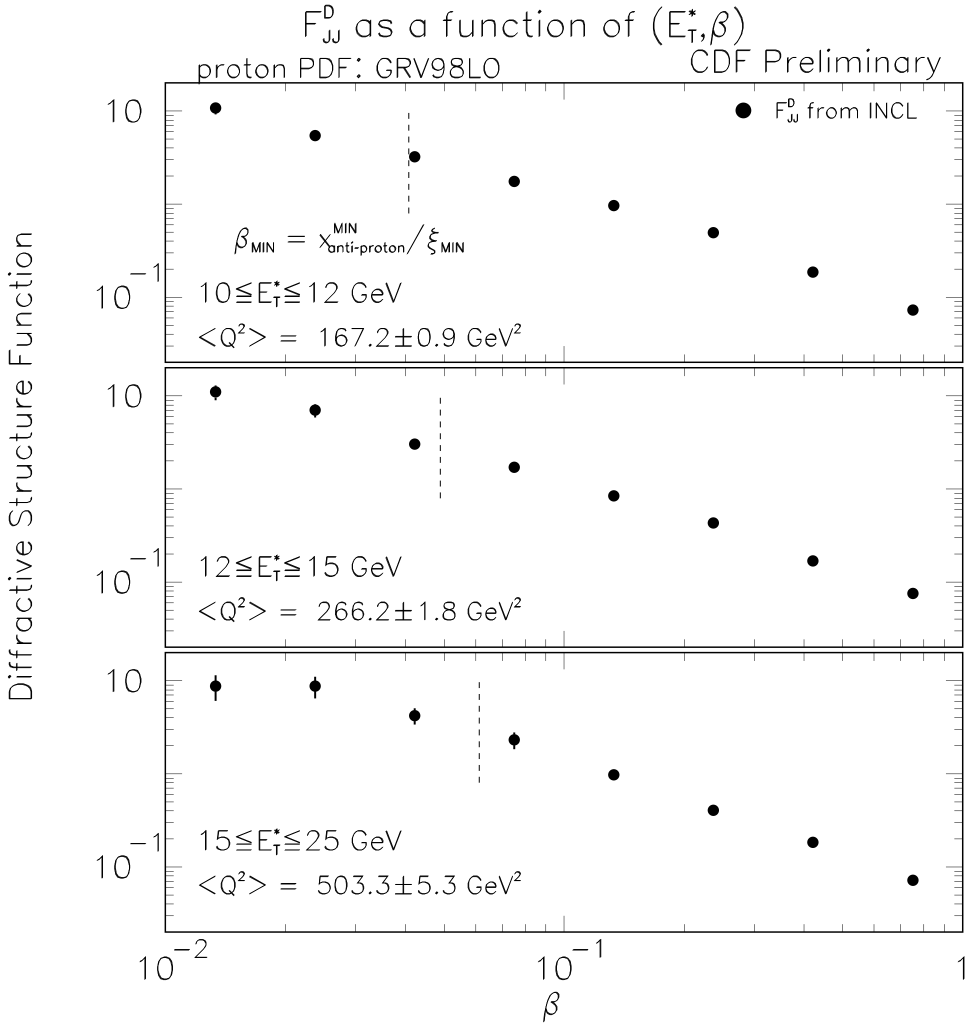

Figure 5.1: Diffractive structure function as a function of β in the three E_T^* regions of $10 \leq E_T^* \leq 12\,\mathrm{GeV}$ (top), $12 \leq E_T^* \leq 15\,\mathrm{GeV}$ (middle), and $15 \leq E_T^* \leq 25\,\mathrm{GeV}$ (bottom). Dashed lines show the lower limit of the kinematical acceptance.

E_T^* range	average Q^2 (GeV^2)		
	diffractive dijets	non-diffractive dijets	combined
$10 \leq E_T^* \leq 12\,\mathrm{GeV}$	162.7 ± 1.4	170.1 ± 1.1	167.2 ± 0.9
$12 \leq E_T^* \leq 15\,\mathrm{GeV}$	261.1 ± 3.2	268.7 ± 2.2	266.2 ± 1.8
$15 \leq E_T^* \leq 25\,\mathrm{GeV}$	522.7 ± 10.2	496.3 ± 6.1	503.3 ± 5.3
β range	$10 \leq E_T^* \leq 12\,\mathrm{GeV}$	$12 \leq E_T^* \leq 15\,\mathrm{GeV}$	$15 \leq E_T^* \leq 25\,\mathrm{GeV}$
$3.2 \times 10^{-2} \leq \beta \leq 5.6 \times 10^{-2}$	171.1 ± 4.4		
$5.6 \times 10^{-2} \leq \beta \leq 1.0 \times 10^{-1}$	163.4 ± 3.9	287.0 ± 8.5	624.0 ± 25.6
$1.0 \times 10^{-1} \leq \beta \leq 1.8 \times 10^{-1}$	161.2 ± 3.2	272.5 ± 7.2	574.1 ± 22.7
$1.8 \times 10^{-1} \leq \beta \leq 3.2 \times 10^{-1}$	163.4 ± 3.2	260.1 ± 7.8	523.9 ± 22.9
$3.2 \times 10^{-1} \leq \beta \leq 5.6 \times 10^{-1}$	162.3 ± 3.7	247.0 ± 7.6	500.4 ± 24.4
$5.6 \times 10^{-1} \leq \beta \leq 1.0$	140.6 ± 4.0	207.0 ± 7.4	440.6 ± 23.3

Table 5.1: Average Q^2 in each E_T^* and β bin.

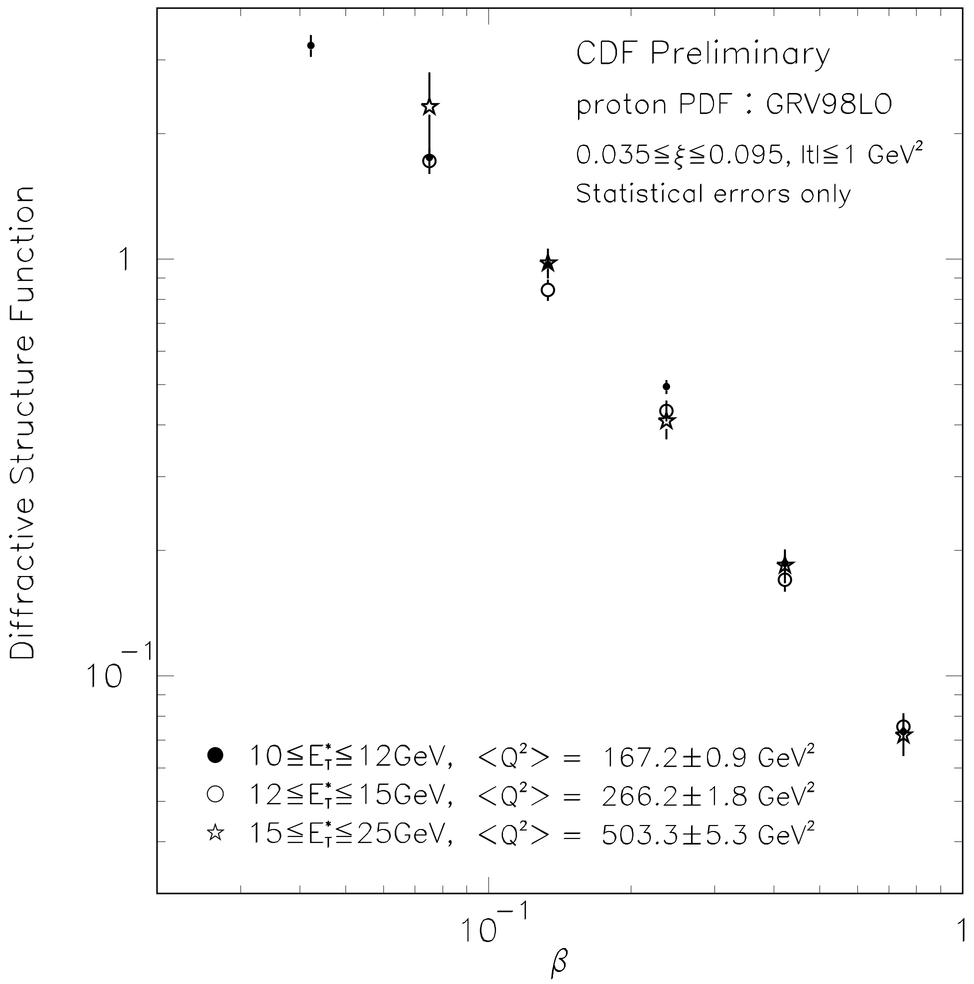

Figure 5.2: Diffractive structure function as a function of β after rejecting the points outside of the kinematical acceptance.

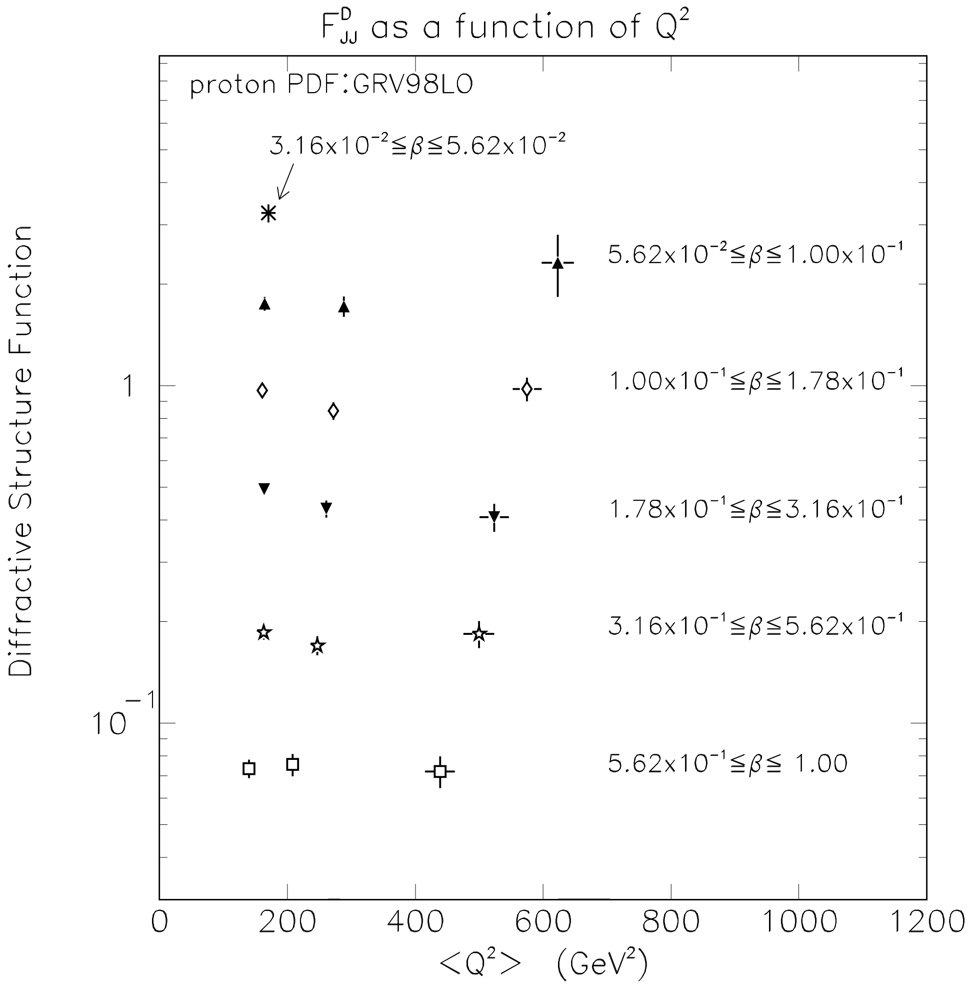

Figure 5.3: Diffractive structure function as a function of Q^2 for 6 β bins. The error bars show statistical uncertainties only.

5.2 Systematic uncertainty

In this section, we discuss the systematic uncertainty. The systematic uncertainty is categorized into two parts; (1) the common systematic uncertainty which is only on the absolute value of the diffractive structure function (all points are correlated), and (2) the independent systematic uncertainty. The main source of the former is the cross section normalization, and that of the latter is the efficiencies which is a function of jet energy. At first, we define the results of the cross section ratio described in section 4.10 and the diffractive structure function described in section 5 as "standard, STD". And we extract the deviation of the test result from the standard one as an systematic uncertainty;

$$dev = (test - STD)/STD.$$

5.2.1 The common systematic uncertainty

The source of the common systematic uncertainty is the uncertainties of the cross section normalization (20%) and the efficiencies that do not depend on jet energy as listed in Table 5.2. Since the background fractions for the dijet events are almost constant ($\sim$ 3%) and their uncertainties are less than 0.63% as listed in Table 4.1, we assign the systematic uncertainty to be 1% for the common systematic uncertainty. We ignore the systematic uncertainties due to the west multiplicity cut efficiency (0.1%, in Table 4.2), the background fraction in diffractive inclusive event (0.01%, in Table 4.1), and the other small systematics. We include the uncertainty due to BBC cross section (3.1%) [43]. We assign the 2.0% systematic uncertainty due to the Z-vertex cut efficiency as described in section 4.8, and the 1.0% systematic uncertainty due to the average number of interactions per one bunch crossing in the non-diffractive dijet cross section. The systematic uncertainty due to calorimeter noise filter must be canceled when we obtain the cross section ratio of the diffractive to non-diffractive dijet production. But because the difference of data taking condition (instantaneous luminosity and so on), we assign 2.0% to the systematic uncertainty on the cross section ratio. In total, the common systematic uncertainty is 20.5%.

The source of the common systematic uncertainty	the systematic uncertainty
$\boxed{\text{Diffractive dijet cross section}}$	
Total diffractive cross section $\sigma_{\rm SD}^{\rm INCL}$ as shown in Equation 4.1	20%
Background fraction of diffractive dijet event	1.0%
$\boxed{\text{Non-diffractive dijet cross section}}$	
BBC cross section $\sigma_{\rm BBC}$ as shown in Equation 2.6	3.1%
$Z_{\rm VTX}$ cut efficiency	2.0%
Average number of interactions per one bunch crossing	1.0%
$\boxed{\text{Cross section ratio}}$	
Efficiency for the calorimeter noise filter $\epsilon_{\rm HTFLT}$	2.0%
Total common systematic uncertainty	20.5%

Table 5.2: Summary table of the common systematic uncertainty.

5.2.2 The independent systematic uncertainty

Jet energy scale

The uncertainty on the jet energy scale for jets with $E_T \geq 8\,\mathrm{GeV}$ and $|\eta| \leq 2.4$ is estimated to be 4.1% for the cone 0.4 clustering [46]. In this analysis, we choose the 0.7 cone radius for the jet clustering. We assign the same systematic uncertainty as that for jets with $R = 0.4$, namely $\pm 4.1\%$. We further add the systematic uncertainty $\pm 3.0\%$, since our E_T threshold (corrected $E_T \geq 5$ GeV) is lower than that of raw $E_T = 8$ GeV. For the jet with $E_T \geq 15$ GeV, we do not add the extra $\pm 3.0\%$ uncertainty, because jets with corrected $E_T \geq 15$ GeV mostly have raw E_T larger than 8 GeV. For jets in the forward calorimeter ($|\eta| \geq 2.4$), we add an extra $\pm 2.5\%$ uncertainty. Thus, the total uncertainty on jet energy scale is

$$\Delta E_T \;=\; \begin{cases} \pm 5.6\% & 5 \leq E_T \leq 15\,\mathrm{GeV}, \quad |\eta| < 2.4 \\ \pm 6.1\% & 5 \leq E_T \leq 15\,\mathrm{GeV}, \quad |\eta| \geq 2.4 \\ \pm 4.1\% & E_T \geq 15\,\mathrm{GeV}, \quad |\eta| < 2.4 \\ \pm 4.8\% & E_T \geq 15\,\mathrm{GeV}, \quad |\eta| \geq 2.4 \end{cases} .$$

Changing the jet energy scale for the diffractive dijet and the non-diffractive dijet, we estimate the largest deviation of the cross section ratio from the standard result to be the systematic uncertainty due to the jet energy scale conservatively.

change	deviation (%)		
	$10 \leq E_T^* \leq 12$ GeV	$12 \leq E_T^* \leq 15$ GeV	$15 \leq E_T^* \leq 25$ GeV
+1 standard deviation	$+11.2 \pm 0.3$	$+8.1 \pm 0.3$	-0.1 ± 0.0
−1 standard deviation	-8.9 ± 0.2	-11.2 ± 0.4	-1.3 ± 0.1

Table 5.3: Deviations of the results changing the jet energy scale from the standard result.

Underlying energy subtraction

The uncertainty due to the underlying E_T subtraction is mainly due to the difference in the underlying event E_T between the diffractive dijet events and the non-diffractive dijet ones. For jets in the diffractive events, we assign the 100% uncertainty to the measured underlying event E_T, namely 0.54 ± 0.54 GeV. For jets in the non-diffractive events, the difference in the measured underlying event E_T between the high luminosity run and the low luminosity run is 0.82 GeV, so that we assign the uncertainty on the underlying event E_T in the non-diffractive dijet events to be ± 0.82 GeV. Changing the underlying event E_T for the diffractive dijet and the non-diffractive dijet, we estimate the largest deviation of the cross section ratio from the standard result to be the systematic uncertainty due to the underlying energy subtraction conservatively.

change	deviation (%)		
	$10 \leq E_T^* \leq 12$ GeV	$12 \leq E_T^* \leq 15$ GeV	$15 \leq E_T^* \leq 25$ GeV
+1 standard deviation	$+2.7 \pm 0.1$	$+1.7 \pm 0.1$	$+9.7 \pm 0.5$
−1 standard deviation	$-0.0_3 \pm 0.0$	-2.9 ± 0.1	-11.0 ± 0.5

Table 5.4: Deviations of the results changing the underlying event energy from the standard result.

E_T^* correction

The systematic uncertainties on the diffractive structure function is estimated based on the previous analysis [47]. Since we made an additional correction on E_T^*, we need to estimate the systematic uncertainty due to the E_T^* correction. We perform the following three kinds of systematic studies in order to estimate this systematic uncertainty;

- second jet E_T threshold,
- fit function, and
- fit range.

The standard second jet E_T threshold is 5 GeV. Changing the second jet E_T threshold to 0 GeV and 7 GeV, we obtain the E_T^* correction functions and calculate its deviation from the standard one as listed in Table 5.5, which results in the systematic uncertainty on the diffractive structure function.

Changing the fit function to a power law function (Fit function $= Ax^B$), we obtain the diffractive structure function in the same procedure as the standard. The deviation of the result from the standard one is listed in Table 5.6. The E_T^* correction factors are shown as a function of E_T^* in Figures 5.4 and 5.5 for the diffractive and non-diffractive dijet events, respectively.

The fit range dependence is studied by scanning the minimum threshold from -1.0 GeV to $+1.0$ GeV with a 0.5 GeV pitch with respect to the standard fit threshold. Conservatively, we choose the most different fit results in both sides, to estimate the systematic uncertainty due to the fit range. The relative deviations of the E_T^* correction factors with various fit ranges from the standard one are shown as a function of E_T^* for the diffractive and non-diffractive dijet data in Figures 5.6 and 5.7, respectively. The deviations are listed in Table 5.7. As shown in the table, the combination of the positive deviation for the diffractive events and the negative deviations for the non-diffractive events gives the largest deviations, therefore we assign this result to the systematic uncertainty due to the fit range, conservatively.

In order to estimate the overall systematic uncertainty due to the E_T^* correction, we sum all systematic uncertainties in a quadrature. The total systematic uncertainty is listed in Table 5.8. For the reference, we show the deviation of the result before E_T^* cor-

β range	$10 \leq E_T^* \leq 12$ GeV	$12 \leq E_T^* \leq 15$ GeV	$15 \leq E_T^* \leq 25$ GeV
$\boxed{E_T^{\rm Jet2} \geq 7 \text{ GeV}, E_T^* \geq 10 \text{ GeV}}$			
$3.2 \times 10^{-2} \leq \beta \leq 5.6 \times 10^{-2}$	-4.08%		
$5.6 \times 10^{-2} \leq \beta \leq 1.0 \times 10^{-1}$	-9.08%	-0.25%	-0.56%
$1.0 \times 10^{-1} \leq \beta \leq 1.8 \times 10^{-1}$	-5.22%	$+0.16\%$	-0.72%
$1.8 \times 10^{-1} \leq \beta \leq 3.2 \times 10^{-1}$	-3.70%	-0.08%	-1.29%
$3.2 \times 10^{-1} \leq \beta \leq 5.6 \times 10^{-1}$	-4.85%	-0.95%	$+0.22\%$
$5.6 \times 10^{-1} \leq \beta \leq 1.0$	-7.55%	-2.29%	$+0.23\%$
$\boxed{E_T^{\rm Jet2} > 0 \text{ GeV}, E_T^* \geq 10 \text{ GeV}}$			
$3.2 \times 10^{-2} \leq \beta \leq 5.6 \times 10^{-2}$	-3.58%		
$5.6 \times 10^{-2} \leq \beta \leq 1.0 \times 10^{-1}$	-2.72%	$+0.25\%$	$+0.13\%$
$1.0 \times 10^{-1} \leq \beta \leq 1.8 \times 10^{-1}$	-2.34%	$+0.09\%$	$+0.10\%$
$1.8 \times 10^{-1} \leq \beta \leq 3.2 \times 10^{-1}$	-1.43%	-0.26%	$+0.02\%$
$3.2 \times 10^{-1} \leq \beta \leq 5.6 \times 10^{-1}$	-0.51%	-0.58%	-0.09%
$5.6 \times 10^{-1} \leq \beta \leq 1.0$	-0.10%	-0.40%	-0.05%

Table 5.5: Deviations of the results changing the second jet E_T threshold from the standard result.

β range	$10 \leq E_T^* \leq 12$ GeV	$12 \leq E_T^* \leq 15$ GeV	$15 \leq E_T^* \leq 25$ GeV
$3.2 \times 10^{-2} \leq \beta \leq 5.6 \times 10^{-2}$	-7.40%		
$5.6 \times 10^{-2} \leq \beta \leq 1.0 \times 10^{-1}$	-9.44%	-0.30%	-0.34%
$1.0 \times 10^{-1} \leq \beta \leq 1.8 \times 10^{-1}$	-4.93%	$+0.85\%$	-0.97%
$1.8 \times 10^{-1} \leq \beta \leq 3.2 \times 10^{-1}$	-7.90%	$+0.65\%$	-2.31%
$3.2 \times 10^{-1} \leq \beta \leq 5.6 \times 10^{-1}$	-11.7%	-0.45%	-3.14%
$5.6 \times 10^{-1} \leq \beta \leq 1.0$	-8.46%	-2.74%	-4.22%

Table 5.6: Deviations of the results with the power law fit function from the standard result.

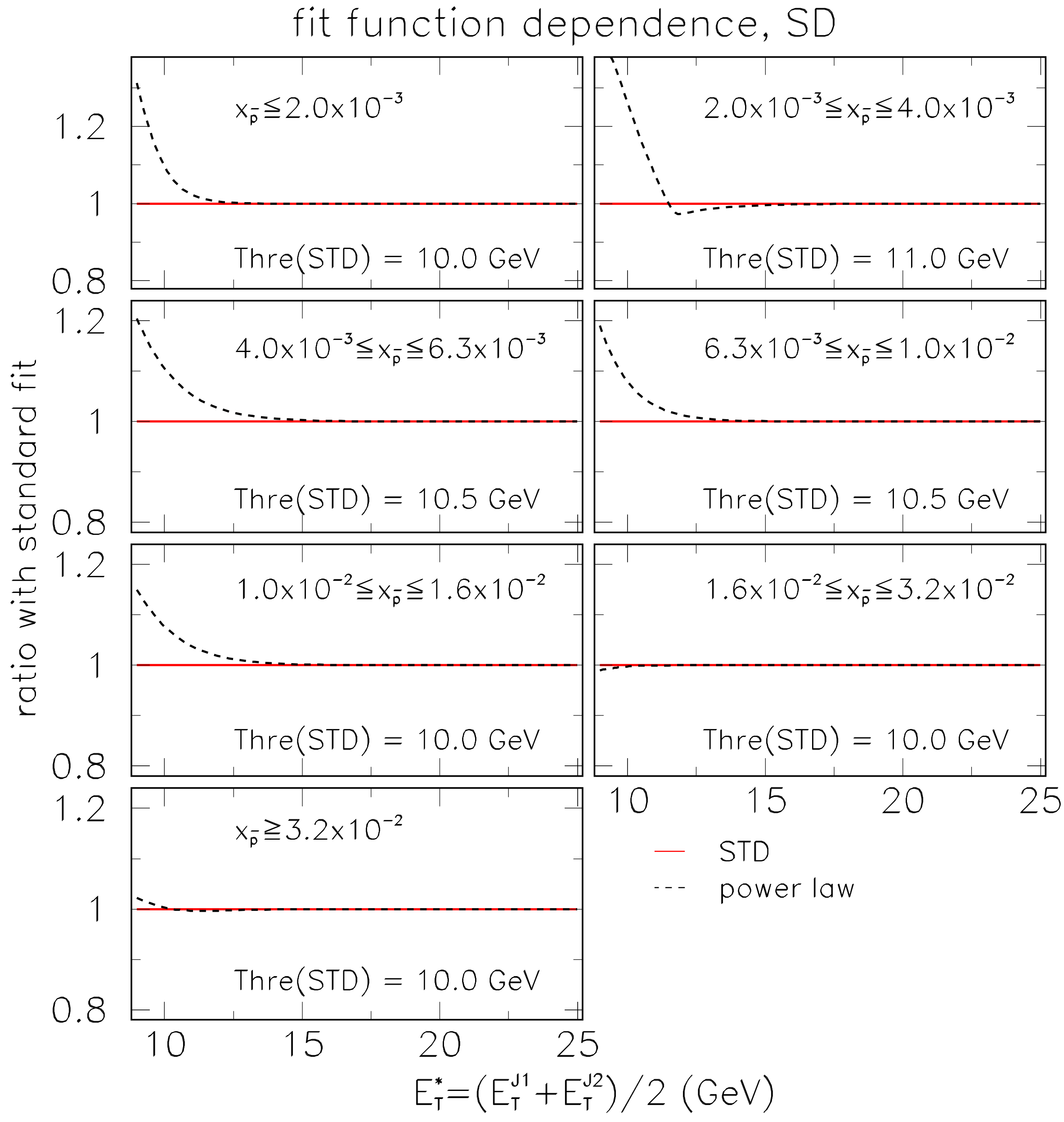

Figure 5.4: E_T^* correction factor estimated by the power law fit as a function of E_T^* relative to the standard fit in various $x_{\overline{p}}$ ranges for diffractive dijet data.

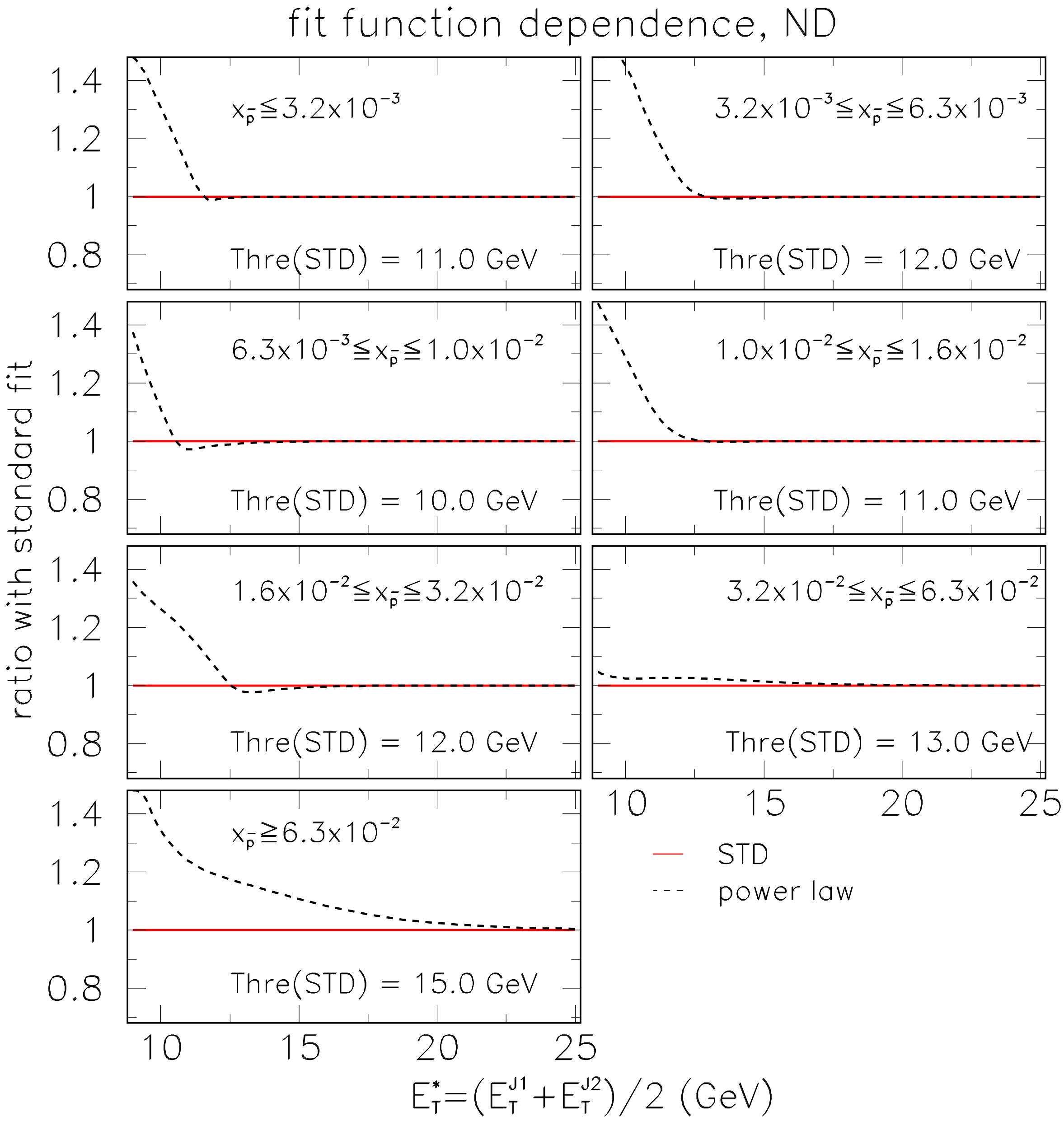

Figure 5.5: E_T^* correction factor estimated by the power law fit as a function of E_T^* relative to the standard fit in various $x_{\overline{p}}$ ranges for non-diffractive dijet data.

rection from that after E_T^* correction in Table 5.9. The obtained systematic uncertainty due to the E_T^* correction is comparable to the magnitude of the E_T^* correction.

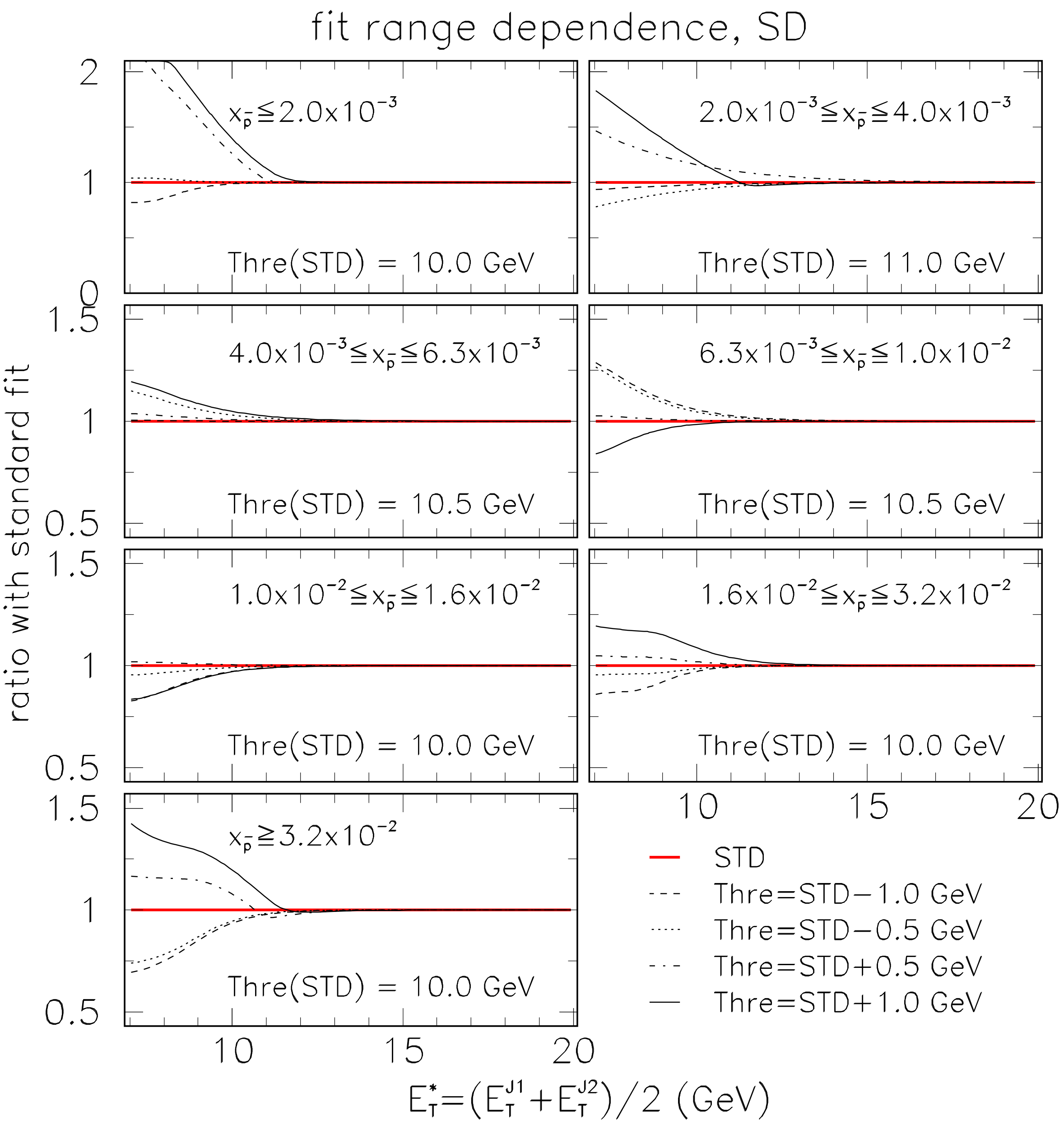

Figure 5.6: Relative deviations of the E_T^* correction factor with various fit ranges from the standard fit as a function of E_T^* in various $x_{\overline{p}}$ ranges for diffractive dijet data.

Total independent systematic uncertainty

We sum all systematic uncertainties in a quadrature. The total independent systematic uncertainty is listed in Table 5.10.

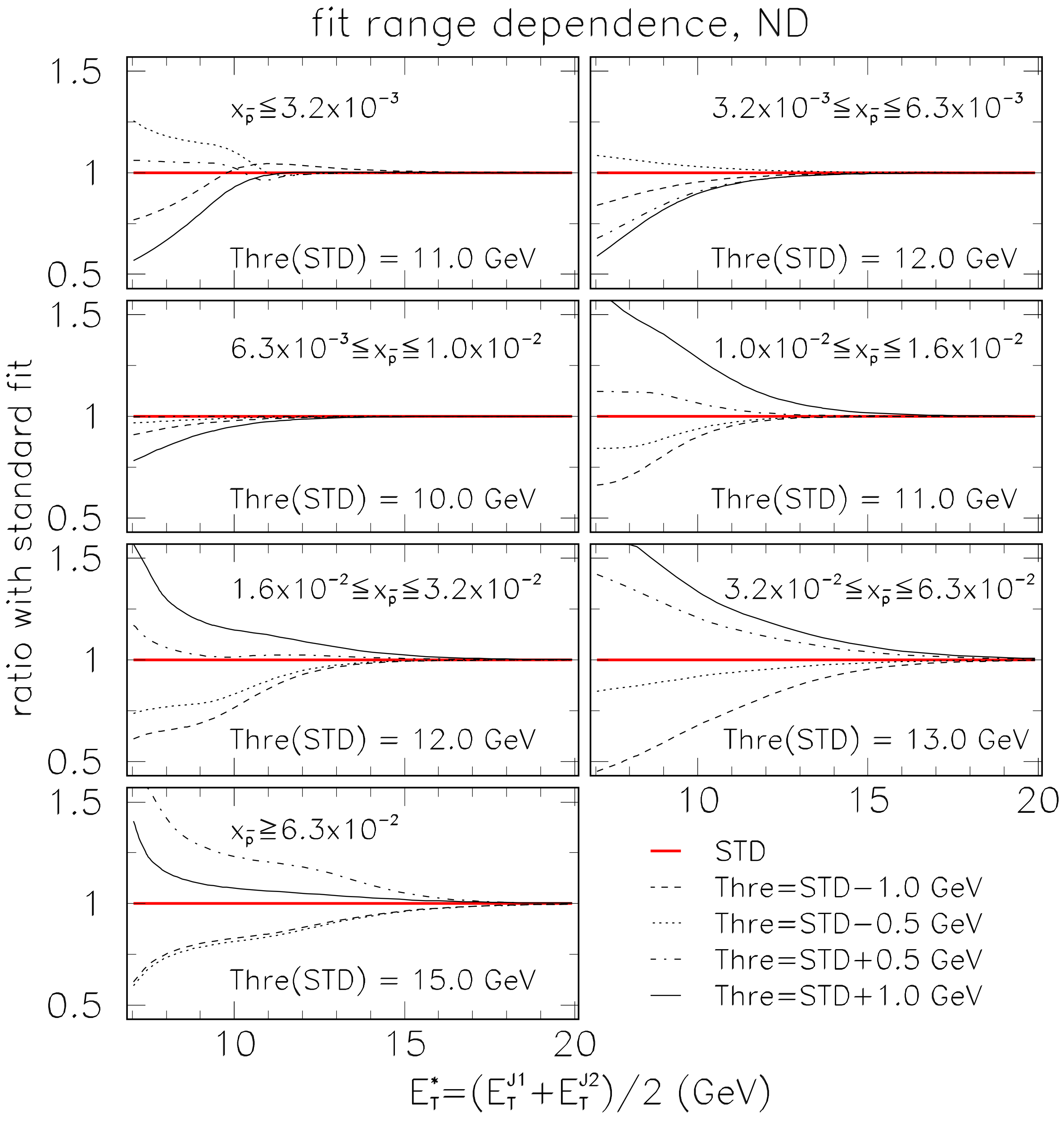

Figure 5.7: Relative deviations of the E_T^* correction factor with various fit ranges from the standard fit as a function of E_T^* in various $x_{\overline{p}}$ ranges for non-diffractive dijet data.

β range	$10 \leq E_T^* \leq 12$ GeV	$12 \leq E_T^* \leq 15$ GeV	$15 \leq E_T^* \leq 25$ GeV
$\boxed{\text{SD:+max, ND:+max}}$			
$3.2 \times 10^{-2} \leq \beta \leq 5.6 \times 10^{-2}$	+6.18%		
$5.6 \times 10^{-2} \leq \beta \leq 1.0 \times 10^{-1}$	+3.00%	−0.70%	−0.16%
$1.0 \times 10^{-1} \leq \beta \leq 1.8 \times 10^{-1}$	−1.33%	−0.82%	−0.14%
$1.8 \times 10^{-1} \leq \beta \leq 3.2 \times 10^{-1}$	−9.32%	−3.81%	−0.58%
$3.2 \times 10^{-1} \leq \beta \leq 5.6 \times 10^{-1}$	−10.7%	−7.00%	−1.47%
$5.6 \times 10^{-1} \leq \beta \leq 1.0$	−11.8%	−10.1%	−2.47%
$\boxed{\text{SD:+max, ND:−max}}$			
$3.2 \times 10^{-2} \leq \beta \leq 5.6 \times 10^{-2}$	+13.5%		
$5.6 \times 10^{-2} \leq \beta \leq 1.0 \times 10^{-1}$	+11.0%	+0.93%	+0.01%
$1.0 \times 10^{-1} \leq \beta \leq 1.8 \times 10^{-1}$	+7.94%	+1.63%	+0.15%
$1.8 \times 10^{-1} \leq \beta \leq 3.2 \times 10^{-1}$	+12.0%	+2.15%	+0.14%
$3.2 \times 10^{-1} \leq \beta \leq 5.6 \times 10^{-1}$	+26.6%	+5.92%	+0.62%
$5.6 \times 10^{-1} \leq \beta \leq 1.0$	+38.8%	+9.61%	+1.44%
$\boxed{\text{SD:−max, ND:+max}}$			
$3.2 \times 10^{-2} \leq \beta \leq 5.6 \times 10^{-2}$	−5.75%		
$5.6 \times 10^{-2} \leq \beta \leq 1.0 \times 10^{-1}$	−4.08%	−1.00%	−0.17%
$1.0 \times 10^{-1} \leq \beta \leq 1.8 \times 10^{-1}$	−4.76%	−1.43%	−0.19%
$1.8 \times 10^{-1} \leq \beta \leq 3.2 \times 10^{-1}$	−12.6%	−4.31%	−0.60%
$3.2 \times 10^{-1} \leq \beta \leq 5.6 \times 10^{-1}$	−16.1%	−7.36%	−1.47%
$5.6 \times 10^{-1} \leq \beta \leq 1.0$	−19.9%	−10.1%	−2.46%
$\boxed{\text{SD:−max, ND:−max}}$			
$3.2 \times 10^{-2} \leq \beta \leq 5.6 \times 10^{-2}$	+7.52%		
$5.6 \times 10^{-2} \leq \beta \leq 1.0 \times 10^{-1}$	+3.39%	+0.63%	-0.00_2%
$1.0 \times 10^{-1} \leq \beta \leq 1.8 \times 10^{-1}$	+4.25%	+1.02%	+0.11%
$1.8 \times 10^{-1} \leq \beta \leq 3.2 \times 10^{-1}$	+7.91%	+1.62%	+0.12%
$3.2 \times 10^{-1} \leq \beta \leq 5.6 \times 10^{-1}$	+18.6%	+5.51%	+0.61%
$5.6 \times 10^{-1} \leq \beta \leq 1.0$	+26.0%	+9.70%	+1.45%

Table 5.7: Systematic uncertainty due to the fit range.

β range	$10\leq E_T^* \leq 12$ GeV	$12\leq E_T^* \leq 15$ GeV	$15\leq E_T^* \leq 25$ GeV
$3.2\times10^{-2}\leq\beta\leq5.6\times10^{-2}$	$\pm16.3\%$		
$5.6\times10^{-2}\leq\beta\leq1.0\times10^{-1}$	$\pm17.3\%$	$\pm1.0\%$	$\pm0.7\%$
$1.0\times10^{-1}\leq\beta\leq1.8\times10^{-1}$	$\pm11.0\%$	$\pm1.8\%$	$\pm1.2\%$
$1.8\times10^{-1}\leq\beta\leq3.2\times10^{-1}$	$\pm14.9\%$	$\pm2.3\%$	$\pm2.6\%$
$3.2\times10^{-1}\leq\beta\leq5.6\times10^{-1}$	$\pm29.5\%$	$\pm6.0\%$	$\pm3.2\%$
$5.6\times10^{-1}\leq\beta\leq1.0$	$\pm40.4\%$	$\pm10.3\%$	$\pm4.5\%$

Table 5.8: Total systematic uncertainty due to the E_T^* correction.

β range	$10\leq E_T^* \leq 12\,$GeV	$12\leq E_T^* \leq 15\,$GeV	$15\leq E_T^* \leq 25\,$GeV
$3.2\times10^{-2}\leq\beta\leq5.6\times10^{-2}$	-2.06%		
$5.6\times10^{-2}\leq\beta\leq1.0\times10^{-1}$	-2.92%	-0.64%	-0.44%
$1.0\times10^{-1}\leq\beta\leq1.8\times10^{-1}$	-4.24%	-1.05%	-0.43%
$1.8\times10^{-1}\leq\beta\leq3.2\times10^{-1}$	-9.62%	-1.91%	-0.38%
$3.2\times10^{-1}\leq\beta\leq5.6\times10^{-1}$	-24.5%	-7.01%	-0.85%
$5.6\times10^{-1}\leq\beta\leq1.0$	-37.6%	-13.3%	-1.87%

Table 5.9: Deviation of the result before E_T^* correction from that after E_T^* correction ($dev = \{STD - NOCR\}/NOCR$). The result indicates the magnitude of E_T^* correction effect in each bin.

β range	$10\leq E_T^* \leq 12$ GeV	$12\leq E_T^* \leq 15$ GeV	$15\leq E_T^* \leq 25$ GeV
$3.2\times10^{-2}\leq\beta\leq5.6\times10^{-2}$	$\pm20.2\%$		
$5.6\times10^{-2}\leq\beta\leq1.0\times10^{-1}$	$\pm20.8\%$	$\pm11.6\%$	$\pm11.1\%$
$1.0\times10^{-1}\leq\beta\leq1.8\times10^{-1}$	$\pm15.9\%$	$\pm11.7\%$	$\pm11.1\%$
$1.8\times10^{-1}\leq\beta\leq3.2\times10^{-1}$	$\pm18.8\%$	$\pm11.8\%$	$\pm11.4\%$
$3.2\times10^{-1}\leq\beta\leq5.6\times10^{-1}$	$\pm31.6\%$	$\pm13.1\%$	$\pm11.5\%$
$5.6\times10^{-1}\leq\beta\leq1.0$	$\pm42.0\%$	$\pm15.5\%$	$\pm11.9\%$

Table 5.10: Total independent systematic uncertainty.

5.2.3 Comparison of this result with the H1 results

The diffractive structure function as a function of β with the systematic uncertainty and the statistical uncertainty is shown in Figure 5.8. The solid points show the diffractive dijet events with $10 \leq E_T^* \leq 12$ GeV, the open circles show that with $12 \leq E_T^* \leq 15$ GeV, and the stars show that with $15 \leq E_T^* \leq 25$ GeV. Note that the solid points (stars) are 10% shifted toward the negative (positive) β direction. The solid curve shows the prediction according to the QCD evolution fit result from the H1 Collaboration [25]. The prediction curve is obtained by extrapolating Q^2 up to 167.2 GeV^2 using the H1 leading order fit-3 result (This extrapolation is the H1 preliminary [51]). The dashed curve shows that with $Q^2 = 266.2$ GeV^2, and the dotted curve shows that with $Q^2 = 503.3$ GeV^2. And the diffractive structure function of the antiproton with the systematic uncertainty and the statistical uncertainty is shown in Figure 5.9. The diffractive structure function of the antiproton has no Q^2 dependence. This is consistent with the H1 result [25]. However, the absolute value of the diffractive structure function measured at CDF is smaller than that of the H1 result by a factor of 7 as shown in Figure 5.8. The discrepancy is observed in the other results from CDF [23, 24].

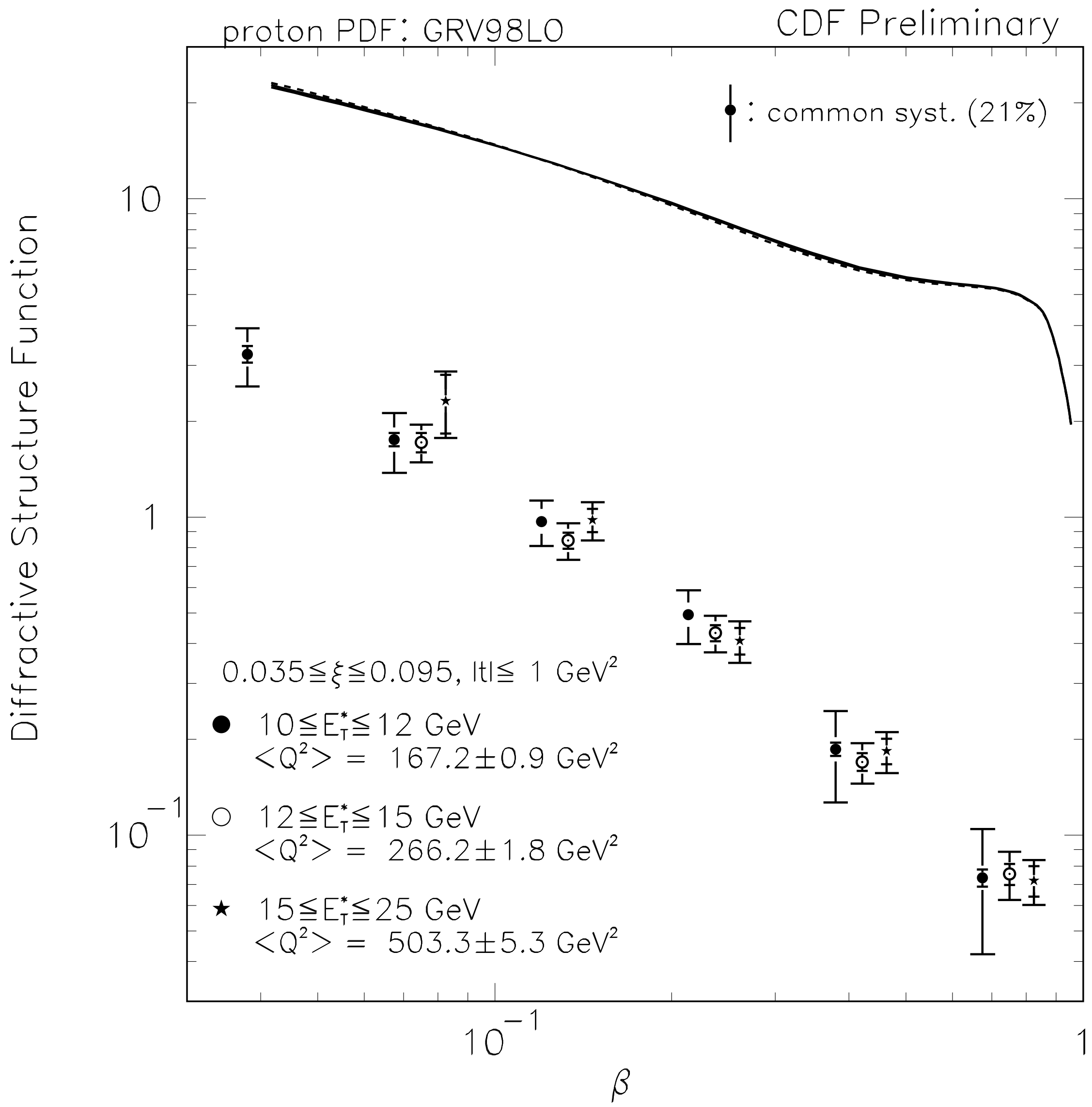

Figure 5.8: Diffractive structure function as a function of β. The solid points show β distribution in the E_T^* region of $10 \leq E_T^* \leq 12\,\text{GeV}$. Note that the distribution is 10% shifted toward the negative β direction. The open circles show that in E_T^* region of $12 \leq E_T^* \leq 15\,\text{GeV}$ (no shift). The star show that in E_T^* region of $15 \leq E_T^* \leq 25\,\text{GeV}$ (+10% shifted). The inner error bar shows the statistical uncertainty only, and the outer error bar shows the quaduratic sum of statistical uncertainty and the independent systematic uncertainty. The extra common systematic uncertainty (21%) is shown in the top-right of the plot. The solid curve shows the prediction according to the QCD evolution fit result from the H1 Collaboration [25]. The prediction curve is obtained by extrapolating Q^2 up to 167.2 GeV^2 using the H1 leading order fit-3 result (This extrapolation is the H1 preliminary [51]). The dashed curve shows that with $Q^2 = 266.2$ GeV^2, and the dotted curve shows that with $Q^2 = 503.3$ GeV^2.

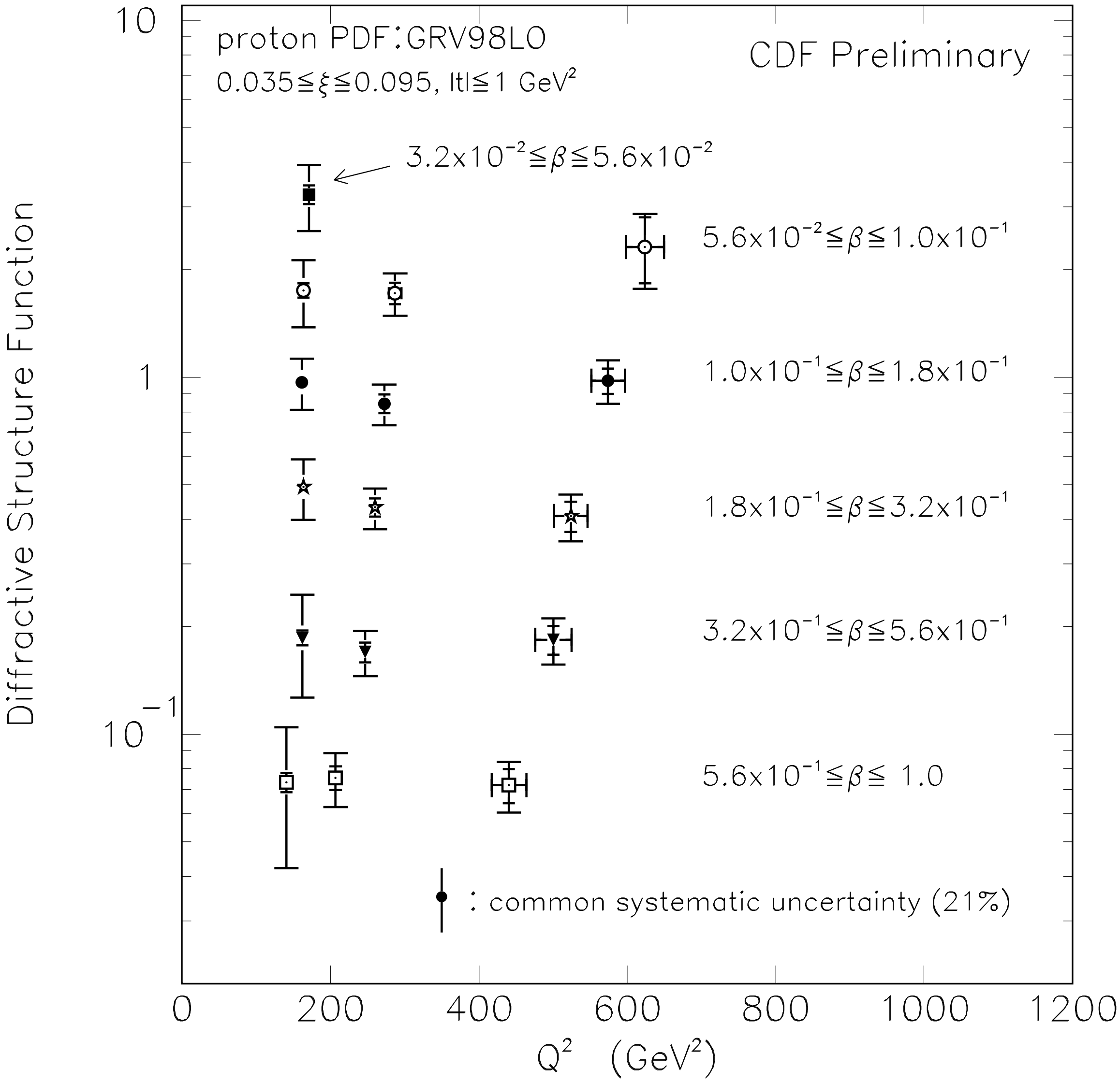

Figure 5.9: Diffractive structure function as a function of (β, Q^2). The inner error bar shows the statistical uncertainty only, and the outer error bar shows the quadratic sum of statistical uncertainty and the independent systematic uncertainty. The extra common systematic uncertainty (21%) is shown in the bottom of the plot.

Chapter 6

Conclusion

We collected events with a recoil antiproton in the final state in proton-antiproton collisions at the center-of-mass energy of 1.8 TeV with the CDF detector during 1995 and 1996. We selected the diffractive events in the kinematical region of $0.035 \leq \xi \leq 0.095$ and $|t| \leq 1.0\,\mathrm{GeV}^2$ by tagging the recoil $\bar{p}$ with a Roman-pot type antiproton spectrometer (RPS), and detecting a rapidity gap with the forward calorimeter and the beam-beam counter. In addition we identified a hard collision, by requiring two or more jets with $E_T \geq 5$ GeV and the average E_T of the leading two jets to be larger than 10 GeV.

For the diffractive dijet events, we measured the distributions of several kinematical variables (ξ, t, average E_T, Q^2, average pseudorapidity, and azimuthal angle difference of leading two jets). The diffractive dijet system was found to be boosted against the recoil $\overline{p}$ direction much more than the non-diffractive dijet system. The dijets in the diffractive events were found to be more back-to-back than those in the non-diffractive ones.

We also measured the cross section ratio of the diffractive to the non-diffractive dijet production as a function of the average E_T of the leading two jets, and also as a function of $x_{\overline{p}}$. The cross section ratio of the diffractive to the non-diffractive dijet production is almost constant in the whole average E_T region. above 10 GeV.

We measured the diffractive structure function of the antiproton as a function of β and Q^2 in the kinematic region of $0.035 \leq \xi \leq 0.095$ and $|t| \leq 1$ GeV^2. We found it had no Q^2 dependence in the Q^2 region measured in this study. This is consistent with the H1 result in diffractive deep inelastic scattering processes. The absolute value of the diffractive structure function measured at CDF is smaller than that of the H1 result by, approximately, a factor of 1/7. The discrepancy is also observed in other results at CDF such as the diffractive W boson and b-quark production where the cross section is about 20% of the prediction using the DL pomeron flux. These results suggest that the diffractive cross section is not described by using the universal diffractive structure function of the antiproton. One of possible explanation of the observed discrepancy is due to the pomeron flux based on the Regge theory.

Bibliography

[1] F. Abe *et al.*, (The CDF Collaboration), Phys. Rev. Lett. **77**, 438–443 (1996).

[2] F. Abe *et al.*, (The CDF Collaboration), Phys. Rev. D **54**, 4221–4233 (1996).

[3] F. Abe *et al.*, (The CDF Collaboration), Phys. Rev. Lett. **73**, 2662–2666 (1994), Erratum-ibid. **74**, 1891–1893 (1995).

[4] F. Abe *et al.*, (The CDF Collaboration), Phys. Rev. Lett. **81**, 1367–1372 (1998).

[5] F. Abe *et al.*, (The CDF Collaboration), Phys. Rev. Lett. **73**, 2296–2300 (1994).

[6] P. D. Collins, "An Introduction to Regge Theory and High-Energy Physics", *Cambridge University Press* (1977).

[7] A. Donnachie, P. V. Landshoff, Phys. Lett. B **296**, 227 (1992).

[8] J. R. Cudell *et al.*, Phys. Rev. D **61**, 034019 (2000).

[9] V. N. Gribov, JETP Lett. **41**, 667 (1961).

[10] M. L. Good and W. D. Walker, Phys. Rev. **120**, 1857 (1960).

[11] A. Donnachie, P. V. Landshoff, Phys. Lett. B **191**, 309 (1987),
A. Donnachie, P. V. Landshoff, Nucl. Phys. **B303**, 634 (1988).

[12] R. L. Cool *et al.*, (Fermilab E396 experiment), Phys. Rev. Lett. **47**, 701 (1981).

[13] M. G. Albrow *et al.*, (CHLM Collaboration), Nucl. Phys. **B108**, 1 (1976).

[14] J. C. M. Armitage *et al.*, (CERN-R207 experiment), Nucl. Phys. **B194**, 365 (1982).

[15] D. Bernard *et al.*,(UA4 Collaboration), Phys. Lett. B **186**, 227 (1987).

[16] F. Abe *et al.*, (The CDF Collaboration), Phys. Rev. D **50**, 5535 (1994).

[17] K. Goulianos, hep-ph/9806363, (1998),
K. Goulianos, J. Montanha, Phys. Rev. D **59**, 114017 (1999).

[18] S. Erhan, P. Schlein, Phys. Lett. B **427**, 389 (1998),
Erratum, Phys. Lett. B **445**, 455 (1999),
S. Erhan, P. Schlein, Phys. Lett. B **481**, 177 (2000).

[19] Chung-I Tan, hep-ph/9706276, (1997).

[20] G. Ingelman and P. Schlein, Phys. Lett. B **152**, 256 (1985).

[21] R. Bonino *et al.*, (UA8 Collaboration), Phys. Lett. B **211**, 239 (1988).

[22] M. Derrick *et al.*, (The ZEUS Collaboration), Phys. Lett. B **356**, 129 (1995).

[23] F. Abe *et al.*, (The CDF Collaboration), Phys. Rev. Lett. **78**, 2698 (1997).

[24] T. Affolder *et al.*, (The CDF Collaboration), "Observation of Diffractive Beauty Production at the Fermilab Tevatron", Phys. Rev. Lett. **84**, 232 (2000).

[25] C. Adloff *et al.*, (The H1 Collaboration), Z. Phys. C **76** 613 (1997).

[26] M. Derrick *et al.*, (The ZEUS Collaboration), Euro. Phys. J. C **6** 43 (1999).

[27] The Hard Diffraction Group of CDF, "Proposal for Hard Diffraction Studies in CDF", CDF-2940 (Aug,1995).

[28] T. Affolder *et al.*, (The CDF Collaboration), "Diffractive Dijets with a Leading Antiproton in $p\overline{p}$ Collisions at $\sqrt{s} = 1800$ GeV", Phys. Rev. Lett. **84**, 5043 (2000).

[29] C. Royon *et al.*, hep-ph/0010015, Submitted to Phys. Rev. D.

[30] M. Gluck *et al.*, Eur. Phys. J. C **5**, 461–470 (1998).

[31] The CDF Collaboration, F. Abe *et al.*, Nucl. Instrum. Methods Phys. Res., Sect. **A271**, 387–403 (1988), and references therein.

[32] F. Abe *et al.*, (The CDF Collaboration), Phys. Rev. D **45**, 2249–2263 (1992).

[33] D. Amidei *et al.*, Nucl. Instrum. Methods Phys. Res., Sect. **A350**, 73 (1994).

[34] F. Bedeschi *et al.*, Nucl. Instrum. Methods Phys. Res., Sect. **A268**, 50–74 (1988).

[35] L. Balka *et al.*, Nucl. Instrum. Methods Phys. Res., Sect. **A267**, 272–279 (1988).

[36] S. Bertolucci *et al.*, Nucl. Instrum. Methods Phys. Res., Sect. **A267**, 301–314 (1988).

[37] Y. Fukui *et al.*, Nucl. Instrum. Methods Phys. Res., Sect. **A267**, 280–300 (1988).

[38] C. Haber *et al.* : "Performance and Calibration Studies of the CDF Endplug Hadronic Calorimeter", Published Proceedings of 1985 Gas Sampling Calorimetry, Batavia, 1985.

[39] Y. Fukui *et al.*, Nucl. Instrum. Methods Phys. Res., Sect. **A267**, 280–300 (1988).

[40] S. Cihangir *et al.*, Nucl. Instrum. Methods Phys. Res., Sect. **A267**, 249–256 (1988).

[41] F. Abe *et al.*, (The CDF Collaboration), Phys. Rev. D **50**, 5550 (1994).

[42] F. Abe *et al.*, (The CDF Collaboration), Phys. Rev. D **50**, 5518 (1994).

[43] F. Abe *et al.*, (The CDF Collaboration), "Measurement of $\sigma B(W \to e\nu)$ and $\sigma B(Z^0 \to e^+e^-)$ in $p\bar{p}$ Collisions at $\sqrt{s}$=1.8 TeV", Phys. Rev. Lett. **76**, 3070 (1996).

[44] F. Abe *et al.*, The CDF Collaboration, Phys. Rev. D **45**, 1448–1458 (1992).

[45] ** Hosai Nakada, Koji Terashi, Ken-ichi Hatakeyama, "Study of Underlying Events in Diffractive Dijets", CDF note 4716 (V1.1), 12/9/1998.

[46] * L. Galtieri *et al.*, "How well do we understand jets in Run I? Study of the jet Energy Scale for Raw Jet $E_T \geq 8$ GeV", CDF note 3983.

[47] * Kerstin Borras *et al.*, "Update of the Studies of the Structure of the Pomeron with Roman Pot Dijet Events", CDF note 4920, 4/24/00.

[48] * A. Beretvas *et al.*, "Event Z Vertex Cut Efficiency as a Luminosity Correction for Run Ib", CDF note 5066.

The documents with the symbol "" are CDF internal notes.

[49] * B. Flaugher, "Efficiency of the 60 cm Z-vertex cut", CDF note 5094.

[50] * Daniel P. Cronin-Hennessy *et al.*, " Getting Your Luminosity", CDF note 4317, 9/15/97.

[51] F. Niebergall, (The H1 Collaboration), "Diffractive structure function measurements at HERA" 29th International Conference on High-Energy Physics, July 1998, Vancouver, Canada.

[52] D.C. Carey (Fermilab), K.L. Brown and F. Rothacker (SLAC), Fermilab-Pub-95/069.

[53] * Brenna Flaugher and Pat Lukens, "Positioning and Alignment of CDF for Run 1", CDF note 4637, June 12, 1998.

[54] F. Abe *et al.*, The CDF Collaboration, "B Hadron Lifetimes Using J/psi Final States at CDF", Phys. Rev. D **57**, 5382 (1998).

[55] V. Bharadwaj *et al.*, Fermilab, FERMILAB-TM-1970, (April 1996),
http://www-lib.fnal.gov/archive/1996/tm/TM-1970.html,
Gerry Jackson, Fermilab, FERMILAB-TM-1981 (July 1996),
http://www-lib.fnal.gov/archive/1996/tm/TM-1981.html.

Appendix A

RPS position calibration and its performance

A.1 Position calibration of RPS

It is important to know reliable positions of fiber-layers in the RPS. Therefore we calibrated the RPS positions (nominal position is 1.3cm away from $\overline{p}$ orbit). We compared the diffractive inclusive data to the pseudoexperiment based on Run-0 CDF measurement for the RPS hit occupancies, track parameters, and reconstructed ξ, t. In order to make the calibration;

- we improved the beam transportation calculation using a second order transport matrix [52],
- we take account of the relation between the CDF coordinate system and accelerator coordinate system [53],
- we take account of the initial beam information in SVXBPO database, and
- we make a diffractive inclusive event generator and a RPS simulation.

A.1.1 Initial beam study

Before calibration, we studied characteristics of an initial beam. We measured average initial beam trajectories and their transverse profile by using SVX [54]. In case of high luminosity runs in Run-1B, the beam position variation was measured to be 22 μm [54]. It was corresponding to (95% normalized) transverse emittance $24.22\pi\,(\times 10^{-6}$m-radians) for proton and $12.70\pi\,(\times 10^{-6}$m-radians) for antiproton*[55].

According to accelerator division, the maximum width of the $\overline{p}$ is 85 μm, and the maximum angular spread is 0.24 milli-radians.

In this study, we use the diffractive trigger data, and require at least four 3-D tracks with four hits in the SVX. We show the results of this study in Figures A.1–A.2.

From the results, we obtained the averaged beam position variation to be 47.4 μm as one standard deviation of Gaussian. Since we cannot measure beam angular spread, we assigned one standard deviation of it to be 0.133 $(= 0.24 \times 47.4/85)$ milli-radians.

A.1.2 Beam transportation and ξ, t reconstruction

In general, a beam line is comprised of a set of magnetic elements placed sequentially at intervals along an assumed reference trajectory. The reference trajectory is the path of a particular charged particle with the central design momentum p_0, passing through idealized magnets. A position and an angle of the beam is described by a displacement and an angle from the reference trajectory [52]. When a beam is transported from one of the place (A) to another (B), the coordinate system is defined as follows;

- The coordinate system is right-handed,
- The reference trajectory from A to B is the $+z$ axis, and
- The vertical up is y axis with positive pointing up, thus $+x$ axis is from right to left.

The beam position at B is described by the following formula;

$$X_i(\mathrm{B}) \;=\; X_{\mathrm{kick}} + \sum_j R_{ij} X_j(\mathrm{A}) + \sum_{jk} T_{ijk} X_j(\mathrm{A}) X_k(\mathrm{A}), \tag{A.1}$$

*$\sigma^2 = \beta^* \frac{\epsilon}{6\beta_\gamma\gamma_\gamma}, \beta^* = 0.35$ (m), $\beta_\gamma\gamma_\gamma = 959 \rightarrow \sigma_p = 38.4\,\mu\mathrm{m}, \sigma_{\bar{p}} = 27.8\,\mu\mathrm{m}$,
$\frac{1}{\sigma^2_{\mathrm{VTX}}} = \frac{1}{\sigma_p^2} + \frac{1}{\sigma_{\bar{p}}^2}, \rightarrow \sigma_{\mathrm{VTX}} = 22.5\,\mu\mathrm{m}$.

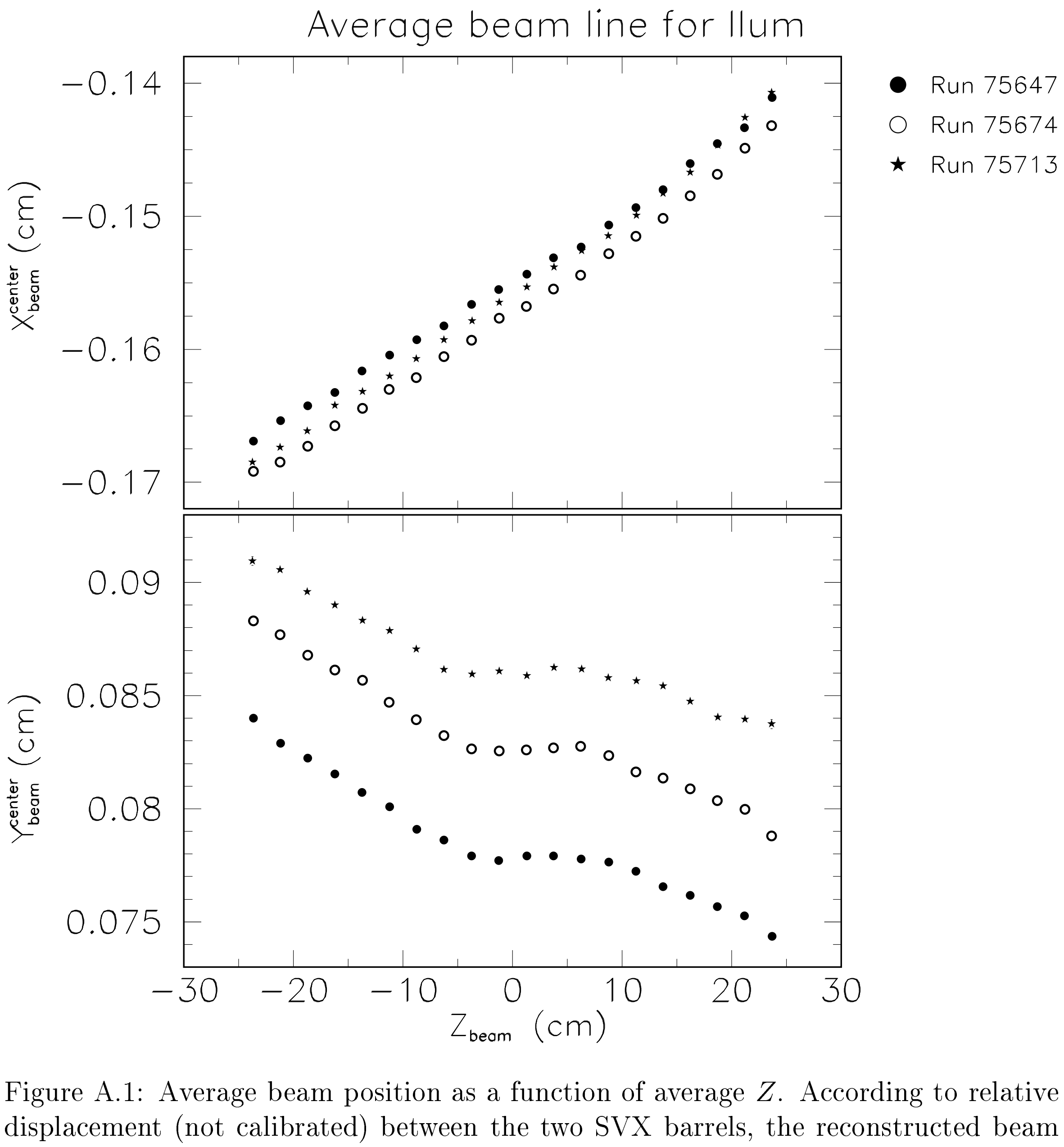

Figure A.1: Average beam position as a function of average Z. According to relative displacement (not calibrated) between the two SVX barrels, the reconstructed beam line is not on the straight line.

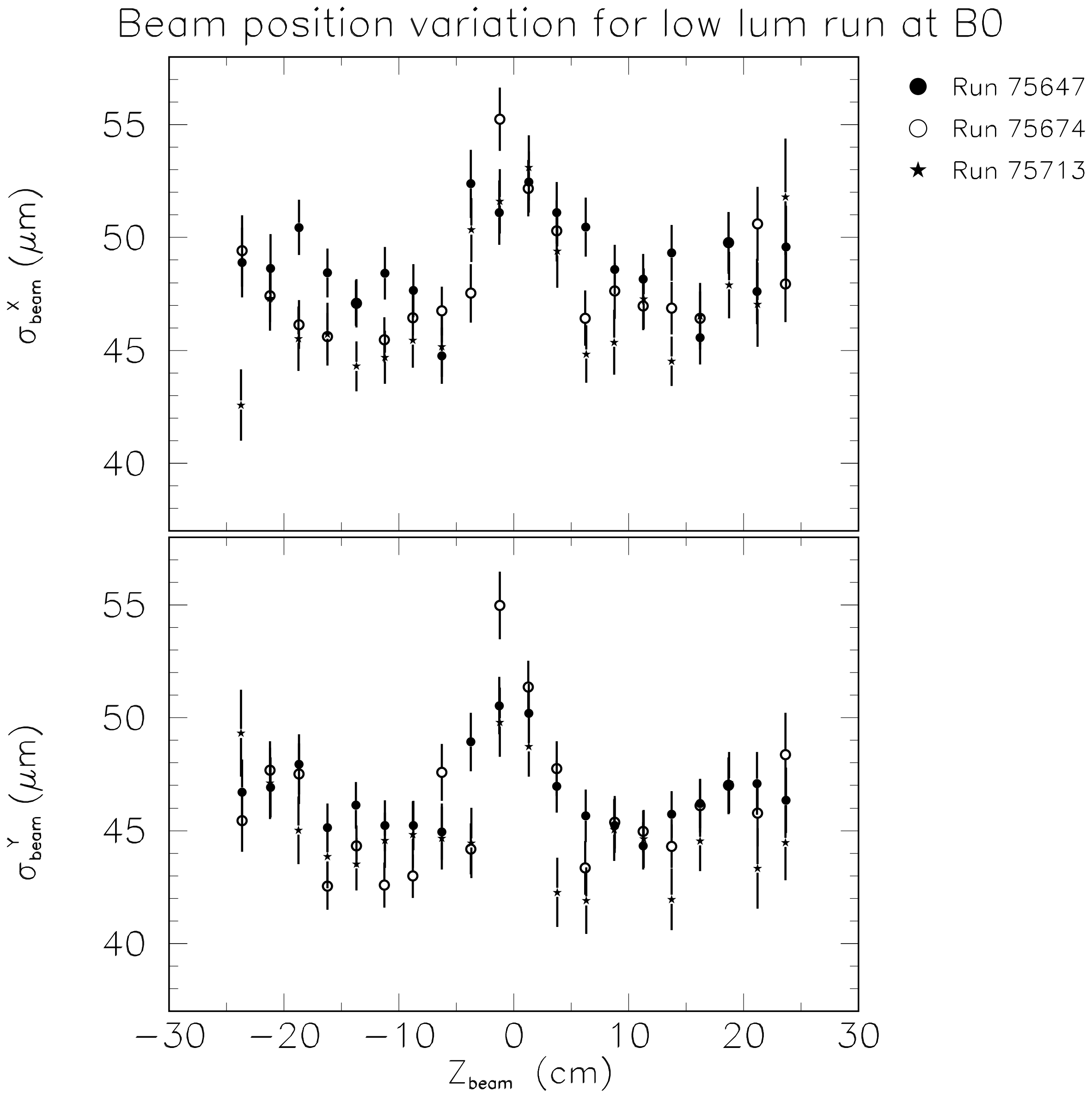

Figure A.2: Beam position variation as a function of average Z. This variation indicates beam width. According to relative displacement (not calibrated) between the two SVX barrels, the variation around $Z = 0$ becomes large.

$$X = \begin{pmatrix} x \\ dx/dz \\ y \\ dy/dz \\ l \\ \delta \end{pmatrix}, \tag{A.2}$$

$$\delta = \frac{(p_{final} - p_{init})}{p_{init}} = (-\xi), \tag{A.3}$$

where the $X_{\rm kick}$ is a vector of kicking effects from EM-separator, the R_{ij} and T_{ijk} are the first and second order transport matrices, the l is the path length difference between the arbitrary ray and the central trajectory, and the δ is the fractional momentum deviation of the ray from the assumed central trajectory.

In the Tevatron, the reference trajectory is the beam pipe center (the same as the z axis in the accelerator coordinate system). Since the positions of the CDF detector were measured just before Run-1A, we have the relation between the CDF coordinate system and the accelerator coordinate system [53]. We show the relation in Table A.1. Table A.2 shows the configuration of Tevatron elements. From the accelerator database, we obtain the transport matrices by using the program TRANSPORT [52]. The SVX detector can measure the transverse profile of the initial beam, and the VTX detector has about 2 cm position resolution along the z axis. We can get an initial beam information from the CDF database (SVXBPO). We show two sets of scatter plots for the averaged initial beam line in the Run-1C SVXBPO database in Figures A.3–A.4. The differences between these two sets of plots come from the CDF displacement. From this information, we can reproduce realistic recoil $\overline{p}$ orbits, and reconstruct kinematics of the recoil $\overline{p}$. ξ is obtained by using the above equations directly. For t, we can calculate it by using the angles of out-going recoil $\overline{p}$, dx/dz and dy/dz at CDF, and reconstructed ξ. Then t is defined by the following equation;

$$\begin{aligned} t &= (p_{\rm out} - p_{\rm in})^2, \qquad (A.4) \\ p_{\rm in} &= (E_{\rm in}, \vec{p}_{\rm in}), \text{ and} \\ p_{\rm out} &= (E_{\rm out}, \vec{p}_{\rm out}). \end{aligned}$$

From the Equation (A.4), we obtain the following equation;

$$t = 2m_{\overline{p}}^2 - 2E_{\rm in}E_{\rm out} + \frac{2|\vec{p}_{\rm in}||\vec{p}_{\rm out}|}{\sqrt{1 + \Delta(dx/dz)^2 + \Delta(dy/dz)^2}}, \tag{A.5}$$

where the $\Delta(dx/dz)$ and $\Delta(dy/dz)$ are defined by;

$$\begin{aligned}\Delta(dx/dz) &= (dx/dz)_{\mathrm{out}} - (dx/dz)_{\mathrm{in}}, \text{ and} \\ \Delta(dy/dz) &= (dy/dz)_{\mathrm{out}} - (dy/dz)_{\mathrm{in}}.\end{aligned}$$

	Offset	
X	0.6337	(mm)
dX/dZ	-0.4130	(milli-radian)
Y	-0.3420	(mm)
dY/dZ	0.0797	(milli-radian)

Table A.1: Magnitude of CDF displacement with respect to the accelerator coordinate system

A.1.3 Diffractive inclusive event simulation

We simulate the diffractive inclusive events according to the following procedure;

1. Decide an interaction point.
   (a) Generate Z position of an interaction point with $\sigma = 30.9\,\mathrm{cm}$.
   (b) Decide X, Y positions according to SVXBPO of the simulated run.
   (c) Optionally, smear the interaction point X and Y, and the beam angle by a spread of $\sigma^{\mathrm{beam}}_{\mathrm{spot}} = 47.4\,\mu\mathrm{m}$ and $\sigma^{\mathrm{beam}}_{\mathrm{angle}} = 0.133$ milli-radians.
   (d) Transform the interaction point and the beam line from the CDF coordinate system to the accelerator coordinate system.
2. Generate ξ, t, and ϕ, and calculate a four-momentum of the recoil $\overline{p}$.
   (a) ξ, t : According to the Run-0 CDF measurement [16].
   (b) ϕ : Uniform.
   (c) Save ξ, t and ϕ as $\xi_{\mathrm{GEN}}, \mathrm{t}_{\mathrm{GEN}}$ and ϕ_{GEN}.

Element	Effective length (m)	field
drift	7.633436	
quad	3.3528	Gradient = 1255.1807 (kGauss/m)
drift	0.8763	
quad	5.8928	Gradient = -1241.3511
drift	0.8763	
quad	3.3528	Gradient = 1255.1807
drift	1.413	
V-sep	2.57175	Voltage = 129.834 (kV), d = 0.05 (m)
drift	0.187	
V-sep	2.57175	Voltage = 129.834, d = 0.05
drift	0.187	
V-sep	2.57175	Voltage = 140.27, d= 0.05
drift	0.847	
corr. dipole	0.762	Kicking Angle = 0.00004410821 (radian)
		Tilt Angle = 0.7114591 (radian)
drift	0.847	
quad	1.402	Gradient = -24.9062
drift	0.307	
dipole	6.1214	Angle = 0.0081178101 (radian)
drift	0.2794	
dipole	6.1214	Angle = 0.0081178101
drift	0.2794	
dipole	6.1214	Angle = 0.0081178101
drift	2.185987	

Table A.2: Configuration of Tevatron accelerator elements from center of CDF detector to A48 Roman-pot1. The "drift" means a free drift space, the "quad" means a quadrupole magnet. The "V-sep" and the "H-sep" mean vertical and horizontal electrostatic separators. The "(corr.) dipole" means a (correction) dipole magnet.

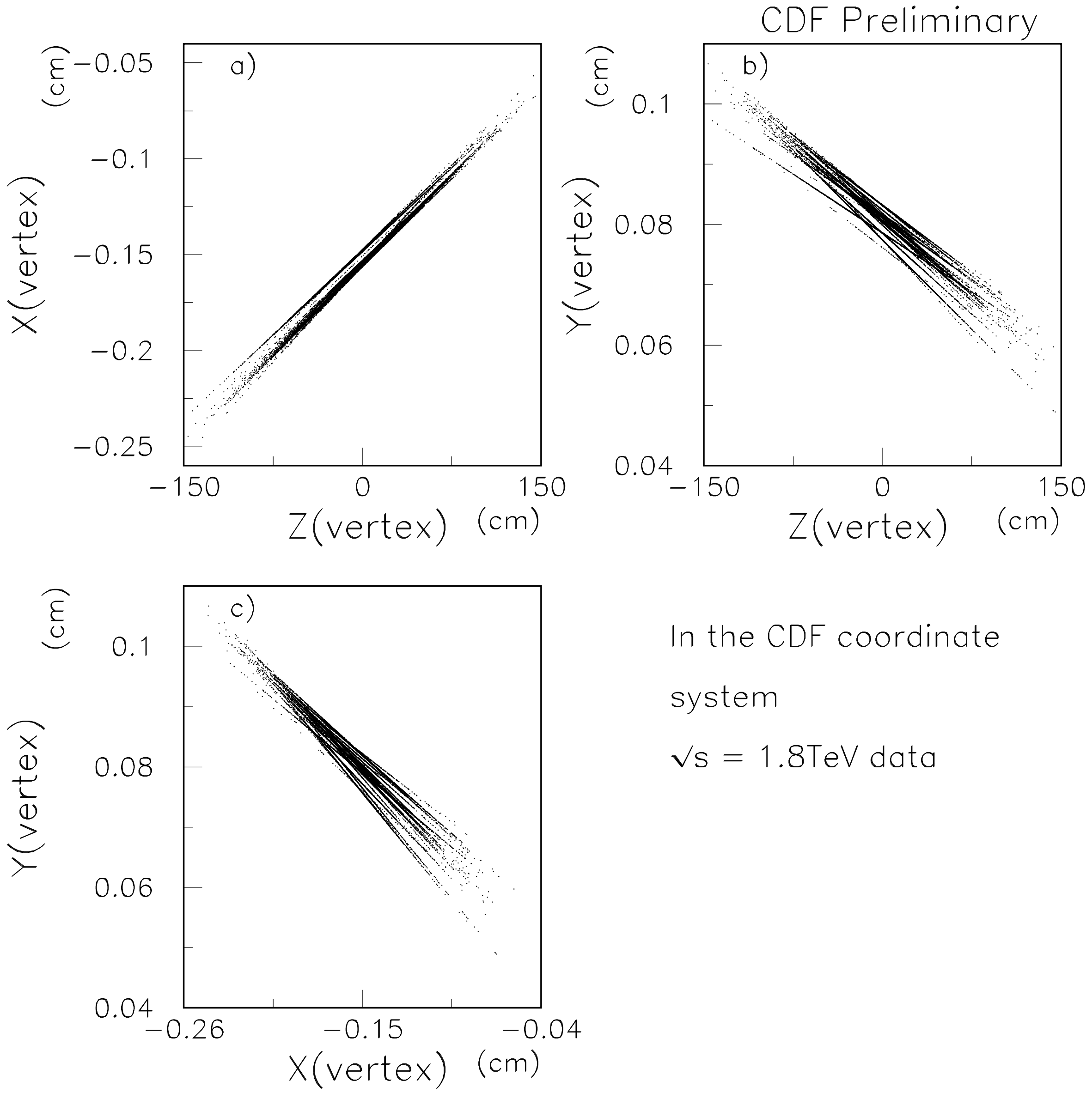

Figure A.3: The scatter plots show averaged beam lines during Run-1C in the CDF coordinate system. The dot shows an interaction point. The data were obtained from the SVXBPO database.

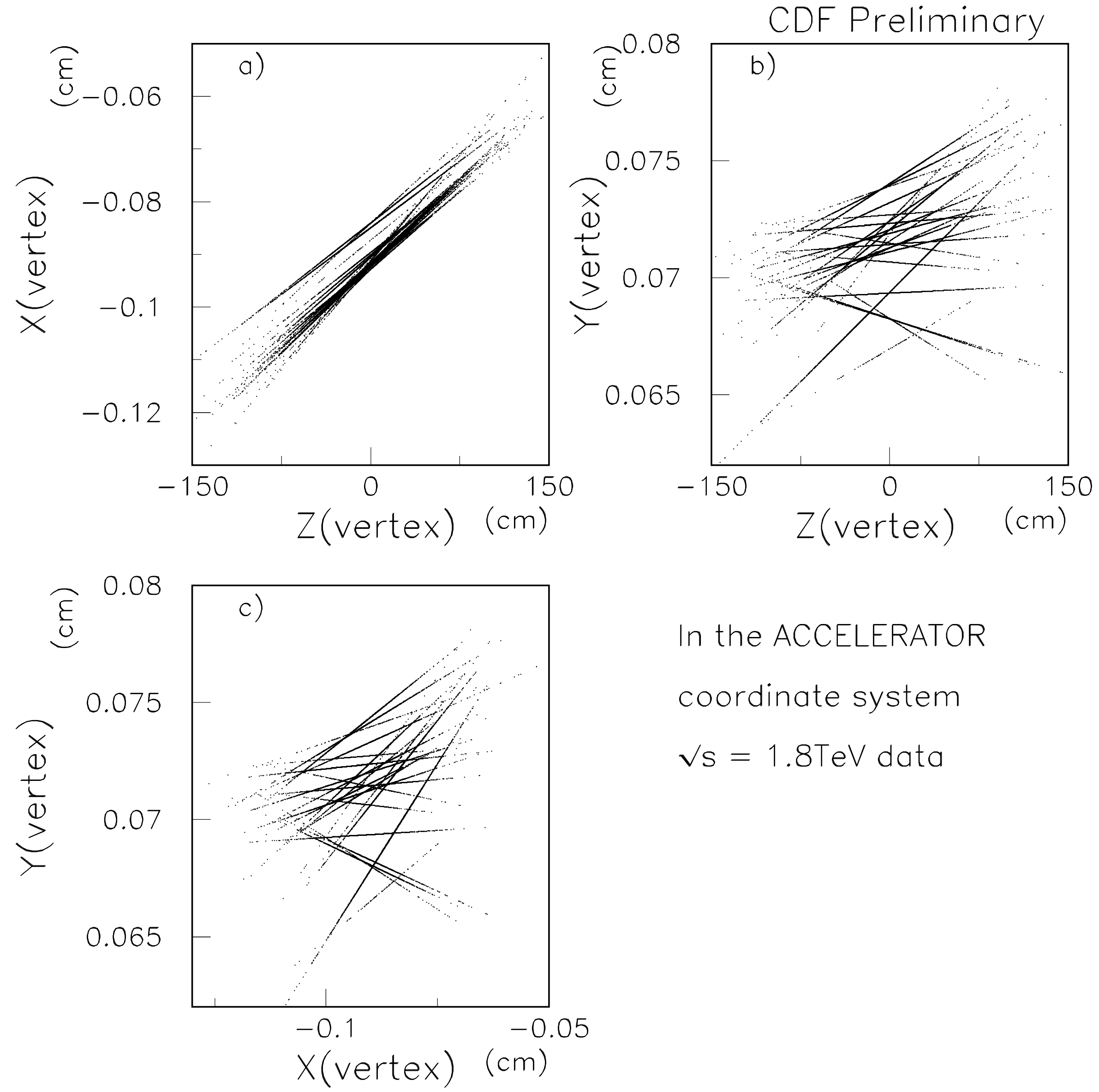

Figure A.4: The scatter plots show averaged beam lines during Run-1C in the accelerator coordinate system. The dot shows an interaction point. The data were obtained from the SVXBPO database.

3. Transport the recoil $\overline{p}$ to the RPS position and check whether it is in the RPS fiducial region.

4. Reconstruct ξ, t and ϕ, and save them as $\xi_{\mathrm{REC}}, \mathrm{t}_{\mathrm{REC}}$ and ϕ_{REC}.

5. Perform the RPS simulation.

6. Reconstruct ξ, t and ϕ, and save them as $\xi_{\mathrm{RPS}}, \mathrm{t}_{\mathrm{RPS}}$ and ϕ_{RPS}.

A.1.4 RPS simulation

A detecting part of the RPS consists of fiber sub-layers as shown in Figure 2.13 (precise description about the RPS structure is written in the subsection 2.2.7). We take account of the fiber layer structure in the simulation. First, we find the hit bins corresponding to the hit positions for X and Y at the three pots. Note that we simulate neither the exact fiber layer structure, nor hit finding efficiencies from the light yields. When we find a hit bin, we define the hit position as the center of the bin. Unfortunately, we had several dead channels (no response fibers), therefore we masked the bins corresponding to the dead channels. We listed the dead channel numbers in Table A.3.

Pot #	Dead fiber #	Dead bin #
Y axis		
Pot 1	11	20, 21, 22
Pot 1	39	76, 77, 78
Pot 2	6	10, 11, 12

Table A.3: List of dead bins corresponding to the dead fibers.

A.1.5 RPS position calibration

To compare the diffractive inclusive data with the RPS simulation data for the RPS hit occupancies, the track parameters, and the reconstructed ξ and t, we calibrate the RPS position. The calibration is performed in the following procedure;

1. At first, the RPS is assumed to be completely aligned.

2. Compare the diffractive inclusive data with the soft diffraction simulation.
   If we find a discrepancy, then goto 3
   If the simulation agrees well with the data , then finish the calibration.

3. Estimate the magnitude of the displacement.
   Changing the 3 pots positions by the magnitude of displacements, simulate the RPS responses.

4. Compare the diffractive inclusive data with the simulation.
   If we find a discrepancy, then goto 3
   If the simulation reproduces the data, then goto 5.

5. Data : Move the RPS positions, and re-select.
   Simulation : Move the RPS positions, and re-generate events. Compare the new data with the new simulation.
   If we find a discrepancy, then goto 3
   If the simulation agrees well with the data, then finish the calibration.

As the diffractive inclusive data, we used the events from the diffractive inclusive trigger sample, and additionally required the single vertex, the single track in the RPS, the SVXBPO available runs, and acceptance region in ξ and t ($0.035 \geq \xi \geq 0.095, |t| \leq 0.5\,\mathrm{GeV}^2$). Our diffractive trigger data were taken in Run-1C, mostly in low luminosity run. Therefore, we use fourteen low luminosity runs for the calibration. Shown in Figures A.5–A.8 are the distributions of the RPS hit occupancies, the track parameters, and ξ, t, and ϕ before any calibrations.

RPS detector length calibration

We first include the arm length information of the RPS detector. Because we found that the arms of three pots were 759, 764, and 764 μm shorter than design values.

Relative position calibration

Next, we calibrate the RPS detector position in each run. Moving the three RPS positions to each direction, we find the RPS best positions to make agreement. The

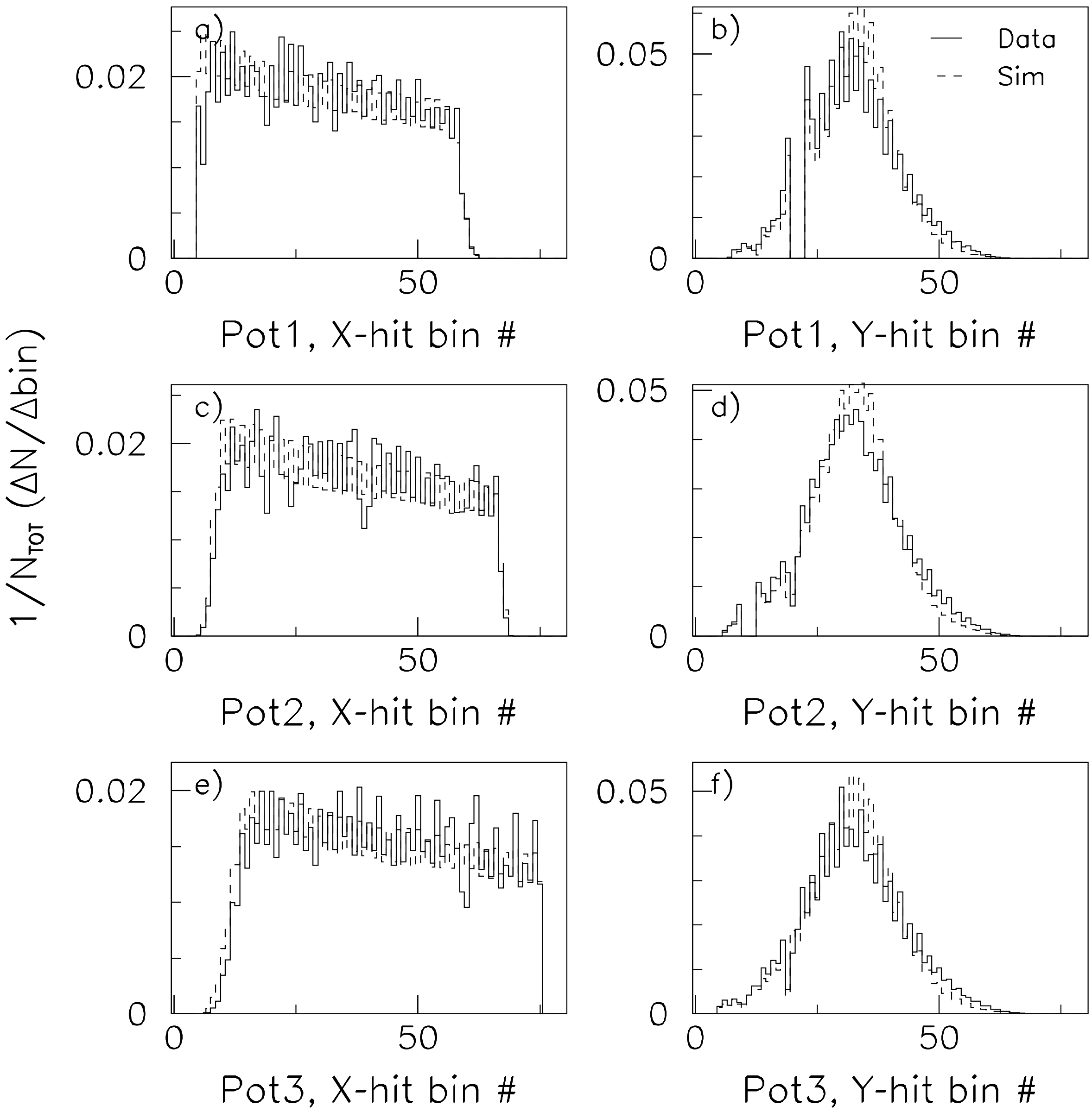

Figure A.5: The RPS hit occupancy distributions before RPS position correction for 14 low luminosity runs. The top two plots are for pot 1 X and Y, the middle plots are for pot 2, and the bottom plots are for pot 3. The solid line shows the diffractive inclusive data and the dashed line shows the diffractive inclusive simulation after the RPS simulation.

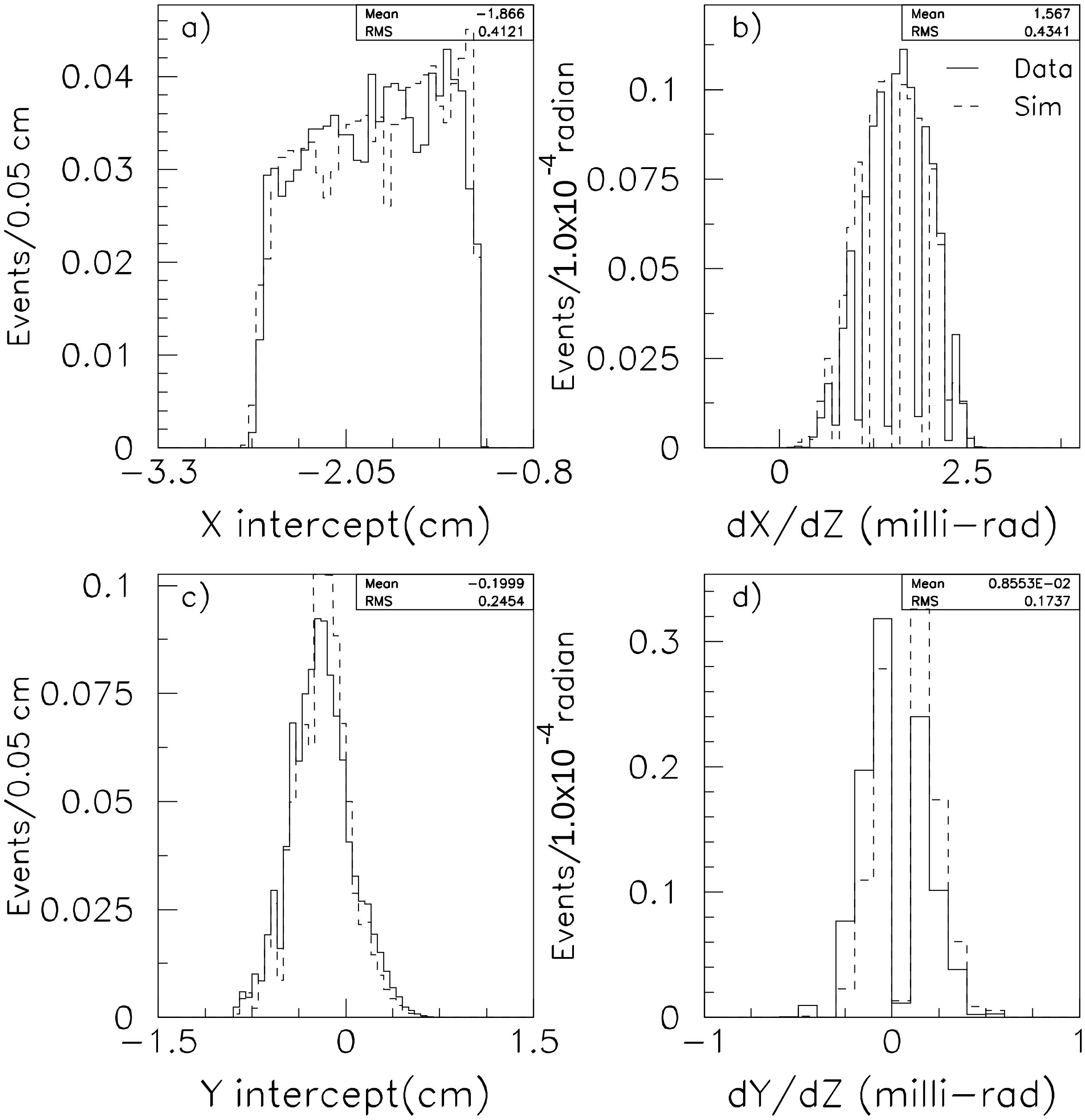

Figure A.6: The intercept and angle distributions of recoil $\overline{p}$ track at the RPS 1 before the RPS position correction for low luminosity 14 runs. The solid line shows the diffractive inclusive data and the dashed line shows the diffractive inclusive simulation after the RPS simulation.

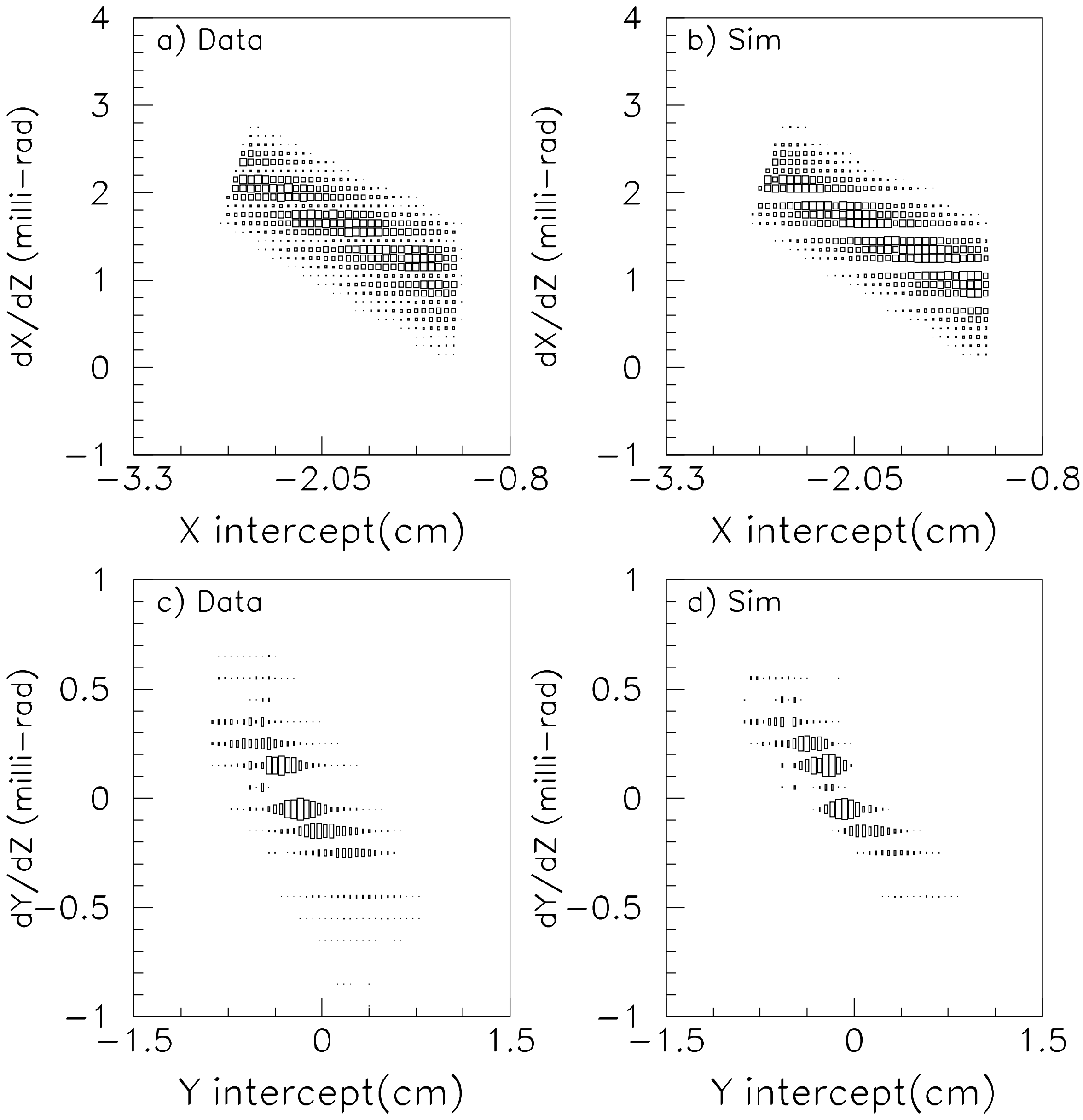

Figure A.7: The scatter plots of X vs. dX/dZ and Y vs. dY/dZ before the RPS position correction. The left two plots show the diffractive inclusive data. And the right two plots show the diffractive inclusive simulation after the RPS simulation.

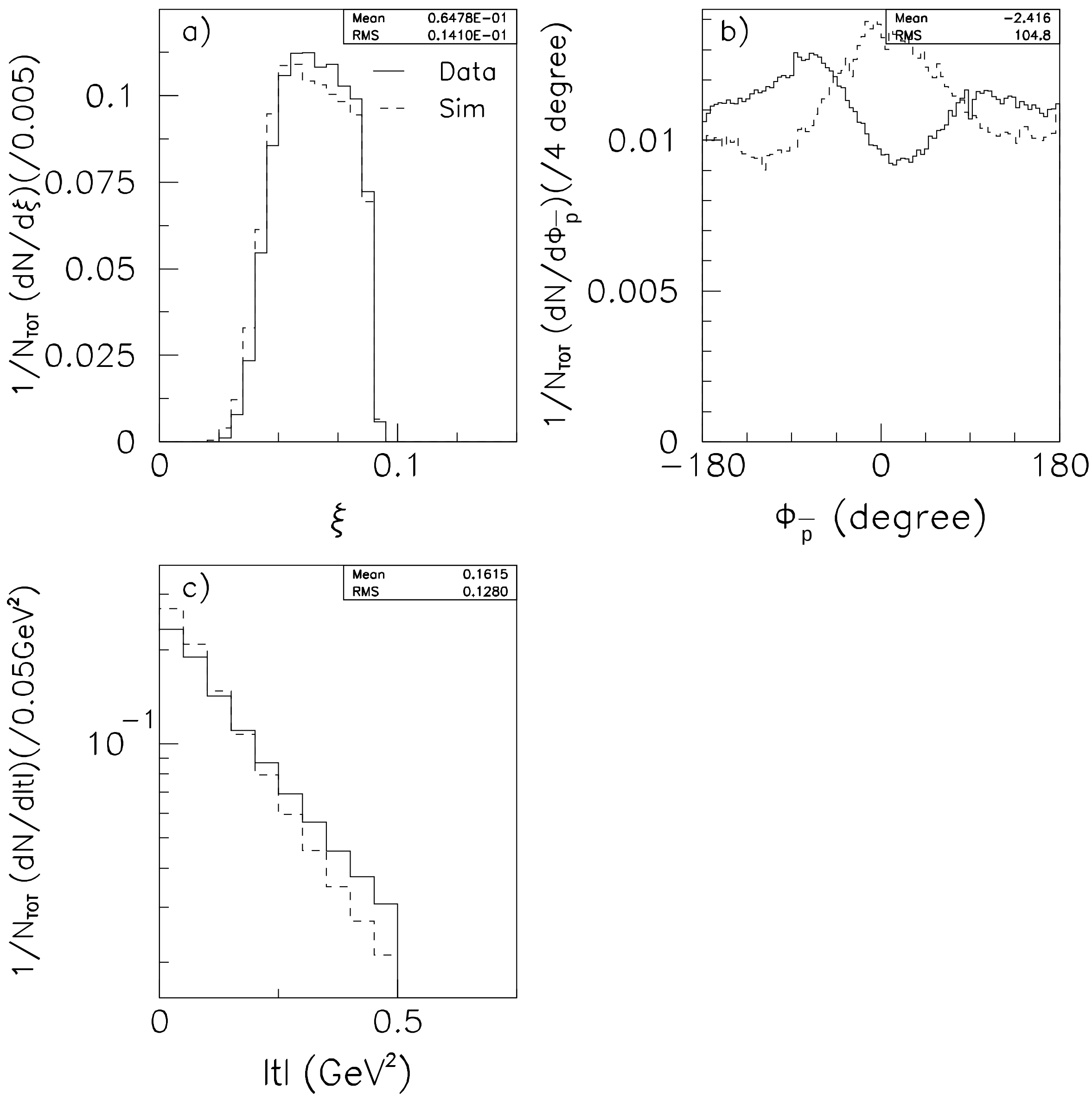

Figure A.8: The distributions of reconstructed diffractive kinematical variables before the RPS position correction. The solid line shows the diffractive inclusive data and the dashed line shows the diffractive inclusive simulation after the RPS simulation.

distribution of the azimuthal angle ($\phi_{\bar{p}}$) of the recoil $\overline{p}$ is sensitive to the reconstructed track angle in the RPS. Therefore the detector position displacement influences the $\phi_{\bar{p}}$ distribution. In Figure A.9, we show the correlations. The magnitude of overall displacements for each run is 800 μm at maximum. And we also show the distributions after all corrections in Figures A.10–A.13.

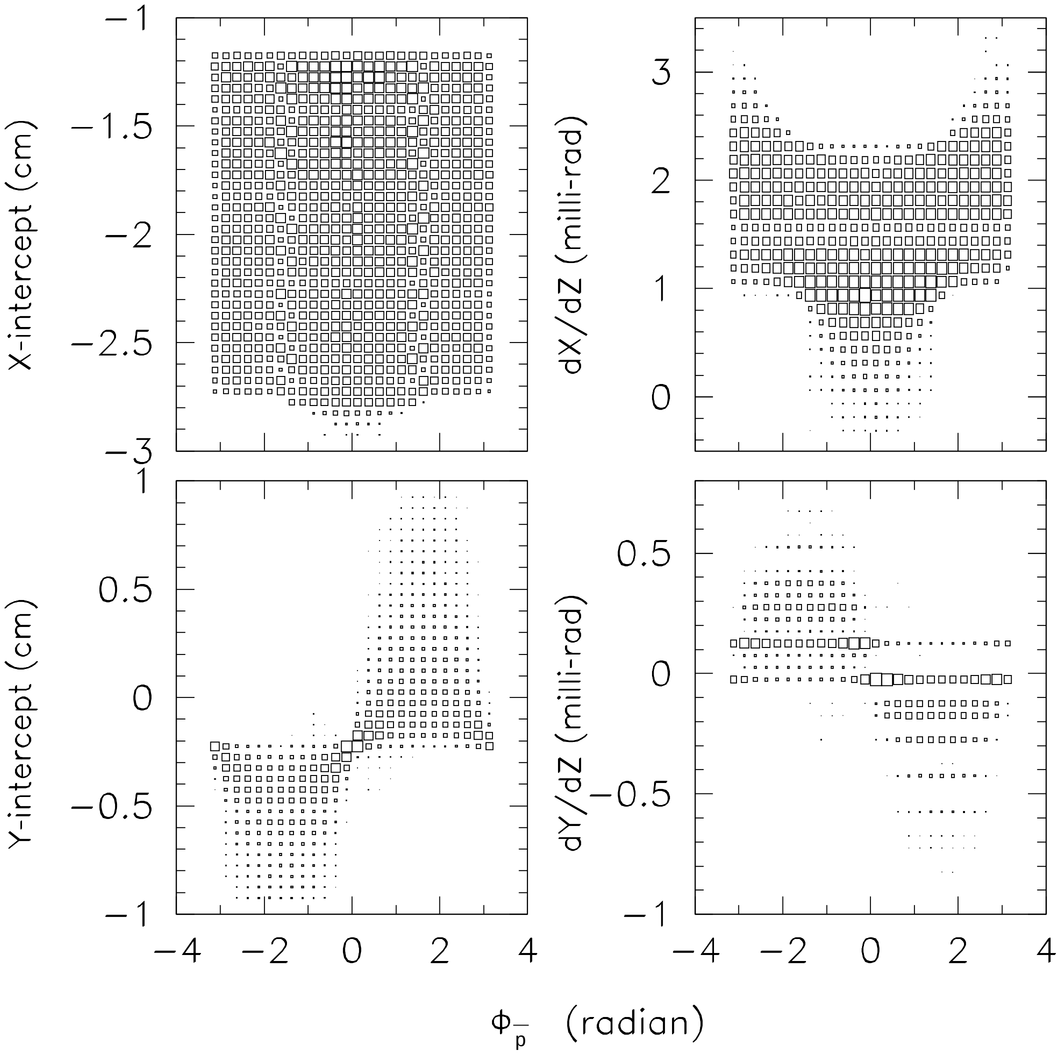

Figure A.9: Correlations between (X-intercept, dX/dZ, Y-intercept, dY/dZ) and $\phi_{\bar{p}}$. These plots are made from simulation of run 75647.

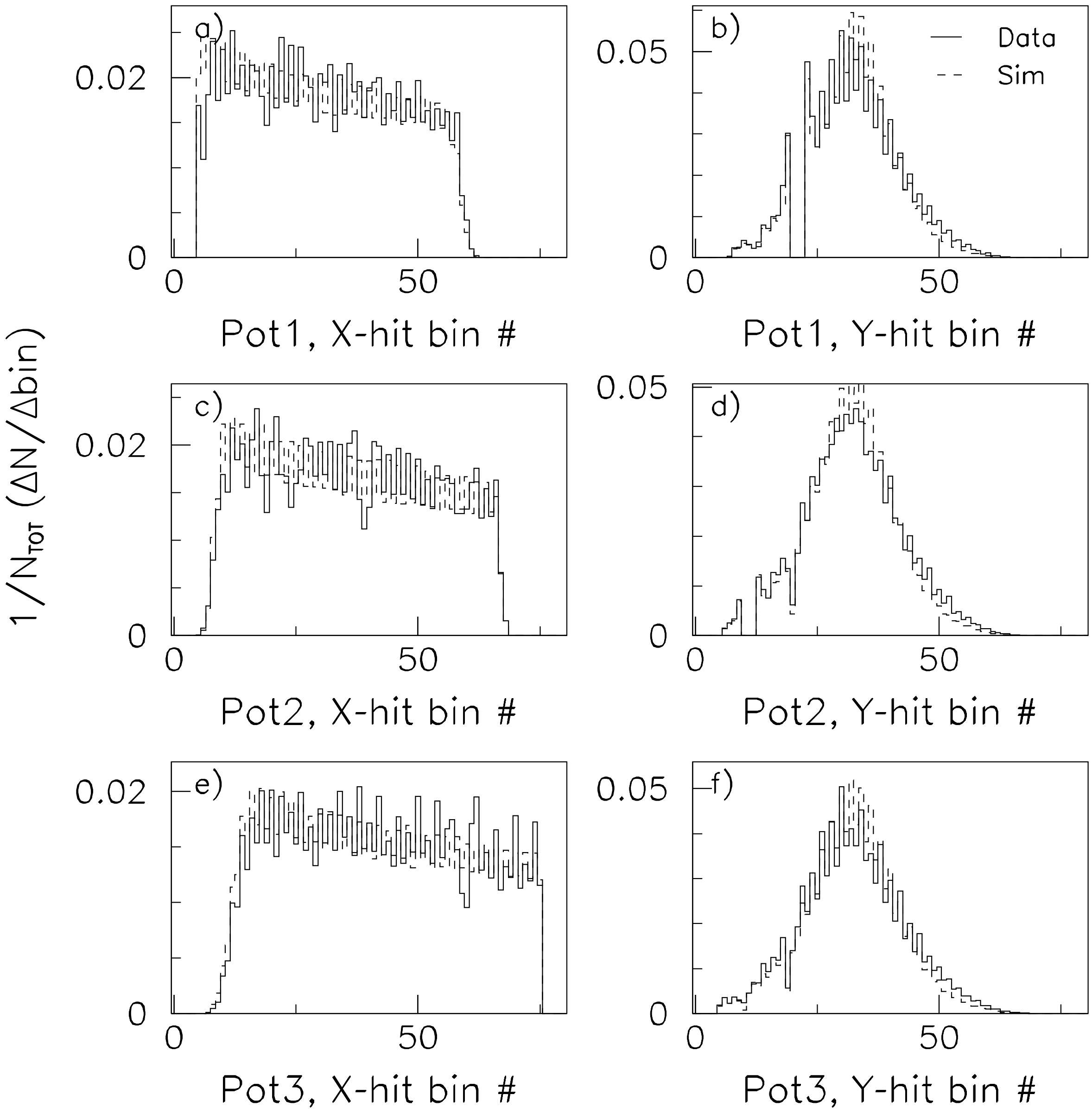

Figure A.10: The RPS hit occupancy distributions after RPS position correction for 14 low luminosity runs. The top two plots are for pot 1 X and Y, the middle plots are for pot 2, and the bottom plots are for pot 3. The solid line shows the diffractive inclusive data and the dashed line shows the diffractive inclusive simulation after the RPS simulation.

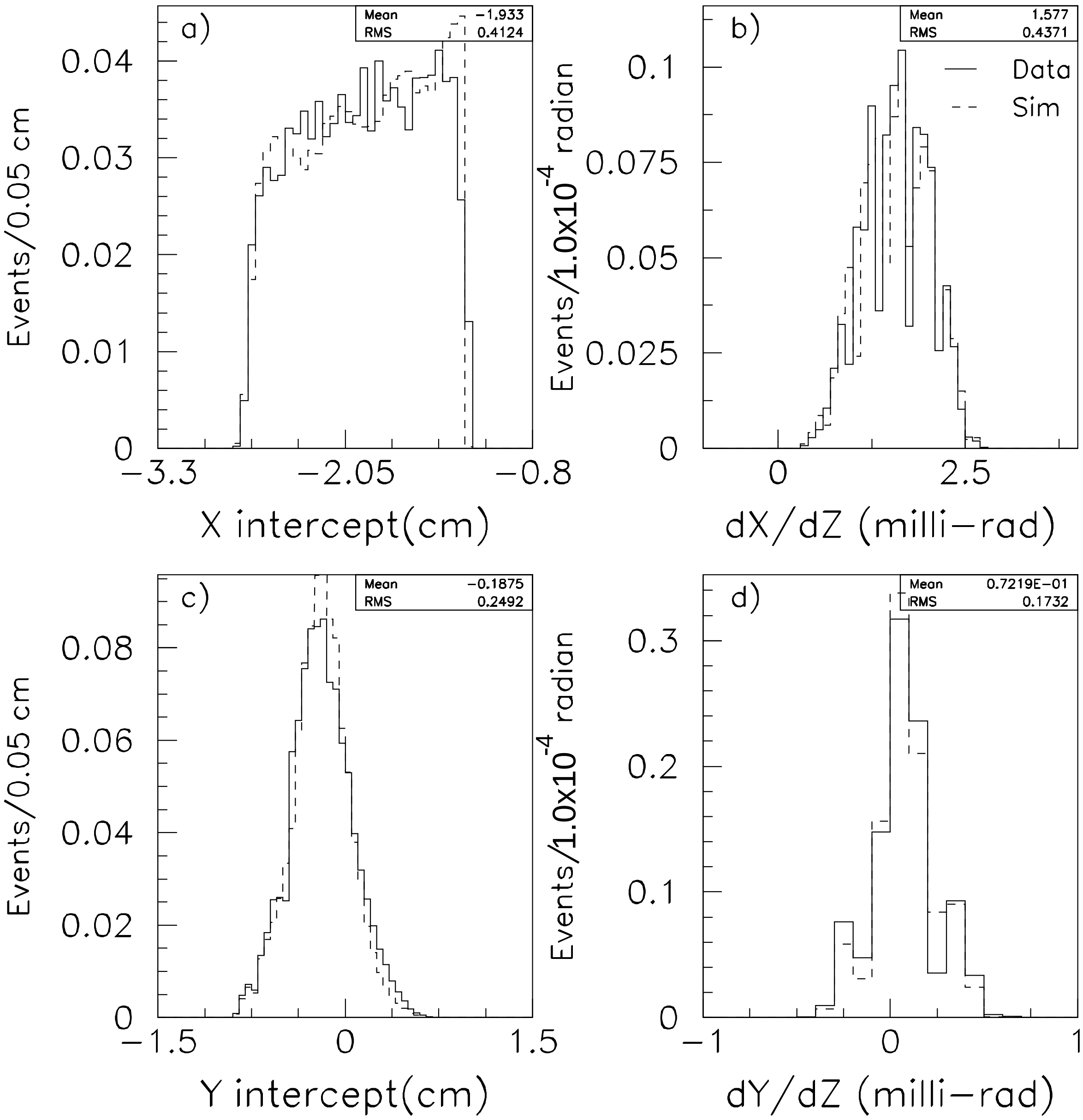

Figure A.11: The intercept and angle distributions of recoil $\overline{p}$ track at the RPS 1 after the RPS position correction for 14 low luminosity runs. The solid line shows the diffractive inclusive data and the dashed line shows the diffractive inclusive simulation after the RPS simulation.

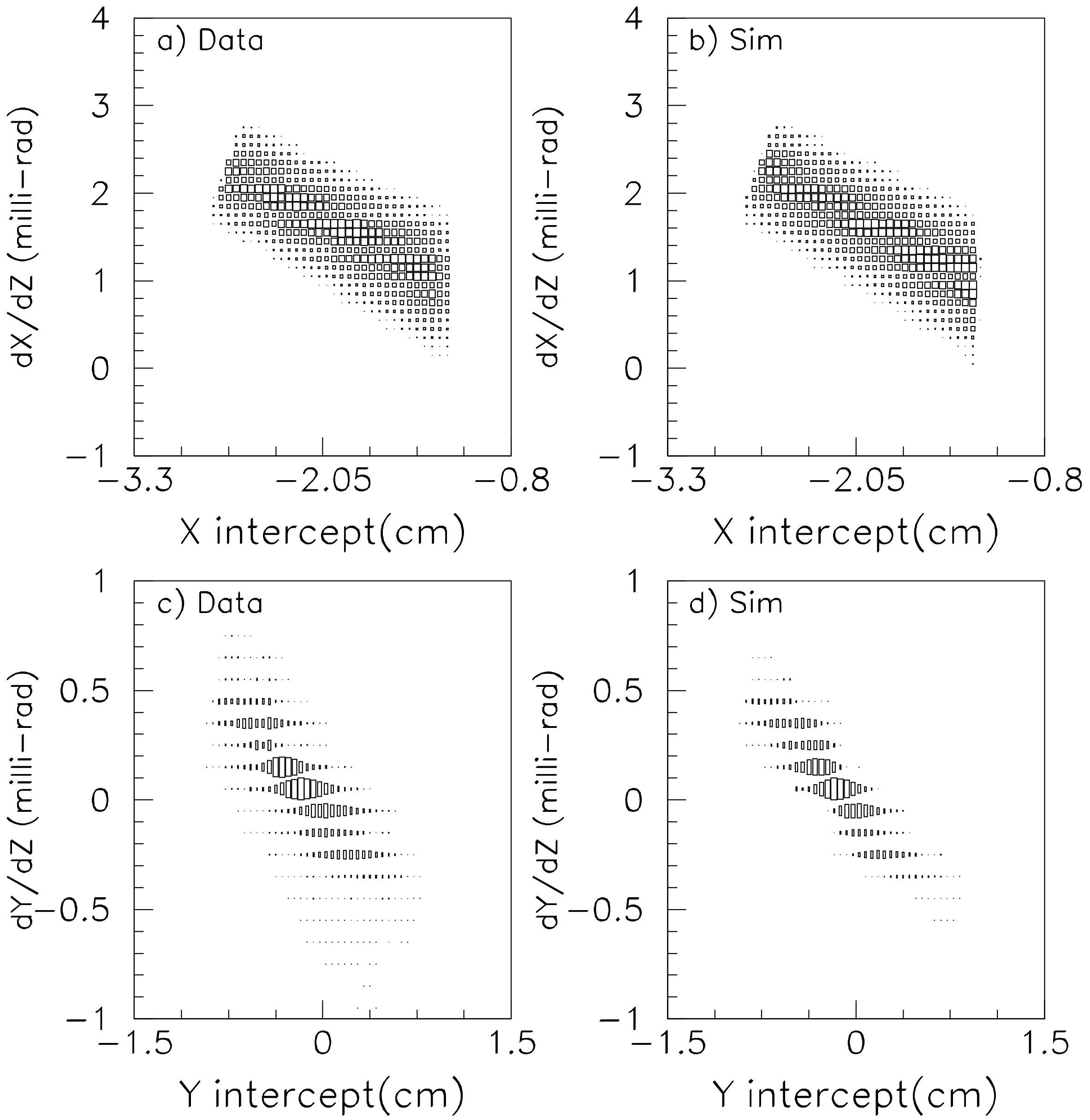

Figure A.12: The scatter plots of X vs. dX/dZ and Y vs. dY/dZ after the RPS position correction. The left two plots show the diffractive inclusive data. And the right two plots show the diffractive inclusive simulation after the RPS simulation.

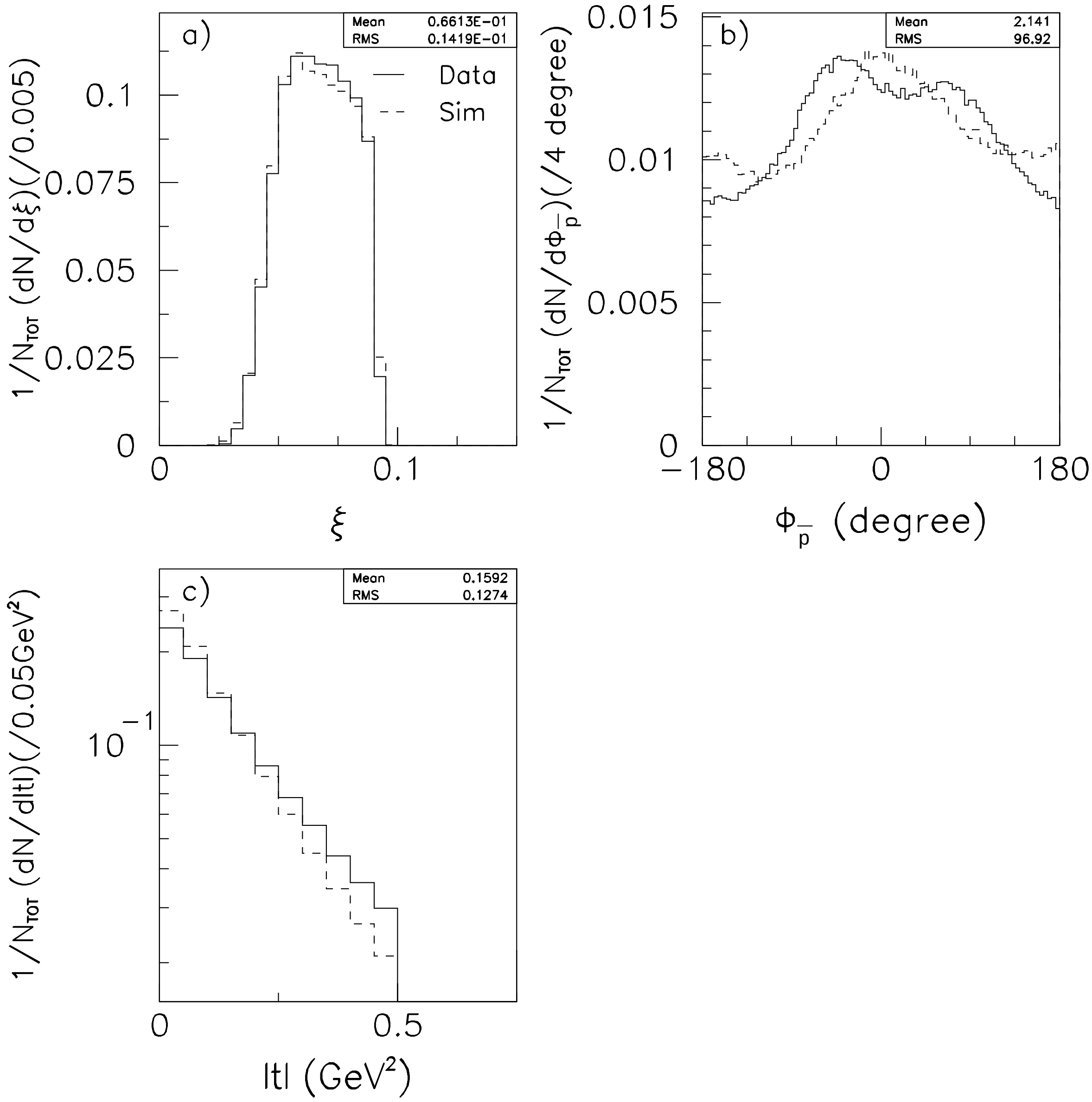

Figure A.13: The distributions of reconstructed diffractive kinematical variables after the RPS position correction. The solid line shows the diffractive inclusive data and the dashed line shows the diffractive inclusive simulation after the RPS simulation.

A.2 RPS performance

A.2.1 Position, angle, and ξ, t resolution and RPS acceptance

After the calibration, we show the RPS acceptance plots in Figure A.14. From the result, we decide the acceptance region of the RPS to be $0.035 \leq \xi \leq 0.095$ and $|t| \leq 1$ GeV^2. Shown in Figure A.15 is the residual distributions of the RPS hit position. Assuming the position resolution of each fiber hodoscope is the same as each other, we can estimate the position resolution and the angle resolution as follows:

$$\begin{aligned}
X^{\rm fit}_{\rm pot2} &= \frac{X_{\rm pot1} + X_{\rm pot3}}{2}, \\
R_X &= X_{\rm pot2} - X^{\rm fit}_{\rm pot2}, \\
\sigma^2_{R_X} &= \sigma^2_{X_{\rm pot2}} + \left(\frac{1}{2}\right)^2 (\sigma^2_{X_{\rm pot1}} + \sigma^2_{X_{\rm pot3}}) \\
&= \frac{3}{2}\sigma^2_X, (\sigma_X = \sigma_{X_{\rm pot1}} = \sigma_{X_{\rm pot2}} = \sigma_{X_{\rm pot3}}) \\
Angle &= \frac{X_{\rm pot3} - X_{\rm pot1}}{2L}, \\
\sigma^2_{Angle} &= \left(\frac{1}{2L}\right)^2 (\sigma^2_{X_{\rm pot1}} + \sigma^2_{X_{\rm pot3}}) \\
&= \frac{1}{2L^2}\sigma^2_X,
\end{aligned}$$

where the σ_{R_X} is a sigma of the residual distribution, and the $\sigma_{X_{\rm pot1}}(\sigma_{X_{\rm pot2}}, \sigma_{X_{\rm pot3}})$ is a position resolution of fiber hodoscope of the Roman-pot1 (pot2, pot3). We estimate the RPS position resolution of X (Y) to be 103 (99) μm, and the angle resolution to be 0.074 (0.071) milli-radians. And we confirmed them by using the simulation as shown in Figure A.16. The result of expected position resolution of X (Y) is 72 (77) μm, and That of expected angle resolution is 0.056 (0.059) milli-radians. In order to estimate effects of the RPS and ambiguity of $\overline{p}$ -beam on ξ and t, we investigate ξ, t, and ϕ resolutions as shown in Figures A.17 and A.20. Each two top plots in Figures A.17 and A.20 show their resolutions making from diffractive inclusive event simulation with ideal beam (without beam degradation), and each two bottom plots in Figures A.17 and A.20 show those making from diffractive inclusive event simulation with degradation of beam realistically.

Comparing left two plots in Figure A.17, we estimate an intrinsic beam effect on ξ resolution to be 1.9×10^{-4} (negligible small). And also comparing two top plots in Figure A.17, we estimate the intrinsic Roman-pot detector effect on ξ resolution to be 9.6×10^{-4}. The number is consistent with the expected overall ξ resolution as shown in Figure A.17 (bottom right). For the t resolution, we look at the residual distributions for several t intervals, and ϕ. We show the t and θ resolutions (mean value shifts) as a function of t and θ in Figure A.18 (A.19). Comparing left two plots in Figure A.20, we estimate an intrinsic beam effect on the ϕ resolution to be 39.6 degree. And also comparing two top plots in Figure A.20, we estimate the intrinsic Roman-pot detector effect on the ϕ resolution to be 14.6 degree. The number is consistent with the expected overall ϕ resolution 41.5 degree ($\approx \sqrt{39.6^2 + 14.6^2} = 42.2$) as shown in Figure A.20 (bottom right).

Figure A.21 shows the correlation plots between ξ and t. The bottom two plots show the effect on the Roman-pot detector due to non-uniform stripes. The simulation reproduces the CDF data very well.

A.3 Summary

We performed the RPS position calibration for each run taken during the Run-1C low luminosity runs. We obtained the good RPS acceptance of $0.035 \leq \xi \leq 0.095$ and $|t| \leq 1$ GeV^2. The ξ resolution is estimated to be 1.0×10^{-3}. The t resolution is estimated to be 0.08 GeV^2 at $|t| = 0.1$ GeV^2, 0.25 GeV^2 at $|t| = 1$ GeV^2.

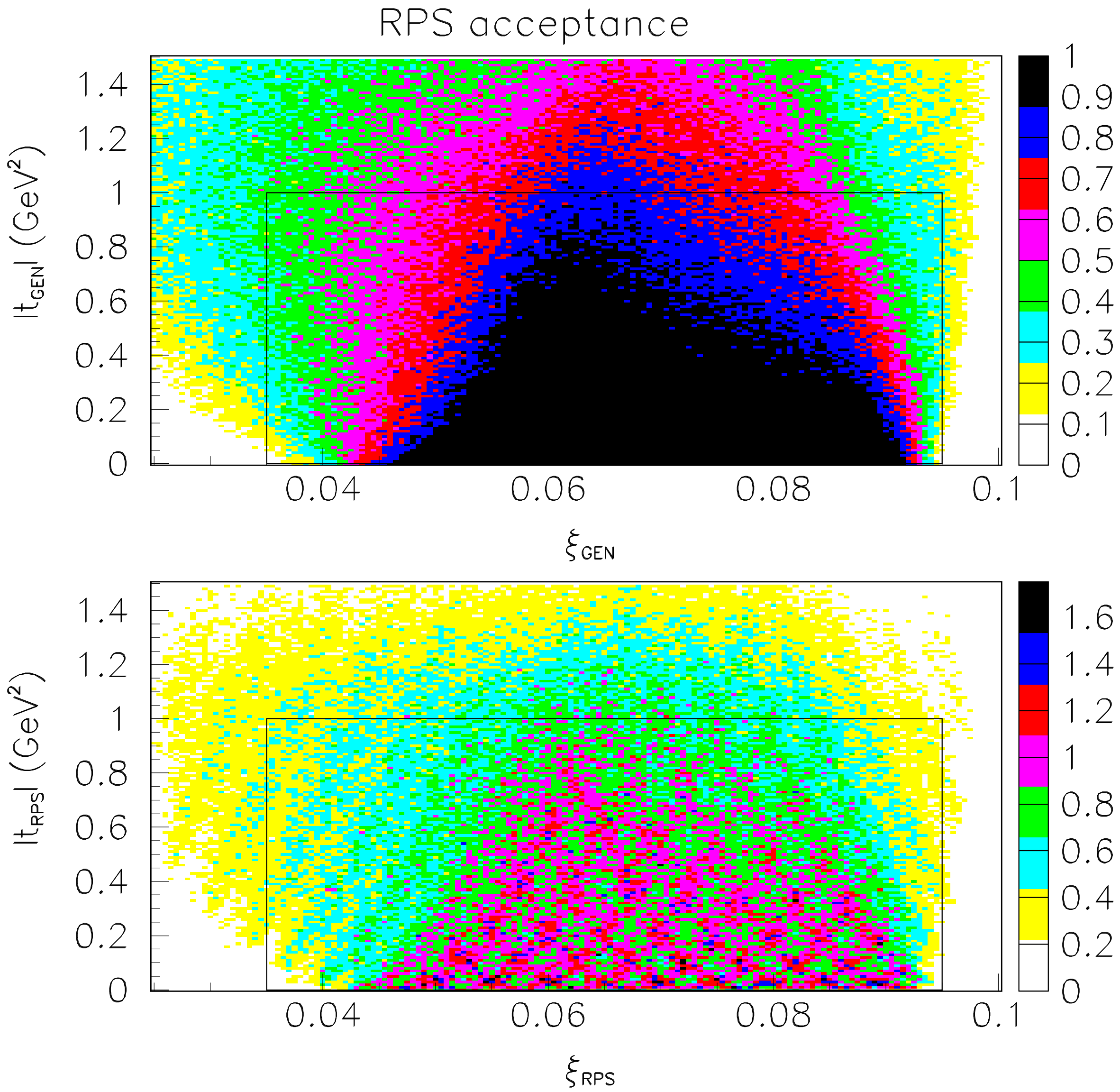

Figure A.14: The RPS acceptance for 1.8 TeV low luminosity runs. Interaction point degradation is made with $\sigma_{\rm spot}^{\rm beam} = 47.4\,\mu$m and $\sigma_{\rm angle}^{\rm beam} = 0.133$ milli-radians. The top (bottom) plot shows ξ, t are reconstructed one without (with) RPS simulation. Inside of the box for each plot is the good acceptance region of RPS. The values above 1 in the bottom plot are due to coming from neighbor $(\xi, |t|)$ bins by its resolution.

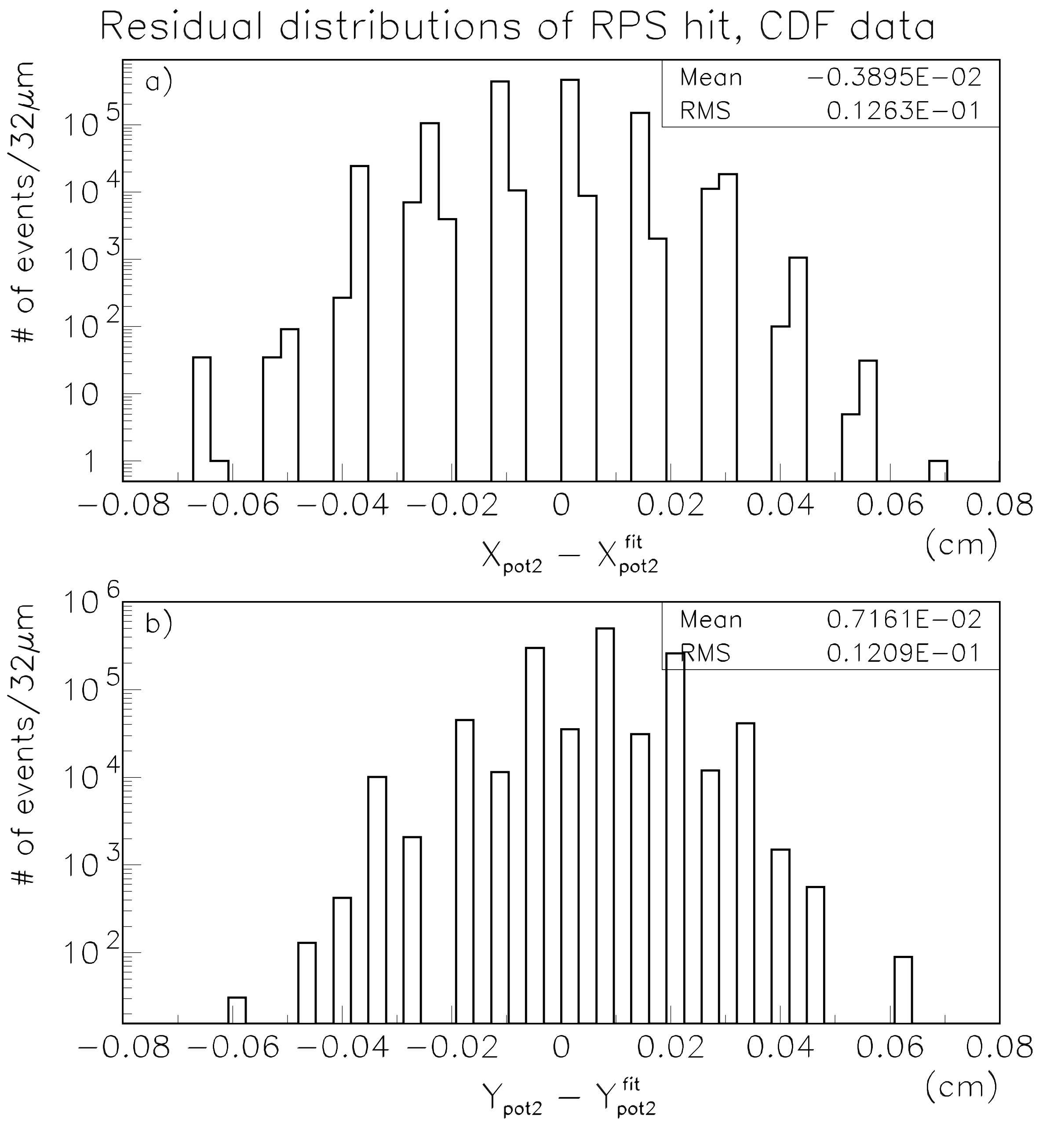

Figure A.15: Residual distributions of RPS hit position for X and Y. $X(Y)^{\mathrm{fit}}_{\mathrm{pot2}} = [X(Y)_{\mathrm{pot1}} + X(Y)_{\mathrm{pot3}}]/2$. From the results, we estimate an RPS position resolution of X (Y) to be 103 (99) μm, and an angle resolution to be 0.074 (0.071) milli-radians.

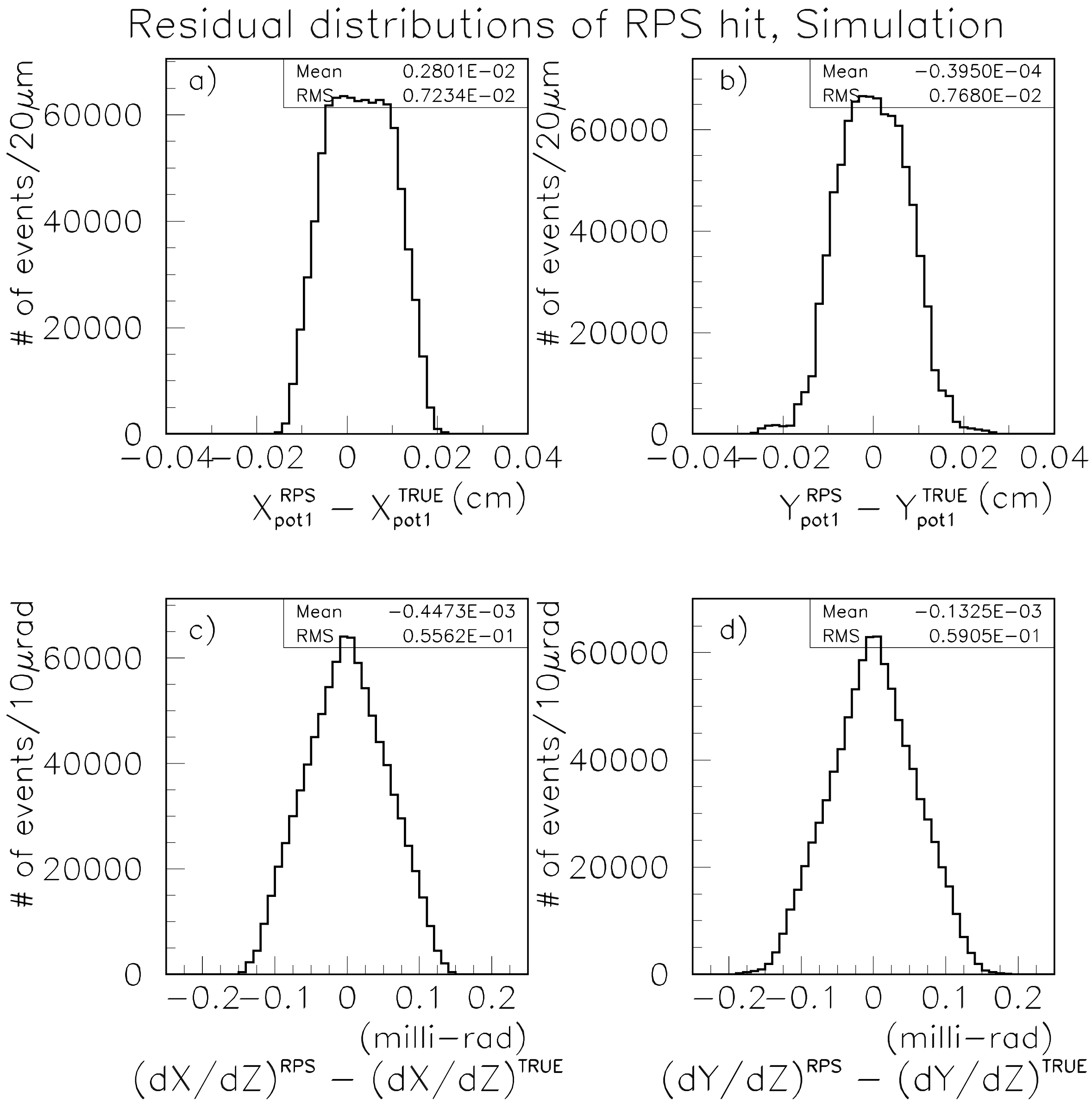

Figure A.16: Expected RPS position and angle resolution. We expect an RPS position resolution of X (Y) to be 72 (77) μm, and an angle resolution to be 0.056 (0.059) milliradians.

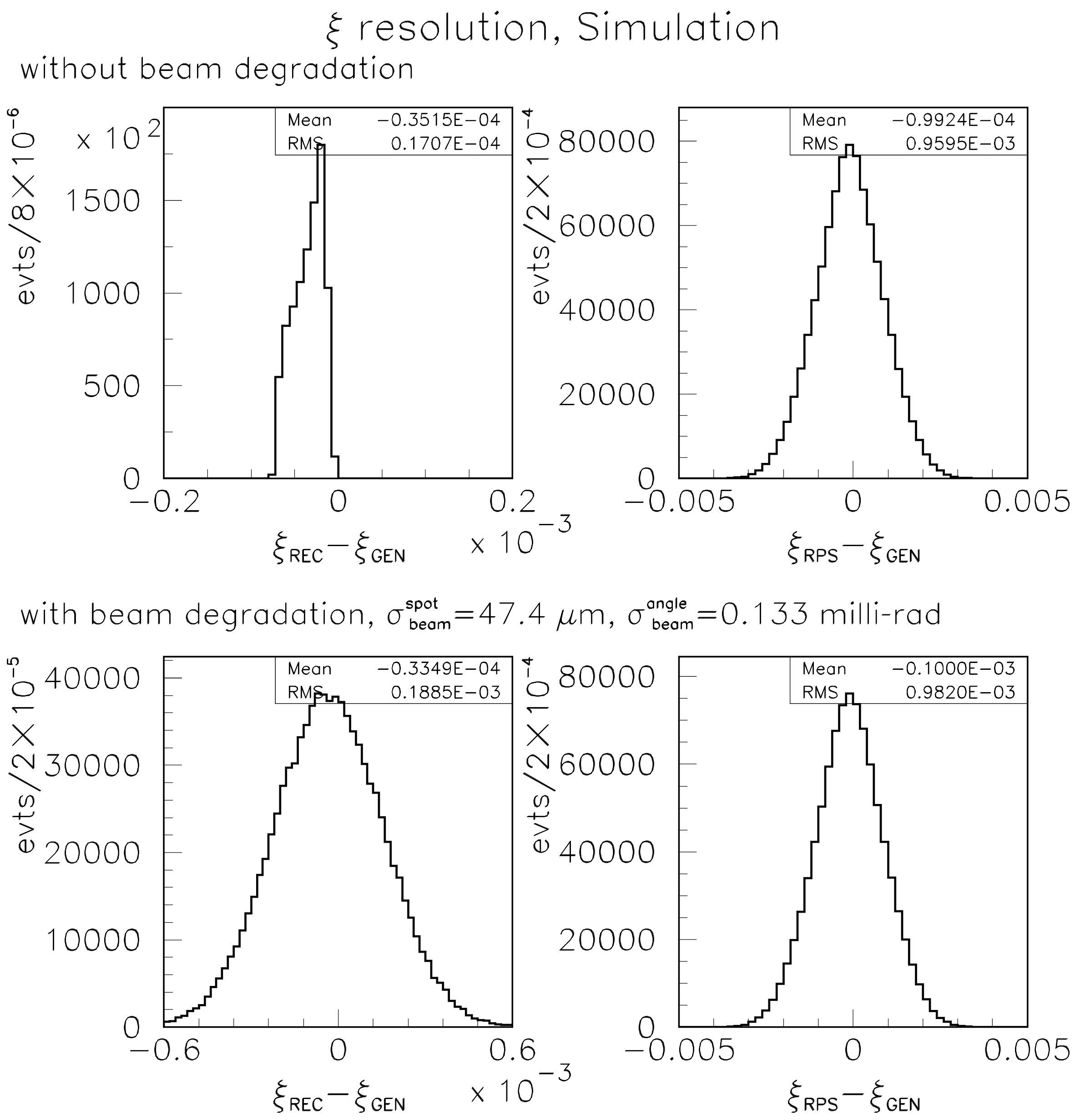

Figure A.17: Residual distributions from generator level ξ to reconstructed ones with/without RPS simulation. Two top (bottom) plots show the case without (with) initial beam degradation. Overall ξ resolution is estimated to be 1.0×10^{-3}.

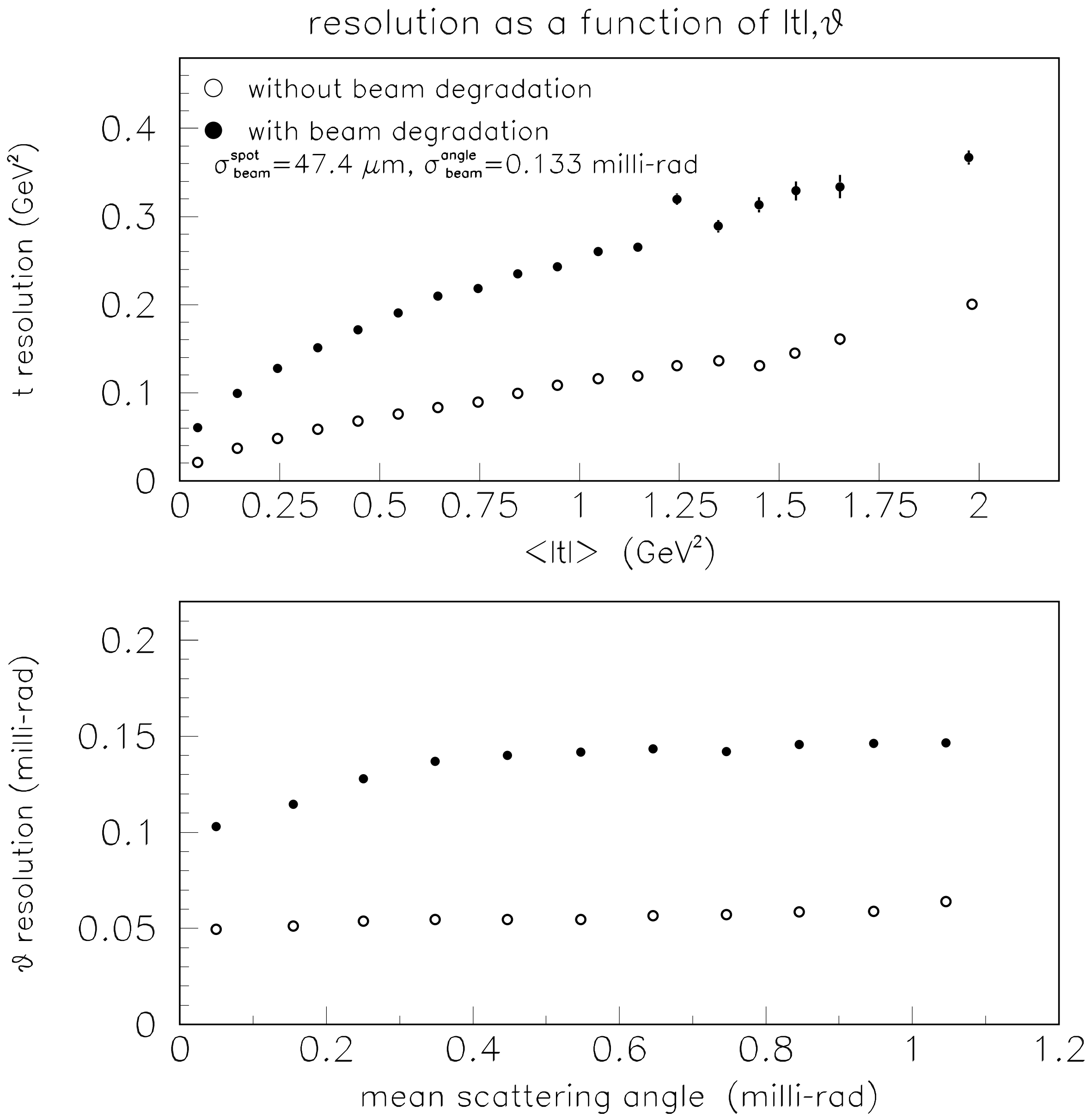

Figure A.18: t and scattering angle resolution as a function of t, and θ. Open circle (solid point) shows the case without (with) initial beam degradation.

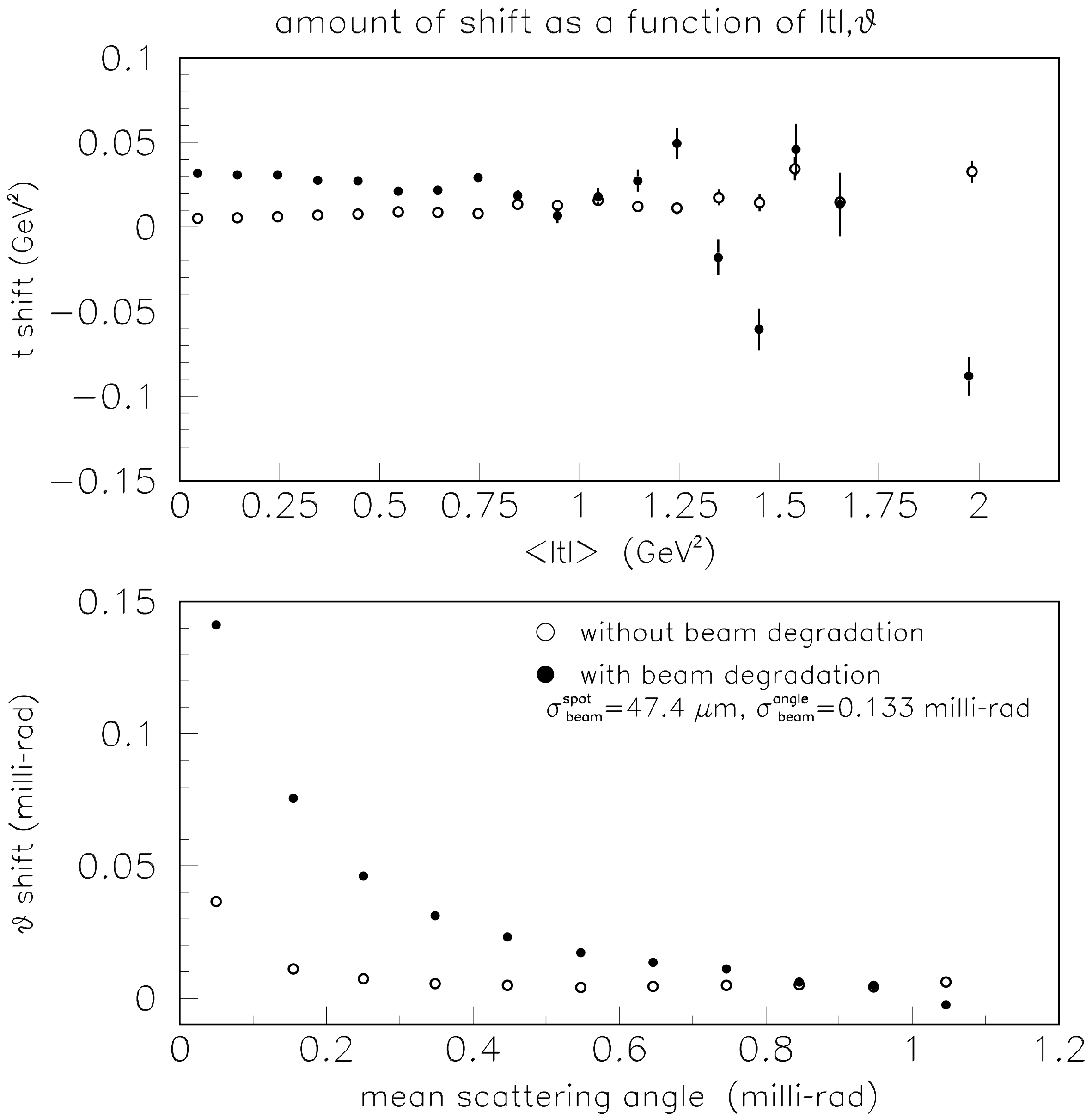

Figure A.19: t and scattering angle shift as a function of t and θ. Open circle (solid point) shows the case without (with) initial beam degradation.

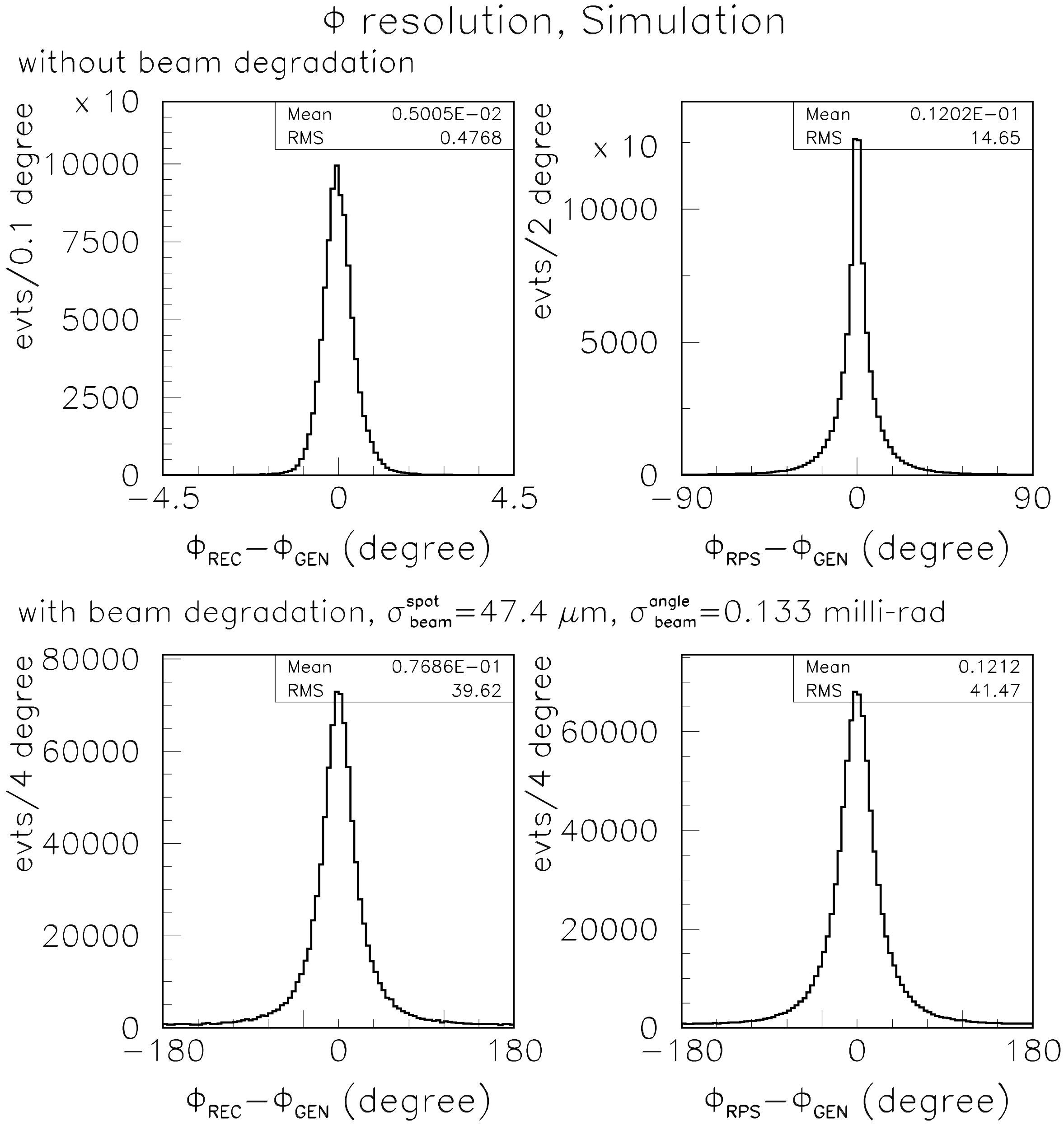

Figure A.20: Residual distributions from generator level ϕ to reconstructed ones with/without RPS simulation. Two top (bottom) plots show the case without (with) initial beam degradation. Overall ϕ resolution is estimated to be 45.8 degree.

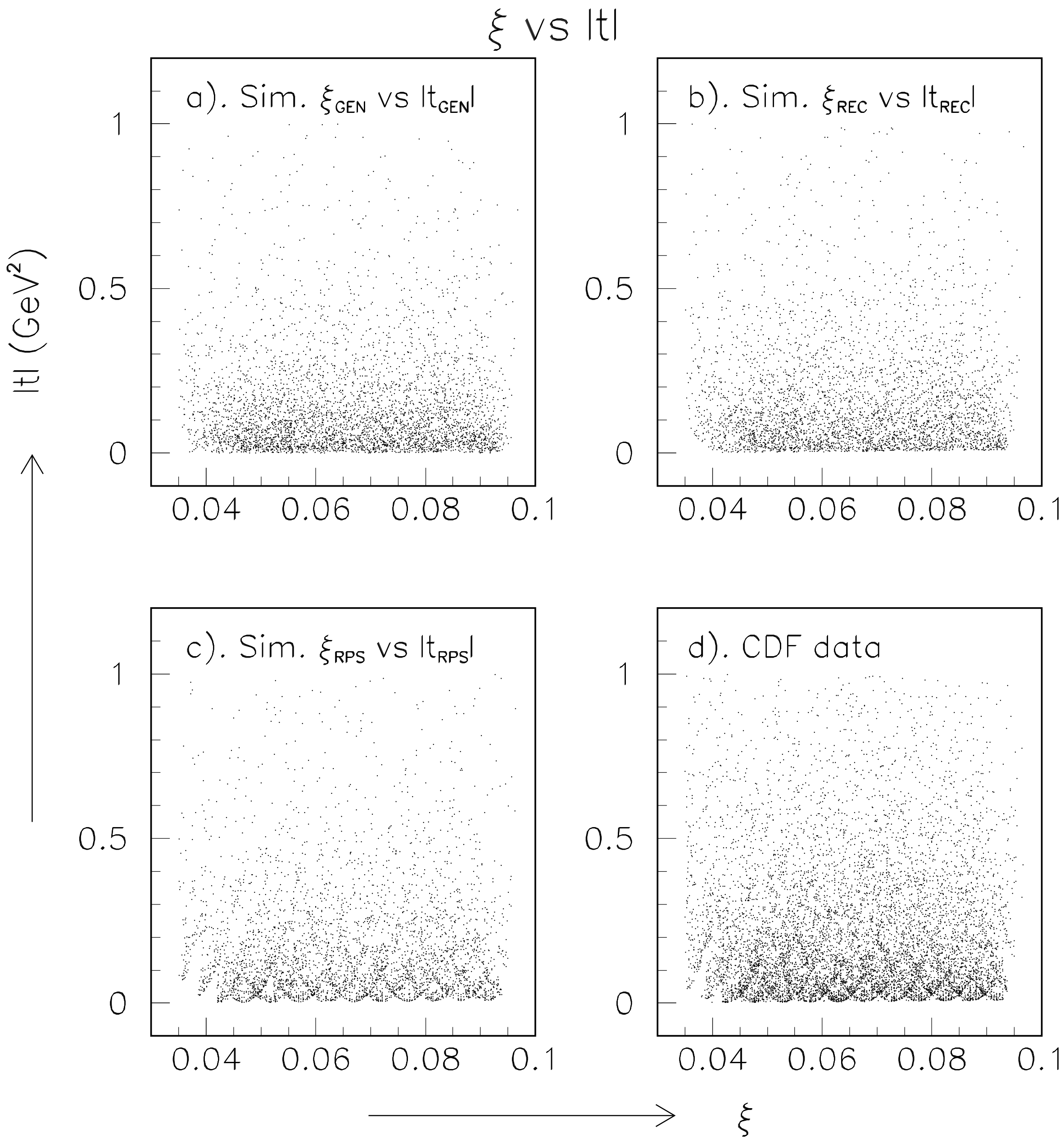

Figure A.21: Correlation between ξ and t. The bottom two plots show the RPS effect as non-uniform stripes. Reconstructed ξ, t with RPS simulation reproduces CDF data.

Appendix B

Underlying event energy for diffractive trigger data

In general, the underlying event energy has process dependence. Since the diffractive event must have a recoil $\overline{p}$ and/or p , the underlying event energy originating from spectator partons in the diffractive dijet events must be smaller than that in the non-diffractive ones. In order to understand the diffractive dijet events better, it is necessary to investigate the amount of the energy from the spectators.

There are two kinds of methods, "20-degree bands method" and "random cone method"*, to estimate the underlying event energy. The procedure of the first one is:

1. Select a clean dijet event.

2. Find a thrust axis of the dijet.

3. Define the wedges formed by 20-degree bands in ϕ (hereafter we call the wedge "20-degree bands") which are perpendicular to the thrust axis of the dijet in the central detector region ($|\eta| < 1.1$).

4. Sum over four-momenta of towers in the 20-degree bands with $E_T^{\mathrm{TWR}} \geq 100\,\mathrm{MeV}$. And measure the average transverse energy in the 20-degree bands as $E_T^{20-\mathrm{deg}}$.

*In CDF, the random cone method is the standard, so that when we apply our jet energy correction, we subtract the underlying event E_T measured by the random cone method.

5. Calculate the transverse energy density in the 20-degree bands (ρ) to be $\rho = E_T^{20-\mathrm{deg}}/(2.2 \times 2 \times 20^\circ \times \pi/180)$.

6. Calculate the transverse underlying event energy within a 0.7 cone (E_T^{UE}) to be $E_T^{\mathrm{UE}}(20 - \mathrm{deg}) = \rho \times 0.7^2\pi \times 1.6$.

The procedure of the second one is:

1. Select a clean inclusive event.

2. Decide a cone axis in the region of $0.1 \leq |\eta| \leq 0.7$ randomly for each event.

3. Sum up E_T of calorimeter towers within a cone radius of 0.7 with $E_T^{\mathrm{TWR}} \geq 100\,\mathrm{MeV}$.

4. Estimate the transverse underlying event energy to be $E_T^{\mathrm{UE}}(\mathrm{random}) = E_T(R \leq 0.7) \times 1.6$.

We use events from the diffractive trigger data. We select the diffractive inclusive events by the following criteria:

- VTX cuts as,
  - $N_{\mathrm{VTX}}(\mathrm{class} \geq 5) = 1$
  - $|Z_{\mathrm{VTX}}^{\mathrm{primary}}| \leq 60\,\mathrm{cm}$,
- Missing E_T cuts
- one-MIP cut

About 580K events survived the selection cuts.

In order to make a sample for the 20-degree bands method study, we further apply the following dijet exclusive cuts:

- $E_T^{\mathrm{Jet2}} \geq 5$ GeV after applying jet energy correction for the diffractive inclusive trigger data, and $E_T^{\mathrm{Jet2}} \geq 10$ GeV for the diffractive dijet trigger data,
- $E_T^{\mathrm{Jet3}} \leq 5$ GeV (jet energy correction applied),
- $\Delta\phi_{\mathrm{JJ}} \geq 175^\circ$.

Source		$E_T^{20-\text{deg}}$ (GeV)	$\rho\,(\text{GeV}/d\eta/d\phi)$	E_T^{UE} (GeV)
$\Delta\phi$ cut dependence, $\Delta\phi \geq 170°$, GAP cut on				
TRG.	$\mathcal{L}$			
INCL	Low	0.403 ± 0.010	0.26 ± 0.01	$0.65 \pm 0.02\,(2.5\%)$
INCL	High	0.367 ± 0.051	0.24 ± 0.03	$0.59 \pm 0.08\,(14\%)$
combined result				$0.65 \pm 0.02\,(2.4\%)$
JJ	Low	0.417 ± 0.047	0.27 ± 0.03	$0.67 \pm 0.08\,(11\%)$
JJ	High	0.445 ± 0.037	0.29 ± 0.02	$0.71 \pm 0.06\,(8.2\%)$
combined result				$0.70 \pm 0.05\,(6.7\%)$
		Deviation (GeV)		
INCL.		$+0.02$ $(+3\%)$		
JJ.		-0.04 (-5%)		

Table B.1: Summary of systematic uncertainty from $\Delta\phi_{\text{JJ}}$ cut.

About 1600 events survived the dijet exclusive cuts.

At first, we measure $E_T^{20-\text{deg}}$. We show the result plots in Figures B.1–B.2. We obtained the underlying event $E_T(R = 0.7)$ to be 0.61 ± 0.02 (inclusive trigger) and 0.73 ± 0.06 (dijet trigger) by calculating weighted mean between each result with "GAP cut†" on.

Systematic uncertainty can be estimated as a function of luminosity, thresholds of third jet E_T and $\Delta\phi_{\text{JJ}}$. We varied the threshold of the third jet E_T from 5 GeV to 3 or 7 GeV by using the diffractive dijet trigger data and that of $\Delta\phi_{\text{JJ}}$ from 175 degree to 170 degree. We summarized the results in Tables B.1–B.2, where the $\mathcal{L}$ is instantaneous luminosity.

Next, we measured E_T in $R = 0.7$ random cone. The results are summarized in Table B.3.

From this study, we conclude the underlying event E_T in the single diffractive events to be $0.34 \times 1.6 \approx 0.54\,(\text{GeV})$. And we assign the uncertainty of 30% on underlying event E_T subtraction.

†Definition of GAP cut is West BBC multiplicity ≤ 6.

Source		$E_T^{20-\mathrm{deg}}$ (GeV)	$\rho\,(\mathrm{GeV}/d\eta/d\phi)$	E_T^{UE} (GeV)
E_T^{Jet3} cut dependence, Dijet TRG.				
$\mathcal{L}$	GAP cut			
$E_T^{\mathrm{Jet3}} < 7\,\mathrm{GeV}$				
Low	off	0.486 ± 0.051	0.32 ± 0.03	$0.78 \pm 0.08\,(10\%)$
Low	on	0.471 ± 0.054	0.31 ± 0.04	$0.76 \pm 0.09\,(11\%)$
High	off	0.575 ± 0.034	0.38 ± 0.02	$0.92 \pm 0.05\,(5.9\%)$
High	on	0.495 ± 0.045	0.32 ± 0.03	$0.79 \pm 0.07\,(9.2\%)$
combined result				
	off			$0.89 \pm 0.05\,(5.2\%)$
	on			$0.78 \pm 0.06\,(7.2\%)$
$E_T^{\mathrm{Jet3}} < 3\,\mathrm{GeV}$				
Low	off	0.481 ± 0.061	0.31 ± 0.04	$0.77 \pm 0.10\,(13\%)$
Low	on	0.459 ± 0.063	0.30 ± 0.04	$0.74 \pm 0.10\,(14\%)$
High	off	0.493 ± 0.036	0.32 ± 0.02	$0.79 \pm 0.06\,(7.3\%)$
High	on	0.454 ± 0.050	0.30 ± 0.03	$0.73 \pm 0.08\,(11\%)$
combined result				
	off			$0.79 \pm 0.05\,(6.3\%)$
	on			$0.73 \pm 0.06\,(8.6\%)$
		Deviation (GeV)		
	off	+0.10 (+13%)	0.00 (0%)	
	on	−0.04 (+5%)	−0.01 (−1%)	

Table B.2: Summary of systematic uncertainty from the third jet veto. The error of "0.00 GeV (0%)" means that we cannot observe it.

TRG.	$\mathcal{L}$	GAP cut	$E_T^{\mathrm{UE}}(R = 0.7)$ (GeV)
INCL	Low	off	0.340 ± 0.001
	Low	on	0.339 ± 0.001
	High	off	0.438 ± 0.005
	High	on	0.355 ± 0.005
combined result		off	0.34 ± 0.00
		on	0.34 ± 0.00

Table B.3: Summary of underlying event E_T measured by random cone method. The error of "0.00 GeV" means that we cannot observe it.

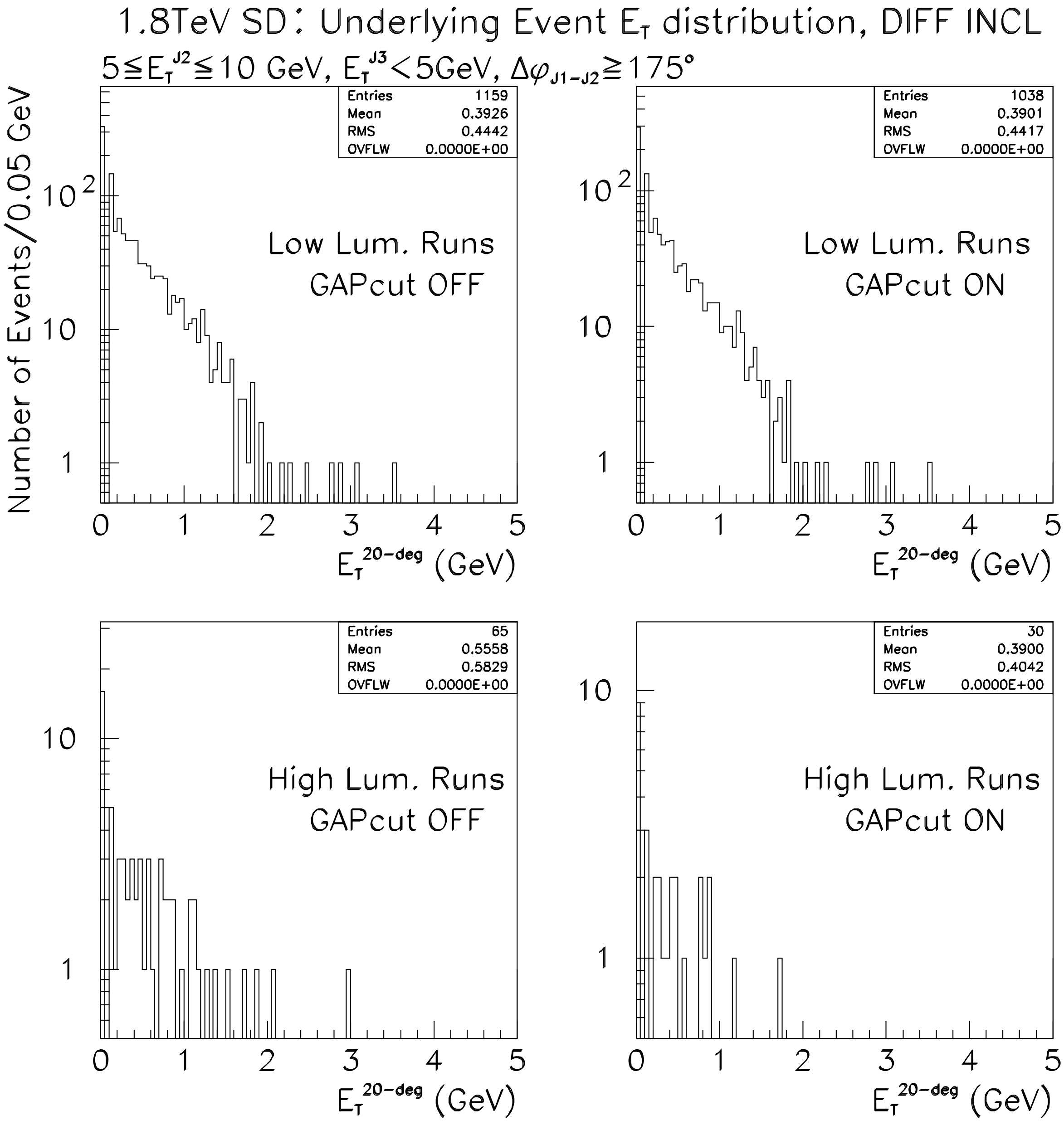

Figure B.1: 20-degree bands E_T distributions for diffractive inclusive trigger data. The two top (bottom) plots show those from low (high) luminosity runs.

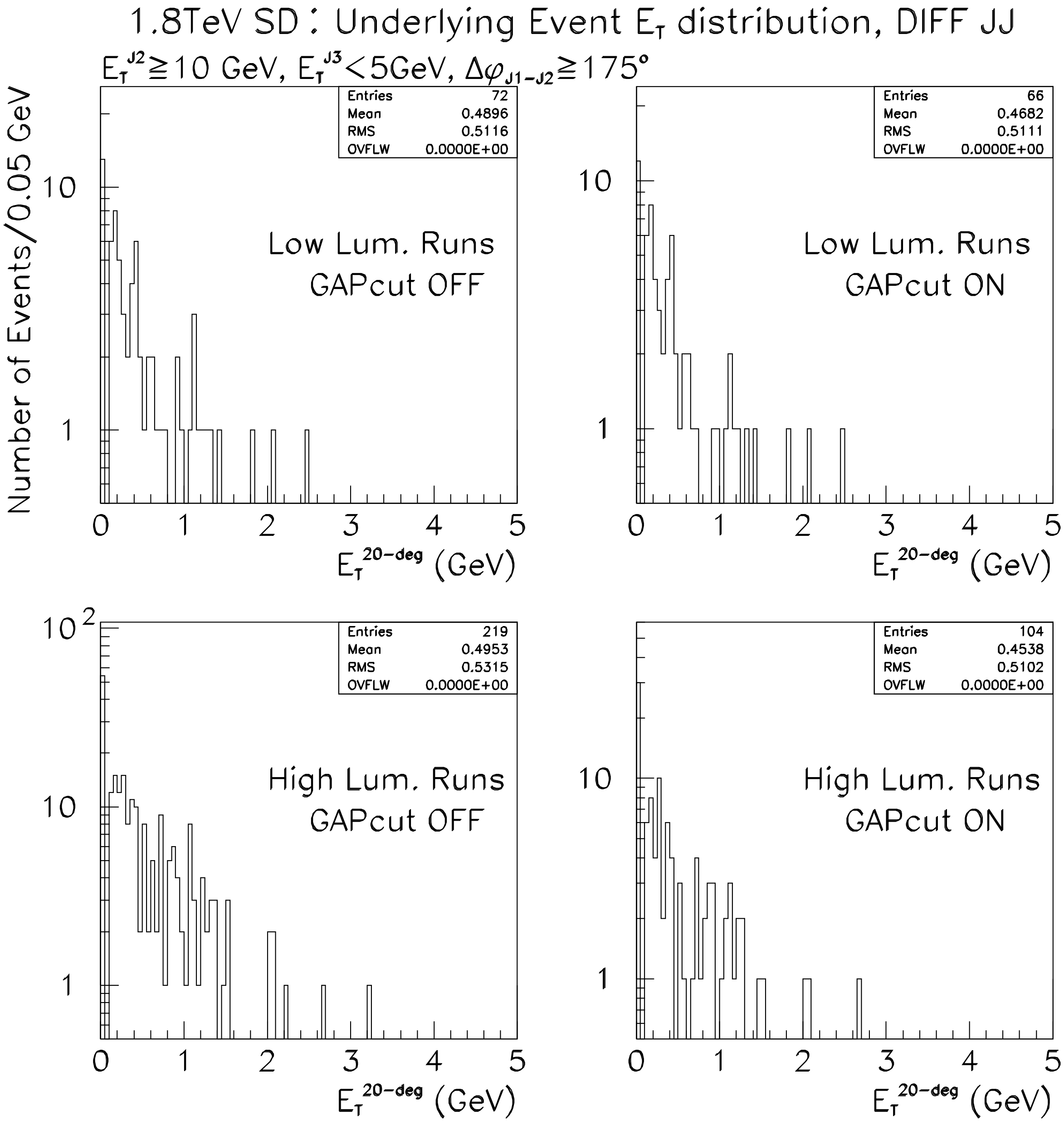

Figure B.2: 20-degree bands E_T distributions for diffractive dijet trigger data. The two top (bottom) plots show those from low (high) luminosity runs.

Appendix C

Calorimeter noise filter

During runs 75644-75713, very significant and distinct fake jet contributions due to calorimeter noise ("Hot tower") emerged in the plug and forward regions as shown in Figures C.1 and C.2. At each noise spot, we observe that the fake jets have unusual and unique EM fraction distributions as shown in figure C.3. To remove the events with these fake jets we apply a "hot tower" filter (HTFLT), whose requirements are listed in Table C.1. Shown in Figure C.4 is the detector-η versus ϕ plots for the diffractive and non-diffractive dijet events after applying the HTFLT. The efficiency of the HTFLT is estimated to be 97.5% by applying the filter to the minimum-bias events having jets with $E_T \geq 7\,\mathrm{GeV}$ from Run-1B and evaluating the fraction of events rejected. We assign the 1.9% systematic uncertainty on the efficiency (the total uncertainty to be $2\% = \sqrt{0.5\%^2 + 1.9\%^2}$). Finally, we obtain the efficiency to be;

$$\epsilon_{\mathrm{HTFLT}} = 97.5 \pm 0.5\% \text{ (stat.)} \pm 1.9\% \text{ (syst.)}. \tag{C.1}$$

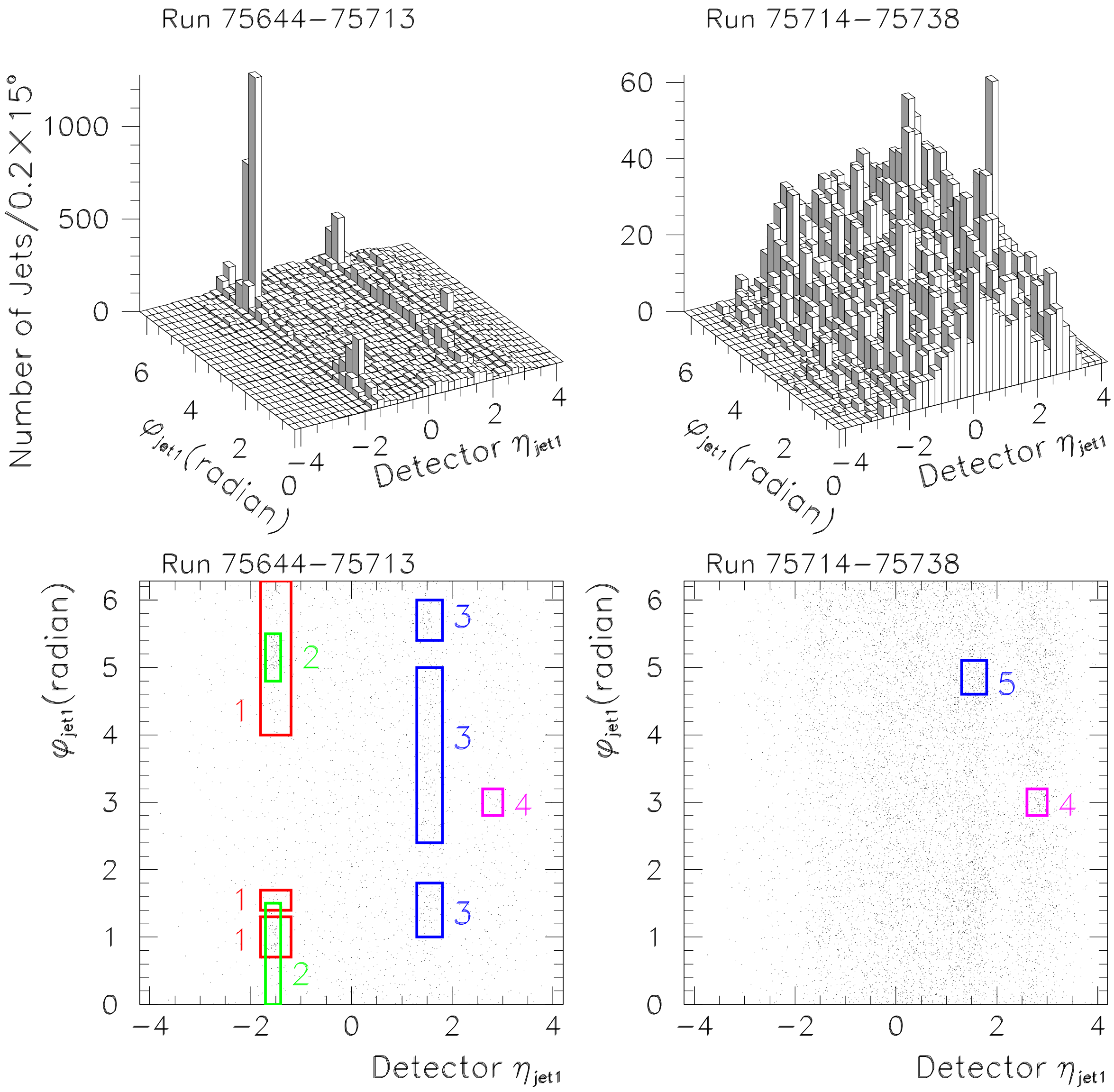

Figure C.1: Distributions of leading jets on the detector-η versus ϕ plane for the diffractive events with at least two jets with $E_T \geq 7\,\mathrm{GeV}$ in runs of 75644-75713 (left plots), and 75714-75738 (right plots). The five calorimeter noise spots listed in Tbale C.1 are indicated by boxes in the bottom two plots.

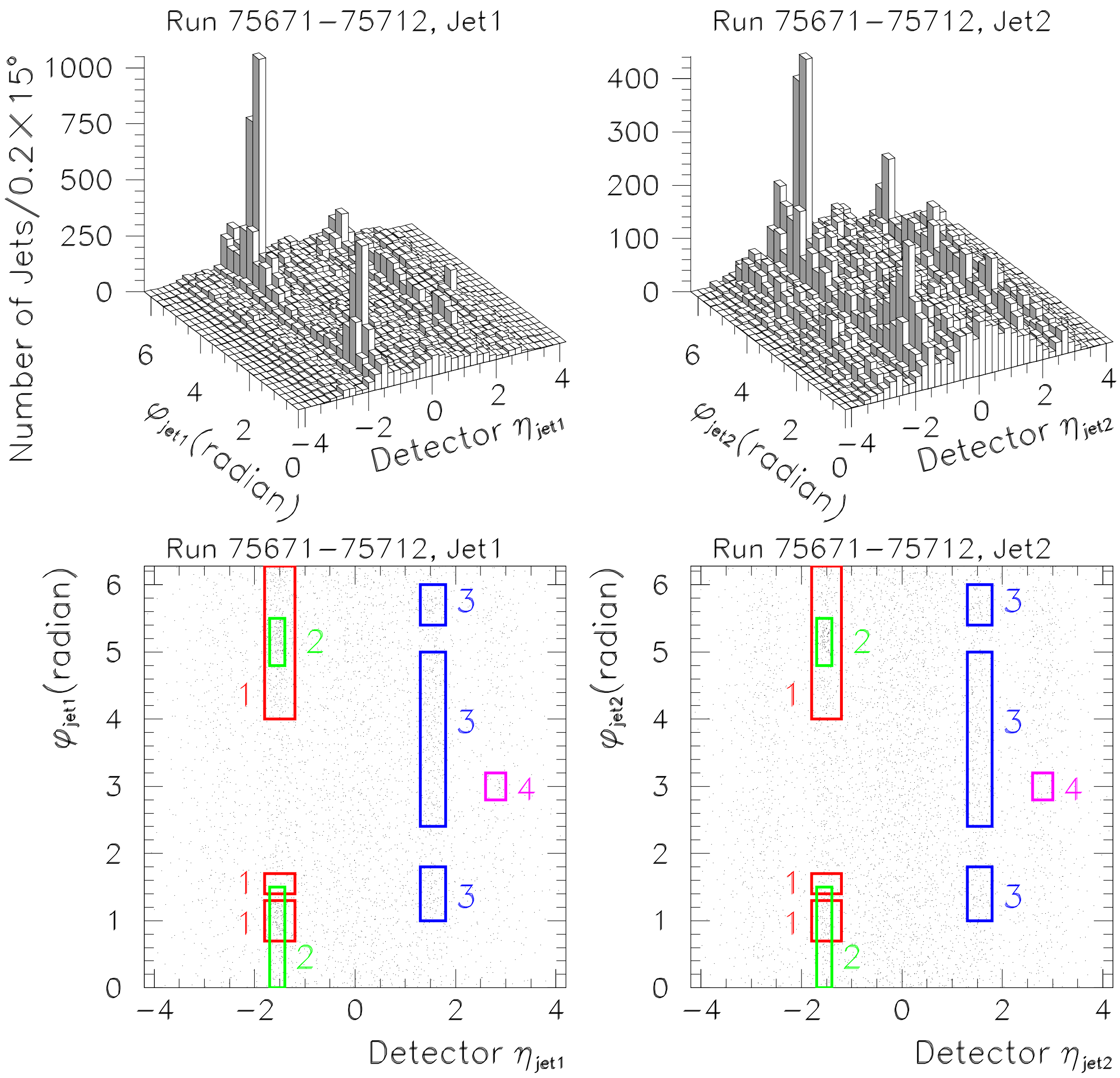

Figure C.2: Distributions of leading (left) and next-to-leading (right) jets on the detector-η versus ϕ plane for the non-diffractive events with at least two jets with $E_T \geq 7\,\mathrm{GeV}$. The five calorimeter noise spots listed in Table C.1 are indicated by boxes in the bottom two plots.

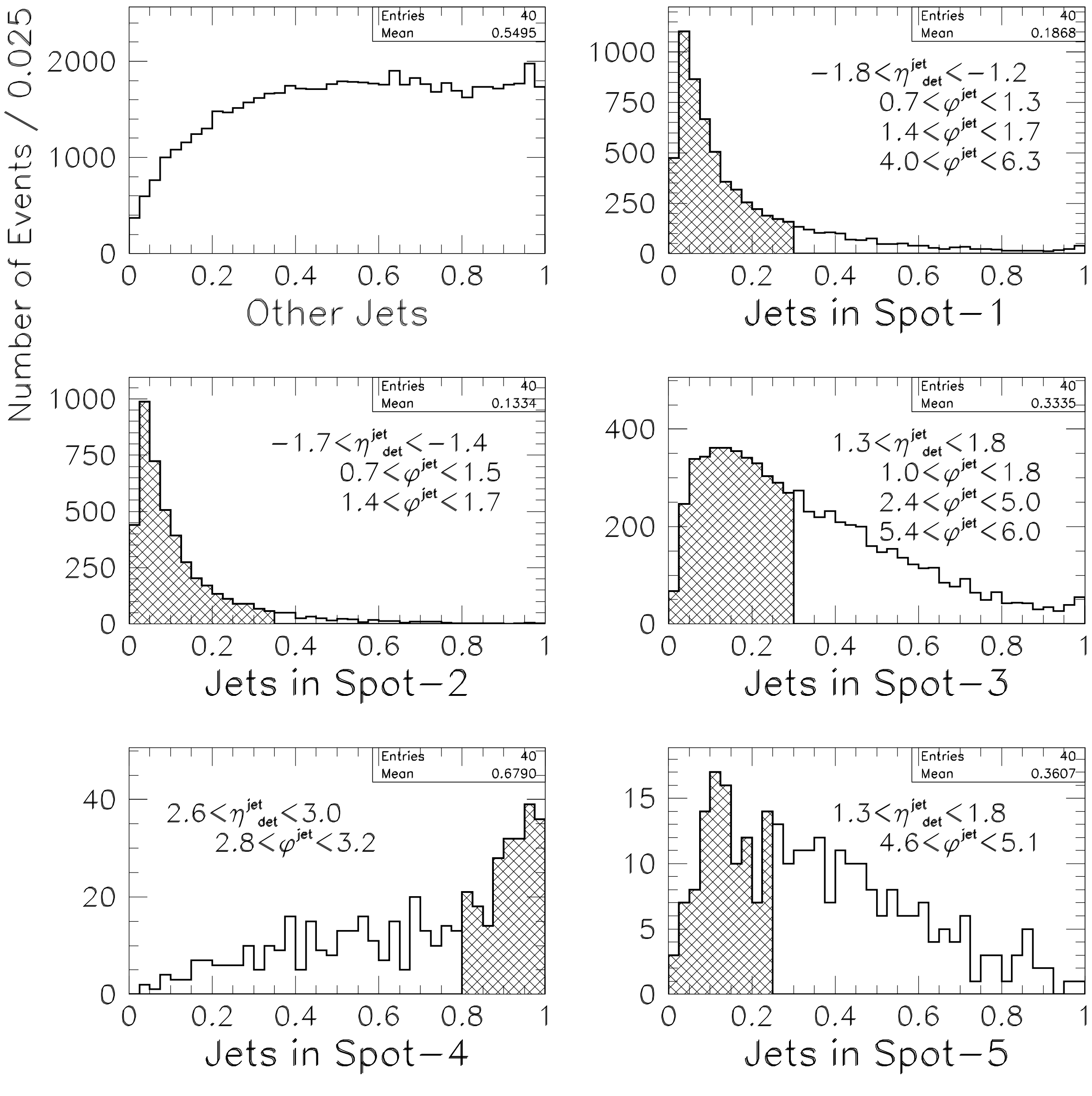

Figure C.3: Distributions of the EM fraction of jets in the five calorimeter noise spots for the diffractive data. Jet events with shaded EM fraction are rejected by the HTFLT.

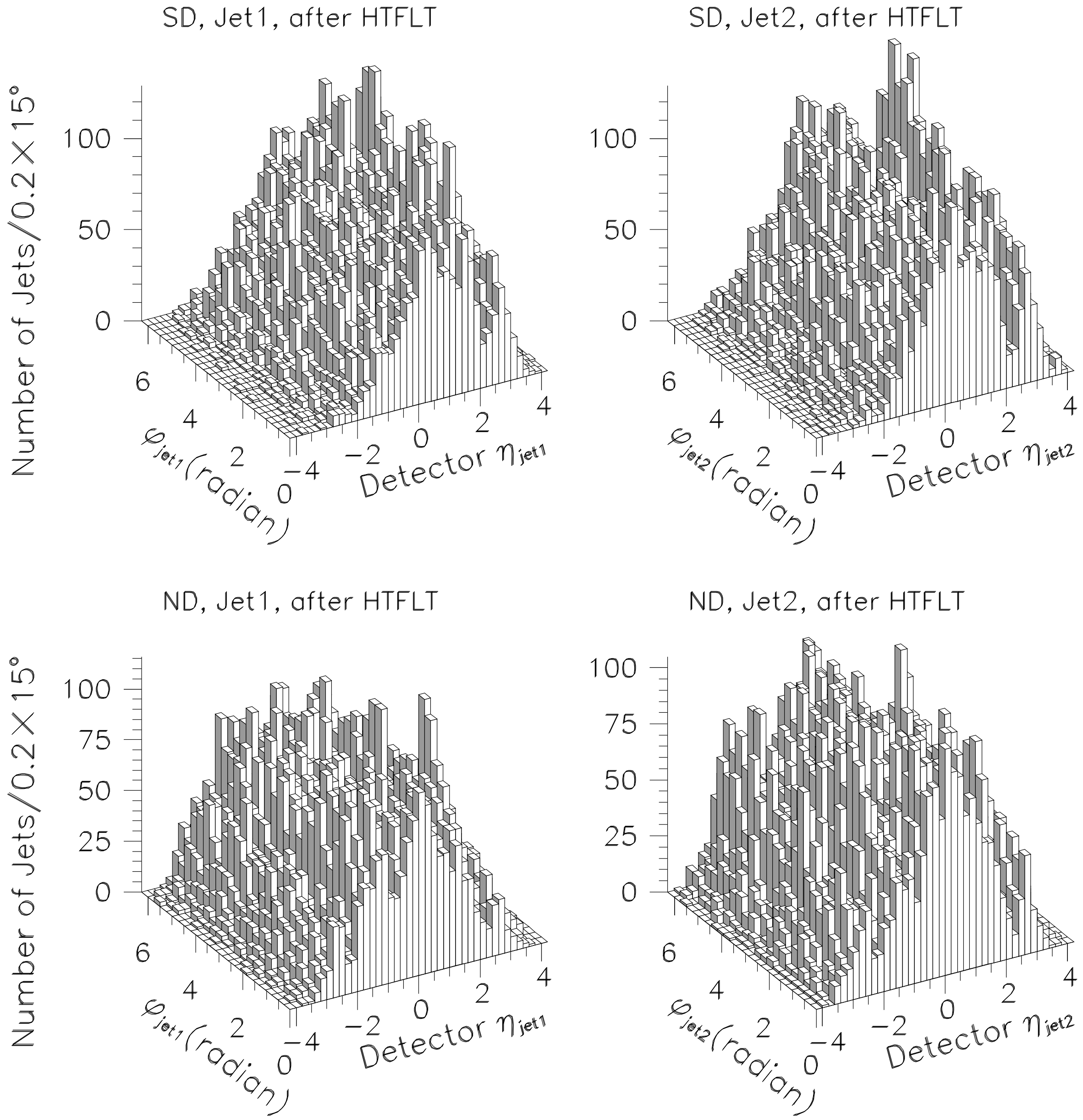

Figure C.4: Distributions of leading (left) and next-to-leading jets on the $\eta - \phi$ plane for the diffractive (top) and non-diffractive (bottom) events with at least two jets with $E_T \geq 7\,\mathrm{GeV}$ which survive the HTFLT.

Calorimeter Noise Spot (Run Range)	Detector-η	ϕ (radian)	EM fraction
Spot 1 (75644 – 75713)	$-1.8 < \eta < -1.2$	$0.7 < \phi < 1.3$	$fr_{\mathrm{EM}} < 0.3$
		$1.4 < \phi < 1.7$	
		$4.0 < \phi < 6.3$	
Spot 2 (75644 – 75713)	$-1.7 < \eta < -1.4$	$\phi < 1.5$	$fr_{\mathrm{EM}} < 0.35$
		$4.8 < \phi < 5.5$	
Spot 3 (75644 – 75713)	$1.3 < \eta < 1.8$	$1.0 < \phi < 1.8$	$fr_{\mathrm{EM}} < 0.3$
		$2.4 < \phi < 5.0$	
		$5.4 < \phi < 6.0$	
Spot 4 (75644 – 75738)	$2.6 < \eta < 3.0$	$2.8 < \phi < 3.2$	$fr_{\mathrm{EM}} > 0.8$
Spot 5 (75714 – 75738)	$1.3 < \eta < 1.8$	$4.6 < \phi < 5.1$	$fr_{\mathrm{EM}} < 0.25$

Table C.1: Summary of Calorimeter noise spots and HTFLT criteria.